Fundamental Principles of Optoelectronic Tweezers

A comprehensive summary for the necessary theoretical background

G.J. Gorsse

Thesis supplementary document
MSc System & Control
MSc Applied Physics

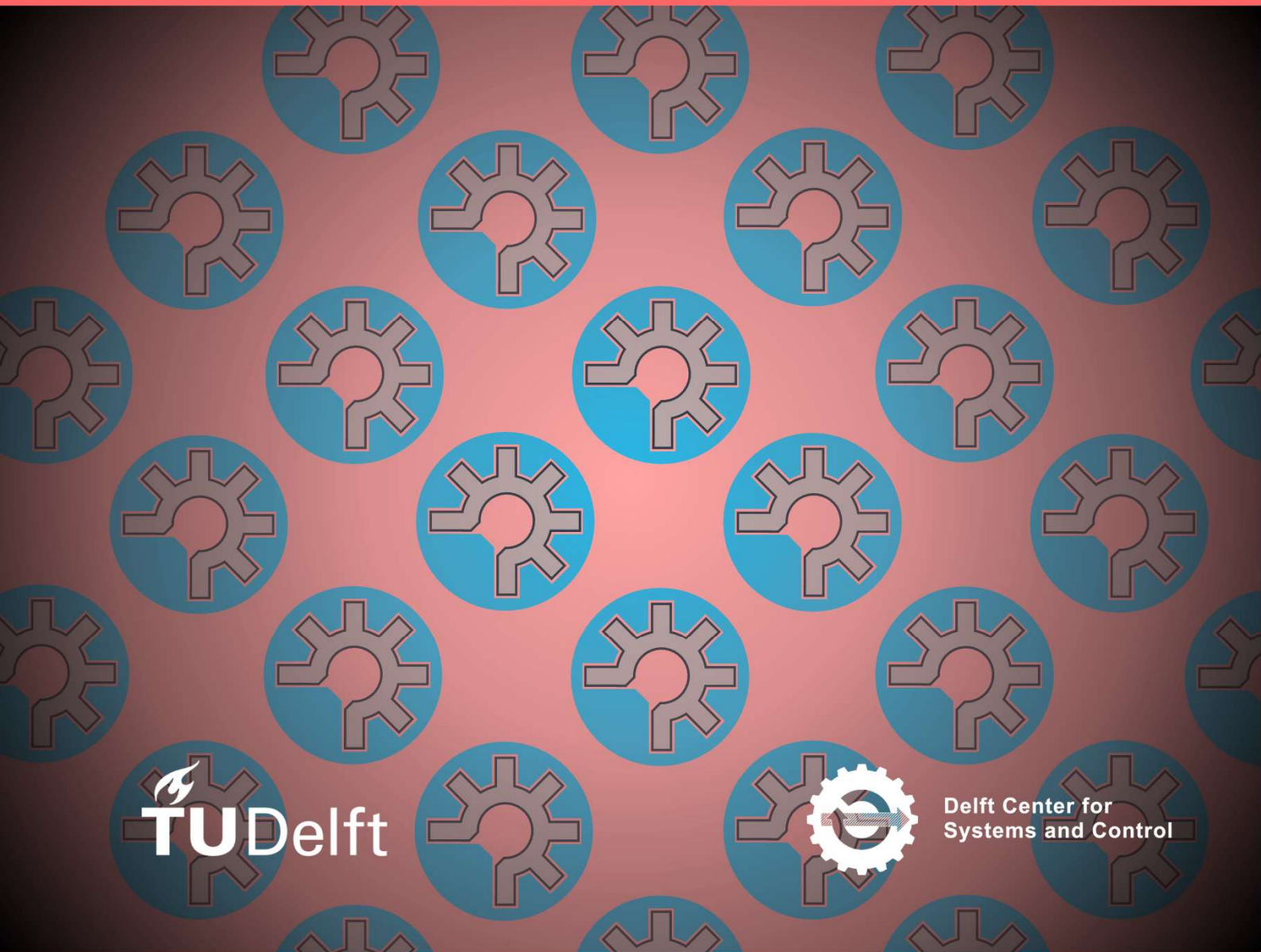

Fundamental Principles of Optoelectronic Tweezers

A comprehensive summary for the necessary theoretical background

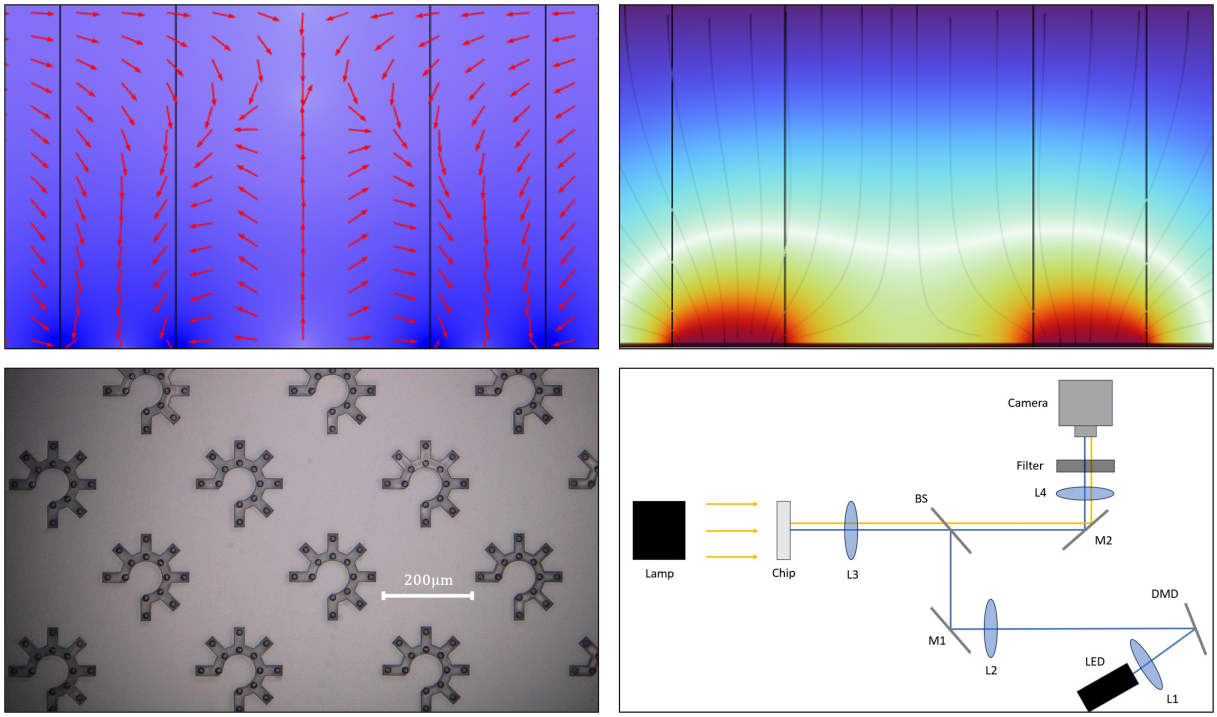

Guus Gorsse

April 2, 2025

TU Delft

Contents

0

Preface

This book—if we may call it that—is a collection of derivations and descriptions intended to deepen the understanding of the optoelectronic tweezer. It is written as supplementary material to my master's thesis, titled "Microgear Robots: Characterization and Control of Shapeable Microparticles in an Optoelectronic Tweezer Setup," submitted in fulfillment of the System Control and Applied Physics master's program at Delft University of Technology. Unlike the thesis, this document has not undergone the same level of academic review or formal scrutiny. It is deliberately written in a more colloquial and accessible style, with the intention of making the topic understandable even to readers with little or no background in physics. While it is not meant to serve as a formal academic source, it aims to provide helpful intuition and a broader context, complementing the main thesis rather than replacing it.

An optoelectronic tweezer (OET) is a device that controls and moves microscopic particles under a microscope accurately. This is done by shining a pattern on a photoconductive layer to adjust an electrical field in a microfluidic chip. This sentence does not make much sense to the general public and needs explanation. This work should cover the complete understanding of the OET at a bachelor's level of physics.

I am Guus, a master's student at the TU Delft on Applied Physics and Systems & Control. The subject of optoelectronic tweezers is part of my master thesis. One of the hardest things about OET is to explain how it works without getting into much detail. This way, a lot of necessary information is not provided that should be known to understand this system's limitations and possibilities fully. This work has been used to explain the subject, in parts but in detail, to several bachelor students, Dion Jetulahi, Rens van Elk, and Mirthe Folkerts, who also put work in the OET. By explaining it to them and writing it down, I got a good understanding of how the OET essentially works. Most formulas used in the literature on OET are really complex. To understand them, I kept asking why until we arrived at a law of physics. This is, therefore, how the derivations are built up in this work. By understanding the physics from the ground up, it should be clear which assumptions we had to make to arrive at the used formulas. This can help us understand the limits and validity when we want to apply them in an optoelectronic tweezer system. The derivations have small steps, making it understandable to follow them.

At the beginning of each section, we included a "Jip en Janneke" translation of the subject talked about. Jip and Janneke, created by Annie M.G. Schmidt and Fiep Westendorp, are two famous figures in Dutch kids' books. A lot of children grew up with them. I have chosen these figures as the face of the elementary-level understanding of OET. The "Jip en Janneke" parts explain the physics as if it were explained to a child. Therefore, these parts should be read to help understand the OET but not as scientific material.

This work has been build up in six sections. Each section explains in detail an essential part of the OET. This work starts with describing the dielectrophoretic force, which is the main driving force of the OET. In section 2, we discuss the microfluidic chip, used as a medium for the particles that are to be controlled. Section 3 discusses how we can adjust the dielectrophoretic force using the photoconductive layer. All the dynamics of the dielectric particle are discussed and put together in section 4. To activate the photoconductive layer and control the particles accurately, we need to use an optical setup to pattern and image the microfluidic chip. This optical setup is discussed in section 5. Finally, to control and create the setup, we need some instrumentation to make the photoconductive layer and to adjust the applied voltages and control inputs. This is discussed in section 6. A schematic overview describing the layout of this work can be seen in figure 1.

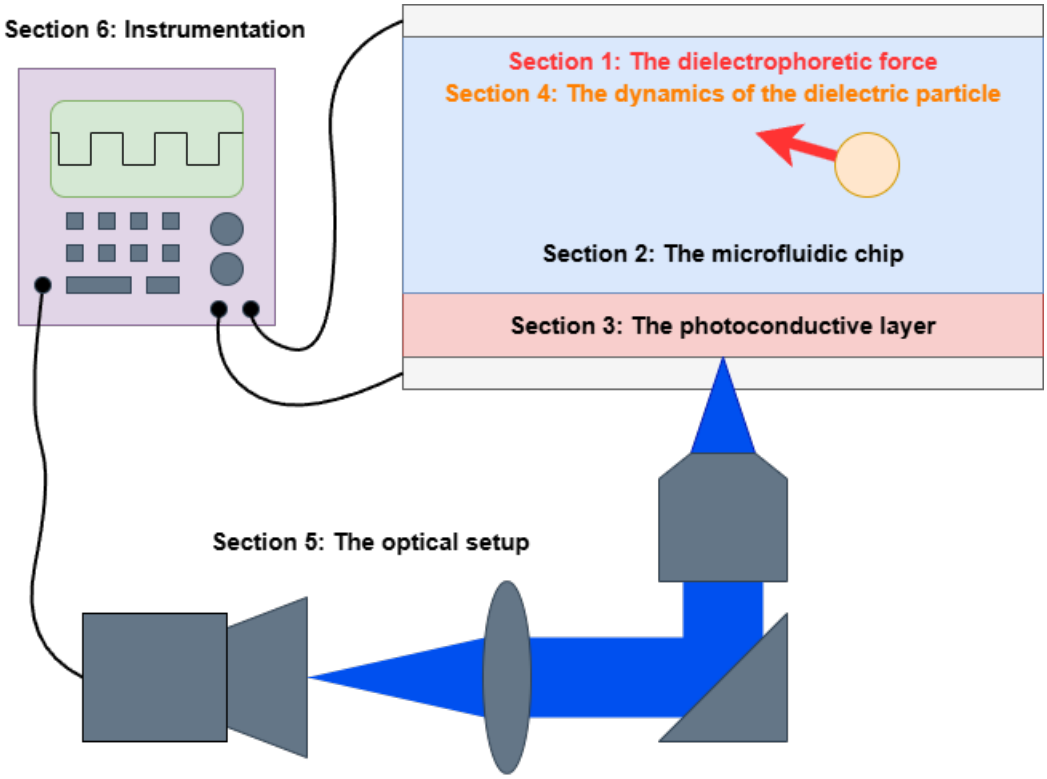

Figure 1: A schematic depiction of an optoelectronic tweezer setup. This describes the structure of this book.

I have used some simulations to back up some claims. The simulations are discussed in detail in their respective sections. The complete data for these simulations is included in the appendices. This work was done under the supervision of Dr. Carlas Smith of the TU Delft. I want to thank him for enabling this project and for the freedom to set up this incredible subject at the TU Delft. A special thanks to Dr. Daniel Fan from the University of Melbourne for his help and insights in this field. I also want to thank Yabin Wang, Dimitri Kromm, Martijn Tijssen, Arno Smets, and Jacob Hoogenboom for helping me understand the topics of the sections in detail. I want to thank Dion Jetulahi, Rens van Elk, and Mirthe Folkerts for helping me make the explanations make sense and make the project more fun. I also want to thank Hadassah Fidder for enabling me to write this work and encourage me to finish it.

I hope I can show you a glimpse of the fascinating world of physics—tucked neatly into the tiny universe of optoelectronic tweezers—and maybe even spark your curiosity for science as a whole.

1

Dielectrophoretic force

This section will discuss the dielectrophoretic force (DEP), the main driving force of OET setups. We will use the electromagnetic laws, as stated by Maxwell, to derive from the ground up how a neutrally charged particle would move due to a non-uniform electrical field in a neutrally charged medium. This interaction is due to the electromagnetic stress tensor, which we will solve for spherical particles in a linearized non-uniform field. We will compare what happens if we include higher orders of this linearized force and conclude which order of linearization is valid. We will also discuss what happens if we add more complexity to the system, such as different waveforms of the alternating applied electrical field, various types of particle compositions, and particle shapes. This section extensively explains the origins of the DEP force to ensure that each assumption and simplification can be well understood. This understanding can be essential when simulating the dynamics in an OET setup.

Dielectrophoretic force for "Jip en Janneke"

In this section, we will explain a concept called dielectrophoretic force, which is essential in optoelectronic tweezers. When we talk about electrodynamics and magnetism, we often refer to fields that help us understand how charged particles move through space. You can think of these fields as a 3D landscape made up of hills and valleys. Imagine a particle sitting on a steep hillside; it will naturally roll down toward the valleys below. This is similar to the concept of dielectrophoresis.

How a particle moves depends on the properties of both the particle and the surrounding material. To describe this interaction properly, we would need to solve many hard equations. So, to make it simpler, we will make some assumptions and simplifications to make it easier and create a more useful formula for the dielectrophoretic force.

Additionally, we will talk about what happens when we introduce more complexity to the particles and the electric field. We show you that it was a good idea to make the formula more simple because it still works. Finally, we will share some simulations that illustrate what the fields and forces look like in optoelectronic tweezers. Here, we can see the hills and valleys the particle goes through in the optoelectronic tweezer. Understanding this force is very important. It is the basis of the optoelectronic tweezers.

The Jip and Janneke illustration is created by the renowned artist Fiep Westendorp.

1.1 Maxwell equations

On June 13, 1831, in Edinburgh, Scotland, one of the leading scientists in the field of electromagnetism, James Clerk Maxwell, was born [1]. He stated the four elegant laws that describe electromagnetic phenomena [2] found in nature denoted in a vacuum and a material (respectively, left and right column).

$$\begin{aligned} \nabla \cdot \mathbf{E} &= \frac{\rho}{\epsilon_0} & \nabla \cdot \mathbf{D} &= \rho_f \\ \nabla \cdot \mathbf{B} &= 0 & \nabla \cdot \mathbf{H} &= 0 \\ \nabla \times \mathbf{E} &= -\frac{\partial \mathbf{B}}{\partial t} & \nabla \times \mathbf{D} &= -\epsilon_0 \mu_0 \frac{\partial \mathbf{H}}{\partial t} \\ \nabla \times \mathbf{B} &= \mu_0 \mathbf{j} + \frac{1}{c^2} \frac{\partial \mathbf{E}}{\partial t} & \nabla \times \mathbf{H} &= \mathbf{j}_f + \frac{\partial \mathbf{D}}{\partial t} \end{aligned} \tag{1}$$

with electrical field $\mathbf{E}$, magnetic field $\mathbf{B}$, free charge density ρ_f, permittivity in free space ϵ_0, permeability of free space μ_0, speed of light c auxiliary field $\mathbf{D}$ and $\mathbf{H}$ and free current density $\mathbf{j}_f$.

In a medium, there can be a current- and a charge density depending on the system's properties and dynamics. We can say that the charge density and current density can be divided into a free part (denoted with a small f) and a bounded part. The bounded parts cannot leave the atoms they are connected to and depend on the polarization[1] $\mathbf{P}$ and magnetization[2] $\mathbf{M}$. The free charge density and current density are extrinsic to the matter.

$$\rho(\mathbf{r},t) = \rho_f(\mathbf{r},t) - \nabla \cdot \mathbf{P}(\mathbf{r},t)$$
$$\mathbf{j}(\mathbf{r},t) = \mathbf{j}_f(\mathbf{r},t) - \nabla \times \mathbf{M}(\mathbf{r},t) + \frac{\partial \mathbf{P}(\mathbf{r},t)}{\partial t}$$

$\mathbf{r}$ denotes the position where we have a point of interest. $\mathbf{D}$ and $\mathbf{H}$ are the auxiliary macroscopic fields and depend on the electrical field, the polarization, the magnetic field, and the magnetization.

$$\mathbf{D}(\mathbf{r},t) = \epsilon_0 \mathbf{E}(\mathbf{r},t) + \mathbf{P}(\mathbf{r},t)$$
$$\mathbf{H}(\mathbf{r},t) = \frac{1}{\mu_0}\mathbf{B}(\mathbf{r},t) - \mathbf{M}(\mathbf{r},t)$$

In the static limit (for "simple" media), we can approximate these auxiliary fields to

$$\begin{aligned} \mathbf{D}(\mathbf{r}) &= \hat{\epsilon}\mathbf{E}(\mathbf{r}) \\ \mathbf{H}(\mathbf{r}) &= \mu \mathbf{B}(\mathbf{r}) \end{aligned} \tag{2}$$

with $\hat{\epsilon}$ denoting the complex dielectric permittivity

$$\hat{\epsilon}(\omega) = \epsilon + i\frac{\sigma}{\omega} \tag{3}$$

with frequency ω and conductivity σ. The i denotes the complex number $\sqrt{-1}$. ϵ denotes the permittivity, and μ, from equation 2, denotes the magnetic permeability, which both depend on the medium the field is in. The speed of light can also described in terms of ϵ and μ as $\frac{1}{c^2} = \epsilon\mu$. In the case of a monochromatic plane, i.e., when the applied electrical field is harmonic with a certain frequency, the auxiliary field $\mathbf{D}$ will be harmonic with a similar frequency dependence. The auxiliary field has, however, a slower response to the electrical field due to the polarization $\mathbf{P}$ not changing instantaneously. The permittivity covers these losses by being partly imaginary [3].

[1] The direction in which the bounded charges are most prominently distributed.
[2] The microscopic current densities within a material.

1.2 The electromagnetic force

For this complete section, a lot of information was gathered from X. Wang et al. and is used to create a clear understanding of the assumptions made to derive the DEP force [4]. The electrical and magnetic fields affect the charges and the current densities in a medium. These effects are captured by the Coulomb-Lorentz force [5]

$$\mathbf{F}_{mech} = \int_V (\rho\mathbf{E} + \mathbf{j} \times \mathbf{B}) d^3r \tag{4}$$

The charge density and current densities are difficult to measure in a medium, which, therefore, gives enough reason to eliminate them from the equation

$$\begin{aligned}
\mathbf{F}_{mech} &= \int_V d^3r \left[(\hat{\epsilon}\nabla \cdot \mathbf{E})\mathbf{E} + \frac{1}{\mu}(\nabla \times \mathbf{B}) \times \mathbf{B} - \hat{\epsilon}\left(\frac{\partial \mathbf{E}}{\partial t} \times \mathbf{B}\right)\right] \\
&= \int_V d^3r \left[(\hat{\epsilon}\nabla \cdot \mathbf{E})\mathbf{E} + \frac{1}{\mu}\left[(\mathbf{B} \cdot \nabla)\mathbf{B} - \frac{1}{2}\nabla(\mathbf{B} \cdot \mathbf{B})\right] - \hat{\epsilon}\left(\frac{\partial}{\partial t}(\mathbf{E} \times \mathbf{B}) - \mathbf{E} \times \frac{\partial \mathbf{B}}{\partial t}\right)\right] \\
&= \int_V d^3r \left[(\hat{\epsilon}\nabla \cdot \mathbf{E})\mathbf{E} + \frac{1}{\mu}\left[(\mathbf{B} \cdot \nabla)\mathbf{B} - \frac{1}{2}\nabla(\mathbf{B} \cdot \mathbf{B})\right] - \hat{\epsilon}\left(\frac{\partial}{\partial t}(\mathbf{E} \times \mathbf{B}) + \mathbf{E} \times (\nabla \times \mathbf{E})\right)\right] \\
&= \int_V d^3r \left[\hat{\epsilon}\left[(\nabla \cdot \mathbf{E})\mathbf{E} - \mathbf{E} \times (\nabla \times \mathbf{E})\right] + \frac{1}{\mu}\left[(\mathbf{B} \cdot \nabla)\mathbf{B} + (\nabla \cdot \mathbf{B})\mathbf{B} - \frac{1}{2}\nabla(\mathbf{B} \cdot \mathbf{B})\right] - \hat{\epsilon}\frac{\partial}{\partial t}(\mathbf{E} \times \mathbf{B})\right] \\
&= \int_V d^3r \left[\hat{\epsilon}\left[(\nabla \cdot \mathbf{E})\mathbf{E} + (\mathbf{E} \cdot \nabla)\mathbf{E} - \frac{1}{2}\nabla(\mathbf{E} \cdot \mathbf{E})\right] + \frac{1}{\mu}\left[(\nabla \cdot \mathbf{B})\mathbf{B} + (\mathbf{B} \cdot \nabla)\mathbf{B} - \frac{1}{2}\nabla(\mathbf{B} \cdot \mathbf{B})\right] - \hat{\epsilon}\frac{\partial}{\partial t}(\mathbf{E} \times \mathbf{B})\right] \\
&= \int_V d^3r \left[\nabla \cdot \mathbf{T} - \hat{\epsilon}\frac{\partial}{\partial t}(\mathbf{E} \times \mathbf{B})\right]
\end{aligned}$$

In the first step, we used equation 1 to eliminate the charge and current densities. We rewrote the double cross product in $\mathbf{B}$ using a vector identity in the second step.

$$\begin{aligned}
(\nabla \times \mathbf{A}) \times \mathbf{A} &= -\mathbf{A} \times (\nabla \times \mathbf{A}) \\
&= -\left(\frac{1}{2}\nabla(\mathbf{A} \cdot \mathbf{A}) - (\mathbf{A} \cdot \nabla)\mathbf{A}\right)
\end{aligned}$$

In the fourth step, we added $(\nabla \cdot \mathbf{B})\mathbf{B}(= 0)$ to create symmetry in the formula. In the fifth step, we rewrote the double cross product in $\mathbf{E}$ using the same identity as we did with $\mathbf{B}$.

We see that the force acting on a volume V can not only be described using a time-dependent cross-product of $\mathbf{E}$ and $\mathbf{B}$ but also by a tensor $\mathbf{T}$. This tensor is called the Maxwell stress tensor and is defined as the dyadic

$$\mathbf{T} = \hat{\epsilon}(\mathbf{EE} - \frac{1}{2}\mathbf{I}|\mathbf{E}|^2) + \mu(\mathbf{BB} - \frac{1}{2}\mathbf{I}|\mathbf{B}|^2) \tag{5}$$

Or when written down in Einstein notation

$$T_{ij} = \hat{\epsilon}(E_iE_j - \frac{1}{2}\delta_{ij}E^2) + \mu(B_iB_j - \frac{1}{2}\delta_{ij}B^2)$$

with i and j coordinates such as x, y, or z. $\mathbf{I}$ is the identity matrix. The remaining term in the force integral, not the tensor $\mathbf{T}$, is known as the Poynting vector [6] and is time-dependent.

In a capacitor (which our system is very similar to), we know that the electric field, due to an applied potential $V(t)$, is given as $\mathbf{E}(t) = -\frac{V(t)}{d}\hat{z}$ with d the height of the capacitor which is in z-direction. Due to the third equation of equation 1, the Ampere-Maxwell law, we know that a magnetic field is created due to the changing field. This field is given as $\mathbf{B} = -\frac{r}{2dc^2}\frac{dV(t)}{dt}\hat{\phi}$ with distance r from the center of the capacitor and the speed of light c. The magnetic field rotates around the z-axis, denoted by the ϕ-direction [7]. If we use these formulas using our known orders of magnitude of the values, we will see why we can ignore all effects due to the magnetic field in the capacitor:

$$\begin{aligned}
d &> 50\mu m,\\
r &< 5cm,\\
\omega &< 50MHz,\\
V(t) &< 25\sin(\omega t) = 25\sin\big(50 * 10^6 t\big),\\
\frac{dV(t)}{dt} &< 25\omega\cos(\omega t) = 125 * 10^6\cos\big(50 * 10^6 t\big),\\
|\mathbf{E}(t)| &< 5 * 10^5\hat{z},\\
|\mathbf{B}(t)| &< 7 * 10^{-6}\hat{\phi}
\end{aligned}$$

The magnetic field is 10^{11} times smaller than the electrical field. Therefore, we will ignore the magnetic, making the Maxwell stress tensor much more understandable and workable.

The remaining part of the Maxwell stress tensor can be simplified even further. When using the Maxwell stress tensor to calculate the force, we are only interested in the real part of the tensor. The complex part is not physical and represents losses. Therefore, we will rewrite the stress tensor to only the real part for convenience. Also, we will write the electrical field in a complex harmonic form[3] such as $\hat{\mathbf{E}}(\mathbf{r},t) = \mathbf{E}(\mathbf{r})e^{i\omega t}$. Therefore, $\mathbf{E} = \mathrm{Re}(\hat{\mathbf{E}}) = \frac{1}{2}(\hat{\mathbf{E}} + \hat{\mathbf{E}}^*)$ which we can use to simplify the useful part of the Maxwell stress tensor more.

$$\begin{aligned}
\mathrm{Re}[\mathbf{T}(\mathbf{r},t)] &= \mathrm{Re}(\hat{\epsilon})\mathrm{Re}\left[\hat{\mathbf{E}}\hat{\mathbf{E}} - \frac{1}{2}(\hat{\mathbf{E}}\cdot\hat{\mathbf{E}})\right]\\
&= \mathrm{Re}(\hat{\epsilon})\left[\frac{1}{2}(\hat{\mathbf{E}}+\hat{\mathbf{E}}^*)\frac{1}{2}(\hat{\mathbf{E}}+\hat{\mathbf{E}}^*) - \frac{1}{2}\left(\frac{1}{2}(\hat{\mathbf{E}}+\hat{\mathbf{E}}^*)\cdot\frac{1}{2}(\hat{\mathbf{E}}+\hat{\mathbf{E}}^*)\right)\right]\\
&= \frac{1}{4}\mathrm{Re}(\hat{\epsilon})\left[\hat{\mathbf{E}}\hat{\mathbf{E}} + \hat{\mathbf{E}}\hat{\mathbf{E}}^* + \hat{\mathbf{E}}^*\hat{\mathbf{E}} + \hat{\mathbf{E}}^*\hat{\mathbf{E}}^* - \frac{1}{2}(\hat{\mathbf{E}}\cdot\hat{\mathbf{E}} + \hat{\mathbf{E}}\cdot\hat{\mathbf{E}}^* + \hat{\mathbf{E}}^*\cdot\hat{\mathbf{E}} + \hat{\mathbf{E}}^*\cdot\hat{\mathbf{E}}^*)\right]\\
&= \frac{1}{4}\mathrm{Re}(\hat{\epsilon})[\mathbf{E}\mathbf{E}e^{2\omega it} + \mathbf{E}\mathbf{E}^* + \mathbf{E}^*\mathbf{E} + \mathbf{E}^*\mathbf{E}^*e^{-2\omega it}\\
&\quad - \frac{1}{2}(\mathbf{E}\cdot\mathbf{E}e^{2\omega it} + \mathbf{E}\cdot\mathbf{E}^* + \mathbf{E}^*\cdot\mathbf{E} + \mathbf{E}^*\cdot\mathbf{E}^*e^{-2\omega it})]\\
&= \frac{1}{4}\mathrm{Re}(\hat{\epsilon})\left[\mathbf{E}\mathbf{E}^* + \mathbf{E}^*\mathbf{E} - \frac{1}{2}\left(|\mathbf{E}|^2 + |\mathbf{E}|^2\right)\mathbf{I}\right] +\\
&\quad \frac{1}{4}\mathrm{Re}(\hat{\epsilon})\left[\mathbf{E}\mathbf{E}e^{2\omega it} + \mathbf{E}^*\mathbf{E}^*e^{-2\omega it} - \frac{1}{2}\left(|\mathbf{E}|^2e^{2\omega it} + |\mathbf{E}|^2e^{-2\omega it}\right)\mathbf{I}\right]\\
&= \mathbf{T}_1(\mathbf{r}) + \mathbf{T}_2(\mathbf{r},t)
\end{aligned} \tag{6}$$

The frequency of the applied field is high so that we will measure many periods of the harmonic signal. This is why we are interested in the time-average effects of the applied field on the dielectric particles. As can be seen, the time-average of the real part of the Maxwell stress tensor is zero for $\mathbf{T}_2(\mathbf{r},t)$ for it only depends on harmonic signals with zero mean[4]. The only thing that remains unsolved is the Poynting vector, but as we already explained, we will ignore the effects of the magnetic field, for it is too small compared to the electrical field effects.

[3] This form can include other terms such as phase in the exponential, but this example is to show the simplification of the equation.

[4] The average of sinusoidal functions is 0 when we take into account many periods.

We can rewrite the force integral using the divergence theorem [8]. Using all these results and methods, we can simplify the time-average dielectrophoretic force due to the Maxwell stress tensor to the final form given as

$$\begin{aligned}\langle \mathbf{F}_{DEP} \rangle &= \int_V d^3r \left[\nabla \cdot \mathbf{T} - \hat{\epsilon} \frac{\partial}{\partial t} (\mathbf{E} \times \mathbf{B}) \right] \\ &\approx \int_V d^3r [\nabla \cdot \mathbf{T}_1] \\ &= \oint_A \mathbf{T}_1 \cdot \hat{n} dS \\ &= \frac{1}{4} \mathrm{Re}(\hat{\epsilon}) \oint_A [\mathbf{E}\mathbf{E}^* + \mathbf{E}^*\mathbf{E} - |\mathbf{E}|^2 \mathbf{I}] \cdot \hat{n} dS\end{aligned} \tag{7}$$

with $\hat{n}$ being the normal vector pointing outwards of the surface A, which is the surface of the particle for which we will derive the DEP force.

1.3 Imposing the boundary conditions

In the dielectric medium, so outside the particle, we denote the electrical field as $\mathbf{E}_1$; in the dielectric particle, we denote it as $\mathbf{E}_2$. The applied harmonic electrical field will be denoted as $\mathbf{E}_0$. We can relate the first two by using interface conditions [9].

$$\begin{aligned}\hat{\epsilon}_1 \mathbf{E}_1 \cdot \hat{n} = \hat{\epsilon}_2 \mathbf{E}_2 \cdot \hat{n} \Rightarrow \mathbf{E}_1 \cdot \hat{n} = \frac{\hat{\epsilon}_2}{\hat{\epsilon}_1} \mathbf{E}_2 \cdot \hat{n} \\ \mathbf{E}_1 \times \hat{n} = \mathbf{E}_2 \times \hat{n} \Rightarrow \mathbf{E}_{1,\parallel} = \mathbf{E}_{2,\parallel}\end{aligned} \tag{8}$$

We can fully relate $\mathbf{E}_1$ and $\mathbf{E}_2$ using these tools.

$$\begin{aligned}\mathbf{E}_1 &= \mathbf{E}_{1,\perp} + \mathbf{E}_{1,\parallel} \\ &= (\mathbf{E}_1 \cdot \hat{n})\hat{n} + \mathbf{E}_{2,\parallel} \\ &= (\mathbf{E}_1 \cdot \hat{n})\hat{n} + \mathbf{E}_2 - (\mathbf{E}_2 \cdot \hat{n})\hat{n} \\ &= \frac{\hat{\epsilon}_2}{\hat{\epsilon}_1}(\mathbf{E}_2 \cdot \hat{n})\hat{n} + \mathbf{E}_2 - (\mathbf{E}_2 \cdot \hat{n})\hat{n} \\ &= \mathbf{E}_2 + \hat{b}(\mathbf{E}_2 \cdot \hat{n})\hat{n}\end{aligned} \tag{9}$$

with $\mathbf{E}_\perp$ denoting the field perpendicular to the boundary (so in the direction of outward pointing $\hat{n}$ of boundary). $\mathbf{E}_\parallel$ denotes the field parallel to the boundary. The equation is written more concise using $\hat{b} = \frac{\hat{\epsilon}_2 - \hat{\epsilon}_1}{\hat{\epsilon}_1}$. We can use this information now to write some identities that will be useful in a short time.

$$\begin{aligned}\mathbf{E}_1\mathbf{E}_1^* \cdot \hat{n} &= [\mathbf{E}_2 + \hat{b}(\mathbf{E}_2 \cdot \hat{n})\hat{n}][\mathbf{E}_2^* + \hat{b}^*(\mathbf{E}_2^* \cdot \hat{n})\hat{n}] \cdot \hat{n} \\ &= [\mathbf{E}_2 + \hat{b}(\mathbf{E}_2 \cdot \hat{n})\hat{n}][\mathbf{E}_2^* \cdot \hat{n} + \hat{b}^*(\mathbf{E}_2^* \cdot \hat{n})\hat{n} \cdot \hat{n}] \\ &= [\mathbf{E}_2 + \hat{b}(\mathbf{E}_2 \cdot \hat{n})\hat{n}](\hat{b}^* + 1)(\mathbf{E}_2^* \cdot \hat{n})\end{aligned}$$

combining this with its complex conjugate,

$$\begin{aligned}\mathbf{E}_1\mathbf{E}_1^* \cdot \hat{n} + \mathbf{E}_1^*\mathbf{E}_1 \cdot \hat{n} &= [\mathbf{E}_2 + \hat{b}(\mathbf{E}_2 \cdot \hat{n})\hat{n}](\hat{b}^* + 1)(\mathbf{E}_2^* \cdot \hat{n}) + [\mathbf{E}_2^* + \hat{b}^*(\mathbf{E}_2^* \cdot \hat{n})\hat{n}](\hat{b} + 1)(\mathbf{E}_2 \cdot \hat{n}) \\ &= (\hat{b}^* + 1)[(\mathbf{E}_2^* \cdot \hat{n})\mathbf{E}_2 + \hat{b}(\mathbf{E}_2 \cdot \hat{n})(\mathbf{E}_2^* \cdot \hat{n})\hat{n}] + \\ &+ (\hat{b} + 1)[(\mathbf{E}_2 \cdot \hat{n})\mathbf{E}_2^* + \hat{b}^*(\mathbf{E}_2^* \cdot \hat{n})(\mathbf{E}_2 \cdot \hat{n})\hat{n}] \\ &= (\hat{b}^* + 1)[A + \hat{b}B] + (\hat{b} + 1)[C + \hat{b}^*B] \\ &= (\hat{b}^* + 1)A + (\hat{b} + 1)C + (\hat{b} + 2\hat{b}\hat{b}^* + \hat{b}^*)B\end{aligned} \tag{10}$$

using $A = (\mathbf{E}_2^* \cdot \hat{n})\mathbf{E}_2$, $C = (\mathbf{E}_2 \cdot \hat{n})\mathbf{E}_2^*$ and $B = (\mathbf{E}_2 \cdot \hat{n})(\mathbf{E}_2^* \cdot \hat{n})\hat{n} = |\mathbf{E}_2 \cdot \hat{n}|^2 \hat{n}$.

$$
\begin{aligned}
|\mathbf{E}_1|^2 &= \mathbf{E}_1 \cdot \mathbf{E}_1^* \\
&= [\mathbf{E}_2 + \hat{b}(\mathbf{E}_2 \cdot \hat{n})\hat{n}] \cdot [\mathbf{E}_2^* + \hat{b}^*(\mathbf{E}_2^* \cdot \hat{n})\hat{n}] \\
&= \mathbf{E}_2 \cdot \mathbf{E}_2^* + \hat{b}(\mathbf{E}_2 \cdot \hat{n})\hat{n} \cdot \mathbf{E}_2^* + \hat{b}^*(\mathbf{E}_2^* \cdot \hat{n})\hat{n} \cdot \mathbf{E}_2 + \hat{b}\hat{b}^*(\mathbf{E}_2 \cdot \hat{n})(\mathbf{E}_2^* \cdot \hat{n}) \\
&= |\mathbf{E}_2|^2 + (\hat{b} + \hat{b}^*)(\mathbf{E}_2 \cdot \hat{n})(\mathbf{E}_2^* \cdot \hat{n}) + \hat{b}\hat{b}^*|\mathbf{E}_2 \cdot \hat{n}|^2 \\
&= |\mathbf{E}_2|^2 + (\hat{b} + \hat{b}\hat{b}^* + \hat{b}^*)|\mathbf{E}_2 \cdot \hat{n}|^2
\end{aligned} \tag{11}
$$

Using equations 10 and 11, we can rewrite equation 7 to represent the DEP force due to the electric field outside of the particle boundary.

$$
\begin{aligned}
\langle \mathbf{f}_{DEP} \rangle &= \frac{1}{4}\mathrm{Re}(\hat{\epsilon}_1) \oint_A [\mathbf{E}_1\mathbf{E}_1^* + \mathbf{E}_1^*\mathbf{E}_1 - |\mathbf{E}_1|^2\mathbf{I})] \cdot \hat{n} dS \\
&= \frac{1}{4}\mathrm{Re}(\hat{\epsilon}_1) \oint_A [(\hat{b}^* + 1)A + (\hat{b} + 1)C + (\hat{b} + 2\hat{b}\hat{b}^* + \hat{b}^*)B - |\mathbf{E}_1|^2\hat{n}] dS \\
&= \frac{1}{4}\mathrm{Re}(\hat{\epsilon}_1) \oint_A [(\hat{b}^* + 1)A + (\hat{b} + 1)C + (\hat{b} + 2\hat{b}\hat{b}^* + \hat{b}^*)B - |\mathbf{E}_2|^2\hat{n} - (\hat{b} + \hat{b}\hat{b}^* + \hat{b}^*)|\mathbf{E}_2 \cdot \hat{n}|^2\hat{n}] dS \\
&= \frac{1}{4}\mathrm{Re}(\hat{\epsilon}_1) \oint_A [(\hat{b}^* + 1)A + (\hat{b} + 1)C + (\hat{b} + 2\hat{b}\hat{b}^* + \hat{b}^*)B - |\mathbf{E}_2|^2\hat{n} - (\hat{b} + \hat{b}\hat{b}^* + \hat{b}^*)B] dS \\
&= \frac{1}{4}\mathrm{Re}(\hat{\epsilon}_1) \oint_A [(\hat{b}^* + 1)A + (\hat{b} + 1)C + \hat{b}\hat{b}^*B - |\mathbf{E}_2|^2\hat{n}] dS \\
&= \frac{1}{4}\mathrm{Re}(\hat{\epsilon}_1) \oint_A [(\hat{b}^* + 1)(\mathbf{E}_2^* \cdot \hat{n})\mathbf{E}_2 + (\hat{b} + 1)(\mathbf{E}_2 \cdot \hat{n})\mathbf{E}_2^* + \hat{b}\hat{b}^*|\mathbf{E}_2 \cdot \hat{n}|^2\hat{n} - |\mathbf{E}_2|^2\hat{n}] dS
\end{aligned} \tag{12}
$$

1.4 Linearizing the electrical field

Equation 12 is not trivial to solve; therefore, we will write the electrical field as a Maclaurin series to simplify the formula even more such that we can solve it analytically [10].

$$
\begin{aligned}
\mathbf{E}_2(\mathbf{r}) &= \mathbf{E}_2(r\hat{n}) \\
&= \sum_{s=0} \frac{1}{s!} r^s (\hat{n} \cdot \nabla)^s \mathbf{E}_2(0) \\
&= \underbrace{\mathbf{E}_2(0) + r(\hat{n} \cdot \nabla)\mathbf{E}_2(0)}_{\text{first-order}} + \underbrace{\frac{1}{2} r^2 (\hat{n} \cdot \nabla)^2 \mathbf{E}_2(0)}_{\text{second-order}} + \dots
\end{aligned} \tag{13}
$$

This way, we can rewrite the components in equation 12, which we will show first only using the first-order approximation and then expanding it to higher orders. From this point forward, we will also approximate the particle as a perfect sphere. This shape is symmetric in every direction,n making it much easier to calculate the surface integral using this shape. The Maxwell stress tensor must be solved numerically for other particle shapes.

1.4.1 Relation between $\mathbf{E}_2$ and $\mathbf{E}_0$

Let's consider a spherical particle with (complex) permittivity $\hat{\epsilon}_2$ in a medium with (complex) permittivity $\hat{\epsilon}_1$. We can relate the applied electrical field $\mathbf{E}_0$ to the electrical field inside the particle $\mathbf{E}_2$. $\mathbf{E}_1$ is the electrical field outside the particle. These fields are depicted schematically in figure 2.

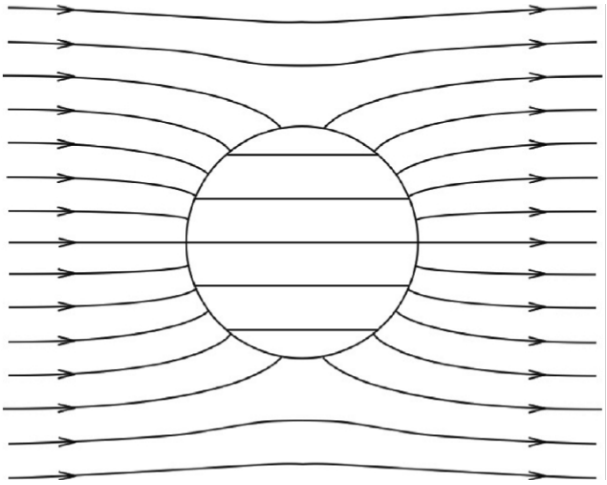

Figure 2: A schematic depiction of the field $\mathbf{E}_1$ outside the particle and the field $\mathbf{E}_2$ inside the particle. The uniform field $\mathbf{E}_0$, which we would expect in a capacitor, is disturbed by the dielectric particle [11].

We can relate the field by writing the applied potential using spherical harmonics[5].

$$\begin{aligned}
\mathbf{\Phi}_0(r,\theta,\phi) &= \sum_{l=0}^{N}\sum_{m=-l}^{l} A_{lm} r^l Y_{lm}(\theta,\phi) \\
\mathbf{\Phi}_1(r,\theta,\phi) &= \mathbf{\Phi}_0(r,\theta,\phi) + \mathbf{\Phi}_{induced}(r,\theta,\phi) \\
&= \sum_{l=0}^{N}\sum_{m=-l}^{l} A_{lm} r^l Y_{lm}(\theta,\phi) + \sum_{l=0}^{N}\sum_{m=-l}^{l} \frac{B_{lm}}{r^{l+1}} Y_{lm}(\theta,\phi) \\
\mathbf{\Phi}_2(r,\theta,\phi) &= \sum_{l=0}^{N}\sum_{m=-l}^{l} C_{lm} r^l Y_{lm}(\theta,\phi)
\end{aligned} \tag{14}$$

To solve this, we need more information on the constants A, Y, B, and C for all l and m. The electric potentials on the boundary of the particle are related by continuity at r_0, which is the radius of the spherical particle.

$$\begin{aligned}
\mathbf{\Phi}_1(r_0,\theta,\phi) &= \mathbf{\Phi}_2(r_0,\theta,\phi) \\
\hat{\epsilon}_1 \frac{\partial \mathbf{\Phi}_1(r,\theta,\phi)}{\partial r}\bigg|_{r=r_0} &= \hat{\epsilon}_2 \frac{\partial \mathbf{\Phi}_2(r,\theta,\phi)}{\partial r}\bigg|_{r=r_0}
\end{aligned} \tag{15}$$

Giving us

$$\begin{aligned}
\mathbf{\Phi}_1(r_0,\theta,\phi) &= \mathbf{\Phi}_2(r_0,\theta,\phi) \\
\sum_{l=0}^{N}\sum_{m=-l}^{l} A_{lm} r^l Y_{lm}(\theta,\phi) + \sum_{l=0}^{N}\sum_{m=-l}^{l} \frac{B_{lm}}{r^{l+1}} Y_{lm}(\theta,\phi) &= \sum_{l=0}^{N}\sum_{m=-l}^{l} C_{lm} r^l Y_{lm}(\theta,\phi) \\
\sum_{l=0}^{N}\sum_{m=-l}^{l} (A_{lm} r^l + \frac{B_{lm}}{r^{l+1}}) Y_{lm}(\theta,\phi) &= \sum_{l=0}^{N}\sum_{m=-l}^{l} C_{lm} r^l Y_{lm}(\theta,\phi) \\
A_{lm} r^l + \frac{B_{lm}}{r^{l+1}} &= C_{lm} r^l \\
A_{lm} + \frac{B_{lm}}{r^{l+2}} &= C_{lm}
\end{aligned} \tag{16}$$

[5]Please note that this is not valid for all forms of particles but only for spherical ones.

and giving us

$$\hat{\epsilon}_1 \frac{\partial \mathbf{\Phi}_1(r,\theta,\phi)}{\partial r}\bigg|_{r=r_0} = \hat{\epsilon}_2 \frac{\partial \mathbf{\Phi}_2(r,\theta,\phi)}{\partial r}\bigg|_{r=r_0}$$

$$\hat{\epsilon}_1 \sum_{l=0}^{N}\sum_{m=-l}^{l} lA_{lm} r^{l-1} Y_{lm}(\theta,\phi) + \hat{\epsilon}_1 \sum_{l=0}^{N}\sum_{m=-l}^{l} -(l+1)\frac{B_{lm}}{r^{l+2}} Y_{lm}(\theta,\phi) = \hat{\epsilon}_2 \sum_{l=0}^{N}\sum_{m=-l}^{l} lC_{lm} r^{l-1} Y_{lm}(\theta,\phi)$$

$$\sum_{l=0}^{N}\sum_{m=-l}^{l} \hat{\epsilon}_1 \left(lA_{lm} r^{l-1} - (l+1)\frac{B_{lm}}{r^{l+2}} \right) Y_{lm}(\theta,\phi) = \sum_{l=0}^{N}\sum_{m=-l}^{l} \hat{\epsilon}_2 lC_{lm} r^{l-1} Y_{lm}(\theta,\phi) \tag{17}$$

$$\hat{\epsilon}_1 \left(lA_{lm} r^{l-1} - (l+1)\frac{B_{lm}}{r^{l+2}} \right) = \hat{\epsilon}_2 lC_{lm} r^{l-1}$$

$$\frac{\hat{\epsilon}_1}{\hat{\epsilon}_2} \left(A_{lm} - \frac{(l+1)}{l}\frac{B_{lm}}{r^{2l+1}} \right) = C_{lm}$$

Using equation 16 and equation 17, we can find a way to write both constant B_{lm} and C_{lm} in terms of A_{lm}.

$$C_{lm} = A_{lm} + \frac{B_{lm}}{r^{l+2}} = \frac{\hat{\epsilon}_1}{\hat{\epsilon}_2} \left(A_{lm} - \frac{(l+1)}{l}\frac{B_{lm}}{r^{2l+1}} \right)$$

$$A_{lm} + \frac{B_{lm}}{r^{l+2}} = \frac{\hat{\epsilon}_1}{\hat{\epsilon}_2} \left(A_{lm} - \frac{(l+1)}{l}\frac{B_{lm}}{r^{2l+1}} \right)$$

$$\frac{B_{lm}}{r^{2l+1}} = \left(1 + \frac{\hat{\epsilon}_1}{\hat{\epsilon}_2}\frac{l+1}{l} \right)^{-1} \left(\frac{\hat{\epsilon}_1}{\hat{\epsilon}_2} - 1 \right) A_{lm} = \frac{\hat{\epsilon}_2 l(\hat{\epsilon}_1 - \hat{\epsilon}_2)}{\hat{\epsilon}_2(\hat{\epsilon}_2 l + \hat{\epsilon}_1 l + \hat{\epsilon}_1)} A_{lm} \tag{18}$$

$$B_{lm} = \frac{l(\hat{\epsilon}_1 - \hat{\epsilon}_2)}{\hat{\epsilon}_2 l + (l+1)\hat{\epsilon}_1} r^{2l+1} A_{lm}$$

$$C_{lm} = A_{lm} + \frac{l(\hat{\epsilon}_1 - \hat{\epsilon}_2)}{\hat{\epsilon}_2 l + (l+1)\hat{\epsilon}_1} A_{lm} = \frac{(2l+1)\hat{\epsilon}_1}{\hat{\epsilon}_2 l + (l+1)\hat{\epsilon}_1} A_{lm} = K_l A_{lm}$$

The last thing we need to do is to relate $\mathbf{\Phi}_2$ to $\mathbf{\Phi}_0$ in the center of the spherical particle, and rewriting this using $E = \nabla\mathbf{\Phi}$[12].

$$\mathbf{\Phi}_2(r,\theta,\phi) = \sum_{l=0}^{N}\sum_{m=-l}^{l} C_{lm} r^l Y_{lm}(\theta,\phi) = \sum_{l=0}^{N}\sum_{m=-l}^{l} K_l A_{lm} r^l Y_{lm}(\theta,\phi) = \sum_{l=0}^{N}\sum_{m=-l}^{l} K_l \mathbf{\Phi}_{0,lm}(r,\theta,\phi)$$

$$\frac{\partial^l \mathbf{\Phi}_2}{\partial x^i \partial y^j \partial z^k}\bigg|_{r=0} = K_l \frac{\partial^l \mathbf{\Phi}_0}{\partial x^i \partial y^j \partial z^k}\bigg|_{r=0} \tag{19}$$

$$(\nabla^l \mathbf{\Phi}_2)(0) = K_l (\nabla^l \mathbf{\Phi}_0)(0)$$

$$(\nabla^{l-1} \mathbf{E}_2)(0) = K_l (\nabla^{l-1} \mathbf{E}_0)(0)$$

for any i, j and k satisfying $i + j + k = l - 1$. Using this beautiful relation, we can rewrite all terms in equation 13 accordingly.

1.4.2 First-order DEP force

When we consider only a slightly non-uniform field, we can neglect all terms in equation 13 to the order $\mathcal{O}(1)$ meaning

$$\begin{aligned}
\mathbf{E}_2(\mathbf{r}) &= \mathbf{E}_2(0) + r(\hat{n}\cdot\nabla)\mathbf{E}_2(0) \\
&= (\nabla^{1-1}\mathbf{E}_2)(0) + r(\hat{n}\cdot\nabla^{2-1})\mathbf{E}_2(0) \\
&= K_1(\nabla^0\mathbf{E}_0)(0) + K_2 r(\hat{n}\cdot\nabla^1)\mathbf{E}_0(0) \\
&= K_1\mathbf{E}_0(0) + rK_2(\hat{n}\cdot\nabla)\mathbf{E}_0(0) \\
(\mathbf{E}_2(\mathbf{r})\cdot\hat{n}) &= K_1\mathbf{E}_0(0)\cdot\hat{n} + rK_2(\hat{n}\cdot\nabla)\mathbf{E}_0(0)\cdot\hat{n}
\end{aligned} \tag{20}$$

Using this, we can express the terms in equation 12 as functions of $\mathbf{E}_0$.

$$\begin{aligned}
(\mathbf{E}_2(\mathbf{r})\cdot\hat{n})\mathbf{E}_2^*(\mathbf{r}) &= K_1^*K_1(\mathbf{E}_0(0)\cdot\hat{n})\mathbf{E}_0^*(0) + rK_1^*K_2(\hat{n}\cdot\nabla)(\mathbf{E}_0(0)\cdot\hat{n})\mathbf{E}_0^*(0) + \\
&+ rK_1K_2^*(\mathbf{E}_0(0)\cdot\hat{n})(\hat{n}\cdot\nabla)\mathbf{E}_0^*(0) + r^2K_2K_2^*(\hat{n}\cdot\nabla)^2(\mathbf{E}_0(0)\cdot\hat{n})\mathbf{E}_0^*(0) \\
(\mathbf{E}_2^*(\mathbf{r})\cdot\hat{n})\mathbf{E}_2(\mathbf{r}) &= K_1^*K_1(\mathbf{E}_0^*(0)\cdot\hat{n})\mathbf{E}_0(0) + rK_1K_2^*(\hat{n}\cdot\nabla)(\mathbf{E}_0^*(0)\cdot\hat{n})\mathbf{E}_0(0) + \\
&+ rK_1^*K_2(\mathbf{E}_0^*(0)\cdot\hat{n})(\hat{n}\cdot\nabla)\mathbf{E}_0(0) + r^2K_2K_2^*(\hat{n}\cdot\nabla)^2(\mathbf{E}_0^*(0)\cdot\hat{n})\mathbf{E}_0(0) \\
|\mathbf{E}_2(\mathbf{r})|^2\hat{n} &= [\mathbf{E}_2(\mathbf{r})\cdot\mathbf{E}_2^*(\mathbf{r})]\hat{n} \\
&= [K_1\mathbf{E}_0(0) + rK_2(\hat{n}\cdot\nabla)\mathbf{E}_0(0)]\cdot[K_1^*\mathbf{E}_0^*(0) + rK_2^*(\hat{n}\cdot\nabla)\mathbf{E}_0^*(0)]\hat{n} \\
&= K_1K_1^*[\mathbf{E}_0(0)\cdot\mathbf{E}_0^*(0)]\hat{n} + rK_1K_2^*[\mathbf{E}_0(0)\cdot(\hat{n}\cdot\nabla)\mathbf{E}_0^*(0)]\hat{n} + \\
&+ rK_1^*K_2[\mathbf{E}_0^*(0)\cdot(\hat{n}\cdot\nabla)\mathbf{E}_0(0)]\hat{n} + r^2K_2K_2^*[(\hat{n}\cdot\nabla)^2\mathbf{E}_0(0)\cdot\mathbf{E}_0^*(0)]\hat{n} \\
|\mathbf{E}_2(\mathbf{r})\cdot\hat{n}|^2\hat{n} &= [(\mathbf{E}_2(\mathbf{r})\cdot\hat{n})\cdot(\mathbf{E}_2^*(\mathbf{r})\cdot\hat{n})]\hat{n} \\
&= [(K_1\mathbf{E}_0(0)\cdot\hat{n} + rK_2(\hat{n}\cdot\nabla)\mathbf{E}_0(0)\cdot\hat{n})\cdot(K_1^*\mathbf{E}_0^*(0)\cdot\hat{n} + rK_2^*(\hat{n}\cdot\nabla)\mathbf{E}_0^*(0)\cdot\hat{n})]\hat{n} \\
&= K_1K_1^*(\mathbf{E}_0(0)\cdot\hat{n})\cdot(\mathbf{E}_0^*(0)\cdot\hat{n})\hat{n} + rK_1K_2^*(\mathbf{E}_0(0)\cdot\hat{n})\cdot(\hat{n}\cdot\nabla)(\mathbf{E}_0^*(0)\cdot\hat{n})\hat{n} + \\
&+ rK_1^*K_2(\mathbf{E}_0^*(0)\cdot\hat{n})\cdot(\hat{n}\cdot\nabla)(\mathbf{E}_0(0)\cdot\hat{n})\hat{n} + r^2K_2K_2^*(\hat{n}\cdot\nabla)(\mathbf{E}_0(0)\cdot\hat{n})\cdot(\hat{n}\cdot\nabla)(\mathbf{E}_0^*(0)\cdot\hat{n})\hat{n}
\end{aligned} \tag{21}$$

We can, therefore, rewrite equation 12 fully using the terms from equation 21. We will rewrite $\mathbf{E}_0(0)$ as $\mathbf{E}_0$, i.e., we will derive the DEP force as a function of the applied electrical field in the center of the spherical particle. The next step is to solve this integral, which is not trivial, to say the least. The first thing we can do here is simplify every integral part that involves odd powers of $\hat{n}$. Those parts will vanish under the surface integral[13]. Also, at the center of the particle, we have one more boundary condition due to the field's uniformity and continuity, i.e., $\nabla\cdot\mathbf{E}_0 = 0$. It is first necessary to show which trick we are using to solve the integrals of the normal vectors. These tricks are related to the second and fourth-order isotropic symmetric tensors. For a sphere, we have for $\hat{n} = [n_x, n_y, n_z]$, $n_x^2 + n_y^2 + n_z^2 = 1$ and therefore $\langle n_i^2\rangle + \langle n_j^2\rangle + \langle n_k^2\rangle = 1$. Due to symmetry in the sphere, we have the same expected values for i, j and k and therefore $\langle n_i^2\rangle = \frac{1}{3}$. We used $i, j, k = x, y, z$ as different notations for the coordinate system. The expected value of $\langle n_i n_j\rangle = 0$ for $i \neq j$ [14].

$$\begin{aligned}
\langle n_i n_j\rangle &= \begin{cases} 0, & \text{if } i \neq j. \\ \frac{1}{3}, & \text{if } i = j. \end{cases} \\
\langle n_i n_j\rangle &= \frac{\oint_S n_i n_j dA}{\oint_S dA} = \langle n_i n_j\rangle \oint_S dA = \frac{1}{3}\int_0^{2\pi}\int_0^{\pi} r^2\sin(\phi)d\phi d\theta = \frac{1}{3}2\pi r^2[-\cos(\phi)]_0^{\pi} = \frac{4\pi}{3}r^2
\end{aligned} \tag{22}$$

For the fourth order, we have a tensor that we can write as a combination of Kronecker delta functions and some constants α, β and γ, using tensor algebra [15]. Here, we used that $\hat{n} = \hat{n}(\phi, \theta) = [\cos(\theta)\sin(\phi), \sin(\theta)\cos(\phi), \cos(\phi)]$.

$$
\begin{aligned}
\langle n_i n_j n_k n_m \rangle &= \alpha\delta_{ij}\delta_{km} + \beta\delta_{ik}\delta_{jm} + \gamma\delta_{im}\delta_{jk} \\
\langle n_i^4 \rangle &= \alpha\delta_{ii}^2 + \beta\delta_{ii}^2 + \gamma\delta_{ii}^2 = \alpha + \beta + \gamma \\
&= \frac{\oint_S n_i^4 dA}{\oint_S dA} = \frac{\int_0^{2\pi}\int_0^{\pi} \cos^4(\phi) r^2 \sin(\phi) d\phi d\theta}{4\pi r^2} = \frac{1}{2}\int_0^{\pi} \cos^4(\phi)\sin(\phi) d\phi \\
u = \cos(\phi) &\rightarrow d\phi = \frac{du}{-\sin(\phi)} \\
\langle n_i^4 \rangle &= \frac{1}{2}\int_1^{-1} u^4 \frac{\sin(\phi)}{-\sin(\phi)} du = \frac{1}{2}[-\frac{u^5}{5}]_1^{-1} = \frac{1}{5}
\end{aligned}
\tag{23}
$$

We found that $\alpha + \beta + \gamma = \frac{1}{5}$ for the fourth-order tensor. When $i = j \neq k = m$, we can derive the values of these constants.

$$
\begin{aligned}
\langle n_i^2 n_j^2 \rangle &= \langle n_i n_i n_j n_j \rangle = \langle n_i n_j n_i n_j \rangle = \langle n_i n_j n_j n_i \rangle \\
\langle n_i n_i n_j n_j \rangle &= \alpha\delta_{ii}\delta_{jj} + \beta\delta_{ij}\delta_{ij} + \gamma\delta_{ij}\delta_{ij} = \alpha \\
\langle n_i n_j n_i n_j \rangle &= \alpha\delta_{ij}\delta_{ij} + \beta\delta_{ii}\delta_{jj} + \gamma\delta_{ij}\delta_{ji} = \beta \\
\langle n_i n_j n_j n_i \rangle &= \alpha\delta_{ij}\delta_{ji} + \beta\delta_{ij}\delta_{ji} + \gamma\delta_{ii}\delta_{jj} = \gamma \\
\alpha &= \beta = \gamma \\
\langle n_i^2 n_j^2 \rangle &= \frac{\alpha + \beta + \gamma}{3} = \frac{\frac{1}{5}}{3} = \frac{1}{15} \\
\oint_S n_i^2 n_j^2 dA &= \langle n_i^2 n_j^2 \rangle \oint_S dA = \frac{4\pi}{15} r^2
\end{aligned}
\tag{24}
$$

We finally have enough tools to solve the integral of equation 12 part by part by looking at the terms in equation 21 and using the integrals from equation 22 and 24 and using that $\nabla \cdot \mathbf{E}_0 = 0$. All the derivations are shown to make clear how these parts will simplify equation 12.

$$
\begin{aligned}
\oint_S (\hat{n}\cdot\nabla)(\mathbf{E}_0\cdot\hat{n})\mathbf{E}_0^* dA &= \oint_S n_i \partial_i E_{0j} n_j E_{0k}^* dA \hat{e}_k \\
&= \partial_i E_{0j} E_{0k}^* \hat{e}_k \oint_S n_i n_j dA (\neq 0 \text{ if } i=j) \\
&= \frac{4\pi}{3} r^2 \partial_i E_{0i} E_{0k}^* \hat{e}_k = \frac{4\pi}{3} r^2 (\nabla\cdot\mathbf{E}_0)\mathbf{E}_0^* = 0 \\
\oint_S (\mathbf{E}_0\cdot\hat{n})(\hat{n}\cdot\nabla)\mathbf{E}_0^* dA &= \oint_S E_{0i} n_i n_j \partial_j E_{0k}^* \hat{e}_k dA \\
&= E_{0i}\partial_i E_{0k}^* \hat{e}_k \oint_S n_i^2 dA = \frac{4\pi}{3} r^2 (\mathbf{E}_0\cdot\nabla)\mathbf{E}_0^* \\
\oint_S (\hat{n}\cdot\nabla)(\mathbf{E}_0^*\cdot\hat{n})\mathbf{E}_0 dA &= 0 \\
\oint_S (\mathbf{E}_0^*\cdot\hat{n})(\hat{n}\cdot\nabla)\mathbf{E}_0 dA &= \frac{4\pi}{3} r^2 (\mathbf{E}_0^*\cdot\nabla)\mathbf{E}_0 \\
\oint_S [\mathbf{E}_0\cdot(\hat{n}\cdot\nabla)\mathbf{E}_0^*]\hat{n} dA &= \oint_S E_{0i} n_i \partial_i E_{0j}^* n_k \hat{e}_k dA \\
&= E_{0i}\partial_i E_{0j}^* \hat{e}_j \oint_S n_i^2 dA = \frac{4\pi}{3} r^2 (\mathbf{E}_0\cdot\nabla)\mathbf{E}_0^* \\
\oint_S [\mathbf{E}_0^*\cdot(\hat{n}\cdot\nabla)\mathbf{E}_0]\hat{n} dA &= \frac{4\pi}{3} r^2 (\mathbf{E}_0^*\cdot\nabla)\mathbf{E}_0 \\
\oint_S (\mathbf{E}_0\cdot\hat{n})\cdot(\hat{n}\cdot\nabla)(\mathbf{E}_0^*\cdot\hat{n})\hat{n} dA &= \oint_S E_{0i} n_i n_i \partial_i E_{0j} n_j n_k \hat{e}_k dA \\
&= E_{0i}\partial_i E_{0j}^* \hat{e}_j \oint_S n_i n_i n_j n_j dA + E_{0i}\partial_i E_{0k}^* \hat{e}_k \oint_S n_i n_i n_k n_k dA \\
&= (\mathbf{E}_0\cdot\nabla)\mathbf{E}_0^* \frac{4\pi}{15} r^2 + (\mathbf{E}_0\cdot\nabla)\mathbf{E}_0^* \frac{4\pi}{15} r^2 = \frac{8}{15}\pi r^2 (\mathbf{E}_0\cdot\nabla)\mathbf{E}_0^* \\
\oint_S (\mathbf{E}_0^*\cdot\hat{n})\cdot(\hat{n}\cdot\nabla)(\mathbf{E}_0\cdot\hat{n})\hat{n} dA &= \frac{8}{15}\pi r^2 (\mathbf{E}_0^*\cdot\nabla)\mathbf{E}_0
\end{aligned}
\tag{25}
$$

We can write the terms in equation 12 as fully worked out integrals from equation 25.

$$
\begin{aligned}
\oint_S (\mathbf{E}_2\cdot\hat{n})\mathbf{E}_2^* dA &= \frac{4}{3}\pi r^3 K_1 K_2^* (\mathbf{E}_0\cdot\nabla)\mathbf{E}_0^* \\
\oint_S (\mathbf{E}_2^*\cdot\hat{n})\mathbf{E}_2 dA &= \frac{4}{3}\pi r^3 K_1^* K_2 (\mathbf{E}_0^*\cdot\nabla)\mathbf{E}_0 \\
\oint_S |\mathbf{E}_2|^2 \hat{n} dA &= \frac{4}{3}\pi r^3 K_1 K_2^* (\mathbf{E}_0\cdot\nabla)\mathbf{E}_0^* + \frac{4}{3}\pi r^3 K_1^* K_2 (\mathbf{E}_0^*\cdot\nabla)\mathbf{E}_0 \\
\oint_S |\mathbf{E}_2\cdot\hat{n}|^2 \hat{n} dA &= \frac{8}{15}\pi r^3 K_1 K_2^* (\mathbf{E}_0\cdot\nabla)\mathbf{E}_0^* + \frac{8}{15}\pi r^3 K_1^* K_2 (\mathbf{E}_0^*\cdot\nabla)\mathbf{E}_0
\end{aligned}
\tag{26}
$$

We know that $K_l = \frac{(2l+1)\hat{\epsilon}_1}{\hat{\epsilon}_2} l + (l+1)\hat{\epsilon}_1 = \frac{(2l+1)}{l\hat{b}+(2l+1)}$.

Using the parts we derived, we can get closer to the known DEP force formula. We denote the first order DEP force vector as $\mathbf{f}_{DEP}^{(1)}$.

$$\begin{aligned}
\langle \mathbf{f}_{DEP}^{(1)} \rangle &= \frac{1}{4}\mathrm{Re}(\hat{\epsilon}_1) \oint_S [(\hat{b}^* + 1)(\mathbf{E}_2^* \cdot \hat{n})\mathbf{E}_2 + (\hat{b} + 1)(\mathbf{E}_2 \cdot \hat{n})\mathbf{E}_2^* + \hat{b}\hat{b}^* |\mathbf{E}_2 \cdot \hat{n}|^2 \hat{n} - |\mathbf{E}_2|^2 \hat{n}] dA \\
&= \frac{1}{4}\mathrm{Re}(\hat{\epsilon}_1) \left(\frac{4}{3}\pi r^3 (\hat{b} + 1) K_1 K_2^* - \frac{4}{3}\pi r^3 K_1 K_2^* + \hat{b}\hat{b}^* \frac{8}{15}\pi r^3 K_1 K_2^* \right) (\mathbf{E}_0 \cdot \nabla)\mathbf{E}_0^* + \\
&\quad + \frac{1}{4}\mathrm{Re}(\hat{\epsilon}_1) \left(\frac{4}{3}\pi r^3 (\hat{b}^* + 1) K_1^* K_2 - \frac{4}{3}\pi r^3 K_1^* K_2 + \hat{b}\hat{b}^* \frac{8}{15}\pi r^3 K_1^* K_2 \right) (\mathbf{E}_0^* \cdot \nabla)\mathbf{E}_0 \\
&= \pi r^3 \mathrm{Re}(\hat{\epsilon}_1) \left[\left(\frac{1}{3}\hat{b} K_1 K_2^* + \frac{2}{15}\hat{b}\hat{b}^* K_1 K_2^* \right) (\mathbf{E}_0 \cdot \nabla)\mathbf{E}_0^* + \left(\frac{1}{3}\hat{b}^* K_1^* K_2 + \frac{2}{15}\hat{b}\hat{b}^* K_1^* K_2 \right) (\mathbf{E}_0^* \cdot \nabla)\mathbf{E}_0 \right] \\
&= \pi r^3 \mathrm{Re}(\hat{\epsilon}_1) \left[\frac{1}{15}\hat{b} \left(5 + 2\hat{b}^* \right) K_1 K_2^* (\mathbf{E}_0 \cdot \nabla)\mathbf{E}_0^* + \frac{1}{15}\hat{b}^* \left(5 + 2\hat{b} \right) K_1^* K_2 (\mathbf{E}_0^* \cdot \nabla)\mathbf{E}_0 \right] \\
&= \pi r^3 \mathrm{Re}(\hat{\epsilon}_1) \frac{1}{15}\hat{b} \left(5 + 2\hat{b}^* \right) \left(\frac{3}{\hat{b} + 3} \right) \left(\frac{5}{2\hat{b}^* + 5} \right) (\mathbf{E}_0 \cdot \nabla)\mathbf{E}_0^* + \\
&\quad + \pi r^3 \mathrm{Re}(\hat{\epsilon}_1) \frac{1}{15}\hat{b}^* \left(5 + 2\hat{b} \right) \left(\frac{3}{\hat{b}^* + 3} \right) \left(\frac{5}{2\hat{b} + 5} \right) (\mathbf{E}_0^* \cdot \nabla)\mathbf{E}_0 \\
&= \pi r^3 \mathrm{Re}(\hat{\epsilon}_1) \left(\frac{\hat{b}}{\hat{b} + 3} (\mathbf{E}_0 \cdot \nabla)\mathbf{E}_0^* + \frac{\hat{b}^*}{\hat{b}^* + 3} (\mathbf{E}_0^* \cdot \nabla)\mathbf{E}_0 \right) \\
&= \pi r^3 \mathrm{Re}(\hat{\epsilon}_1) \left[K(\omega)(\mathbf{E}_0 \cdot \nabla)\mathbf{E}_0^* + K^*(\omega)(\mathbf{E}_0^* \cdot \nabla)\mathbf{E}_0 \right]
\end{aligned} \tag{27}$$

With $K(\omega)$ being the Clausius-Mossotti factor, which indicates if the force is repellent when $K(\omega) < 1$, or attractive when $K(\omega) > 1$. This formula is widely used for optoelectronic tweezers, giving a simple and relatively accurate approach to the physics behind the electromagnetic phenomenon. The force has a different form depending on the applied electrical field. For example, when we apply an electrical field that does not depend on spatial coordinates, we define the DEP force as conventional dielectrophoresis (cDEP). The field has a form as $\mathbf{E}_0 = E_j(\mathbf{r})e^{i\omega t}\hat{e}_j$ with $i = \sqrt{-1}$ and with j being the field in x, y or z direction. The amplitude of the field is a real scalar, depending on location. We will use that $K(\omega) + K^*(\omega) = 2\mathrm{Re}(K(\omega))$ and $\nabla f^2(\mathbf{r}) = 2f(\mathbf{r})\nabla f(\mathbf{r})$.

$$\begin{aligned}
\langle \mathbf{f}_{cDEP}^{(1)} \rangle &= \pi r^3 \mathrm{Re}(\hat{\epsilon}_1) \left[K(\omega)(\mathbf{E}_0 \cdot \nabla)\mathbf{E}_0^* + K^*(\omega)(\mathbf{E}_0^* \cdot \nabla)\mathbf{E}_0 \right] \\
&= \pi r^3 \mathrm{Re}(\hat{\epsilon}_1) \left[K(\omega)(E_j(\mathbf{r})e^{i\omega t}\hat{e}_j \cdot \nabla)E_j(\mathbf{r})e^{-i\omega t}\hat{e}_j + K^*(\omega)(E_j(\mathbf{r})e^{-i\omega t}\hat{e}_j \cdot \nabla)E_j(\mathbf{r})e^{i\omega t}\hat{e}_j \right] \\
&= \pi r^3 \mathrm{Re}(\hat{\epsilon}_1) \left[K(\omega)(E_j(\mathbf{r})e^{i\omega t}e^{-i\omega t}\partial_j)E_j(\mathbf{r})\hat{e}_j + K^*(\omega)(E_j(\mathbf{r})e^{-i\omega t}e^{i\omega t}\partial_j)E_j(\mathbf{r})\hat{e}_j \right] \\
&= \pi r^3 \mathrm{Re}(\hat{\epsilon}_1) \left[K(\omega)E_j(\mathbf{r})\partial_j E_j(\mathbf{r})\hat{e}_j + K^*(\omega)E_j(\mathbf{r})\partial_j E_j(\mathbf{r})\hat{e}_j \right] \\
&= \pi r^3 \mathrm{Re}(\hat{\epsilon}_1) \left[K(\omega) + K^*(\omega) \right] E_j(\mathbf{r})\partial_j E_j(\mathbf{r})\hat{e}_j \\
&= 2\pi r^3 \mathrm{Re}(\hat{\epsilon}_1)\mathrm{Re}(K(\omega))E_j(\mathbf{r})\partial_j E_j(\mathbf{r})\hat{e}_j \\
&= 2\pi r^3 \mathrm{Re}(\hat{\epsilon}_1)\mathrm{Re}(K(\omega)) \left[\frac{1}{2}\partial_j E_j^2(\mathbf{r})\hat{e}_j \right] \\
&= \pi r^3 \mathrm{Re}(\hat{\epsilon}_1)\mathrm{Re}(K(\omega)) \left[\partial_j (\mathbf{E}_0 \cdot \mathbf{E}_0^*)\hat{e}_j \right] \\
&= \pi r^3 \mathrm{Re}(\hat{\epsilon}_1)\mathrm{Re}(K(\omega))\nabla |\mathbf{E}_0|^2
\end{aligned} \tag{28}$$

This equation is widely used and appears in almost every paper discussing DEP force. We see through the derivation which assumptions lay behind this formula. A different variant of the DEP force formula often uses the rms-value of the applied electrical field. When the electrical field behaves like a sinusoidal function, it adds an extra factor 2 and replaces $|\mathbf{E}_0|^2$ with E_{rms}[16].

Another electrical field which we could consider is when the harmonic exponential is also spatially dependent $\mathbf{E}_0 = E_j(\mathbf{r})e^{i(\omega t+\phi_j(\mathbf{r}))}\hat{e}_j$. This is called the generalized DEP force. Here we use that $iK^*(\omega) - iK(\omega) = 2\text{Im}(K(\omega))$. We also used the product rule $\nabla[f(\mathbf{r})g(\mathbf{r}] = f(\mathbf{r})\nabla g(\mathbf{r}) + g(\mathbf{r})\nabla f(\mathbf{r})$.

$$
\begin{aligned}
\langle \mathbf{f}^{(1)}_{gDEP}\rangle &= \pi r^3 \text{Re}(\hat{\epsilon}_1)\left[K(\omega)(\mathbf{E}_0\cdot\nabla)\mathbf{E}_0^* + K^*(\omega)(\mathbf{E}_0^*\cdot\nabla)\mathbf{E}_0\right] \\
&= \pi r^3 \text{Re}(\hat{\epsilon}_1)[K(\omega)(E_j(\mathbf{r})e^{i\omega t}e^{i\phi_j(\mathbf{r})}\hat{e}_j\cdot\nabla)E_j(\mathbf{r})e^{-i\omega t}e^{-i\phi_j(\mathbf{r})}\hat{e}_j + \\
&\quad + K^*(\omega)(E_j(\mathbf{r})e^{-i\omega t}e^{-i\phi_j(\mathbf{r})}\hat{e}_j\cdot\nabla)E_j(\mathbf{r})e^{i\omega t}e^{i\phi_j(\mathbf{r})}\hat{e}_j] \\
&= \pi r^3 \text{Re}(\hat{\epsilon}_1)[K(\omega)(E_j(\mathbf{r})e^{i\phi_j(\mathbf{r})}\partial_j)E_j(\mathbf{r})e^{-i\phi_j(\mathbf{r})}\hat{e}_j + \\
&\quad + K^*(\omega)(E_j(\mathbf{r})e^{-i\phi_j(\mathbf{r})}\partial_j)E_j(\mathbf{r})e^{i\phi_j(\mathbf{r})}\hat{e}_j] \\
&= \pi r^3 \text{Re}(\hat{\epsilon}_1)[K(\omega)E_j(\mathbf{r})e^{i\phi_j(\mathbf{r})}\hat{e}_j[E_j(\mathbf{r})\partial_j e^{-i\phi_j(\mathbf{r})} + e^{-i\phi_j(\mathbf{r})}\partial_j E_j(\mathbf{r})] + \\
&\quad + K^*(\omega)E_j(\mathbf{r})e^{-i\phi_j(\mathbf{r})}\hat{e}_j[E_j(\mathbf{r})\partial_j e^{i\phi_j(\mathbf{r})} + e^{i\phi_j(\mathbf{r})}\partial_j E_j(\mathbf{r})]] \\
&= \pi r^3 \text{Re}(\hat{\epsilon}_1)[K(\omega)[E_j^2(\mathbf{r})e^{i\phi_j(\mathbf{r})}\partial_j e^{-i\phi_j(\mathbf{r})}\hat{e}_j + E_j\partial_j E_j(\mathbf{r})\hat{e}_j] + \\
&\quad + K^*(\omega)[E_j^2(\mathbf{r})e^{-i\phi_j(\mathbf{r})}\partial_j e^{i\phi_j(\mathbf{r})}\hat{e}_j + E_j\partial_j E_j(\mathbf{r})\hat{e}_j]] \\
&= \pi r^3 \text{Re}(\hat{\epsilon}_1)[K(\omega)[-iE_j^2(\mathbf{r})e^{i\phi_j(\mathbf{r})}e^{-i\phi_j(\mathbf{r})}\partial_j\phi_j(\mathbf{r})\hat{e}_j + E_j\partial_j E_j(\mathbf{r})\hat{e}_j] + \\
&\quad + K^*(\omega)[iE_j^2(\mathbf{r})e^{-i\phi_j(\mathbf{r})}e^{i\phi_j(\mathbf{r})}\partial_j\phi_j(\mathbf{r})\hat{e}_j + E_j\partial_j E_j(\mathbf{r})\hat{e}_j]] \\
&= \pi r^3 \text{Re}(\hat{\epsilon}_1)[K(\omega)[\frac{1}{2}\nabla|\mathbf{E}_0|^2 - i(E_x^2(\mathbf{r})\nabla\phi_x(\mathbf{r}) + E_y^2(\mathbf{r})\nabla\phi_y(\mathbf{r}) + E_z^2(\mathbf{r})\nabla\phi_z(\mathbf{r}))] \\
&\quad + K^*(\omega)[\frac{1}{2}\nabla|\mathbf{E}_0|^2 + i(E_x^2(\mathbf{r})\nabla\phi_x(\mathbf{r}) + E_y^2(\mathbf{r})\nabla\phi_y(\mathbf{r}) + E_z^2(\mathbf{r})\nabla\phi_z(\mathbf{r}))] \\
&= \pi r^3 \text{Re}(\hat{\epsilon}_1)[(\frac{1}{2}K(\omega) + \frac{1}{2}K^*(\omega))\nabla|\mathbf{E}_0|^2 + \\
&\quad + (iK^*(\omega) - iK(\omega))(E_x^2(\mathbf{r})\nabla\phi_x(\mathbf{r}) + E_y^2(\mathbf{r})\nabla\phi_y(\mathbf{r}) + E_z^2(\mathbf{r})\nabla\phi_z(\mathbf{r}))] \\
&= \pi r^3 \text{Re}(\hat{\epsilon}_1)[\text{Re}(K(\omega)\nabla|\mathbf{E}_0|^2 + \\
&\quad + 2\text{Im}(K(\omega))(E_x^2(\mathbf{r})\nabla\phi_x(\mathbf{r}) + E_y^2(\mathbf{r})\nabla\phi_y(\mathbf{r}) + E_z^2(\mathbf{r})\nabla\phi_z(\mathbf{r}))] \\
&= \langle \mathbf{f}^{(1)}_{cDEP}\rangle + \langle \mathbf{f}^{(1)}_{twDEP}\rangle
\end{aligned}
\tag{29}
$$

With the $\langle \mathbf{f}_{twDEP}\rangle$ being the traveling wave DEP force which depends on the imaginary part of the Clausius-Mossotti factor and the spatial gradient of the harmonic exponential [17].

1.4.3 Higher-order DEP force

As we saw in equation 13, we can increase the level of complexity (and correctness) by considering a higher order of the MacLaurin series to describe the electrical field inside the particle. The steps to derive the first-order DEP force are similar to those for the higher orders. The final results are shown here to give an idea of the added dynamics. Before we move on to the formulas, it is important to explain some notation that we will use to describe the forces compactly. We will use that $ae^{ib} = a\cos(b) - ia\sin(b)$.

$$
\begin{aligned}
\partial_{k1}\partial_{k2}\ldots\partial_{k(n-1)}E_{0j} &= (E_{j1,k1,k2,\ldots,k(n-1)} - iE_{j2,k1,k2,\ldots,k(n-1)})e^{i\omega t} \\
\text{1st order: } E_{0j} &= (E_{j1} - iE_{j2})e^{i\omega t} \\
&= [E_j\cos(\phi_j) - i(-E_j\sin(\phi_j))]e^{i\omega t} \\
\text{2nd order: } \partial_k E_{0j} &= (E_{j1,k} - iE_{j2,k})e^{i\omega t} \\
&= [E_{j,k}\cos(\phi_{j,k}) - i(-E_{j,k}\sin(\phi_{j,k}))]e^{i\omega t}
\end{aligned}
\tag{30}
$$

with $k1, k2, \ldots, k(n-1)$ being the coordinates x, y, z for each k. If we want to calculate the nth order, we will need information on the nth derivative of the applied electrical field.

Another changed notation we will use is the nth-order Claussius-Mossotti factor.

$$\begin{aligned} K^{(n)}(\omega) &= \frac{n(\hat{\epsilon}_2 - \hat{\epsilon}_1)}{n\hat{\epsilon}_2 + (n+1)\hat{\epsilon}_1} \\ \text{1st order: } K^{(1)}(\omega) &= \frac{\hat{\epsilon}_2 - \hat{\epsilon}_1}{\hat{\epsilon}_2 + 2\hat{\epsilon}_1} \\ \text{2nd order: } K^{(2)}(\omega) &= \frac{2(\hat{\epsilon}_2 - \hat{\epsilon}_1)}{2\hat{\epsilon}_2 + 3\hat{\epsilon}_1} \end{aligned} \tag{31}$$

Using these notations, we can write the generalized DEP force for the nth order [18] and derive from this point the conventional DEP by setting $\phi(\mathbf{r}) = 0$, at the origin of the particle.

$$\begin{aligned} \langle \mathbf{f}_{gDEP} \rangle &= \sum_{n=1}^{p} \langle \mathbf{f}_{gDEP}^{(n)} \rangle \\ \langle \mathbf{f}_{gDEP}^{(n)} \rangle &= \frac{2\pi r^{2n+1} \mathrm{Re}(\hat{\epsilon}_1)}{n!(2n-1)} [\mathrm{Re}(K^{(n)}(\omega))[E_{j1,k1,k2,\ldots,k(n-1)} \nabla E_{j1,k1,k2,\ldots,k(n-1)} \\ &\qquad + E_{j2,k1,k2,\ldots,k(n-1)} \nabla E_{j2,k1,k2,\ldots,k(n-1)}] \\ &\quad + \mathrm{Im}(K^{(n)}(\omega)[E_{j2,k1,k2,\ldots,k(n-1)} \nabla E_{j1,k1,k2,\ldots,k(n-1)} \\ &\qquad - E_{j1,k1,k2,\ldots,k(n-1)} \nabla E_{j2,k1,k2,\ldots,k(n-1)}]] \\ \langle \mathbf{f}_{cDEP}^{(n)} \rangle &= \frac{2\pi r^{2n+1} \mathrm{Re}(\hat{\epsilon}_1)}{n!(2n-1)} \mathrm{Re}(K^{(n)}(\omega)) E_{j1,k1,k2,\ldots,k(n-1)} \nabla E_{j1,k1,k2,\ldots,k(n-1)} \\ \text{1st order: } \langle \mathbf{f}_{gDEP}^{(1)} \rangle &= 2\pi r^3 \mathrm{Re}(\hat{\epsilon}_1)[\mathrm{Re}(K^{(1)}(\omega))[E_{j1} \nabla E_{j1} + E_{j2} \nabla E_{j2}] \\ &\quad + \mathrm{Im}(K^{(1)}(\omega)[E_{j2} \nabla E_{j1} - E_{j1} \nabla E_{j2}]] \\ \langle \mathbf{f}_{cDEP}^{(1)} \rangle &= 2\pi r^3 \mathrm{Re}(\hat{\epsilon}_1) \mathrm{Re}(K^{(1)}(\omega)) E_j \nabla E_j \\ &= \pi r^3 \mathrm{Re}(\hat{\epsilon}_1) \mathrm{Re}(K^{(1)} \nabla |\mathbf{E}_0|^2 \\ \text{2nd order: } \langle \mathbf{f}_{gDEP}^{(2)} \rangle &= \frac{2\pi r^5 \mathrm{Re}(\hat{\epsilon}_1)}{6} [\mathrm{Re}(K^{(2)}(\omega))[E_{j1,k} \nabla E_{j1,k} + E_{j2,k} \nabla E_{j2,k}] \\ &\quad + \mathrm{Im}(K^{(2)}(\omega)[E_{j2,k} \nabla E_{j1,k} - E_{j1,k} \nabla E_{j2,k}]] \\ \langle \mathbf{f}_{cDEP}^{(2)} \rangle &= \frac{2\pi r^5 \mathrm{Re}(\hat{\epsilon}_1)}{6} \mathrm{Re}(K^{(2)}(\omega)) E_{j1,k} \nabla E_{j1,k} \\ &= \frac{\pi r^5 \mathrm{Re}(\hat{\epsilon}_1)}{6} \mathrm{Re}(K^{(2)}(\omega)) \sum_{i,j} \nabla (\partial_i E_j)^2 \\ \text{3rd order: } \langle \mathbf{f}_{cDEP}^{(3)} \rangle &= \frac{2\pi r^7 \mathrm{Re}(\hat{\epsilon}_1)}{30} \mathrm{Re}(K^{(2)}(\omega)) E_{j1,k1,k2} \nabla E_{j1,k1,k2} \\ &= \frac{\pi r^7 \mathrm{Re}(\hat{\epsilon}_1)}{15} \mathrm{Re}(K^{(3)}(\omega)) \sum_{i,j,k} \nabla [\partial_k (\partial_i E_j)]^2 \end{aligned} \tag{32}$$

If we want, for example, to calculate the complete conventional DEP force on the 3rd order, we would have

$$\begin{aligned} \langle \mathbf{f}_{cDEP} \rangle &= \langle \mathbf{f}_{cDEP}^{(1)} \rangle + \langle \mathbf{f}_{cDEP}^{(2)} \rangle + \langle \mathbf{f}_{cDEP}^{(3)} \rangle \\ &= \pi r^3 \mathrm{Re}(\hat{\epsilon}_1) \mathrm{Re}(K^{(1)}(\omega)) \nabla |\mathbf{E}_0|^2 + \frac{\pi r^5 \mathrm{Re}(\hat{\epsilon}_1)}{6} \mathrm{Re}(K^{(2)}(\omega)) \sum_{i,j} \nabla (\partial_i E_j)^2 \\ &\quad + \frac{\pi r^7 \mathrm{Re}(\hat{\epsilon}_1)}{15} \mathrm{Re}(K^{(3)}(\omega)) \sum_{i,j,k} \nabla [\partial_k (\partial_i E_j)]^2 \end{aligned} \tag{33}$$

1.5 Numerical result of the DEP force calculation

1.5.1 Effects of the higher order Clausius-Mossotti factor

As seen in equation 31, the Clausius-Mossotti factor changes by order n. This nth-order Clausius-Mossotti factor can be rewritten into a real and an imaginary part.

$$\begin{aligned}
K^{(n)}(\omega) &= \frac{n(\hat{\epsilon}_2 - \hat{\epsilon}_1)}{n\hat{\epsilon_2} + (n+1)\hat{\epsilon}_1} \\
&= \frac{n(\epsilon_2 - \epsilon_1) + n\frac{1}{\omega}(\sigma_2 - \sigma_1)i}{[n(\epsilon_2 + \epsilon_1) + \epsilon_1] + \frac{1}{\omega}[n(\sigma_2 + \sigma_1) + \sigma_1]i} \\
&= \frac{n(\epsilon_2 - \epsilon_1) + n\frac{1}{\omega}(\sigma_2 - \sigma_1)i}{[n(\epsilon_2 + \epsilon_1) + \epsilon_1] + \frac{1}{\omega}[n(\sigma_2 + \sigma_1) + \sigma_1]i} \times \frac{[n(\epsilon_2 + \epsilon_1) + \epsilon_1] - \frac{1}{\omega}[n(\sigma_2 + \sigma_1) + \sigma_1]i}{[n(\epsilon_2 + \epsilon_1) + \epsilon_1] - \frac{1}{\omega}[n(\sigma_2 + \sigma_1) + \sigma_1]i} \\
&= \frac{n[(\epsilon_2 - \epsilon_1)(n(\epsilon_2 + \epsilon_1) + \epsilon_1) + \frac{1}{\omega^2}(\sigma_2 - \sigma_1)(n(\sigma_2 + \sigma_1) + \sigma_1)]}{(n(\epsilon_2 + \epsilon_1) + \epsilon_1)^2 + \frac{1}{\omega^2}(n(\sigma_2 + \sigma_1) + \sigma_1)^2} \\
&\quad + \frac{n[\frac{1}{\omega}(\epsilon_1 - \epsilon_2)(n(\sigma_2 + \sigma_1) + \sigma_1) + \frac{1}{\omega}(\sigma_1 - \sigma_2)(n(\epsilon_2 + \epsilon_1) + \epsilon_1)]}{(n(\epsilon_2 + \epsilon_1) + \epsilon_1)^2 + \frac{1}{\omega^2}(n(\sigma_2 + \sigma_1) + \sigma_1)^2} i
\end{aligned} \tag{34}$$

From this, we can easily derive for each order n the limits of the Clausius-Mossotti factor by filling in $\omega = 0$ and $\omega = \infty$.

$$\begin{aligned}
K^{(n)}(\omega = 0) &= \frac{n(\epsilon_2 - \epsilon_1) + n\frac{1}{\omega}(\sigma_2 - \sigma_1)i}{[n(\epsilon_2 + \epsilon_1) + \epsilon_1] + \frac{1}{\omega}[n(\sigma_2 + \sigma_1) + \sigma_1]i} \\
&= \frac{\omega(\epsilon_2 - \epsilon_1) + (\sigma_2 - \sigma_1)i}{\omega[(\epsilon_2 + \epsilon_1) + \frac{1}{n}\epsilon_1] + [(\sigma_2 + \sigma_1) + \frac{1}{n}\sigma_1]i} \\
&= \frac{\sigma_2 - \sigma_1}{\sigma_2 + (1 + \frac{1}{n})\sigma_1}
\end{aligned} \tag{35}$$

$$\begin{aligned}
K^{(n)}(\omega = \infty) &= \frac{n(\epsilon_2 - \epsilon_1) + n\frac{1}{\omega}(\sigma_2 - \sigma_1)i}{[n(\epsilon_2 + \epsilon_1) + \epsilon_1] + \frac{1}{\omega}[n(\sigma_2 + \sigma_1) + \sigma_1]i} \\
&= \frac{\epsilon_2 - \epsilon_1}{\epsilon_2 + (1 + \frac{1}{n})\epsilon_1}
\end{aligned} \tag{36}$$

We can also derive the cross-over frequency, which is defined as the frequency $f_{co} = \frac{\omega_{co}}{2\pi}$ where $\mathrm{Re}[K^{(n)}(\omega_{co})] = 0$.

$$\begin{aligned}
\mathrm{Re}[K^{(n)}(\omega_{co})] &= 0 \\
\frac{n[(\epsilon_2 - \epsilon_1)(n(\epsilon_2 + \epsilon_1) + \epsilon_1) + \frac{1}{\omega_{co}^2}(\sigma_2 - \sigma_1)(n(\sigma_2 + \sigma_1) + \sigma_1)]}{(n(\epsilon_2 + \epsilon_1) + \epsilon_1)^2 + \frac{1}{\omega_{co}^2}(n(\sigma_2 + \sigma_1) + \sigma_1)^2} &= 0 \\
n[(\epsilon_2 - \epsilon_1)(n(\epsilon_2 + \epsilon_1) + \epsilon_1) + \frac{1}{\omega_{co}^2}(\sigma_2 - \sigma_1)(n(\sigma_2 + \sigma_1) + \sigma_1)] &= 0 \\
\frac{1}{\omega_{co}^2}(\sigma_2 - \sigma_1)(n(\sigma_2 + \sigma_1) + \sigma_1) &= (\epsilon_1 - \epsilon_2)(n(\epsilon_2 + \epsilon_1) + \epsilon_1)
\end{aligned}$$

Which gives us the cross-over frequency.

$$\begin{aligned}
\omega_{co} &= \sqrt{\frac{(\sigma_2 - \sigma_1)(n(\sigma_2 + \sigma_1) + \sigma_1)}{(\epsilon_1 - \epsilon_2)(n(\epsilon_2 + \epsilon_1) + \epsilon_1)}} \\
f_{co} &= \frac{1}{2\pi}\sqrt{\frac{(\sigma_2 - \sigma_1)(n(\sigma_2 + \sigma_1) + \sigma_1)}{(\epsilon_1 - \epsilon_2)(n(\epsilon_2 + \epsilon_1) + \epsilon_1)}}
\end{aligned} \tag{37}$$

As can be seen in equation 37, there only exists a real finite cross-over frequency when $\frac{\sigma_2-\sigma_1}{\epsilon_1-\epsilon_2} > 0$ which happens when $\sigma_2 > \sigma_1$ and $\epsilon_1 > \epsilon_2$ or when $\sigma_1 > \sigma_2$ and $\epsilon_2 > \epsilon_1$. We can plot the Clausius-Mossotti factor for certain permittivities and conductivities. We take as medium deionized water and as the dielectric particle a 15 μm diameter polystyrene bead. The relative permittivity of deionized water is given as $\epsilon_{1,r} = 78$ and of polystyrene as $\epsilon_{2,r} = 2.56$. The conductivity of deionized water is given as $\sigma_1 = 2 \times 10^{-4} S/m$ [19]. The conductivity of the bead depends on its radius and is given as

$$\sigma_2 = \sigma_{bulk} = \frac{2K_s}{r} \tag{38}$$

With $\sigma_{bulk} = 10^{-16} S/m$ being the bulk conductivity and $K_s = 2 \times 10^{-9} S$ being the surface conductivity and $r = 7.5 \times 10^{-6} m$ being the beads radius [20] [21]. Therefore, we can find that a $15 \mu m$ diameter polystyrene bead has a conductivity of $\sigma_2 = 5.33 \times 10^{-4} S/m$. Using these parameters and using equations 35, 36 and 37, we can find that

$$K^{(1)}(0) = \frac{5.33 \times 10^{-4} - 2 \times 10^{-4}}{5.33 \times 10^{-4} + 4 \times 10^{-4}} = 0.3569$$

$$K^{(\infty)}(0) = \frac{5.33 \times 10^{-4} - 2 \times 10^{-4}}{5.33 \times 10^{-4} + 2 \times 10^{-4}} = 0.4543$$

$$K^{(1)}(\infty) = \frac{\epsilon_0(2.56 - 78)}{\epsilon_0(2.56 + 156)} = -0.4758$$

$$K^{(\infty)}(\infty) = \frac{\epsilon_0(2.56 - 78)}{\epsilon_0(2.56 + 78)} = -0.9364$$

$$f_{co}^{(1)} = \frac{1}{2\pi}\sqrt{\frac{(5.33 \times 10^{-4} - 2 \times 10^{-4})(5.33 \times 10^{-4} + 4 \times 10^{-4})}{\epsilon_0(78 - 2.56)(2.56 + 156)}} = 9.1609 \times 10^4 Hz$$

$$f_{co}^{(\infty)} = \frac{1}{2\pi}\sqrt{\frac{(5.33 \times 10^{-4} - 2 \times 10^{-4})(5.33 \times 10^{-4} + 4 \times 10^{-4})}{\epsilon_0(78 - 2.56)(2.56 + 156)}} = 1.1392 \times 10^5 Hz$$

These results can also be seen in figure 3, where the different colors denote different orders n. The dynamics of the limits of the Clausius-Mossotti factor and the cross-over frequencies for different orders n are shown in figures 4, 5 and 6.

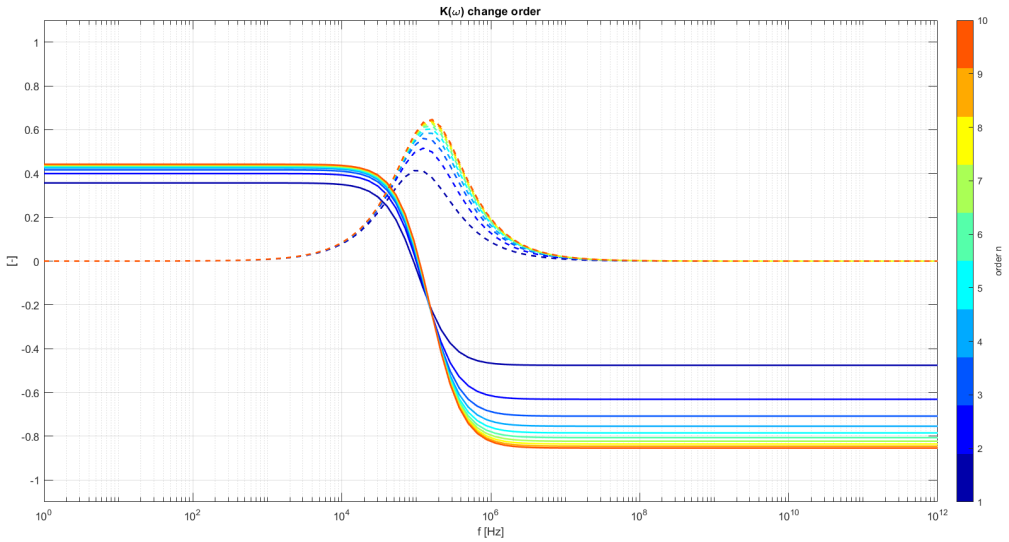

Figure 3: The Claussius-Mossotti factor with frequencies ranging from 1 Hz to 1 THz. The solid line represents the real part, and the dashed line represents the imaginary part. The colors indicate the different orders n.

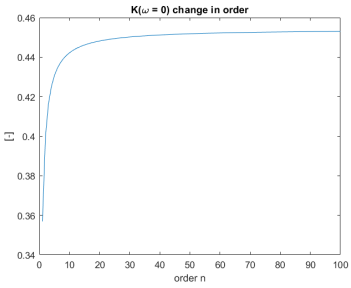

Figure 4: The CM factor at $\omega = 0$ for different orders n

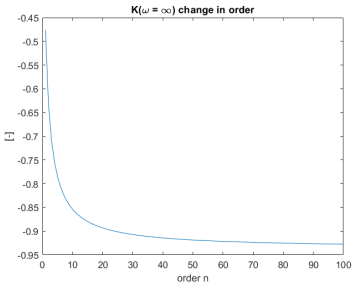

Figure 5: The CM factor at $\omega = \infty$ for different orders n

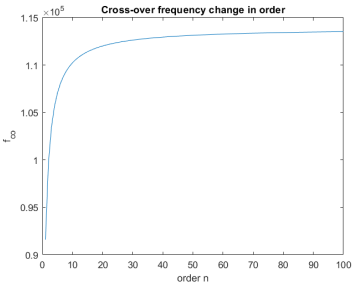

Figure 6: The cross-over frequency for different orders n

As can be seen, at DC voltage ($\omega = 0$), the CM factor at the order of infinity is $\frac{0.4543}{0.3569} = 1.273$ times bigger than at the first order. At the frequency at infinity, the CM factor at the order of infinity is $\frac{-0.9364}{-0.4758} = 1.968$ times bigger than at the first order. These are the maximum differences visible, not including the differences due to the different electrical fields, when including higher orders.

1.5.2 Electrical field simulation in COMSOL

An OET chip was simulated using COMSOL [22]. This OET chip has a total width of 1 mm and consists of 4 layers. The lower layer is made from ITO (In2O3-SnO2) with a height of 200 nm and was given a conductivity of 10^6 S/m [23]. A potential[6] of $25/\sqrt{2}$ V was applied on this bottom ITO layer. On top of this ITO layer, there is a 1 μm layer of amorphous silicon with a light conductivity of $\sigma_L = 10^{-4}$S/m, a dark conductivity of $\sigma_L = 10^{-11}$S/m and a relative permittivity of 11.7 [24]. Two illuminated spots are put symmetric to the center of the chip with an illumination width of 50 μm. On top of this silicon layer is a 150 μm of deionized water with a conductivity of 10^{-4} S/m and a relative permittivity of 78. In this medium, a matrix of 121 by 31 points was inserted, which functions as nodes to pick up structured data. This matrix does not influence the simulation but only creates a way to output the data into a .csv file. On top of this deionized water medium is a final ITO layer with the same parameters as previously discussed. This ITO layer is grounded, which closes the capacitor-like OET chip. Figure 7 shows a zoomed version of the chip with dimensions. The mesh setting was set to "finer" and the physics used was "Electric currents". The simulations were run on an HP Zbook studio G4 with an Intel(R) Core(TM) i7-7700HQ CPU @ 2.80GHz 2.81 GHz, an NVIDIA Quadro M1200, and 8GB RAM. The version used was COMSOL Multiphysics 6.2 (build 339).

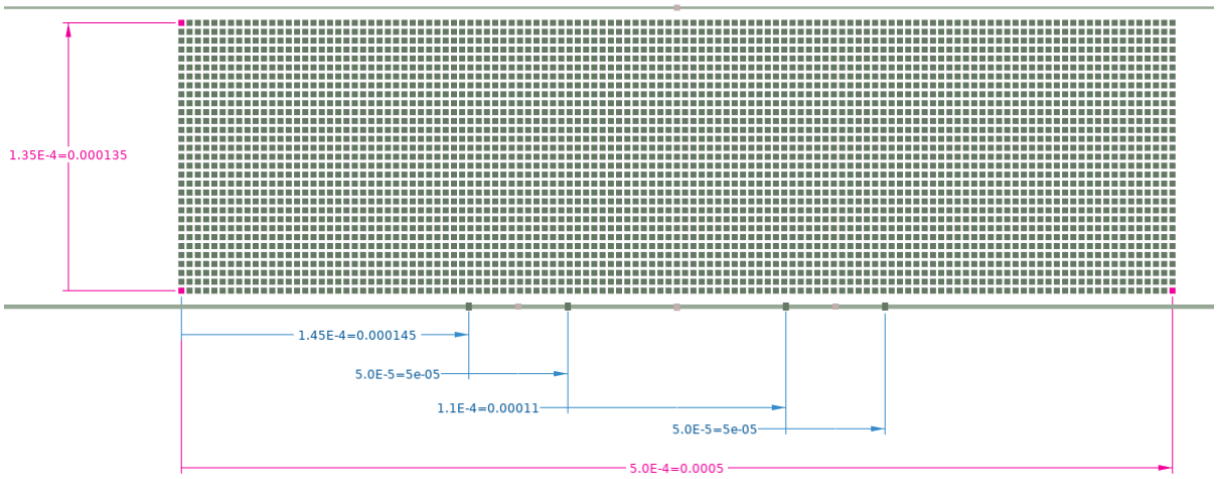

Figure 7: A schematic part of the OET chip created in COMSOL

[6]This is the rms-value of a sinusoidal voltage, which will be discussed later in this section.

The resulting potential distribution and electrical field from this simulation is shown in figure 8. As discussed, the needed information to calculate the DEP force is $\nabla|E_0|^2$, which is also derived in COMSOL and is shown in figure 9.

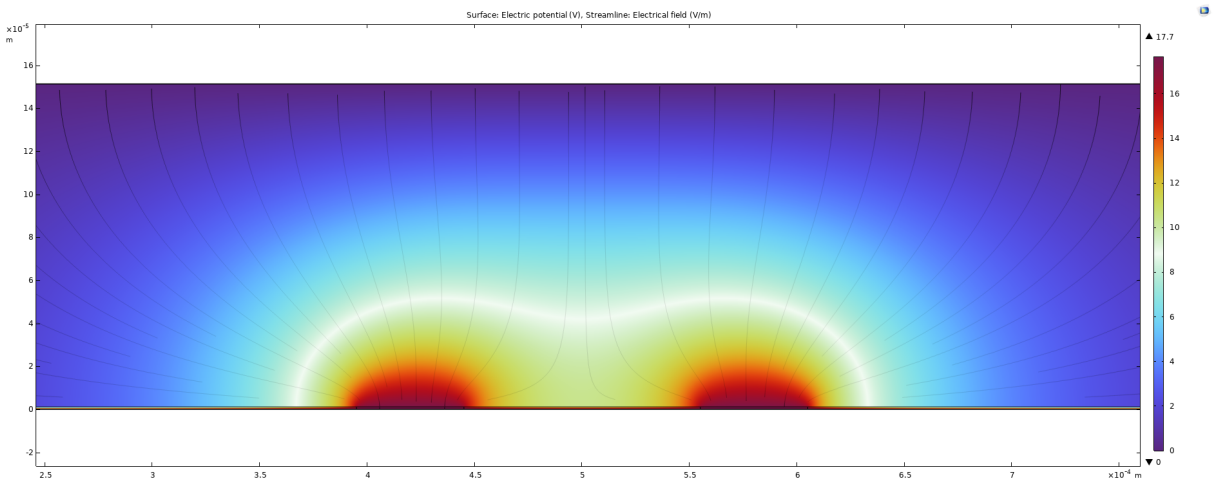

Figure 8: The resulting potential distribution and electrical field from the discussed simulation

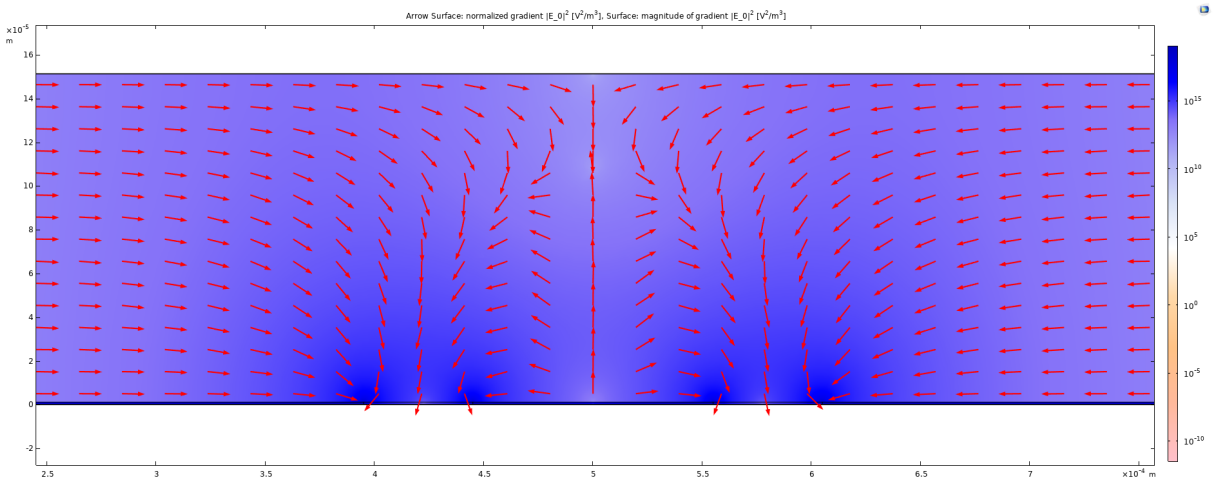

Figure 9: The resulting $\nabla|E_0|^2$ which is needed for the DEP force

In COMSOL, the electrical field was exported on 3751 different points (121 in width direction and 31 in height direction). COMSOL itself was capable of calculating the electrical field's gradient and thus could simulate the first-order DEP force. When applying another gradient, problems arose in COMSOL, which returned null values. Therefore, the exported data was put in MATLAB to simulate the DEP force in higher orders [25]. This was done using the gradient function [26], which takes the central difference for interior data points except on the edges of the set, where it takes the single-sided difference. The simulated electrical field in MATLAB can be seen in figures 10a and 10b. The imported gradients of the electrical field and the derived gradient in MATLAB using only the electrical field data are shown in figures 11a, 12a, 11b and 12b for respectively the derivatives in COMSOL and MATLAB. Figure 13 shows the differences between the imported and derived data. As can be seen, the error has sharp peaks around the peaks of the gradient data itself. This can be explained by some shifting errors. The shape and the magnitude of the COMSOL data and the corresponding MATLAB-derived data are similar enough that we will take this for granted. The primary purpose of this section is to show the working principles and the scaling of the dynamics. Therefore, we will only use the COMSOL data for the electrical field in the x-direction and y-direction, but we will derive all gradients and corresponding forces in MATLAB.

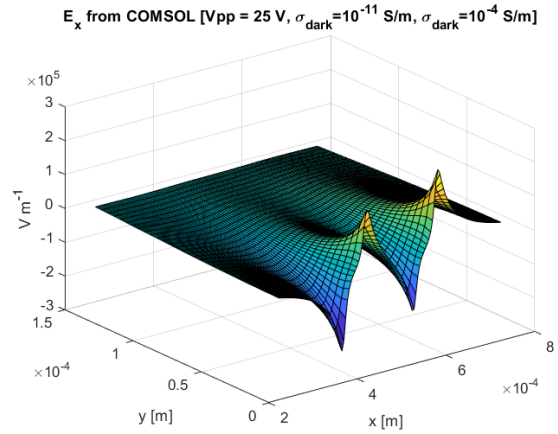

(a) The electrical field in the x-direction from COMSOL

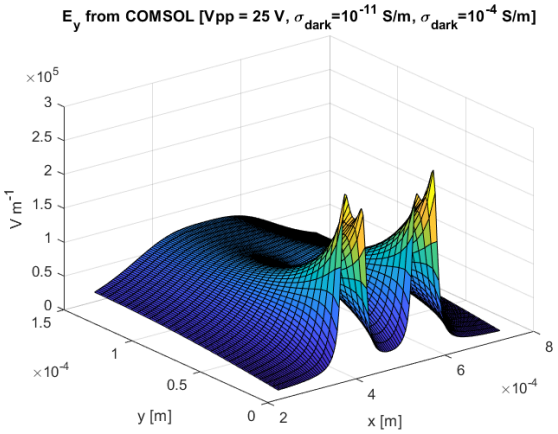

(b) The electrical field in the x-direction from COMSOL

Figure 10: The simulated electrical field from COMSOL opened in MATLAB

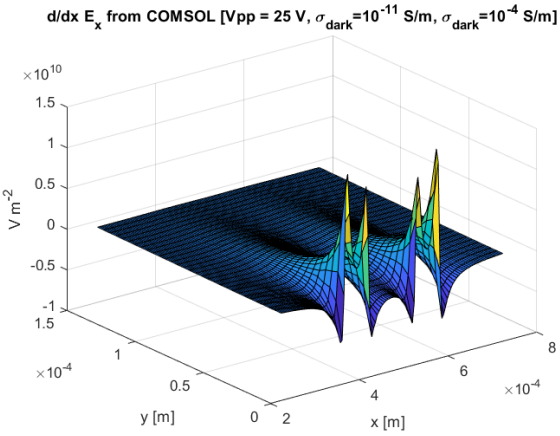

(a) $\frac{d}{dx}E_x$ data from COMSOL

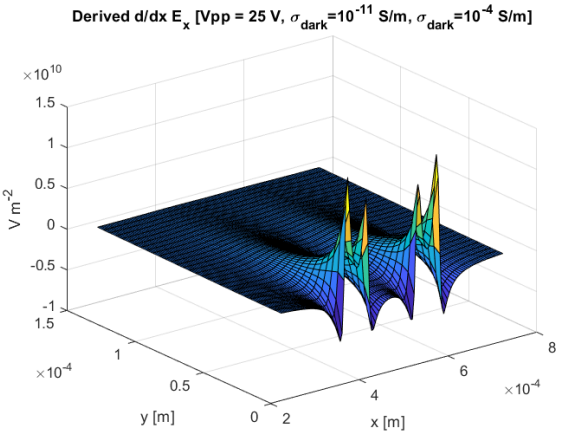

(b) $\frac{d}{dx}E_x$ data derived in MATLAB

Figure 11: A comparison of the gradient of the electrical field in the x-direction using COMSOL and MATLAB

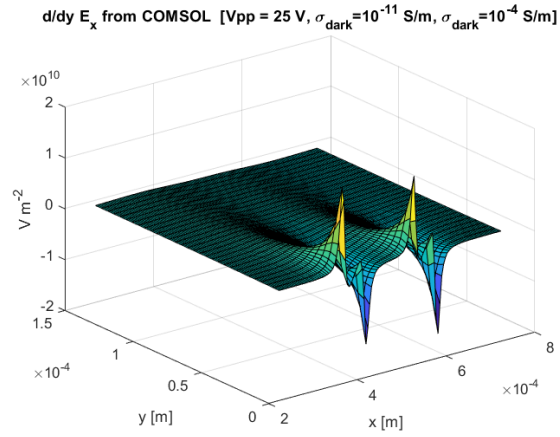

(a) $\frac{d}{dy}E_x$ data from COMSOL

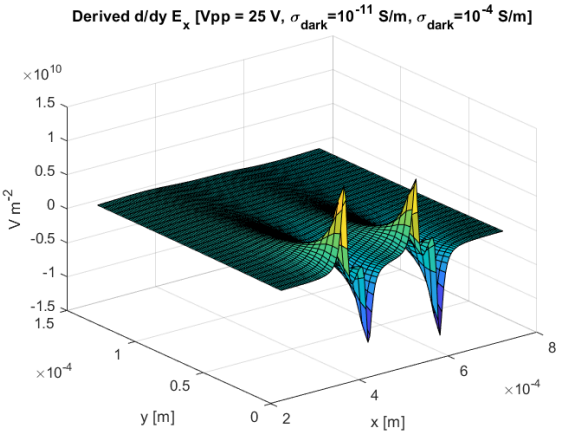

(b) $\frac{d}{dy}E_x$ data derived in MATLAB

Figure 12: A comparison of the gradient of the electrical field in the y-direction using COMSOL and MATLAB

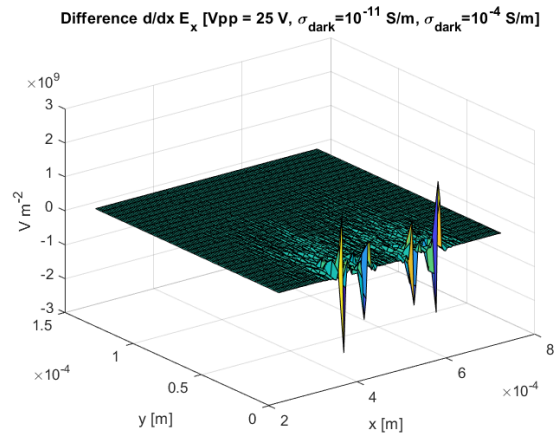

(a) The difference in $\frac{d}{dx}E_x$

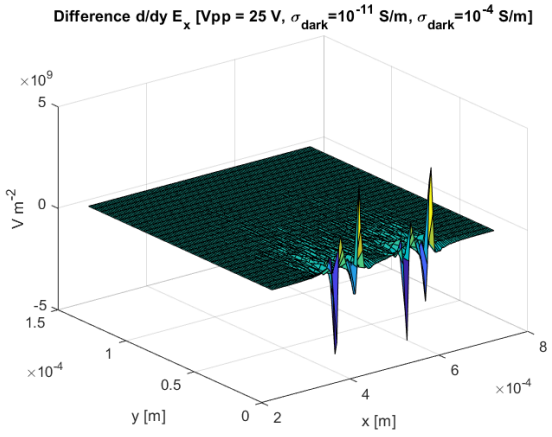

(b) The difference in $\frac{d}{dy}E_x$

Figure 13: The difference between the gradient data created in COMSOL and the data derived in MATLAB

1.5.3 DEP force simulation in MATLAB

We will use MATLAB to derive the factors in equation 33 and see how they scale to each other. The first order factor $\nabla|\mathbf{E}_0|^2$ can be seen in figure 14. The second order factor $\sum_{i,j}\nabla(\partial_i E_j)^2$ can be seen in figure 15. The third order factor $\sum_{i,j,k}\nabla[\partial_k(\partial_i E_j)]^2$ can be seen in figure 16. We already discussed how the Clausius-Mossotti factor behaves at higher orders, so using all this information, we can fill in equation 33.

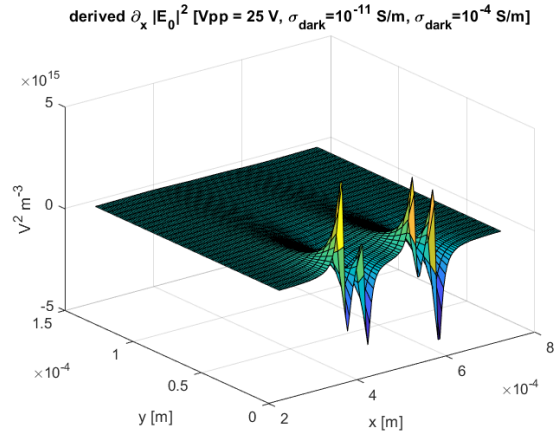

(a) $\nabla|\mathbf{E}_0|^2$ in x-direction

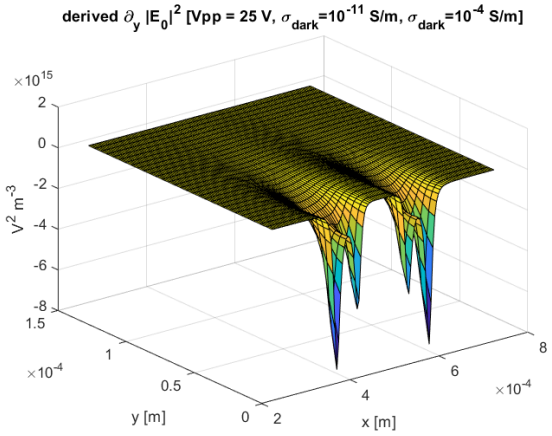

(b) $\nabla|\mathbf{E}_0|^2$ in y-direction

Figure 14: The first order gradient part $\nabla|\mathbf{E}_0|^2$ derived in MATLAB

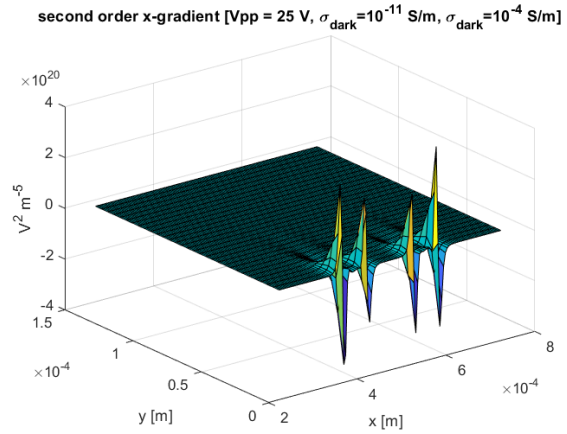

(a) $\sum_{i,j} \nabla(\partial_i E_j)^2$ in x-direction

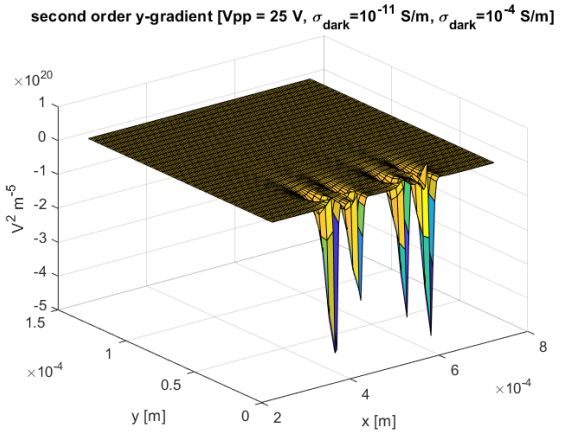

(b) $\sum_{i,j} \nabla(\partial_i E_j)^2$ in y-direction

Figure 15: The second order gradient part $\sum_{i,j} \nabla(\partial_i E_j)^2$ derived in MATLAB

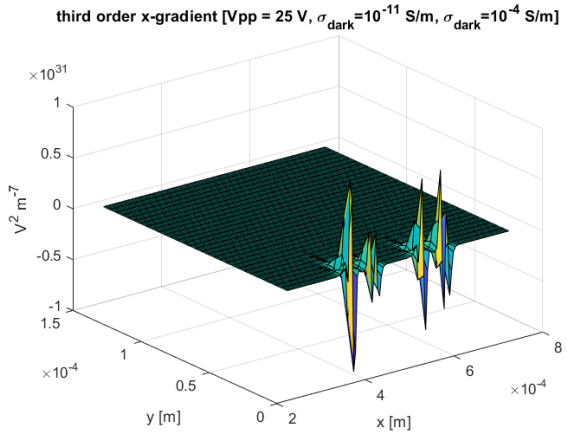

(a) $\sum_{i,j,k} \nabla[\partial_k(\partial_i E_j)]^2$ in x-direction

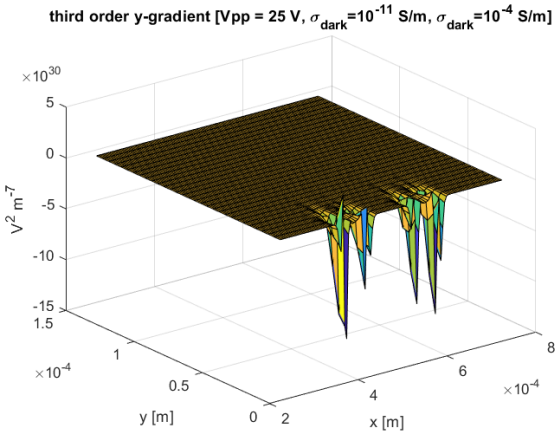

(b) $\sum_{i,j,k} \nabla[\partial_k(\partial_i E_j)]^2$ in y-direction

Figure 16: The third order gradient part $\sum_{i,j,k} \nabla[\partial_k(\partial_i E_j)]^2$ derived in MATLAB

One thing that is already noticeable is the big difference in scaling in each gradient part of each order. The first order part is in the range of 10^{15} whereas the second and third order are respectively in 10^{20} and 10^{31}. This difference decreases with the higher exponents on the bead radius, which grows with an order of 2 for each increasing order in DEP. In fact, they decrease so much that the second and third-order DEP forces are very small compared to the first-order. We can compare how big the gradient parts $E^{(n)}_{factor}$ for each order needs to be compared to $E^{(1)}_{factor}$ so that they are all in the same size range.

$$\begin{aligned}
\pi r^3 \mathrm{Re}(\hat{\epsilon}_1) K^{(1)}_{factor} E^{(1)}_{factor} &= \pi \frac{1}{6} r^5 \mathrm{Re}(\hat{\epsilon}_1) K^{(2)}_{factor} E^{(2)}_{factor} \\
E^{(2)}_{factor} &= \frac{6}{r^2} \frac{K^{(1)}_{factor}}{K^{(2)}_{factor}} E^{(1)}_{factor} \\
&\approx \frac{6}{(7.5\mu m)^2} \frac{1}{1} E^{(1)}_{factor} \approx E^{(1)}_{factor} \times 10^{11} \\
\pi r^3 \mathrm{Re}(\hat{\epsilon}_1) K^{(1)}_{factor} E^{(1)}_{factor} &= \pi \frac{1}{15} r^7 \mathrm{Re}(\hat{\epsilon}_1) K^{(3)}_{factor} E^{(3)}_{factor} \\
E^{(3)}_{factor} &= \frac{15}{r^4} \frac{K^{(1)}_{factor}}{K^{(3)}_{factor}} E^{(1)}_{factor} \\
&\approx \frac{15}{(7.5\mu m)^4} \frac{1}{1} E^{(1)}_{factor} \approx E^{(1)}_{factor} \times 10^{21}
\end{aligned} \tag{39}$$

Due to the small radius, we see that the second and third orders differ by more than a factor 10^5. This can also be seen in figure 17 where the DEP force in the x-direction and y-direction are plotted against each order in a logarithmic scale. As was already predicted, higher-order forces than $n = 1$ are neglectable. Therefore, the first-order DEP force is a pretty good approximation of the DEP force in an optoelectronic tweezer setup.

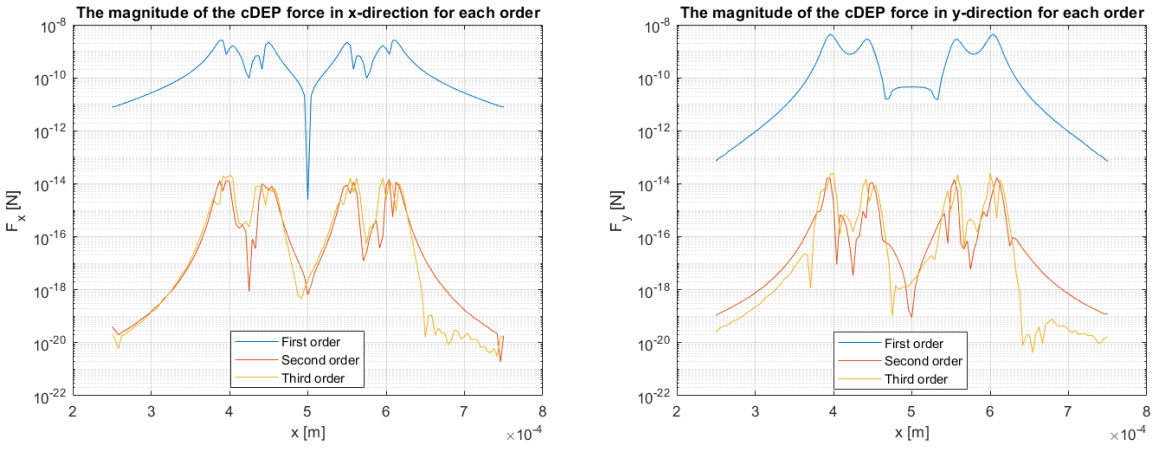

(a) DEP force in x-direction for 3 orders

(b) DEP force in y-direction for 3 orders

Figure 17: A comparison of the DEP force using 3 different orders

The electrical field depends on the applied voltage, the difference between the illuminated and dark conductivity of the photoconductor, the permittivity of the medium, and the bead radius. The force simulated in the previous section is, therefore, on the high side, considering the effects of the parameters. Also, this simulation is done in 2D to show the impact of higher-order DEP force contributions.

When considering a 3D polystyrene bead in a 3D medium, we cannot just take one point in space and decide that it will determine the magnitude of the DEP force. We must take the volume average as a correction to get a more accurate description. For example, the grid is spaced 4.17 μm in the x-direction and 4.50 μm in the y-direction, so if we take a 15 μm diameter bead, it overlaps multiple grid nodes. Therefore, we must calculate the first-order field gradient as average.

$$\nabla|\mathbf{E}_0|^2_{simulation} = \frac{\iiint_V \nabla|\mathbf{E}_0|^2 dV}{\frac{4}{3}\pi r^3} \tag{40}$$

The simulation is the part to be put in the DEP force formula. Suppose we want to compare this with literature. In that case, we need to take a radius that is less than $\approx \frac{4\mu m}{2}$ to fit it within the grid nodes[7]. When we would take a 4 μm diameter bead and an applied signal of 25 Vpp, we would end up with a maximum force of 2.2301 pN and 3.8038 pN in respectively x-direction and y-direction as can be seen in figure 18. Compared to literature, this is in the right ballpark (around $2 \sim 3$ pN) [27]. This was already evident by looking at the scaling of the electrical field and its gradients [28].

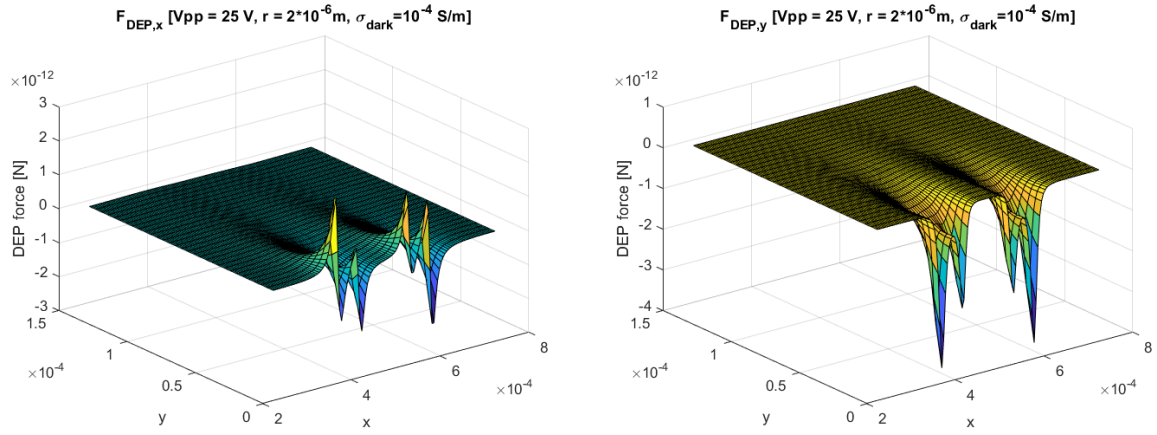

(a) DEP force in x-direction

(b) DEP force in y-direction

Figure 18: A comparison of the DEP force with literature [27].

In literature, the DEP force is often denoted as positive or negative. We talk about a positive DEP force when a particle is attracted to an illuminated spot. In contrast, the DEP is negative when a particle is repelled by the illuminated spot [29]. This is directly related to the Clausius-Mossotti factor. When this factor is positive, we have a positive DEP verse and vice versa. This is schematically shown in figure 19.

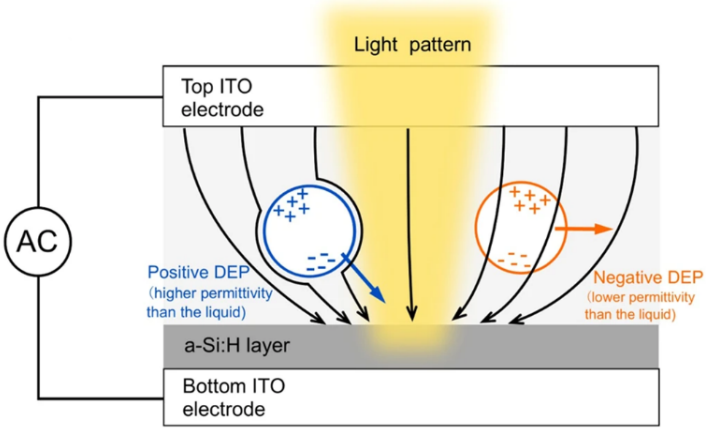

Figure 19: A schematic depiction of a positive and a negative DEP force from [30].

[7] Actually, this is still a tricky description because the integral needs to take more points into account to get an accurate volume average. Nevertheless, this is for benchmarking purposes good enough for this project's scope

1.6 The shape of the applied electrical field

The form of the applied signal in the previous section was sinusoidal. Due to $\nabla|\mathbf{E}_0|^2$, we have the absolute magnitude of the field, meaning that the force depends on the absolute magnitude of the applied signal. This is what we call the root-mean-square [31] and is defined by the square of the integral of the signal in one period divided by the period length.

$$E_{rms} = \sqrt{\frac{1}{T}\int_0^T [E(t)]^2 dt} \tag{41}$$

When we take a sinusoidal function such as $E(t) = A\sin\left(\frac{2\pi}{T}t\right)$, this would result in

$$E_{rms} = \sqrt{\frac{1}{T}\int_0^T \left[A\sin\left(\frac{2\pi}{T}t\right)\right]^2 dt} = \sqrt{\frac{1}{T}\int_0^T A^2\sin^2(\frac{2\pi}{T}t)dt} = \sqrt{\frac{A^2}{T}\left[\frac{t}{2} - \frac{\sin\left(\frac{4\pi}{T}t\right)}{\frac{8\pi}{T}}\right]_{t=0}^{t=T}}$$
$$= \sqrt{\frac{A^2}{T}\left(\frac{T}{2} - \frac{\sin(4\pi)T}{8\pi} - \frac{0}{2} + \frac{\sin(0)}{8\pi}\right)} = \sqrt{\frac{A^2}{2}} = \frac{A}{\sqrt{2}}$$

Therefore, when applying a sinusoidal signal with an amplitude of V, we will have an effective electrical field of 0.707 V. This is different for different signal shapes. For an alternating field, the effective electrical field is the strongest using a square wave because the effective field strength is equal to the amplitude of the square wave [32]. A comparison of the waveform shape effect is shown in figure 20. Keep in mind that in the force equation, the E_{rms} is squared meaning that the ratio between a square wave and a sinusoidal wave is respectively $(A)^2 : \left(\frac{A}{\sqrt{2}}\right)^2 \rightarrow A^2 : \frac{A^2}{2}$.

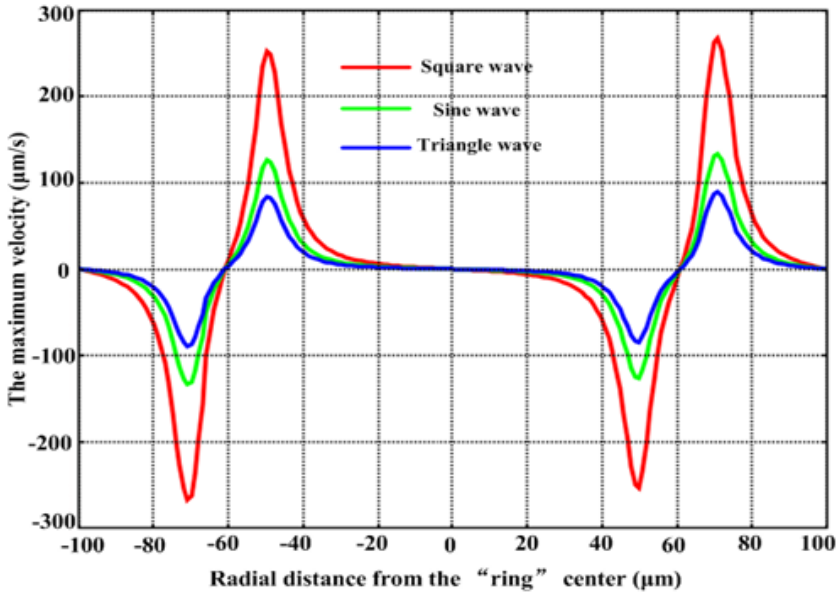

Figure 20: The effect of the waveform shape in an OET trap for alternating potentials with the same amplitude.

1.7 DEP force in multilayer particles

In the previous section, we only looked at particles of a single material. This works for testing subjects such as polystyrene beads but will not be accurate for widely occurring particles of interest, such as e.g. cells. The DEP force from equation 28 depends on the particle material in the Clausius-Mossotti factor in equation 31. Therefore, when working with multilayer particles, another way of describing $\hat{\epsilon}_2$ is necessary. We will show 3 ways the complex permittivity can be approached [33]. These approaches describe the particles shown in figure 21b, c, and d.

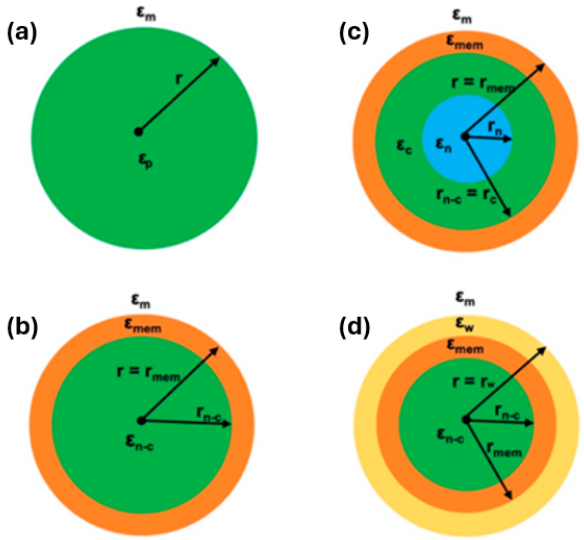

Figure 21: Multilayer models for DEP force calculation. (a) Single-layer model. (b) Two-layer model. (c) Three-layer model for mammalian cells without a cell wall. (d) Three-layer model for plant cells with a cell wall. [33]

When considering a two-layer model, we can denote r_{mem} and $\hat{\epsilon}_{mem}$ as the radius of the whole cell and the complex permittivity of the membrane. We denote r_{n-c} and $\hat{\epsilon}_{n-c}$ as the radius and the complex permittivity of the center of the cell[8].

$$\hat{\epsilon}_2 = \hat{\epsilon}_{cell}^{eff} = -\hat{\epsilon}_{mem}\frac{2(\hat{\epsilon}_{n-c}-\hat{\epsilon}_{mem})r_{n-c}^3 + (\hat{\epsilon}_{n-c}+2\hat{\epsilon}_{mem})r_{mem}^3}{(\hat{\epsilon}_{n-c}-\hat{\epsilon}_{mem})r_{n-c}^3 - (\hat{\epsilon}_{n-c}+2\hat{\epsilon}_{mem})r_{mem}^3} \tag{42}$$

When we consider a three-layer model such as in figure 21c, We introduce a separate nucleus with radius r_n and complex permittivity $\hat{\epsilon_n}$. The cytoplasm has radius r_c and $\hat{\epsilon}_c$. This means that $\hat{\epsilon}_{n-c}$ from equation 42 will get more complex and defined.

$$\hat{\epsilon}_{n-c} = -\hat{\epsilon}_c\frac{2(\hat{\epsilon}_n-\hat{\epsilon}_c)r_n^3 + (\hat{\epsilon}_n+2\hat{\epsilon}_c)r_c^3}{(\hat{\epsilon}_n-\hat{\epsilon}_c)r_n^3 - (\hat{\epsilon}_n+2\hat{\epsilon}_c)r_c^3} \tag{43}$$

Finally, suppose we would consider a three-layer model with instead of a separate nucleus an added cell wall with radius r_w and complex permittivity $\hat{\epsilon}_w$. In that case, we need to define the complex permittivity of the particle again in steps. We define, e.g., the radius to the membrane as $r_{n-c-mem}$.

$$\begin{aligned}
\hat{\epsilon}_p = \hat{\epsilon}_{cell}^{eff} &= -\hat{\epsilon}_w\frac{2(\hat{\epsilon}_{n-c-mem}-\hat{\epsilon}_w)r_{n-c-mem}^3 + (\hat{\epsilon}_{n-c-mem}+2\hat{\epsilon}_w)r_w^3}{(\hat{\epsilon}_{n-c-mem}-\hat{\epsilon}_w)r_{n-c-mem}^3 - (\hat{\epsilon}_{n-c-mem}+2\hat{\epsilon}_w)r_w^3} \\
\hat{\epsilon}_{n-c-mem} &= -\hat{\epsilon}_{mem}\frac{2(\hat{\epsilon}_{n-c}-\hat{\epsilon}_{mem})r_{n-c}^3 + (\hat{\epsilon}_{n-c}+2\hat{\epsilon}_{mem})r_{n-c-mem}^3}{(\hat{\epsilon}_{n-c}-\hat{\epsilon}_{mem})r_{n-c}^3 - (\hat{\epsilon}_{n-c}+2\hat{\epsilon}_{mem})r_{n-c-mem}^3}
\end{aligned} \tag{44}$$

[8] With n-c, we mean the nuclear and the cytoplasm

1.8 DEP force in non-spherical particles

Besides multilayer particles, particles in OET setups can also be non-spherical. In most cases, this is very hard to solve for complex forms and numerical analysis is usually required to solve the Maxwell stress tensor and simulate the DEP phenomena well. A good example is when using a silicon microbot as a particle with a complex shape. In figure 22, we see 3 different complex forms made by SU8. In figure 23, we see the comparison with a spherical bead, which was translated using DEP force and a spherical bead inside a cogwheel-shaped microbot (from figure 22a), which is translated using DEP force. The red line in figure 23 is very similar to the black line in figure 22a. As can be seen, the manipulation force magnitude for a microbot is in the same order as that of a single bead. The shape is not as linear as that of a bead. Therefore, some experimental identification, which will also be discussed later, will need to be done to get a more accurate description of the phenomena and to apply control on this microbot.

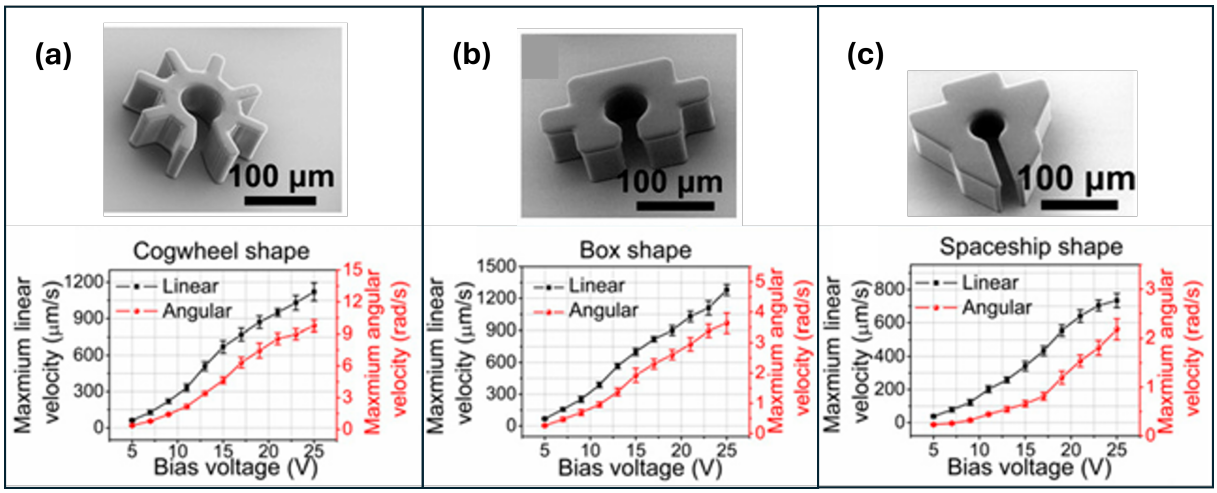

Figure 22: Optoelectronic microrobots SEM images and maximum linear (left axis, black) and angular (right axis, red) velocities as a function of OET bias voltage for translating and rotating. (a) cogwheel-shaped microrobot. (b) box-shaped microrobot. (c) spaceship-shaped microrobot. [34]

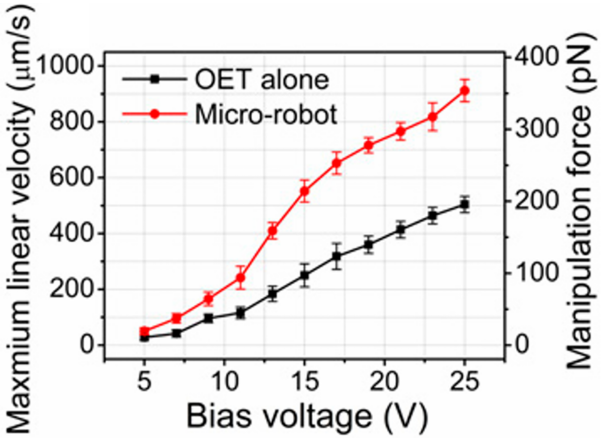

Figure 23: Maximum linear velocity (left axis) and corresponding DEP manipulation force (right axis) as a function of bias voltage for a bead translated alone (black) or inside a microrobot (red). Error bars represent ±1 SD from 5 measurements for each condition. [34]

1.8.1 DEP force in ellipsoid particles

The most straightforward form next to a spherical shape is the elliptical shape, which occurs often in cells, for which the DEP force is better defined. When considering an ellipsoidal particle with principle radii a, b, and c, we can define the DEP force [35].

$$\langle \mathbf{F}_{DEP}^{ellipsoid} \rangle = \frac{2\pi abc}{3} \mathrm{Re}(\hat{\epsilon}_1)[p_x \partial_x + p_y \partial_y + p_z \partial_z]\mathbf{E}_0 \tag{45}$$

with effective dipole moment p_i for $i = x, y, z$.

$$\begin{aligned} p_i &= \frac{4\pi abc}{3} \mathrm{Re}(\hat{\epsilon}_1) \mathrm{Re}\left(\frac{\hat{\epsilon}_2 - \hat{\epsilon}_1}{\hat{\epsilon}_1 + (\hat{\epsilon}_2 - \hat{\epsilon}_1)L_i} \right) E_i \\ L_i &= \frac{abc}{2} \int_0^\infty \frac{ds}{(s + r_i^2)\sqrt{(s + a^2)(s + b^2)(s + c^2)}} \end{aligned} \tag{46}$$

with $r_i = a$ when $i = x$, $r_i = b$ when $i = y$ and $r_i = c$ when $i = z$.

1.9 Torque due to the DEP force

The last thing we need to discuss is the torque on a particle due to the electrophoretic force. We can rewrite the DEP force equation 28 to be a function of the dipole moment $\mathbf{p}$.

$$\begin{aligned} \langle \mathbf{F}_{DEP} \rangle &= \mathbf{p}_{eff} \cdot \nabla \mathbf{E} \\ &= 4\pi r^3 \mathrm{Re}(\hat{\epsilon}_1) \mathrm{Re}(K(\omega)) \mathbf{E} \cdot \nabla \mathbf{E} \end{aligned} \tag{47}$$

Where the force on a dipole moment depends on the dot product with the gradient of the electrical field, so does the torque, which depends on the cross product with the electrical field. Just as the force was different and more complex for an ellipsoid, so is the torque different as well. The torque on a spherical particle is given by equation 48, and the torque on an ellipsoid particle is given by equation 49 [36] [37].

$$\begin{aligned} \mathbf{T}_{DEP}^{Sphere} &= \mathbf{p}_{eff}^{Sphere} \times \mathbf{E}_0 \\ &= -4\pi r^3 \mathrm{Re}(\hat{\epsilon}_1) \mathrm{Im}(K(\omega)) |\mathbf{E}_0|^2 \end{aligned} \tag{48}$$

As seen in equation 48, it depends on the imaginary part of the Clausius-Mossotti factor. This is opposite to the DEP force from equation 28. An applied signal with a frequency on the boundaries is often chosen When the DEP force is desired for it gives the highest values[9]. At those frequencies, the complex part of the Clausius-Mossotti factor is usually zero. Therefore, in practice, the torque is often ignored in literature.

$$\begin{aligned} \mathbf{T}_{DEP}^{Ellipsoid} &= \mathbf{p}_{eff}^{Ellipsoid} \times \mathbf{E}_0 \\ T_{DEP,x}^{Ellipsoid} &= \frac{4\pi abc(\hat{\epsilon}_2 - \hat{\epsilon}_1)^2 (L_z - L_y) E_y E_z}{3\mathrm{Re}(\hat{\epsilon}_1)[1 + (\frac{\hat{\epsilon}_2 - \hat{\epsilon}_1}{\hat{\epsilon}_1})L_y][1 + (\frac{\hat{\epsilon}_2 - \hat{\epsilon}_1}{\hat{\epsilon}_1})L_z]} \\ T_{DEP,y}^{Ellipsoid} &= \frac{4\pi abc(\hat{\epsilon}_2 - \hat{\epsilon}_1)^2 (L_x - L_z) E_x E_z}{3\mathrm{Re}(\hat{\epsilon}_1)[1 + (\frac{\hat{\epsilon}_2 - \hat{\epsilon}_1}{\hat{\epsilon}_1})L_x][1 + (\frac{\hat{\epsilon}_2 - \hat{\epsilon}_1}{\hat{\epsilon}_1})L_z]} \\ T_{DEP,z}^{Ellipsoid} &= \frac{4\pi abc(\hat{\epsilon}_2 - \hat{\epsilon}_1)^2 (L_y - L_x) E_x E_y}{3\mathrm{Re}(\hat{\epsilon}_1)[1 + (\frac{\hat{\epsilon}_2 - \hat{\epsilon}_1}{\hat{\epsilon}_1})L_x][1 + (\frac{\hat{\epsilon}_2 - \hat{\epsilon}_1}{\hat{\epsilon}_1})L_y]} \end{aligned} \tag{49}$$

As seen in equation 49, the vector is less trivial than the one for a spherical particle. The polarization is not homogeneous for an ellipsoid particle. This expression shows that the alignment due to the torque is the biggest for the axis parallel to $\mathbf{E}_0$. For each principal axis, there exists a frequency where there is a stable direction in that axis. In the high and low limits, the longest principal axis is only stable [38].

[9] The extreme values of the Clausius-Mossotti factor are found on $\omega = 0$ and $\omega = \infty$

2

Microfluidic chip

This section will explain the design parameters to consider when making the microfluidic chip for OET purposes. The consistency of the fluidic medium depends on the OET's use case. Therefore, we discuss briefly what this would mean for our chip. Because this chip contains a specific type of fluidic medium and is subject to an alternating electrical field, we will need to discuss different phenomena that could arise that could limit the use of the OET. Vice-versa will discuss how the medium could influence the electrical field inside the microfluidic chip needed for the DEP force. Lastly, we will discover the expected effects from an overhang in the chip, which we will back up with some simulations.

Microfluidic chip for "Jip en Janneke"

In the world of optoelectronic tweezers, we need a tiny see-through box to hold the tiny particles and liquid we want to move around. This box has to be small enough so we can look at it through a microscope. We learned earlier that we need to use electricity to help move things in this box. This special little box is called a microfluidic chip, and it can do many different things that we will talk about here.

The type of liquid we use in the box can change how we move the particles. For example, if we want to move tiny living cells, we need to make sure the liquid has the right food, salt, and temperature for them. But if we want to move small plastic balls, we can just use normal water.

We will also talk about how the liquid and the chip can help or make it harder to move things with the optoelectronic tweezers. Plus, we'll explore how a bent chip might change how everything works, and we will show a simulation to help explain it better.

The Jip and Janneke illustration is created by the renowned artist Fiep Westendorp.

2.1 Dielectric medium

2.1.1 Dionized water

In the Netherlands, regular tap water is very safe to drink [39]. This water is tested to meet strict standards. This water, however, still contains many substances different from H^2O. Consider minerals, salts, bacteria, and pesticides (although in tiny concentrations) [40]. Therefore, deionized water is often chosen as the dielectric medium for a simple medium with uniform electric properties. This is not to be confused with demineralized water. Deionized water is purely H20 with ions removed, while demineralized water could still contain different ions of water [41]. A pure water molecule consists of 1 oxygen atom and 2 hydrogen atoms, which are separated from each other with an angle of 104.5 degrees, which is the energetically optimal geometry for this atom [42]. The water molecules have a polarization angle because this angle is less than 180 degrees. Due to this polarization, water is a dielectric medium. When a dielectric medium is subject to an alternating electric field, the molecules will rotate, and energy will be lost to heat [43].

$$W_{vol} = \frac{V^2}{d}\epsilon_0 \mathrm{Im}(\hat{\epsilon})\omega \tag{50}$$

The power loss per volume is W_{vol}. It depends on the bias voltage on the medium V and the height of the microfluidic chip d. The permittivity of free space is denoted by ϵ_0. The complex permittivity of the medium is denoted by $\hat{\epsilon}$. The frequency of the AC voltage is given by ω.

In the previous section, we already worked with the complex permittivity, which we took as constants. In reality, the real part of the permittivity and the conductivity seem to change with respect to the applied frequency. Figure 24 shows an example of this. The dielectric loss appears to peak around 20 GHz. Electromagnetic waves and that frequency range are known as microwaves and are used by people worldwide to heat food in the kitchen [44]. If we do not want to have this effect play any role in our OET setup, we should avoid frequencies that are too high and induce microwave heating.

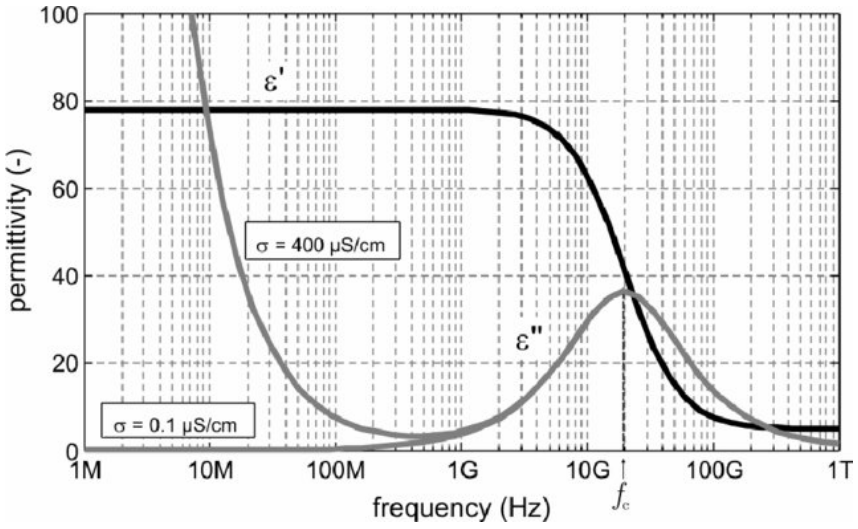

Figure 24: The black line shows the real part of the complex permittivity of water. The grey line shows the complex part of the complex permittivity. Both the values for tap water ($400\mu S/cm$) and for pure water ($0.1\mu S/cm$) are shown [45].

2.1.2 Cell-culture media

If we want to move the OET field to live cell research, we can no longer use simple deionized water in the microfluidic chip. Cells have semipermeable membranes, which means osmotic pressure must be prevented. Also, temperatures should not fluctuate too much, e.g., temperature differences of more than 4 °C are known to kill mammalian cells rapidly [46]. To summarize, for live cell research, cells require some specific care [47]:

- Temperature control
- Appropriate pH and osmolality
- A certain type of culture medium
- Stable conditions

Because this is very cell-specific, one should determine which media is necessary for their use case. Some typical cell culture media often used are shown in table 1 [48].

Cell Line	**Morphology**	**Species**	**Medium**
HeLa B	Epithelial	Human	MEM + 2mM Glutamine + 10% FBS + 1% NEAA
HL60	Lymphoblast	Human	RPMI 1640 + 2mM Glutamine + 10-20% FBS
3T3 clone A31	Fibroblast	Mouse	DMEM + 2mM Glutamine + 5% NBCS + 5% FBS
COS-7	Fibroblast	Monkey	DMEM + 2mM Glutamine + 10% FBS
CHO	Epithelial	Hamster	Ham's F12 + 2mM Glutamine + 10% FBS
HEK 293	Epithelial	Human	EMEM (EBSS) + 2mM Glutamine + 1% NEAA + 10% FBS
HUVEC	Endothelial	Human	F-12 K + 10% FBS + 100 µg/ml Heparin
Jurkat	Lymphoblast	Human	RPMI-1640 + 10% FBS

Table 1: Overview of cell lines, their morphology, species, culture medium, and applications [48].

When cell research is directed toward proliferation and cell growth, culture media often contain a nutrient-rich serum. The needed buffer media are available in powdered form, concentrated form, or ready-to-work form. Because cell culture media is often very complex, it also has a more complex permittivity. Cell culture media is often more conductive and more ionized, which reduces the electrical field strength, which makes it harder to have a working OET [49], and induces effects such as light-induced AC electroosmosis which will be discussed in section 4.2.1. The temperature control of the microfluidic chip can be realized by using a Peltier heater, which uses thermoelectric cooling and has been shown to work in an OET environment [34][50].

2.1.3 Electrolysis

The microfluid chip can also be seen as an electrochemical cell with a positive electrode (anode) and a negative electrode (cathode). When water is put in this system, and the correct voltage is applied, electrons can be added to the water molecules, making them split apart. The reaction of this water-electrolysis is given by breaking them apart into hydrogen and oxygen atoms [51].

$$2H_2O + E_{EL} \rightarrow 2H_2 + O_2 \tag{51}$$

This reaction is the general form but can exist in many half-reaction types depending on the electrochemical cell type and medium. The system's needed potential difference is E_{EL}. This voltage is given by the Gibbs free energy, which describes the energy of a chemical equilibrium with constant pressure and constant temperature [52].

$$E_{EL} = -\frac{\Delta G}{nF} \tag{52}$$

The amount of added electrons is given as n, which is 4 in the case of the water electrolysis reaction. F is the Faraday constant, which is 96485 C/mol. The Gibbs energy for the water electrolysis reaction is 237 kJ/mol, which means that the added voltage for pure water must be at least 1.23 Volts. In practice, this theoretical lower limit is higher due to thermal effects. When ions are added to the electrochemical cell, as is the case for the cell culture medium, the chemical reactions are more complex, and more types of gasses can be created. The electrolysis phenomenon can be increased in efficiency by injecting pulses of direct current in the electrochemical cell instead of standard direct current. This is because double layers, discussed in more detail in section 4.2.1, are reduced, and electrons have more freedom to move [53]. The effect of this pulsed input is shown in figure 25.

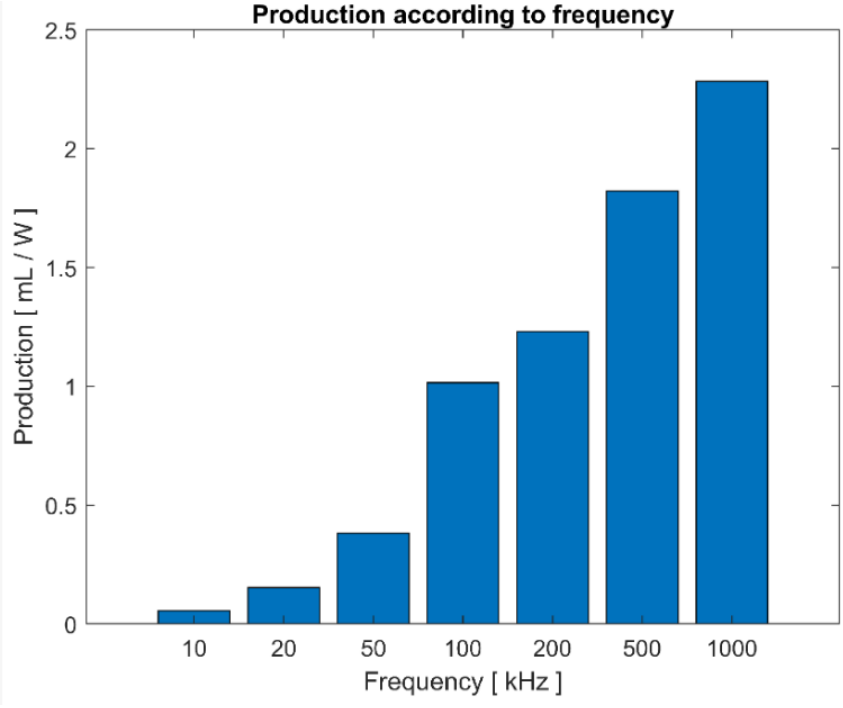

Figure 25: Electrolysis produced gas depending on the applied pulse frequency. The applied pulsed voltage is 4 V, and the electrodes are separated by 0.1 mm [53].

In optoelectronic tweezers, electrolysis is an unwanted phenomenon. The created gas bubbles reduce the freedom of particles to move around. Besides that, can the created gasses destroy the chip's cells or the microfluidic chip itself. Therefore, it is essential to avoid having electrolysis in the OET system. As can be seen in figure 26, electrolysis has been seen to occur at frequencies up to 400 Hz for standard OET setups. This limits the working range of most OET setups in the lower range, as shown in figure 27. Therefore, when using an OET setup, the lower limit should be known and avoided.

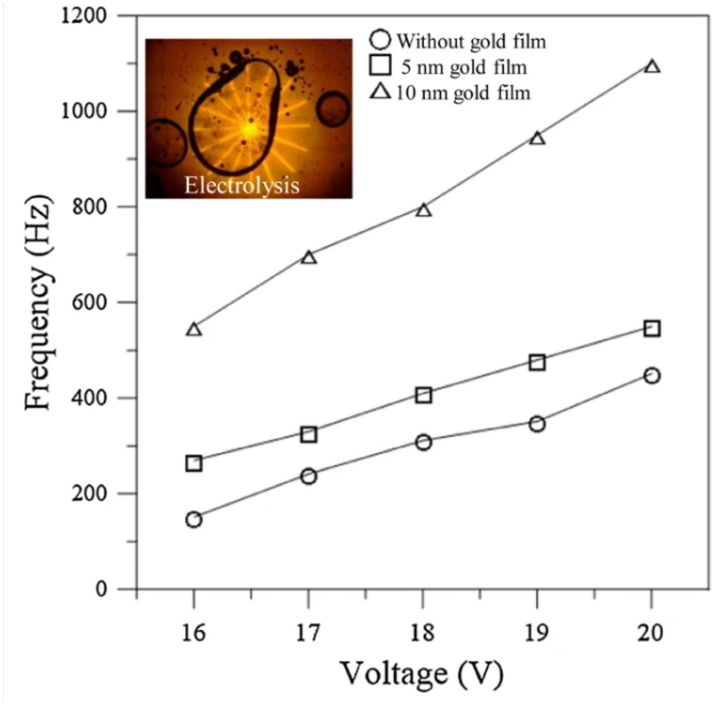

Figure 26: The combination of frequency and voltage of a sinusoidal AC input on which electrolysis happens in a gold film OET setup. The gold film is added to the electrode without the photoconductive layer in a standard OET setup [54].

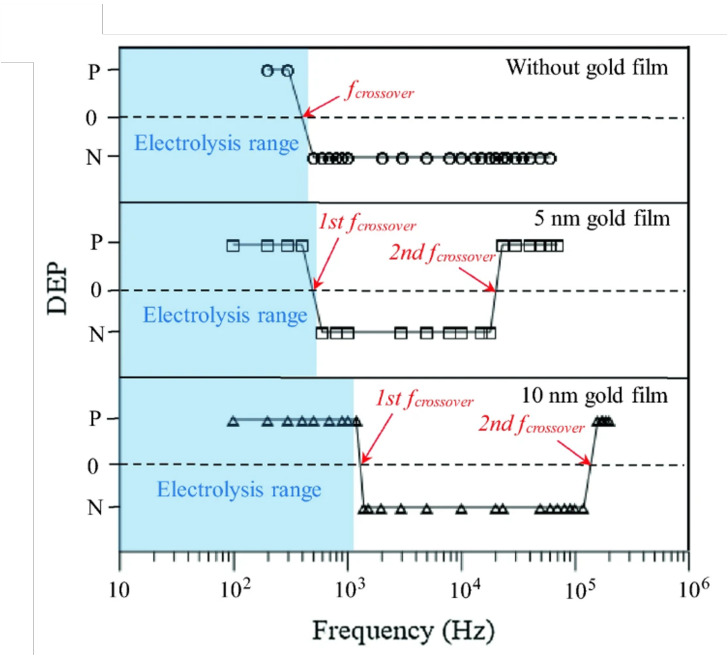

Figure 27: The DEP force for different frequencies on a 90 μm polystyrene bead in a gold film OET setup. The gold film is added to the electrode without the photoconductive layer in a standard OET setup [54].

2.2 ITO electrodes

The electrodes in the microfluidic chip must be see-through enough for the illumination pattern to reach the photoconductive layer. Also, when imaging, it is essential that the electrodes transmit enough light to detect the particles in the chip. To cover this, microscope slides and slips can be covered by a nanoscopic layer of ITO (Indium Tin Oxide). ITO proved very useful in everyday household applications such as touch screens, TV screens, and solar panels [55]. In figure 28, it can be seen that the transmittance of ITO fluctuates for different wavelengths of light but can be seen to decrease with increased ITO thickness generally. In figure 29, it can be seen that the density per centimeter decreases with increasing thickness of the ITO layer. This can be related to the number of carriers in ITO, which is growing with increasing ITO layer thickness [56]. The Hall mobility is the measured mobility of the carriers due to a magnetic field, i.e., the Hall effect [57].

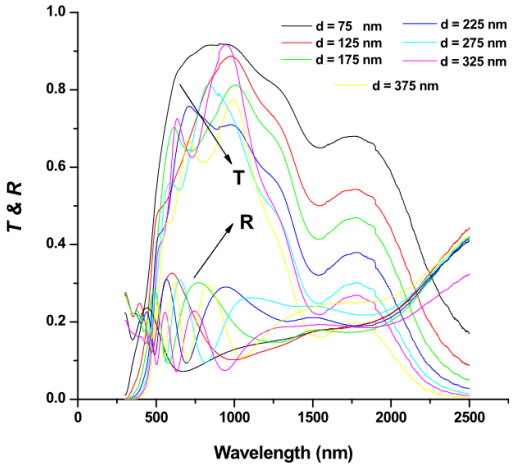

Figure 28: The transmittance and absorbance of different thicknesses of ITO film [56].

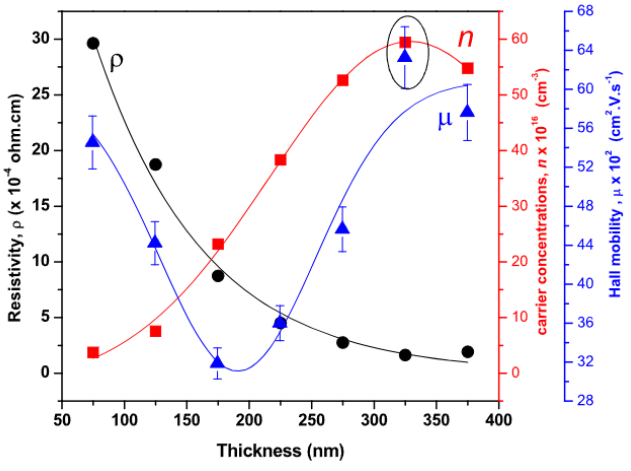

Figure 29: The resistance, carrier concentration, and Hall mobility of different thicknesses of ITO film [56].

2.2.1 Photoconductive layer

The photoconductive layer in the microfluidic chip is the part where precise control can be implemented. When specific wavelengths of light illuminate a part of the photoconductive layer, the resistance drastically drops compared to the not-illuminated state. This way, virtual electrodes can be created that change the shape of the electric field in the microfluidic chip. Because of this, the photoconductive layer can be seen as a resistor with resistance depending on the illumination. The photoconductive layer is discussed in more detail in section 3.

2.3 Electrical circuit

The two conducting glasses, with the photoconductive layer on one side, create a capacitor from the microfluidic chip. Because of that, we can model it as an electric circuit.

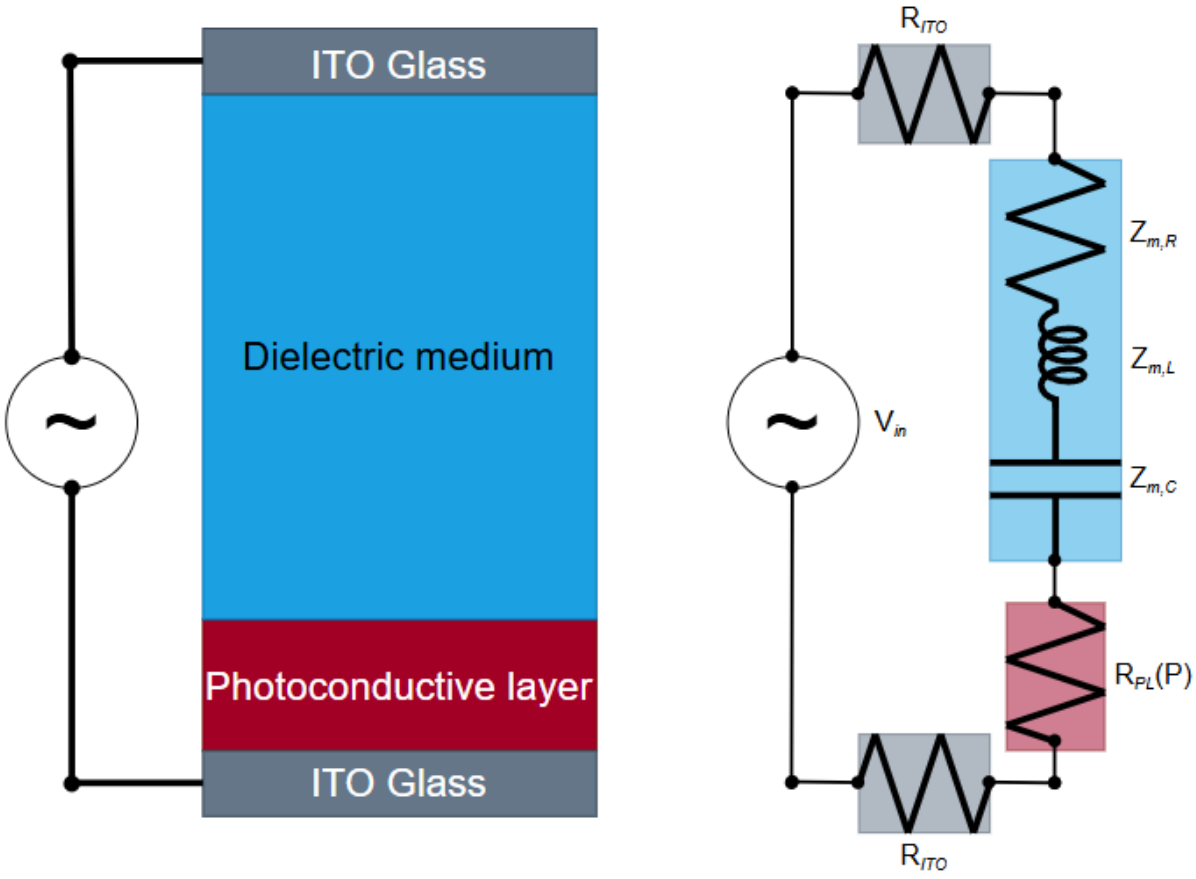

Figure 30: The microfluid chip modeled as an electric circuit.

As can be seen, the current in the circuit is subject to 4 resistances, which are from the electrodes, the photoconductive layer, and one from the dielectric medium. The resistance of the photoconductive layer depends on the wavelength, which will be discussed in section 3. The capacitance of the dielectric medium is often reduced to an ideal capacitor, with no resistance $Z_{m,R}$ and inductance $Z_{m,L}$. In reality, capacitors have some resistance and parasitic inductance [58]. This parasitic inductance makes the capacitor behave like an inductor with applied frequencies that are higher than the cross-over frequency of the capacitor. The resistance of the capacitor is the bias resistance of the capacitor, which can be measured at the cross-over frequency.

The capacitance of a parallel plate capacitor with a dielectric in between the plates is given by the relative permittivity of the medium and the geometry of the plates [59].

$$Z_{m,C} = \left(i\omega\epsilon_r\epsilon_0 \frac{A}{d} \right)^{-1} \tag{53}$$

ϵ_r is the relative permittivity, ϵ_0 is the permittivity of free space, ω is the angular frequency of the applied signal, A is the area of the parallel plates and d is the distance between the plates. The parasitic inductance of this parallel plate capacitor can be estimated by the permeability of the medium and the self-inductance [60].

$$Z_{m,l} = i\omega\mu_r\mu_0 2w \left[\ln \frac{2w}{d} + 1 + \frac{d}{w} \right] \tag{54}$$

mu_r is the relative permeability of the medium, μ_0 is the permeability of free space, ω is the angular frequency of the applied signal, w is the long side of the parallel plates and d is again the separating distance. Suppose we use the permeability and permittivity of deionized water for a microfluidic chip of 20mm by 5mm with a separation of $150\mu m$. In that case, we can find $C \approx 47.8nF$ and $L \approx 31.7\mu H$. The total impedance of the real capacitor can be calculated as the capacitor impedance in series with the parasitic inductance and the parasitic resistance.

$$\begin{aligned} Z_C &= Z_{m,C} + Zm, L + Zm, R \\ &= \frac{1}{i\omega C} + i\omega L + R_c \end{aligned} \tag{55}$$

The norm of this complex number gives the magnitude of this impedance.

$$|Z_c| = \sqrt{R_C^2 - 2\frac{L}{C} + \omega^2 L^2 + \frac{1}{\omega^2 C^2}} \tag{56}$$

The cross-over frequency is the frequency at which this magnitude has a minimum. It can be found when the magnitude's first derivative with respect to the angular frequency is 0.

$$\begin{aligned} \frac{\partial |Z_C|}{\partial \omega} &= \left(2\omega L^2 - 2\frac{1}{\omega^3 C^2} \right) \frac{1}{2} \left(R_C^2 - 2\frac{L}{C} + \omega^2 L^2 + \frac{1}{\omega^2 C^2} \right)^{-1} = 0 \\ &\rightarrow \omega = \frac{1}{\sqrt{LC}} \end{aligned} \tag{57}$$

At this cross-over frequency, also known as the capacitor's self-resonance frequency, the impedance's magnitude is equal to the parasitic resistance R_C. The impedance of the parallel plate capacitor, as discussed, can be seen in figure 31. When we want to find the real capacitance, parasitic inductance, and parasitic resistance, it would be wise to measure the exact chip and fit it on equation 56.

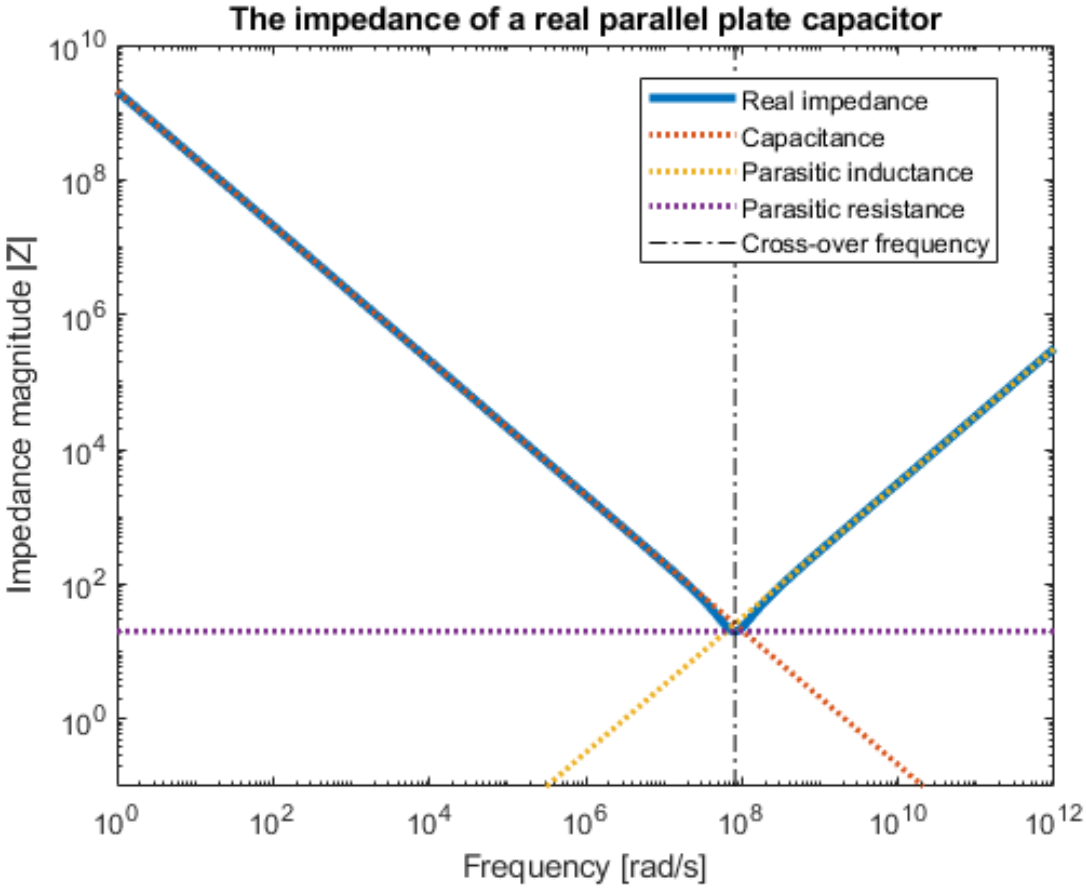

Figure 31: The magnitude of the impedance of a parallel plate capacitor with deionized water as dielectric. The real impedance is a sum of the capacitance, the parasitic inductance, and the parasitic resistance.

Because this system is simply in series, we can say that the current is equal everywhere, the voltage drops at each component, and the circuit's total resistance is the sum of all impedances [61].

$$R_{tot} = R_{ITO} + R_{PL}(P) + Z_C + R_{ITO} \tag{58}$$

We can relate the current in the system to the input voltage and the total resistance using Ohm's Law [62]. This current is equal everywhere in the system because it is in series.

$$I = \frac{V_{in}}{R_{tot}} = \frac{V_{in}}{R_{ITO} + R_{PL}(P) + Z_C + R_{ITO}} \tag{59}$$

The voltage drop at each component is related to the relative resistance compared to the system's total resistance. Thus, the system's voltage, and therefore energy, is divided proportionally. Thus, this proportionality can be used to find the total voltage in the capacitor created by the microfluid chip.

$$\begin{aligned} V_C = IZ_C &= \frac{V_{in}}{R_{tot}} Z_C \\ &= V_{in} \frac{Z_C}{2R_{ITO} + R_{PL}(P) + Z_C} \end{aligned} \tag{60}$$

The uniform electrical field in a parallel plate capacitor is proportional to the voltage drop in the capacitor and the separating distance between the parallel plates [7].

$$E = \frac{V_C}{d} = \frac{V_{in}}{d} \frac{Z_C}{2R_{ITO} + R_{PL}(P) + Z_C} \tag{61}$$

Therefore, the electrical field strength depends highly on the difference between the resistances of the ITO glass and the photoconductive layer and the capacitor's impedance. This could significantly impact the DEP force's usability in certain types of dielectric media, which is discussed in section 3.4.3.

2.4 Overhang

Every material has a specific resistance against deformation. English physicist Thomas Young discovered this property called Young's modulus [63]. This modulus gives the relation between the strain of a material per applied unit of stress in the same direction. The deformation of a material on a certain amount of stress can be calculated using the Cauchy stress tensor, named after Augustin-Louis Cauchy [64]. We would have a perfectly uniform electric field in a perfect parallel plate capacitor. If the plates bend due to some stress, the plates will stop being parallel and produce a non-uniform field. Calculating the deformation of the top ITO glass is complex due to it being clamped in on all sides. Therefore, we want to simplify the deformation case to 1D and argue that for 2D, the deformation will be much smaller. If a 1D rod is clamped in on both sides, it has a smaller deflection than when it is clamped on only one side. When clamping this rod in on the two remaining edges, the deflection should be even smaller [65]. The deformation of a double-clamped rod with a uniform distributed load is given the moment of inertia and Young's modulus of the system [66].

$$\delta_{max} = \frac{wL^4}{384EI} \tag{62}$$

w is the distributed load (N/m), L is the length of the rod, E is Young's modulus, and I is the moment of inertia, which is for a plate with depth b and height h given as $I = \frac{bh^3}{12}$. In the case of the ITO glass that covers the microfluidic channel in the microfluidic chip, we can give some insight into the expected effects on the DEP force. Suppose we have a microfluidic chamber with length A and width B. In that case, we can find the gravitational force to be $F_z = g\rho ABh$, with the density of the ITO glass being ρ, with the thickness of ITO glass being h and with gravitational constant g. If we would only take the rod to be clamped in the direction of the side with length A, we would find the maximum distribution in the middle of the plate

$$\delta_A = \frac{wA^4}{384EI} = \frac{g\rho ABh}{A}\frac{A^4}{384E\left(\frac{Bh^3}{12}\right)} = g\rho BhA^4\frac{1}{4608EBh^3} = \frac{g\rho A^4}{4608Eh^2} \tag{63}$$

If we had clamping in the B-direction, we would only need to change the A in this formula to B. As we can see, the deflection is the biggest in the direction with the largest length. If A is the long side of the unsupported ITO glass, equation 63 gives an upper limit for the deflection due to the weight[10]. Using $A = 2$ cm, $B = 5$ mm, $h = 200$ μm, $\rho = 2380$ kg/m^3 and $E = 70$ GPA, we find that this deflection is smaller than 1 nm.

To understand the impact of this overhang, we simulate the DEP force in this system in COMSOL as was done similarly in section 1.5.2. The only difference is that the top electrode has been modeled to have the sag spherically, similar to figure 32. The actual deflection in the 1D case is quadratic, but this was less complex to implement. Because the calculations done in MATLAB use the point evaluation of the grid as discussed in section 1.5.2, we cannot have the deflection to overlap a point of this grid. This distance in this grid is 7.5 μm in this simulation, much larger than the calculated deflection. Therefore, the deflection has been taken to be proportional to this maximum deflection.

$$d = \frac{d_{max}}{a} \tag{64}$$

d_{max} has been taken to be 7 μm to avoid overlap with grid points even more and for a values were taken as 1,$\frac{4}{3}$, 2, 4, and 330. The radius of the circle can be calculated from figure 32 to be $r = \frac{d}{2} + \frac{b^2}{8d}$. The simulated results of the OET, when two spots are illuminated, can be seen in table 2.

[10] As we already discussed, is the plate going to be less deformed because the plate is clamped in all directions, therefore, this amount of deflection is an exaggeration of the real deflection.

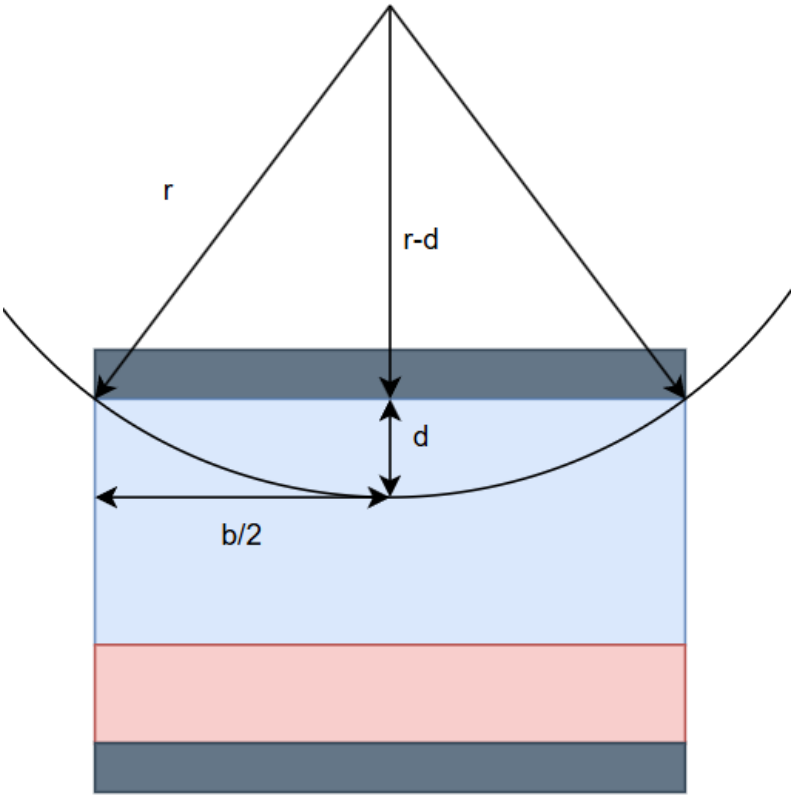

Figure 32: The geometric figure created a circular overhang in the simulation in COMSOL. The lowest part of the overhang is equal to d and is related to the radius of the circle r and the width of the chip b.

The simulated results of the OET, when there is no illumination, can be seen in table 3. The complete data can be found in appendix A.

Table 2: The main results of the DEP simulation with overhang of the electrode on top in illuminated state with alternating deflection factor a as described by equation 64.

a	max E_x [V/m]	max E_y [V/m]	max F_x [pN]	max F_y [pN]	Increase of $\partial_x \lvert\mathbf{E}\rvert^2$ [%]	Increase of $\partial_y \lvert\mathbf{E}\rvert^2$ [%]
$\frac{1}{330}$	254735.3018	293460.0819	3601.9976	6172.6027	N.A.	N.A.
0.25	231291.1983	266675.5767	2980.0495	5114.2547	-17.267	-17.146
0.5	232271.9944	268265.2174	3015.4420	5159.2902	-16.284	-16.416
0.75	233346.9416	269613.3319	3033.2409	5179.7011	-15.790	-16.086
1	234117.6331	271138.8387	3087.2052	5290.1414	-14.292	-14.296

Table 3: The main results of the DEP simulation with an overhang of the electrode on top in the off state with alternating deflection factor a as described by equation 64.

a	max E_x [V/m]	max E_y [V/m]	max F_x [pN]	max F_y [pN]	Increase of $\partial_x \lvert\mathbf{E}\rvert^2$ [%]	Increase of $\partial_y \lvert\mathbf{E}\rvert^2$ [%]
$\frac{1}{330}$	1.5390×10^{-11}	1.7677	1.8910×10^{-18}	2.8486×10^{-18}	N.A.	N.A.
0.25	6.1211×10^{-3}	1.7711	2.7125×10^{-11}	5.6977×10^{-11}	1.4344×10^{7}	5.9553×10^{8}
0.5	1.2290×10^{-2}	1.7745	5.4209×10^{-11}	1.1454×10^{-10}	2.8666×10^{7}	1.1928×10^{9}
0.75	1.8508×10^{-2}	1.7779	8.1350×10^{-11}	1.7269×10^{-10}	4.3018×10^{7}	1.7946×10^{9}
1	2.4773×10^{-2}	1.7814	1.0849×10^{-10}	2.3139×10^{-10}	5.7371×10^{7}	2.3998×10^{9}

As we can see in table 2 and table 3, the difference between a minimal overhang and some overhang is around 16% for the illuminated state and very large for the off state. The amount of overhang does decrease with increasing overhang after $\frac{d_{max}}{4}$. Even though the increase of the DEP effect is considerable for the off-state at the start, the total force is small enough to be ignored. Therefore, using this simulation, we can conclude that a large enough overhang would decrease the DEP effect in the illuminated state. Its effect seems to be unnoticeable in the off-state.

2.5 Dimensions

The last important thing to discuss for the microfluidic chip is the dimensionality. The size of the microfluidic chip depends very much on the particles and the wanted dynamics. The particles in the chip should have enough room to be moved, pass each other, and not get stuck. This also applies to the height of the chip. The electrical field's magnitude depends on the chip's height, as shown in equation 61. The area of the microfluidic channel will influence the amount of overhang deflection as was demonstrated in equation 63. The photoconductive layer's heights can influence this layer's effectiveness, for it can absorb more photons, which is discussed in more detail in section 3. The photoconductor can be shaped into a specific pattern such that there are not only virtual electrodes but also static, stronger electrodes in the OET chip [28]. The size of the microfluidic channel changes influences the thermal and fluidic forces discussed in section 4. The height of the chip also influences the minimal focal distance we can use for an objective, which will be discussed in section 5. We also need to consider the available types of premade (conductive) glasses, which can practically limit the system.

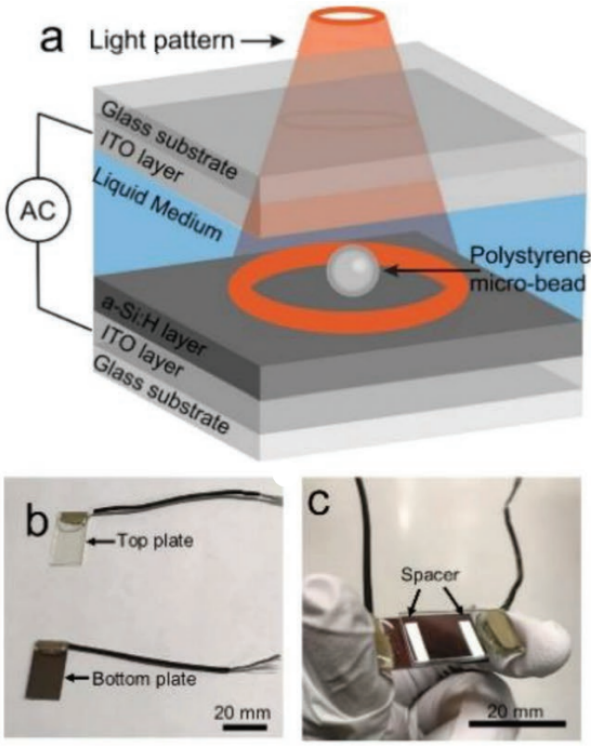

Figure 33: An example of a microfluidic chip used in optoelectronic tweezers. (a) shows the schematic chip with the different layers. (b) and (c) are pictures of an actual microfluidic chip used in literature [67].

3

Photoconductive layer

In this section, we will explore the fundamental physics of the photoconductive layer in the microfluidic chip for optoelectronic tweezers. The conductivity of the photoconductive layer increases at the points illuminated by light, a phenomenon attributed to solid-state physics originating from quantum phenomena. Our focus will be on silicon photoconductive layers, particularly hydrogenated amorphous silicon, the predominant material in the literature on optoelectronic tweezers (OET) devices. We will elucidate the processes occurring within these photoconductive layers upon illumination, detailing how varying wavelengths and light intensities affect the conductivity. Additionally, we will investigate the consequences of prolonged illumination. The macroscopic structure of the photoconductive layer and its implications for the electrical field within the microfluidic chip will be examined and simulated. We will also address the adhesive interactions between the photoconductive layer and particles, including strategies to mitigate these effects. Finally, we will briefly review other types of photoconductive layers documented in the literature beyond just a form of intrinsic silicon.

The photoconductive layer for "Jip en Janneke"

In the last section, we learned about a special box that has particles and fluid inside. There's also a cool part called a photoconductive layer. This layer is made of a unique material that, when we shine light on it, pulls the particles we want to move even more.

It does this because it lets electricity flow better. Now, the way this photoconductive layer works is explained by science called quantum physics and solid-state physics, which tell us about what's happening inside it. We will look at different materials that can be used for this layer and see how they change how it works. We'll also discover what kind of light is best to make sure the particles are pulled really strong. But we have to watch out because if we shine a light on this layer for too long, it can get weaker, and we will talk about why that happens.

The way the photoconductive layer looks can also affect how well it works. The roughness of the layer can influence the pulling force, and it can also be sticky for the particles that we want to move. In the last part of this section, we'll mention some other materials that can work as a photoconductive layer too, even though they are a bit rare.

The Jip and Janneke illustration is created by the renowned artist Fiep Westendorp.

3.1 Solid state physics and electron transition

Within solid materials, many properties can be quantified. One important property is the electrical conductivity. This measures the ease at which an electrical charge can pass through a material [68]. When a material has high conductivity, we call them conductors, and they are, in most cases, metals. When a material has a very high resistance, i.e., low conductivity, we call it an insulator. These insulators are found to be materials such as wood, plastics, or ceramics. The reason this happens can be found in quantum theory. The electrons in the material are bounded by nuclei in specific orbitals. The types of orbitals depend on quanta, i.e., discrete quantity of energy, hence *quantum* theory, such that there are a discrete amount of orbitals. Niels Bohr first theorized these orbitals in 1913 and later worked out further by Erwin Schrödinger in 1926 [69]. A specific energy level is assigned for each orbital, called an energy band. These bands can have as many electrons occupied in them as the connected orbital allows. For example, in the first band, there can be 2 electrons (one spin-up and one spin-down) before it is full. This is why helium, having 2 electrons, is noble [70]. It has only fully occupied bands, as all noble elements normally do. Given the energy levels, we will need to find out how these electrons can move.

3.1.1 The dispersion relation of an electron in a simple solid

Erwin Schrödinger theorized that a particle behaves like a wave. Therefore, the particle needs to have a function that describes what this wave looks like. The general formula Schrödinger created shows this wave function's general solution.

$$i\hbar\frac{\partial}{\partial t}\Psi(\mathbf{r},t) = \left[-\frac{\hbar^2}{2m}\nabla^2 + V(\mathbf{r})\right]\Psi(\mathbf{r},t) \tag{65}$$

With $\hbar$ being the reduced Planck constant, m is the mass of the particle, $V(\mathbf{r})$ is a potential that describes the wave for each position $\mathbf{r}$ and t denotes the dependence on time. This "easy-looking" formula is quite deceiving and needs some simplification to give general solutions. For example, we are only interested in the number of states, which is equal to this system's eigenvalues. Therefore, we can remove the dependence on time and look at stationary wavefunctions to find these eigenvalues.

$$\left[-\frac{\hbar^2}{2m}\nabla^2 + V(\mathbf{r})\right]\Psi(\mathbf{r}) = \hat{H}\Psi(\mathbf{r}) \tag{66}$$

With $\hat{H}$ denoting the Hamiltonian, which is the function on the left side. This Hamiltonian can be an eigenfunction setting it equal to an eigenenergy E. We will discuss only a simple form first, which describes a free particle in a box (i.e., we will set the potential $V(\mathbf{r}) = 0$. This results in the following eigenvalue.

$$-\frac{\hbar^2}{2m}\nabla^2\Psi(\mathbf{r}) = E\Psi(\mathbf{r}) \tag{67}$$

To solve this, we will use the ansatz $\Psi(\mathbf{r}) = Ce^{i\mathbf{k}\cdot\mathbf{r}}$ with $\mathbf{k}$ being the wave vector which gives direction to the wave[11]. This will give us the energy relation depending on this $\mathbf{k}$ called the dispersion relation.

$$\begin{aligned}
-\frac{\hbar^2}{2m}\nabla^2\left[Ce^{i\mathbf{k}\cdot\mathbf{r}}\right] &= \frac{\hbar^2}{2m}C(i\mathbf{k})\cdot(i\mathbf{k})e^{i\mathbf{k}\cdot\mathbf{r}} \\
&= -\frac{\hbar^2}{2m}|\mathbf{k}|^2Ce^{i\mathbf{k}\cdot\mathbf{r}} \\
&= \frac{\hbar^2k^2}{2m}\Psi(\mathbf{r})
\end{aligned} \tag{68}$$

With the magnitude of the wave vector $\mathbf{k}$ denoted by k. This shows us that the energy given this k is given as $E(k) = \frac{\hbar^2k^2}{2m}$. We want to know how electrons move, which we can describe using these quantum particles. We will take each electron in the solid as a particle confined in the crystal lattice of the solid. We simplify each particle to be in a cubic box with length L and, therefore, a volume of $V = L^3$. According to Bloch's theorem, we need to add periodic boundary conditions[12] in each cubic box [71]. We denote the unit carthesian directions $\hat{x}, \hat{y}$ and $\hat{z}$ as $\hat{r}$.

$$\begin{aligned}
\Psi(\mathbf{r}) &= \Psi(\mathbf{r} + \hat{r}L) \\
Ce^{i\mathbf{k}\cdot\mathbf{r}} &= Ce^{i\mathbf{k}\cdot(\mathbf{r}+\hat{r}L)} \\
&= Ce^{i\mathbf{k}\cdot\mathbf{r}}e^{i\mathbf{k}\cdot\hat{r}L} \\
e^{i\mathbf{k}\cdot\hat{r}L} &= 1 \\
\cos(\mathbf{k}\cdot\hat{r}L) + i\sin(\mathbf{k}\cdot\hat{r}L) &= 1 + 0i \\
\mathbf{k}\cdot\hat{r}L &= n2\pi
\end{aligned} \tag{69}$$

This means that in the x-direction, the solutions of possible magnitudes of the k-vector are given as $k_x = n_x\frac{2\pi}{L}$ for all $n_x \in \mathbb{Z}$. The same is true for the y and z directions. Therefore, the k-vector is given as $\mathbf{k} = \frac{2\pi}{L}(n_x, n_y, n_z)$. The physical meaning behind this is that for each discrete state $\mathbf{k}$, there is an accompanying discrete amount of energy given by the dispersion relation $E(k)$. Each state exists in a volume of $V = \left(\frac{2\pi}{L}\right)^3$, which is the product of the spaces between each point in 3D k-space.

[11] This is a very simple, but working, ansatz. We will discuss a more complex and realistic version later on.

[12] Periodic boundary conditions mean that for a specific value, the function repeats. A perfect easy example of this is a normal sinusoidal function $f(x) = \sin(x)$. We can not tell the difference between this function starting at $x = 0$ or $x = 2\pi$. Therefore, this function would be periodic in 2π. In the case of this cubic box, we want it to be periodic in $\hat{r}L$, which is the length L in the direction of one of the sides of the cubic box.

For example, if we are interested in the total number of states in a volume, we need to sum over all n_i in each direction, equal to $\frac{k_i}{2\pi/L}$. This results in a discrete summation[13] where we denote $\Delta\mathbf{k}$ to be the space between each point in k-space.

$$N(\mathbf{k}) = \sum_{\mathbf{n}} = \left(\frac{L}{2\pi}\right)^3 \sum_{\mathbf{k}} \Delta\mathbf{k} \tag{70}$$

If we consider the box length infinite, we will have $\Delta\mathbf{k}$ becoming $d\mathbf{k}$, changing the discrete summation to an integral.

$$\begin{aligned} N(\mathbf{k}) &= \left(\frac{L}{2\pi}\right)^3 \sum_{\mathbf{k}} \Delta\mathbf{k} \\ &\approx \left(\frac{L}{2\pi}\right)^3 \int_V d\mathbf{k} \\ &= \left(\frac{L}{2\pi}\right)^3 \int_0^{2\pi} d\phi \int_0^{\pi} \sin(\theta) d\theta \int_0^{\infty} k^2 dk = \frac{L^3}{2\pi^2} \int_0^{\infty} k^2 dk \end{aligned} \tag{71}$$

where we took the k-space integral in spherical coordinates. We need to include spin degeneracy because we talk about electrons here, which are fermions with half-odd-integer spin. Pauli's exclusion principle tells us that each half-integer-spin particle in an atom needs to have different quantum numbers. In each state k, there can be two similar electrons due to the different spin configurations, i.e., different quantum numbers. Therefore, we must add a factor 2 due to the degeneracy [72]. Also, we can derive k and dk by using the dispersion relation we found.

$$\begin{aligned} E &= \frac{\hbar^2 k^2}{2m} \\ k &= \sqrt{\frac{2mE}{\hbar^2}} \\ dk &= \sqrt{\frac{m}{2\hbar^2 E}} dE \end{aligned} \tag{72}$$

If we would only be interested in the energies $E(\mathbf{k}) < E$ with E being an allowed eigenenergy, we can use this to create the number of states at a certain eigenenergy[14].

$$\begin{aligned} N(\mathbf{k}) &= \frac{L^3}{\pi^2} \int_{E(\mathbf{k})<E} k^2 dk \\ N(E) &= \frac{L^3}{\pi^2} \int \frac{2mE}{\hbar^2} \sqrt{\frac{m}{2\hbar^2 E}} dE \\ &= \frac{L^3 \sqrt{2} m^{3/2}}{\pi^2 \hbar^3} \int \sqrt{E} dE \end{aligned} \tag{73}$$

From this, it is a short step towards the density of states, which is defined as $g(E) = \frac{dN}{dE}$ or $N(E) = \int g(E) dE$. This gives the number of states for each amount of energy [73].

$$\begin{aligned} N(E) &= \int \frac{L^3 \sqrt{2} m^{3/2}}{\pi^2 \hbar^3} \sqrt{E} dE \\ &= \int g(E) dE \\ g(E) &= \frac{L^3 \sqrt{2} m^{3/2}}{\pi^2 \hbar^3} \sqrt{E} \end{aligned} \tag{74}$$

[13] This is a bit of a shaky notation but will make sense when we change this to a continuous sum

[14] Notice that we used a factor 2 due to the spin degeneracy.

3.1.2 The dispersion relation of an electron in a semiconductor

In the beginning, we made the (simple) ansatz that the wavefunction has only spacial dependency in the exponential. In reality, we do not have completely free electrons. This opens up the band gaps due to weak lattice potential. This effect is visualized in figure 34. The blue lines denote the original free dispersion, while the orange lines denote the dispersion of a nearly free electron. The disconnected orange lines create band gaps between each continuous orange line. The band gap is also known as the forbidden gap, for an electron can't be in a state with that amount of energy. This energy gap shifts the density of states such that it is discontinuous at the band gap energy. When we consider more complex potentials, such as general Bloch waves or the tight-binding model, the dispersion and the density of states can be more complicated.

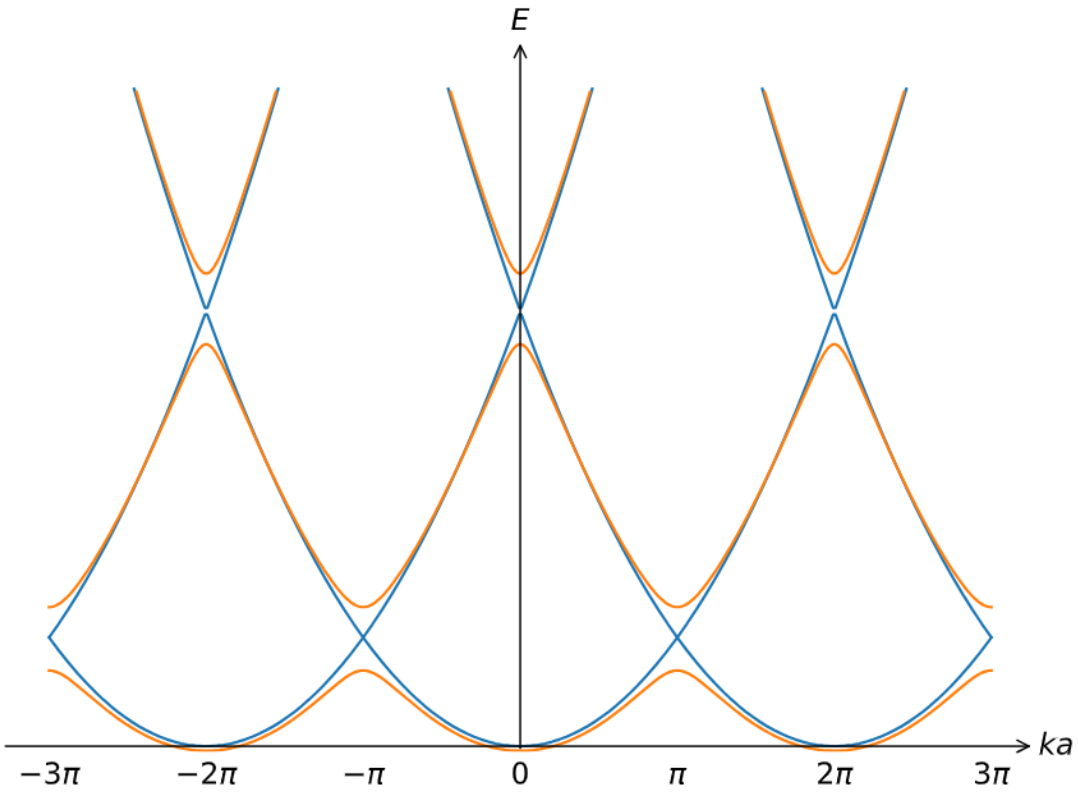

Figure 34: The dispersion relation of a free electron in blue and a nearly-free electron in orange. The dispersion relation is periodic in ka with a being the length of the cubic box, which we denote as L [74].

When the energy of a single electron increases, it can jump to a higher energy band if the increased energy is at least the same as the difference between the bands. When an atom is at 0 Kelvin temperature, all electrons cannot have a bigger energy than the Fermi energy, which is different for each solid [75]. When an electron can move around in a solid, it has its energy in the conduction band. When it cannot move around, it is in the valence band. Both the conduction band and the valence band are groups of multiple different energy bands. The band gap usually denotes the energy gap between the conduction and the valence band. The Fermi energy lies between the conduction and valence band. A conductor has an overlap between the valence band and the conduction band, making the combination of the two include the Fermi energy. This means that there are always electrons free to move in the solid. When the valence band is far below the Fermi energy and the conduction band is far above the Fermi energy, it takes a lot of energy to put electrons in the conduction band, which means it is not a good conductor, hence an insulator. When the band gap is not very big, the solid is an insulator but does not need a lot of energy to become conductive. Those materials are called semiconductors. These three types of materials are shown in figure 35.

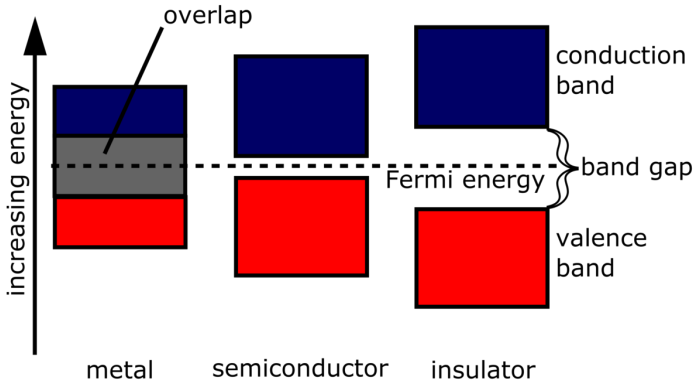

Figure 35: A band gap diagram showing the different sizes of band gaps for conductors, semiconductors, and insulators. [76]

An electron in a solid can have different momenta. This amount of momentum is linearly dependent on the wave vector and is also, therefore, often denoted by k as well. This is called the crystal momentum. The energy of the electron depends on this crystal momentum, meaning that for each k, there is a different band gap. When an electron in a semiconductor transitions from the valence band to the conducting band without changing the crystal momentum, we talk about a direct transition. If an electron changes its momentum, it can transfer to a conduction band energy level that is easier to reach. This is called an indirect transition. Figure 36 shows a schematic of this phenomenon.

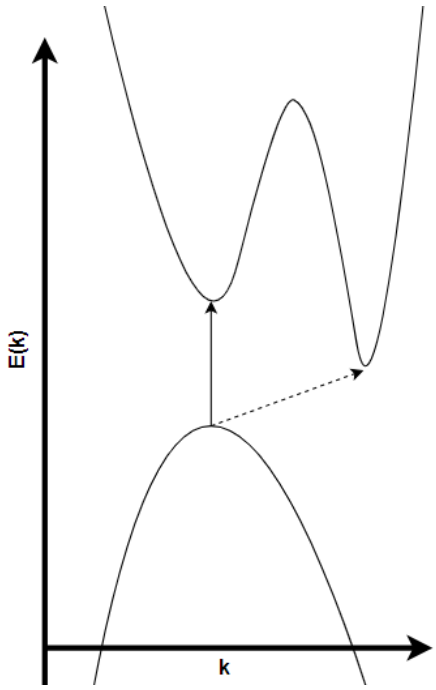

Figure 36: A schematic of the valence band (below) and the conduction band (above) with the straight arrow denoting a direct transition and the dashed arrow denoting the indirect transition.

When an electron moves from the valence band to the conduction band in a semiconductor, it leaves behind a hole. The electron has a charge of -1 C, which means that the valence band misses a charge of -1 C. The hole can, therefore, be seen as having a virtual charge of +1 C to show the change in net charge. This hole can move around the valence band with mobility μ_p. The connected electron in the conduction band can move with mobility μ_n. Both the hole and the electrons are carriers of charge. This is why they are often denoted as "carriers". Semiconductors can be doped with extra holes or extra electrons. This is called p-type with added holes (positive) and n-type with added electrons (negative) [77]. If p- or n-type carriers are added, the ability for electrons to move in the solid increases, i.e., the conductivity increases.

3.1.3 Hydrogenated amorphous silicon semiconductors

As was already discussed, the density of states in a semiconductor has a parabolic shape. To be more exact, $g_c(E) \propto \sqrt{E - E_c}$ for the conduction band and $g_v(E) \propto \sqrt{E_v - E}$ for the valence band. An assumption made to get to these densities was that the solid has a crystal lattice, which is the case for, e.g., crystalized silicon. If we scramble this solid structure up and remove the periodic structure, we get something we call amorphous silicon. The disorder in the structure results in localized states in between the conduction band and the valence band [78]. These localized states can be found in the band tails, also called Urbach tails. An exponential density of states usually describes these localized states. This is shown in figure 37. Due to the added localized states, electrons can jump to the conduction band more easily.

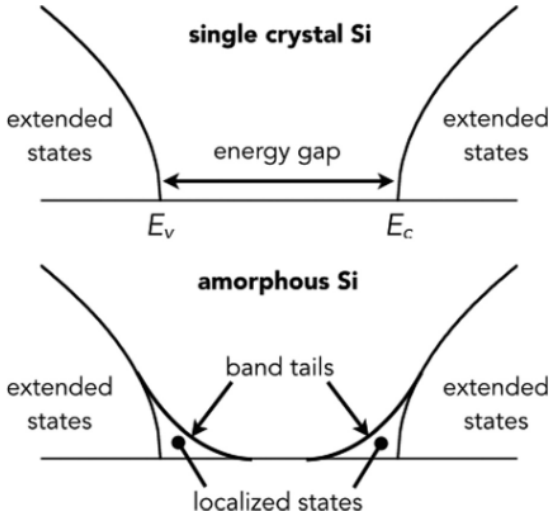

Figure 37: A schematic density of states for crystal silicon and amorphous silicon. E_v is the maximum energy of the valence band. E_c is the minimum energy of the conduction band. The band tails are due to disorder in the structure [79].

In the amorphous structure, there are many dangling bonds. Those are loose ends of the mismatched crystal structure. When an electron frees itself from the valence band, it is often recaptured by the dangling bonds, reducing the amount of carries. Hydrogen atoms are used to cap these dangling bonds by binding on them to compensate for this recombination. A schematic is shown in figure 38. This hydrogenated amorphous silicon (or a-Si:H) is often used in solar cells and OET chips.

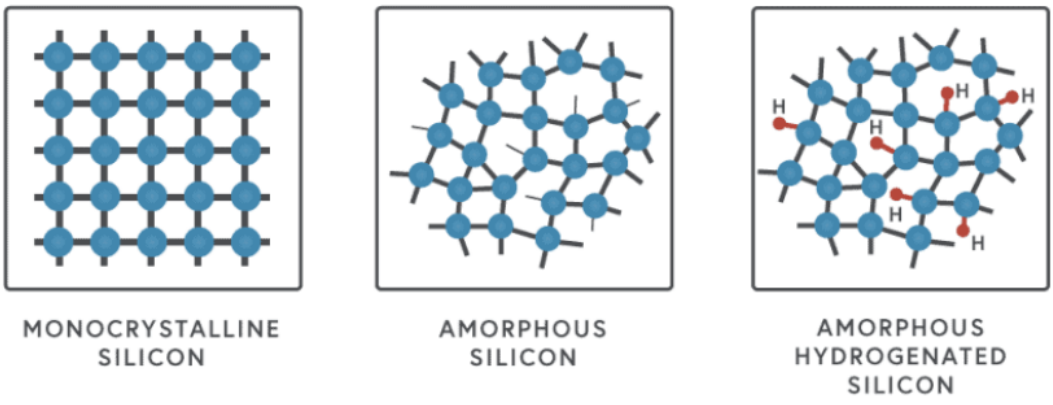

Figure 38: An illustration of the difference in crystal lattice structure. From left to right, monocrystalline silicon, amorphous silicon, and hydrogenated amorphous silicon. [80]

The localized states in the band gap of a-Si:H are often described by 2 Gaussian distributions on top of the Urbach tails to denote possible acceptor-like states and donor-like states [81]. This description uses, on top of the general semiconductor density of states, a combination of 4 densities of states.

$$\begin{aligned} g_{DT}(E) &= G_{D0} \exp\left(-\frac{E}{E_D}\right) \\ g_{AT}(E') &= G_{A0} \exp\left(\frac{E'}{E_A}\right) \\ g_{AG}(E'') &= \left(\frac{N_{AG}}{\sqrt{2\pi}\sigma_{AG}}\right) \exp\left(-\frac{(E''-E_{AG})^2}{2\sigma_{AG}^2}\right) \\ g_{DG}(E''') &= \left(\frac{N_{DG}}{\sqrt{2\pi}\sigma_{DG}}\right) \exp\left(-\frac{(E'''-E_{DG})^2}{2\sigma_{DG}^2}\right) \end{aligned} \tag{75}$$

With E measured from E_v untill E_D. E' is measured from E_A until E_c. E_D and E_A are the characteristic widths of the left and the right Urbach tails. G_{D0} and G_{A0} are defined that way it describes the Urbach tail density of states g_{DT} and g_{AT}. The two Gaussian distributions describe the acceptor-like density of states g_{AG} and the donor-like density of states g_{DG}. N_{AG} and N_{DG} are the number of acceptors and donors such that the peak of the Gaussian describes the density of states correctly. σ_{AG} and σ_{DG} are the standard deviations of the 2 gaussian. E'' and E''' are measured inside the crystal silicon's band gap. A schematic density of states can be found in figure 39.

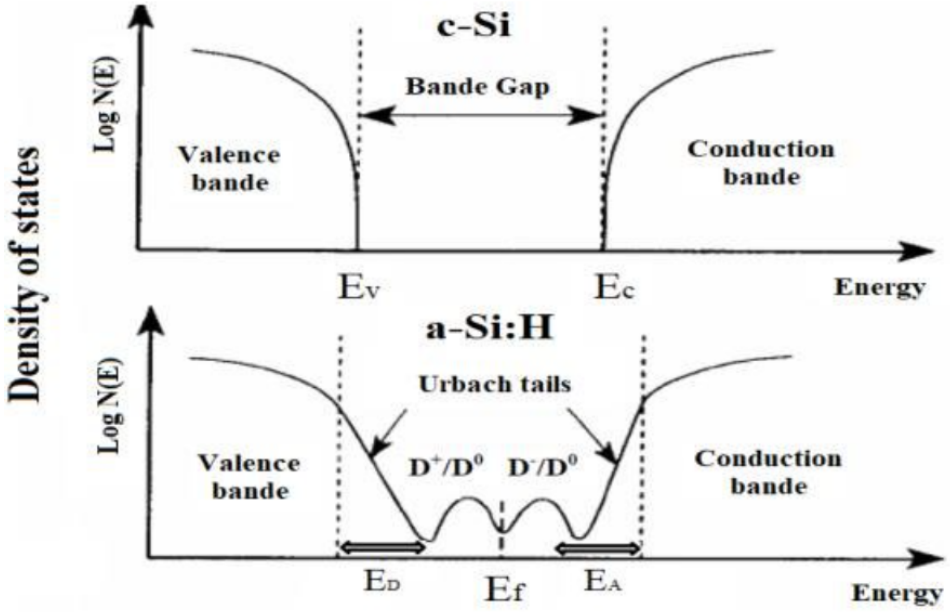

Figure 39: A schematic depiction of the difference in density of states between crystallized silicon and amorphous hydrogenated silicon. E_D and E_A describe the tails of the Urbach tails. E_v, E_c, and E_f are the valence band energy, conduction band energy, and the Fermi energy. D^+/D^0 and D^-/D^0 represent the donor-like gap states per unit volume and the acceptor-like gap states per unit volume [81].

In general, this is still an approximation. The dangling bonds influence the density of states in a complex manner, even when they are capped by hydrogen. The big difference between crystallized silicon and amorphous hydrogenated silicon is how easily carriers are created. There are more possible energy states in the band gap in the latter, making an electron need less energy to jump to a higher energy band. A comparison between the density of states and the energy gaps can be seen in figure 40.

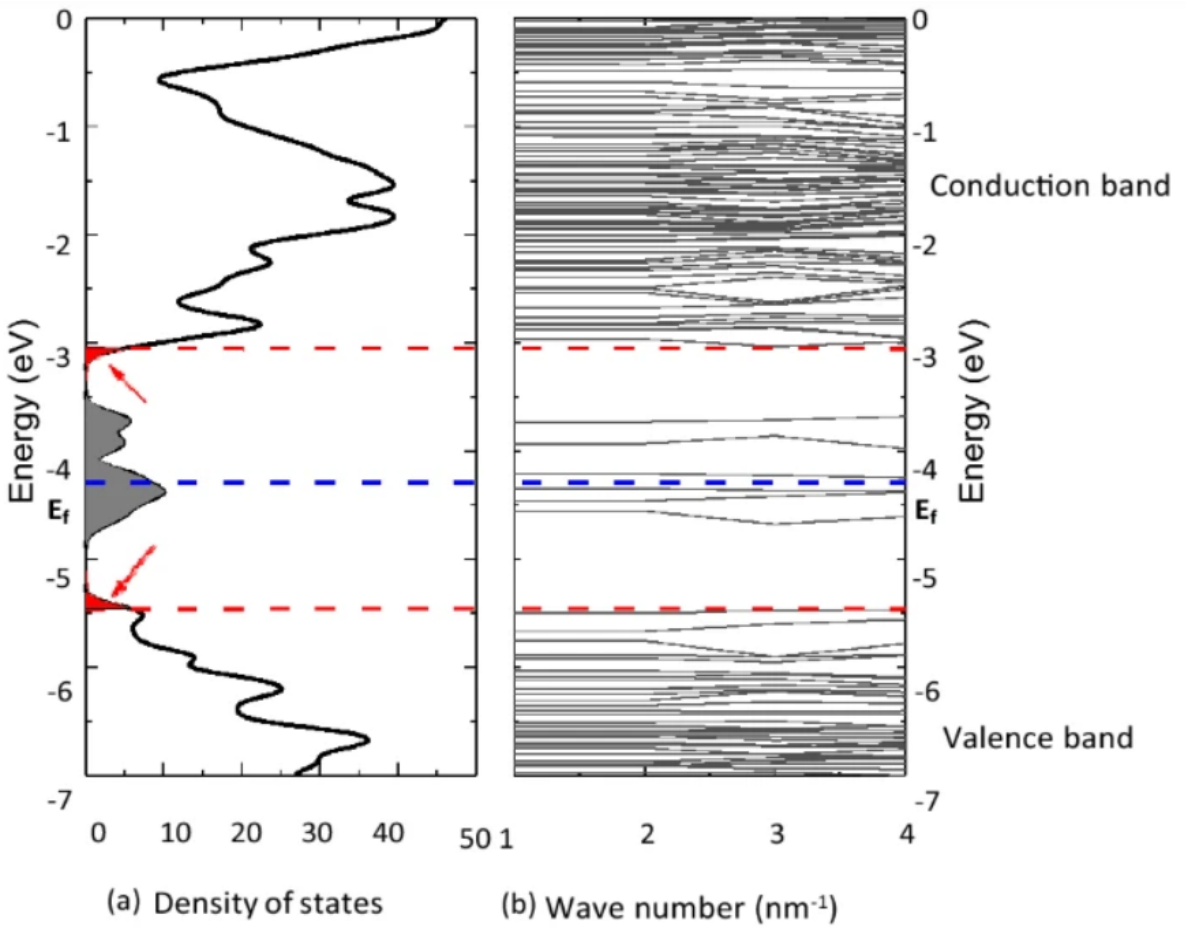

Figure 40: The density of states for a-Si:H with 3% hydrogen concentration. The red arrows denote the Urbach tails, whereas the red dotted lines denote the cutoff energies from the conduction and valence bands. The blue dotted line denotes the Fermi energy. The left figure is the energy against the density of states. The right figure is the energy against the wave number k [82].

3.2 Change in conductivity due to the photoelectric effect

Some semiconductors can create carriers due to light's illumination. Heinrich Rudolf Hertz called this phenomenon in 1887 the photoelectric effect. This effect was quantized[15] by Albert Einstein in 1905 [83]. The energy of a photon is given as

$$E(\lambda) = \frac{hc}{\lambda} \tag{76}$$

With Planck's constant h and the speed of light c. λ is the wavelength of the photon [84]. The magnitude of the optical intensity $|I|$ is defined as the amount of optical power P per illuminated area A. The optical power is the amount of energy E per second.

$$|I| = \frac{P}{A} = \frac{E}{At} = \frac{hc}{\lambda At} \tag{77}$$

The amount of intensity in a material is highly dependent on the thickness of the material. This was discovered by Pierre Bouguer before 1729 and later worked out further by Johann Heinrich Lambert and August Beer [85].

$$\begin{aligned} \frac{dI}{dx} &= -I(x)\alpha \\ I(x) &= I(0)e^{-\alpha x} \end{aligned} \tag{78}$$

$I(0)$ is the intensity at depth $x = 0$, i.e., before the light starts going through the material. α is the absorption coefficient, which is the relative number of photons absorbed per unit distance. This is often has the unit cm^{-1}. We have already seen that electrons can jump up to higher energy bands when provided with enough extra energy in the material. This phenomenon is described by the generation rate, which gives the number of carriers created per volume (often cm^{-1}) per second and depends on the change in intensity [16].

$$g(x) = -\eta \frac{dI(x)}{dx} = \eta\alpha I(0)e^{-\alpha x} \tag{79}$$

With x being the depth of the material and η being the quantum efficiency describing how many carriers are created per photon [86]. In reality, the generation rate depends on the depth and the wavelength of the incoming light. Therefore, a more accurate description is given by

$$g(x, \lambda) = \eta(\lambda)\alpha(\lambda)I_0(\lambda)e^{-\alpha(\lambda)x} \tag{80}$$

In this generation rate, we did not take into account the reflectance of the material which needs to be done as well. This reflection is also depending on the wavelength of the illumination.

$$g(x, \lambda) = \eta(\lambda)I_0(\lambda)\alpha(\lambda)[1 - r(\lambda)]\frac{e^{-\alpha(\lambda)x} + r(\lambda)e^{-\alpha(\lambda)x}e^{-2\alpha(\lambda)d}}{1 - r^2(\lambda)e^{-2\alpha(\lambda)d}} \tag{81}$$

With d being the entire thickness of the material and $r(\lambda)$ being the reflectance at a specific wavelength λ [87]. This is not trivial at all, for it also needs to consider the internal reflection of the material. When the reflectance is taken as 0, we get back the generation rate of equation 80. For now, we will refer to the generation rate of equation 81 as g_o. The wavelength-dependent absorption coefficient is more complex since it comes from the quantum perturbation theory of light-matter interaction [87].

$$\alpha(\lambda) = \frac{e^2\lambda}{6\epsilon_0 n_r c^2 m_0^2 V}|\mathbf{M}_{fi}|^2 J_{c,v} \tag{82}$$

With the charge and mass of an electron e and m_0, with refractive index of the matter n_r and the volume V. The norm of the matrix $|\mathbf{M}_{fi}|^2$ is known as the matrix element of the perturbation[17] describes the disturbance between the final state f and initial state i. This is often denoted in bra-ket notation as $|\langle f|\mathbf{M}|i\rangle|^2$ [88]. The final part in this equation is the joint density of a pair of states $J_{c,v}$, i.e., the density of a hole-electron pair with, e.g., the hole in the valence band and the electron in the conduction band [87].

[15] quite literally for it depends on a quantum of energy.

[16] Remember that the intensity is defined as the number of photons per second multiplied by the photon energy. A positive dI/dx would show an increase in photons per distance, so therefore, a negative dI/dx shows the amount of photons absorbed per distance.

[17] Think of this as the probability of an 'initial state' going to a different 'final state' due to a disturbance in the stable system, i.e., light colliding with the matter. The Hamiltonian matrix $\mathbf{M}$

3.2.1 Intrinsic Photoconductivity

A hole and an electron both have a specific mobility in a material. This is given as μ_p and μ_n because the holes are positive compared to the negative electron, hence the p and n notation. A hole and an electron have the same magnitude[18] of charge $|e|$. The conductivity is defined as the ease of charge moving inside the medium. Therefore, the mobility of holes and carriers add to this [89]. The initial thermal-equilibrium conductivity is given as σ_0.

$$\sigma_0 = |e|(\mu_n n_0 + \mu_p p_0) \tag{83}$$

Where n_0 and p_0 denote the amount of electrons and holes in the initial thermal equilibrium. This is the conductivity of the semiconductor when, e.g., no illumination is applied to excite the material. Therefore, we often call this the *dark conductivity*. The conductivity increases accordingly when we add enough energy to the semiconductor to add holes and electrons.

$$\sigma = |e|\left[\mu_n(n_0 + \delta n) + \mu_p(p_0 + \delta p)\right] \tag{84}$$

The form of interest of this increase in conductivity happens due to illumination by light. Therefore, this is called the *light conductivity* or the *photoconductivity*.

We call this intrinsic photoconductivity when we have exactly enough energy to excite an electron from the valence band to the conduction band. Due to the intrinsic absorption, the photoconductivity is ambipolar, i.e., the amount of electron carriers created equals the number of holes created: $\delta n = \delta p$. Using this, we can simplify the equation further to better grasp the theoretical background of the increase in photoconductivity.

$$\frac{\delta\sigma}{\sigma_0} = \frac{\delta n(\mu_n + \mu_p)}{n_0(\mu_n + \mu_p)} \approx \frac{\delta n}{n_0} \tag{85}$$

Where we considered an undoped semiconductor, i.e., $p_0 \approx n_0$, as we can see, the increase in conductivity is directly related to the rise in the number of carriers. Using the information from the previous section, we can write the increase of electrons over time using the generation rate from equation 81.

$$\frac{dn}{dt} = g(t) - r(t) = g(t) - c_{c,v}np \tag{86}$$

The time dependency of the generation rate $g(t)$ is an on/off state. When the light is turned on, the generation rate equals the generation rate $g(x, \lambda)$ from equation 81. When the light is off, $g(t) = 0$. The recombination rate $r(t)$ is the constant $c_{c,v}$ times the number of holes and electrons. This gives the amount of electrons going from the conduction band back to the valence band. Notice that for intrinsic photoconductivity, equation 86 is equal to the change in the number of holes $\frac{dp}{dt}$. This first-order differential equation can be solved by applying some necessary boundary conditions. We can solve this equation with $n = 0$ at $t < t_0$ where t_0 is the moment the illumination is turned on. We use that $n = p$ to describe intrinsic photoconductivity. We denote the generation rate $g(x, \lambda)$ as g_o and the recombination coefficient $c_{c,v}$ as c_o.

$$\begin{aligned}
\frac{dn}{dt} &= g_o - c_o n^2 \\
\frac{dn}{g_o - c_o n^2} &= dt \\
\frac{1}{g_o}\int_{n=0}^{n=n(t)} \frac{dn}{1 - \frac{c_o}{g_o}n^2} &= \int_{t=t_0}^{t} dt \\
\frac{1}{g_o}\sqrt{\frac{g_o}{c_o}}\tanh^{-1}\left(\sqrt{\frac{c_o}{g_o}}n(t)\right) &= t - t_0 \\
n(t) &= \sqrt{\frac{g_o}{c_o}}\tanh\left(\sqrt{g_o c_o}(t - t_0)\right)
\end{aligned} \tag{87}$$

[18] This is a bit counterintuitive, but look at the hole as the literal opposite of an electron, for it is the absence of the electron. If the hole and the electron are back together, there is a net charge of 0 again, for the system is back to its original state.

Where we used that $f(x) = \tanh^{-1}(ax) \rightarrow \frac{df(x)}{dx} = \frac{a}{1-(ax)^2}$. The $\tanh(t)$ function converges to 1 when t is big enough. Therefore, the steady state amount of carriers n_{max} is given by $\sqrt{\frac{g_o}{c_o}}$. The bigger the absorption, the bigger the generation rate and, thus, the bigger the photoconductivity. When the illumination is turned off after some time, we keep the recombination, which results in an exponential decay of the number of carriers.

$$\begin{aligned}
\left(\frac{dn}{dt}\right)_{\text{decay}} &= -c_{c,v}n^2 \\
\frac{-1}{c_{c,v}}n^{-2}dn &= dt \\
\int_{n_{\max}}^{n(t)} \frac{-1}{c_{c,v}}n^{-2}dn &= \int_{t_1}^{t} dt \\
n(t) &= \frac{n_{\max}}{1 + n_{\max}c_{c,v}(t-t_1)}
\end{aligned} \tag{88}$$

With t_1 denoting the moment the right is switched off, the amount of electron carriers equals $n_{\max}$.

3.2.2 Extrinsic Photoconductivity

When we consider extrinsic photoconductivity, we need to consider the localized states, also called defects, in the band gap due to, e.g., the Urbach tails. There are three types of extrinsic photoconductivity possible.

1. Excitation from a defect with direct recombination into the same type of energy level, i.e., the carrier is directly pulled back to the level it already was.
2. Excitation from a defect with carrier recombination into another type of energy level.
3. Excitation into a band where major trapping occurs. This can be seen as carriers getting stuck in a band, which stops them (temporarily) from adding to the conductivity.

The new dynamics of the carriers are given as

$$\begin{aligned}
\frac{dn}{dt} &= g_o - c_{c,act}p_{act}n - \frac{dn_{trap}}{dt} \\
\frac{dn_{trap}}{dt} &= c_{c,trap}n(N_{trap} - n_{trap}) - e_{trap,c}N_c n_{trap}
\end{aligned} \tag{89}$$

with generation rate g_o, transformation coefficient $c_{c,act}$ from the conduction band to a defect band with the number of holes in the defect states denoted as p_{act}. The trapped electrons are denoted by n_{trap} where N_{trap} is the maximum amount of trapped electrons. $c_{c,trap}$ is the transformation coefficient from the conduction band to a trapped state. Finally, $e_{trap,c}$ denotes the transformation coefficient where an electron is excited out of the trapped state into the conduction band with N_c denoting the number of electrons in the conduction band.

As the amount of trapped electrons increases, the amount of electron carriers decreases, which is unfavorable for the photoconductivity [87]. When an electron is excited, it moves away, leaving a hole behind. Due to this, we have a quasi-neutrality condition relating the amount of holes to the elevated electrons.

$$p_{act} = n + n_{trap} \tag{90}$$

Due to this relation, we can find the steady state solution of equations 89 and determine how the trapped electrons influence the overall photoconductivity analytically.

$$\begin{aligned} \frac{dn_{trap}}{dt} &= 0 \\ c_{c,trap} n (N_{trap} - n_{trap}) - e_{trap,c} N_c n_{trap} &= 0 \\ n_{trap}[e_{trap,c} N_c + c_{c,trap} n] &= c_{c,trap} n N_{trap} \\ n_{trap} &= \frac{c_{c,trap} n N_{trap}}{e_{trap,c} N_c + c_{c,trap} n} \end{aligned} \tag{91}$$

We look at the two limits of this trap occupation to simplify and get a more quantitative understanding. When we have a deep trap, it is harder for an electron to escape the trap in comparison to getting trapped, i.e., $e_{trap,c} N_c << c_{c,trap} n$. In this case, the trap can be considered completely filled, $n_{trap} \cong N_{trap}$. In this case, the steady-state solution of the number of electron carriers, i.e., the first of equation 89, is given as[19]

$$\begin{aligned} g_o &= c_{c,act} p_{act} n \\ &= c_{c,act} n (n + n_{trap}) \\ &\approx c_{c,act} n^2 + c_{c,act} n N_{trap} \\ n &\approx \sqrt{\left(\frac{N_{trap}}{2}\right)^2 + \frac{g_o}{c_{c,act}}} - \frac{N_{trap}}{2} \end{aligned} \tag{92}$$

If we consider a shallow trap, electrons are more easily able to escape compared to the deep trap, i.e., $e_{trap,c} N_c >> c_{c,trap} n$. In this case, n_{trap} still depends on n.

$$n_{trap} = \frac{c_{c,trap} n N_{trap}}{e_{trap,c} N_c}$$

Putting this in the dynamics gives us the steady-state solution.

$$\begin{aligned} g_o &= c_{c,act} p_{act} n \\ &= c_{c,act} n (n + n_{trap}) \\ &= c_{c,act} n^2 + c_{c,act} n^2 \left(\frac{c_{c,trap} N_{trap}}{e_{trap,c} N_c}\right) \\ n &= \sqrt{\frac{g_o}{c_{c,act}[1 + \left(\frac{c_{c,trap} N_{trap}}{e_{trap,c} N_c}\right)]}} \end{aligned} \tag{93}$$

As can be seen, in both the case of the deep and shallow traps, we have a decrease in the available carriers. Therefore, the trapping energy states need to be as small as possible. This can be done, for example, by optimizing the doping[20] concentrations, by optimizing the conditions when depositing the semiconductor, or by optimizing the pre-/post-treatment conditions [90][91][92]. In this section, we just wanted to show the effects of traps explaining the complex dynamics of the semiconductor's photoconductivity. The photoconductivity of an a-Si:H film can also be approximated as being linearly dependent on the optical power [32].

$$\Delta\sigma = e\eta\alpha\mu_n\tau_n\frac{S}{hf_l} \tag{94}$$

With electron charge e, quantum efficiency η, absorption coefficient α, electron mobility μ_n, electron lifetime τ_n, optical power S, Planck's constant h and the frequency of the light f_l. The photoconductivity of hydrogenated amorphous silicon using an optical power of 0.2 mW/cm^2 can be seen in figure 41.

[19] Notice that the square-root is only taken as positive in the solution because n cannot be negative.
[20] Doping is putting initial holes or electrons in the material to have an initial number of carriers.

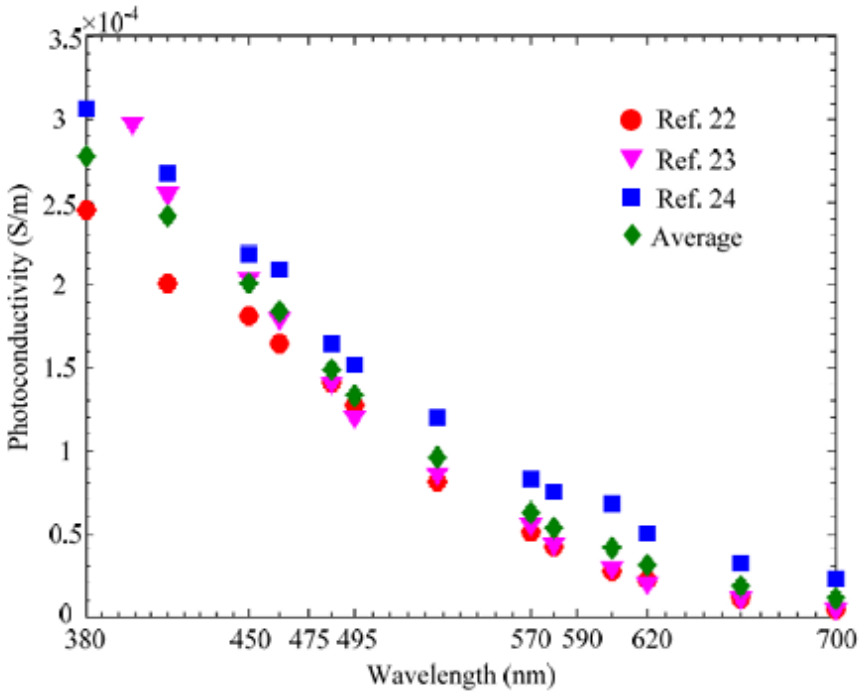

Figure 41: The photoconductivity of hydrogenated amorphous silicon at different wavelengths of light [32]. The data is recovered from 3 different sources. In the bibliography, ref 22 can be found as [93], ref 23 can be found as [94] and ref 24 can be found as [95].

3.2.3 Photoconductivity after long-term illumination

We discussed why the conductivity of certain semiconductors increases when illuminated with light. One thing that is also interesting to mention is the long-term effects of the photoconductivity. The dark conductivity is increased at first due to a phenomenon called persistent photoconductivity. After this increase, the Steabler-Wronski[21] effect takes over, which decreases the dark conductivity. Figure 42 shows an example of this effect. The persistent photoconductivity can be explained by the spatial separation of the holes and carriers due to potential barriers in a superlattice, i.e., a periodic lattice of different materials. Another possible reason could be that electrons have a stronger interaction with the lattice, leaving the holes behind in a self-trapped state, making it harder to recombine [96] [97]. Both these theories give a reason for the different dynamics of the electrons and the holes, increasing the conductivity for some time.

The Steabler-Wronski effect shows that photons could create photo-induced defects like extra dangling bonds[22] in a-Si:H [98]. Those dangling bonds could trap carriers, which remain trapped when the illumination is turned off. This reduces the dark conductivity over time. Both the persistent photoconductivity and Steabler-Wronksi effects can be reversed using thermal annealing.

[21] This effect is present in a-Si:H and not generally in every type of semiconductors.
[22] Remember the loose ends in the lattice of amorphous silicon

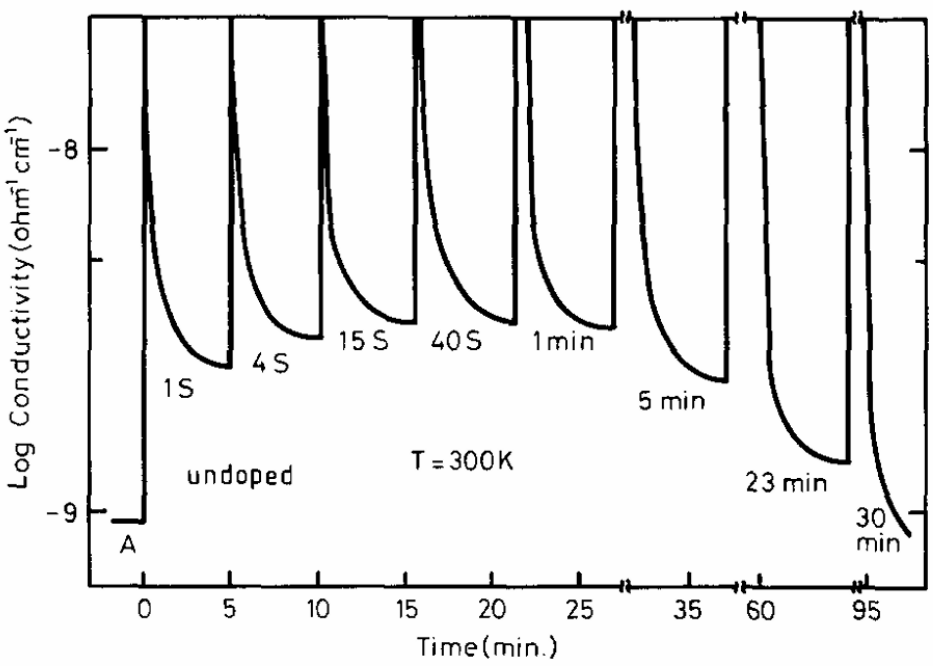

Figure 42: The conductivity of undoped a-Si:H after illuminating it 1 s, 4 s, 15 s, 40 s, 1 min, 5 min, 23 min, and 30 min. Each light exposure is followed by 5 min of rest before the next, longer illumination time. An increase in dark photoconductivity can be seen in the first 22 min, after which it decreases [99].

3.3 Macroscopic structure of the photoconductive layer

We have mainly discussed the internal physics of the photoconductive layer, including its internal structure and the resulting dynamics in conductivity. The surface of this photoconductor is in contact with the chip's medium and influences the dynamics of the dielectric particles. Regarding the outer structure of the photoconductor, two subjects of interest are the surface roughness and the particles' adhesion.

3.3.1 Surface roughness of the photoconductive layer

When looking at the surface roughness of the photoconductive layer, we have to look at the adhesion effects of the particles on the surface and the effects of a rough surface of an electrode in a capacitor. The electrical field lines can never cross and are uniform[23] between the charged electrode and the grounded electrode. If we consider a rough surface, we disturb the uniformity of the electrical field, creating a field with certain gradients. This is especially present in the peaks and troughs [100] [101]. From this logical reasoning alone, we must assume that this will play a role in the DEP force. Therefore, the simulation in COMSOL from section 1.5.2 needs to be tweaked such that the top of the photoconductive layer is randomly distributed to a certain degree. This way, we can discover the expected effects in this OET setup. The computer specifications that ran the simulation were the same as in the previous simulations. The simulation is similar to the last simulations with the added surface roughness. Therefore, we will discuss only the changes made to this simulation here.

We define the height of the photoconductive layer in the simulation as $h(x)$.

$$h(x) = 1[\mu m] + aY(x) \tag{95}$$

with a being the magnitude of the uniform distributed value $Y(x)$ where $Y(x) \sim \mathcal{U}(-1, 1)$. x denotes that the surface is divided in L/x pieces with stepsize x and total surface length L. This means that the total surface is uniformly distributed around $1\mu m$. The effects of a can be seen more clearly in figure 133, 134, 135, 136 and 137 in appendix B.1.2. All results of these simulations can be found in appendix B. The main takeaways will be discussed here.

[23] In a perfect parallel plate capacitor at least.

Two scenarios were considered to determine the impact of the surface roughness on the DEP force. One scenario with illumination, as was done in 1.5.2, and one scenario without illumination, i.e., where the photoconductive layer has a uniform photoconductivity. The second scenario's results are shown in appendices B.1.3, B.2.3 and B.2.4 while the rest of appendix B covers the results from the scenario with illumination. Table 4 shows the main results of the first, illuminated, scenario while table 5 shows the main results of the second scenario where there is no illumination.

Table 4: The main results of the photoconductive layer roughness simulation in the illuminated state with alternating randomness a as described by equation 95.

a	max E_x [V/m]	max E_y [V/m]	max F_x [pN]	max F_y [pN]	Increase of $\partial_x \lvert\mathbf{E}\rvert^2$ [%]	Increase of $\partial_y \lvert\mathbf{E}\rvert^2$ [%]
0	230269.9324	265602.3707	2939.0657	5039.6666	-	-
0.5	230714.7595	265815.1588	2989.0121	5071.2532	1.6994	0.6268
1	232183.7205	266538.0513	3080.2493	5159.4258	4.8037	2.3763
1.5	233870.5916	267444.1682	3195.2635	5269.8918	8.7170	4.5683
2	235892.026	268381.785	3320.7259	5398.8094	12.986	7.1263

Table 5: The main results of the photoconductive layer roughness simulation in off state with alternating randomness a as described by equation 95.

a	max E_x [V/m]	max E_y [V/m]	max F_x [pN]	max F_y [pN]	Increase of $\partial_x \lvert\mathbf{E}\rvert^2$ [%]	Increase of $\partial_y \lvert\mathbf{E}\rvert^2$ [%]
0	5.2433×10^{-7}	117070.6591	5.8293×10^{-9}	1.4644×10^{-8}	-	-
0.5	5.3027×10^{-7}	117070.6591	8.3164×10^{-9}	1.8783×10^{-8}	42.667	19.151
1	5.3000×10^{-7}	117070.6591	8.3456×10^{-9}	1.8573×10^{-8}	43.167	2.4679
1.5	5.1023×10^{-7}	117070.6591	8.5832×10^{-9}	1.5440×10^{-8}	47.243	16.190
2	5.1970×10^{-7}	117070.6591	9.4638×10^{-9}	1.5794×10^{-8}	62.349	-4.4541

As can be seen, the force increases in the illuminated state with increasing surface roughness. This is expected as the gradient increases due to the increased randomness. According to this simulation, the max DEP force in both directions increases faster than linearly. The simulation without illumination shows the roughness's minimal effect on the surface. The magnitude of the electrical field in the y-direction is of the same order as in the illuminated scenario, which can be explained by the electrodes being charged with 25V and 0V in both scenarios. The max DEP force is in an order of -12, smaller than in the illuminated case. As discussed in previous chapters, the amount of force a particle needs is more in the ballpark of pN or nN, which means that these zeptoforces will be no concern regarding the DEP force. Also, as can be seen in appendix B, the difference of the partial derivative in both directions for each scenario quickly falls off in the y-direction, meaning that the roughness effects are only visible (if they already are) very closely to the surface.

Another effect the roughness can have on the particle is surface-particle adhesion. The electrostatic effect, Van der Waals interaction, protein adsorption, or hydrophobic effects could attract particles in the range of nano Newtons while the OET produces forces in the range of pico Newtons [102]. These phenomena highly depend on the type of materials used due to characteristics such as e.g. the surface energy of the materials. When a surface has a high surface energy, a particle will feel a relatively big adhesive force. Materials with high surface energy are metals, while most plastics have low surface energy. The energies[24] of different materials are shown in figure 43.

[24]The surface energy is often denoted as the amount of energy per area [mJ/m^2] but can also be denoted as force per distance [mN/m].

The full force of an elastic particle on frictional contact can be described by the Hertz-Mindlin model [103]. Later, this model was extended by Johnson, Kendall, and Roberts to include van der Waals interactions as well [104]. Those models are too complex to dive into but can be read into when wanting a more detailed understanding of the physics behind the surface adhesion. One interesting takeaway is how the adhesive force is implemented in the JKR-model.

$$F_{adh} = \pi a^2 \gamma^* \tag{96}$$

where a denotes the effective contact radius, which assumes the area of contact between 2 materials being a circle.γ^* is the effective surface energy which can also be written as $\gamma^* = \gamma_1 + \gamma_2 - 2\gamma_{12}$ with γ_1 as the surface energy of, e.g., the photoconductive layer and with γ_2 being the surface energy of, e.g., the dielectric particle that sticks on the photoconductor. γ_{12} is the interface energy between the materials, mainly in liquid or gas states, describing the "ease of mixing". As can be seen, the adhesion force depends on the area of contact, which is without holes for a perfectly smooth sphere on a perfectly smooth surface. If we consider the contact area rough on the side of the photoconductive layer, we will introduce spots where the non-liquid materials don't touch. To give this a physical meaning, we can add an efficiency term in equation 96. The contact area is smaller when the surface is rough, meaning the adhesive force will be smaller. Therefore, a rough surface on the photoconductive layer would create bigger electrical field gradients, which create bigger DEP forces and reduce the adhesion forces, making the effective force in the OET bigger.

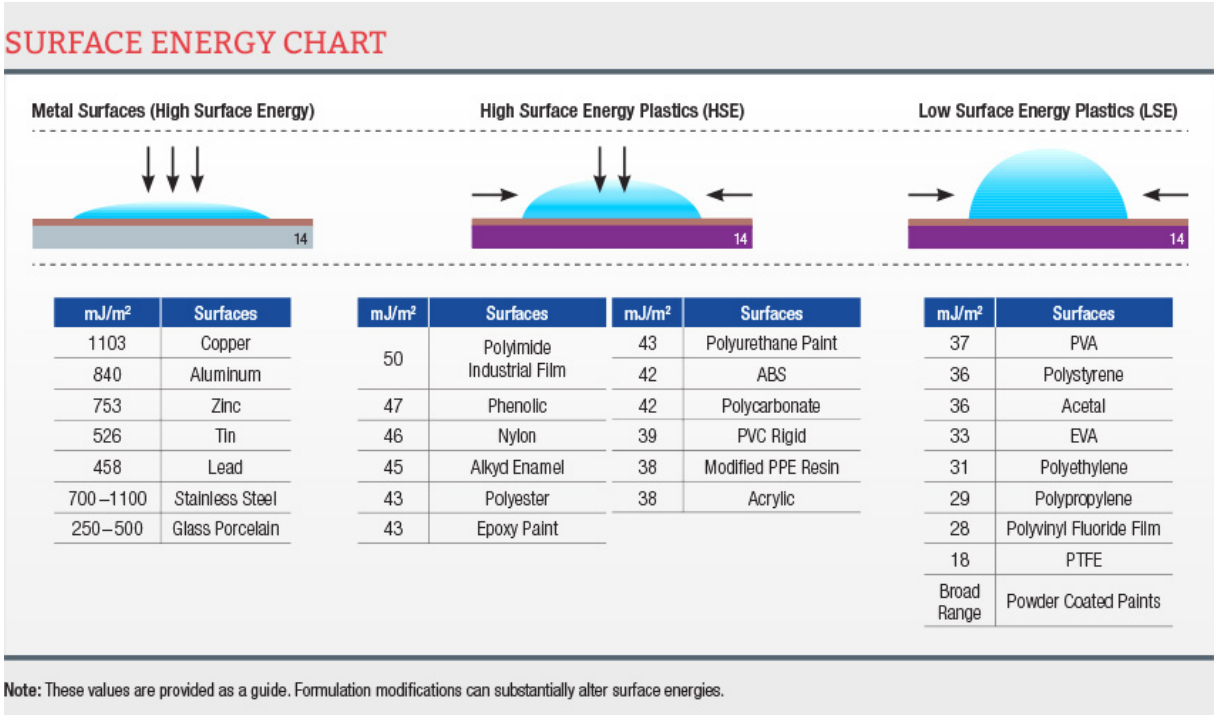

Figure 43: A surface energy chart denoting different surface energies of different materials. The blue dot is a schematic depiction of how well a material attaches to this surface [105].

3.3.2 Surface-Particle adhesion prevention

In microfluidic chips, there can be multiple reasons for the adhesion interaction between particles and the photoconductive layer. Therefore, the adhesion/fouling could give a too big threshold to provide the ability to move the particles. This would create a big problem, for it is quite the opposite of the idea behind the optoelectronic tweezer. Therefore, an antifouling coating between the photoconductive layer and the medium can be added. For the specific optoelectronic setup, two known materials are primarily used: Bovine serum albumin (BSA) and polyethylene glycol (PEG) [106]. BSA is a protein obtained from the bloodstream of a bovine. This protein has a hydrophilic and a hydrophobic end. When two hydrophobic entities are immersed in water, they are attracted to each other with more strength than a hydrophobic entity is attracted to a hydrophilic one [107]. When the hydrophobic ends of the proteins are attached to the photoconductive layer, the hydrophilic ends create a new antifouling surface that does not attract the hydrophobic particles as strongly as the photoconductive layer did. The hydrophilicity of the photoconductive layer creates a new problem, for it mostly attracts the hydrophilic side of the protein. Therefore, a hydrophobic Teflon layer of 50 nm can be put onto the photoconductive layer using, e.g., a spin-coating process. This hydrophobic Teflon layer makes it possible for the BSA to stick to the photoconductive layer.

PEG is a polymer hydrogel with structure HO-(-CH_2CH_2-O-)$_n$-H. A surface made from this polymer has proven itself to be a good antifouling material by reducing the attached particles up to 90% [108]. The PEG works using entropic repulsion and osmotic pressure. When the PEG layer is hydrated, the PEG chain swells and excludes cells and proteins from sticking to the photoconductive layer. The attachment of PEG to the photoconductive layer can be done using SiO_2 as the intermediate layer on which the PEG can be deposited.

An experiment has been conducted to see the antifouling effectivity using HeLa cells[25] which were put into five different optoelectronic tweezer setups [106]. The percentage of free cells was measured after various amounts of time, as shown in figure 44. As can be seen, both antifouling methods show a significant improvement over no coating. Although it is easier to apply, the BSA coating reduces effectiveness over time because it is easily washed off.

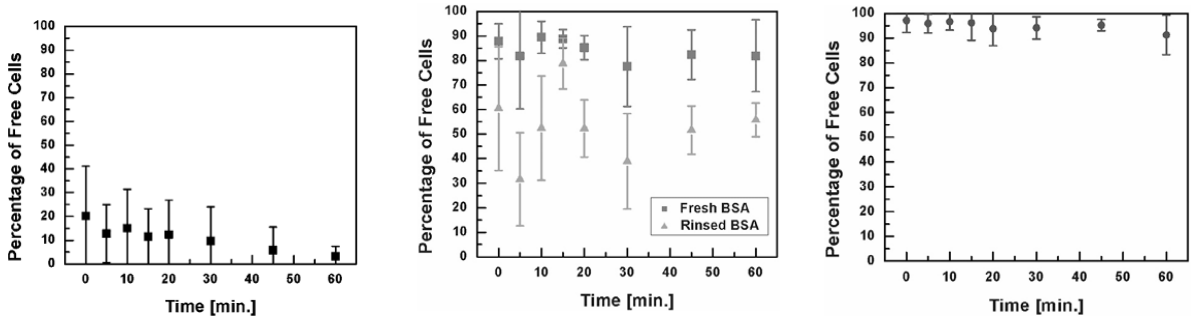

(a) a-Si:H without any fouling-reducing coating.

(b) a-Si:H with a BSA coating on top of a 50 nm Teflon layer.

(c) s-Si:H with a PEG coating on top of a 10 nm SiO_2 layer.

Figure 44: Attachment of HeLa cells after different lengths of time to the a-Si:H layer using different antifouling methods [106].

We can look at the difference in surface energy to put these materials into the perspective of the adhesive force described by equation 96. The average surface energy of amorphous hydrogenated silicon is 340-510 mJ/m^2, comparable to high surface energy materials [110]. The surface energy of BSA is around 59-71 mJ/m^2, and the surface energy of PEG is found to be 48.3 mJ/m^2 making BSA and PEG both low surface energy materials [111] [112]. Another method often used in literature is putting 0.05% TWEEN-20 in the deionized water. This has been shown to improve the surface passivation in microfluidic chips [113].

[25] HeLa cells are cancerous fast multiplying cells that belonged to Henrietta Lacks. Her cells are immortalized due to their high importance and impact in scientific research [109]

3.4 Different types of photoconductive materials

So far, we discussed the most occurring photoconductive material, amorphous hydrogenated silicon, while more photoconductive candidates exist for OET. Theoretically, every photoconductor would work, but only a few materials have been proven useful and strong enough to create a strong enough DEP force.

3.4.1 Bulk-heterojunction polymer

To counter the complicated fabrication process of a hydrogenated amorphous silicon chip, a bulk-heterojunction polymer (BHJ) can be used instead. This polymer is a mixture of poly(3-hexylthiophene) (P3HT) and [6,6]-phenyl C61-butyric acid methyl ester (PCBM). The carrier mobility of BHJ is 7.7×10^{-5} $cm^2V^{-1}s^{-1}$ for electrons and 5.1×10^{-5} $cm^2V^{-1}s^{-1}$ for holes [114]. Compared to a-Si:H with an electron mobility of 1.0×10^{-2} $cm^2V^{-1}s^{-1}$ [115], this shows that the diffusion of carriers is smaller in BHJ than in a-Si:H. This means that BHJ can potentially have more precise manipulation, as it can create a sharper gradient. The BHJ is created by dissolving a certain weight percentage of P3HT:PCBM in 1,2-dichlorobenzene before spin-coating this on a layer of Poly(3,4-ethylenedioxythiophene):poly(styrenesulfonate) (PEDOT:PSS). This PEDOT:PSS layer smoothens the ITO substrate and ensures the photoconductive layer's adhesion on the conductive glass. The amount of weight percentage P3HT:PCBM in the 1,2-dichlorobenzene changes the absorption spectra as is shown in figure 45.

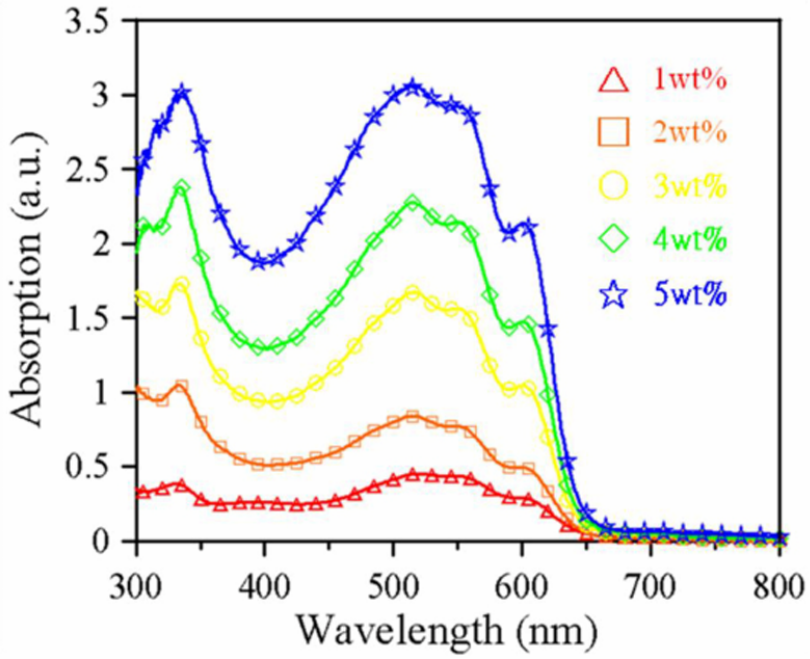

Figure 45: The absorption spectra of the 1,2-dichlorobenzene solution with different weight percentages of P3HT:PCBM spin coated at 600 rpm [116].

On top of this P3HT:PCBM layer, a lithium fluoride (LiF) layer is added to protect the photoconductor from water and oxygen, creating traps by reacting with conjugated molecules in the BHJ layer. The created traps rapidly degrade the chip, giving it a relatively small lifetime. The LiF does not remove this problem entirely but elongates the BHJ chip's lifetime. The maximum DEP force on a 20 μm diameter polystyrene bead is shown over time for a BHJ chip in figure 46.

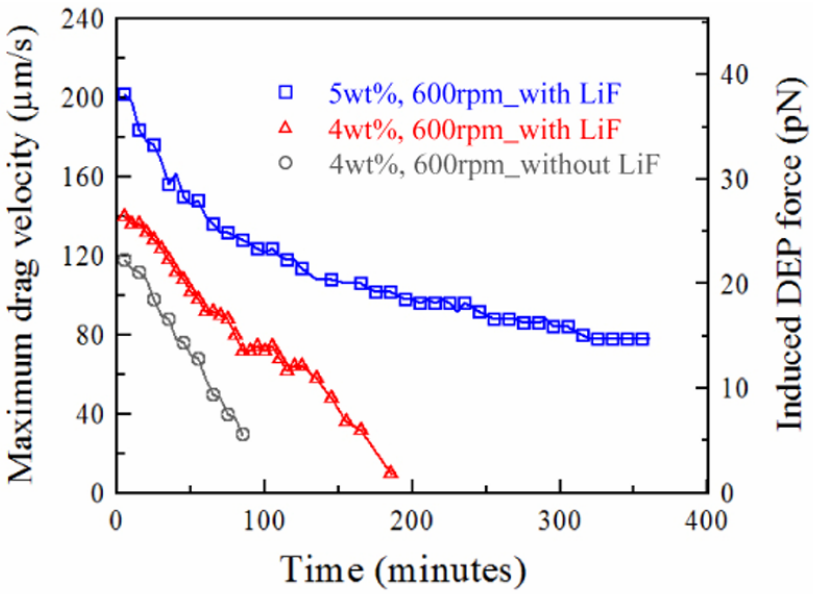

Figure 46: The maximum drag velocity and the respective drag force over time of a 20 μm diameter beads using an AC voltage of 24 Vpp and a frequency of 100 kHz, using white light with an intensity of 7.8 W/cm^2 for illumination. [116].

As can be seen, the maximum DEP force was less than 40 pN, and the chip's lifetime was less than 400 minutes, i.e., less than 7 hours. For comparison, an OET chip using a-Si:H has been found to induce DEP forces around 90 pN for 20 μm polystyrene beads using an AC signal of 20 Vpp and a frequency of 30 kHz [27]. Besides this, a-Si:H has been stable for years and was not found to limit the lifetime of an OET chip [117]. Therefore, a standard a-Si:H chip proves to be more stable and more potent than a chip using a BHJ layer. The main advantage of a BHJ chip is the less complicated and expensive fabrication process, for it does not need PECVD as a-Si:H does. An interesting additional use for BHJ is the ability to be made into a flexible chip [118]. A general (bend) setup of the BHJ polymer photoconductive layer can be seen in figure 47.

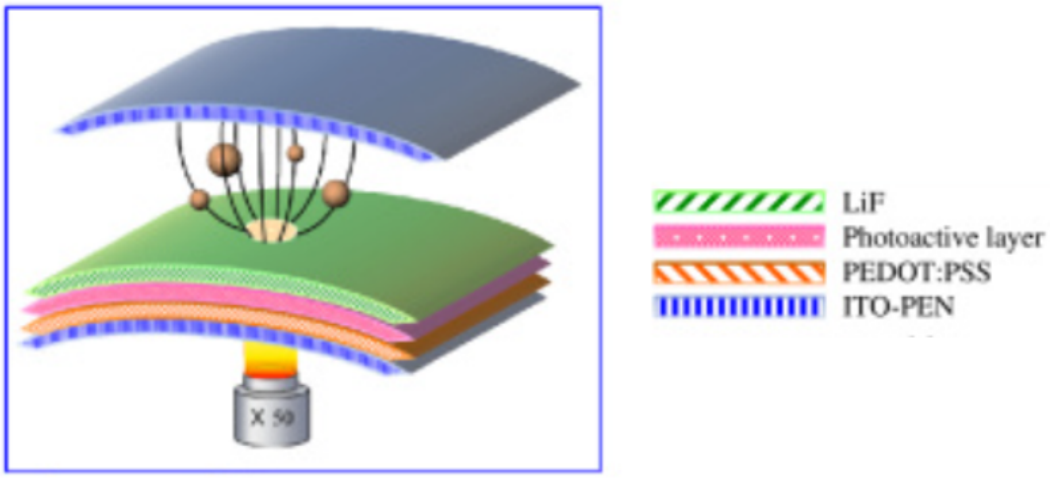

Figure 47: A schematic illustration of the flexible BHJ OET device. The top and bottom layers are the conductive ITO glasses. The second layer from the bottom is the PEDOT:PSS layer, followed by the P3HT:PCBM photoconductive layer. The upper layer from the bottom part is the protective LiF layer [118].

3.4.2 Organic photosensitive material

A promising competent of a-Si:H is titanium oxide phthalocyanine (TiOPc), an organic material (i.e., with carbon atoms). This compound can form in multiple different crystal structures called polymorphs. Each polymorph consists of the same materials but is arranged differently, giving different material structures. The TiOPc type used for OET was Y-TiOPc. The absorption spectrum of this TiOPc lies mainly in the infrared spectrum, as shown in figure 48. TiOPc can be put on a conducting glass by baking it after spin-coating it on the surface. Making a TiOPc-based chip can be finished within 40 minutes and is a relatively quick and easy option for an OET chip [119]. Furthermore, can the TiOPc stay stable for months under normal operation.

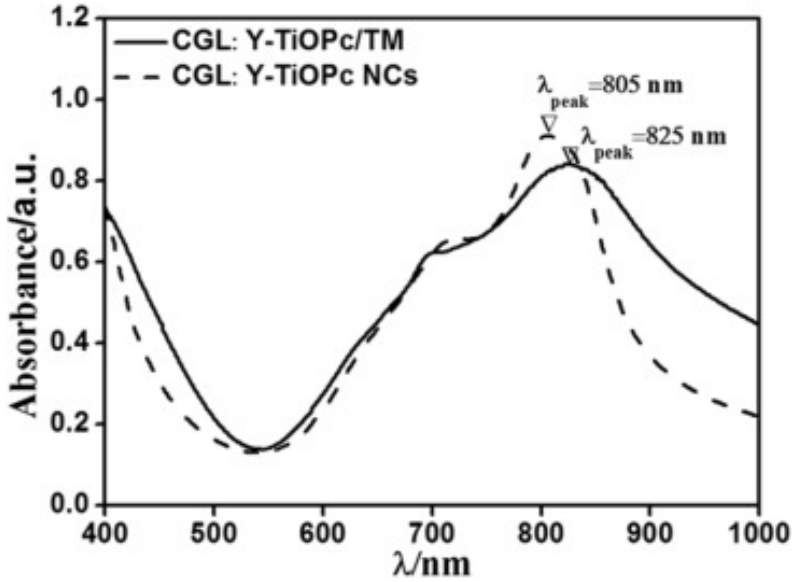

Figure 48: The absorption spectrum of Y-TiOpc made by the traditional method and made with nanocrystals [120].

The light-induced DEP force on a TIOPc has been tested for a 15 μm diameter polymer bead. Figure 49 shows the DEP force for multiple voltages. The maximum measured force is around 11 pN. There has not been an experiment in the literature that uses 4 Vpp to actuate a 15 μm bead using a chip with a-Si:H. Therefore, it is harder to benchmark these results. Nevertheless, can we say that the forces are in the right ballpark considering a bead with 15 μm diameter and an applied voltage of 20 Vpp with a DEP force of around 35 pN [27]. Therefore, on the scaling of the DEP force, the TiOPc chip is a good candidate if the chip performs as well with larger applied signals.

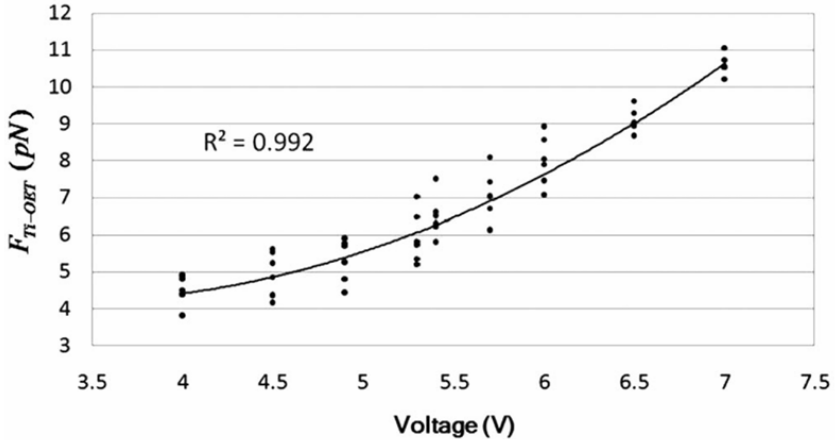

Figure 49: The DEP force using on a TiOPc OET chip. The force actuates a 15 μm diameter polymer bead using an AC voltage with a frequency of 20 kHz [119].

3.4.3 Phototransistor-based material

A chip containing silicon can be tweaked to achieve better results by introducing multiple layers with different doping amounts. Implementing different amounts of holes or electrons than silicon intrinsically has can be used to create p- and n-doped silicon. When making an n-p-n junction[26], we can create a transistor that is activated using light, i.e., a phototransistor. A transistor is an electronic device that behaves like a switch. It is easy for electrons to flow from an n-doped material to a p-doped material. Still, it is hard to go from a p-doped material to an n-doped one[27]. When a small voltage is applied on the p-doped side called the base, the holes get filled up, making this material easier for electrons to traverse. In that case, the charges can go from the n-doped emitter to the p-doped and now neutralized base and go from here to the n-doped collector. Using this phenomenon, a small voltage can enable the base to open the switch and let a large voltage flow from the emitter to the collector. A schematic of a transistor is shown in figure 50. A phototransistor is essentially the same, but the base is activated using light instead of an applied voltage.

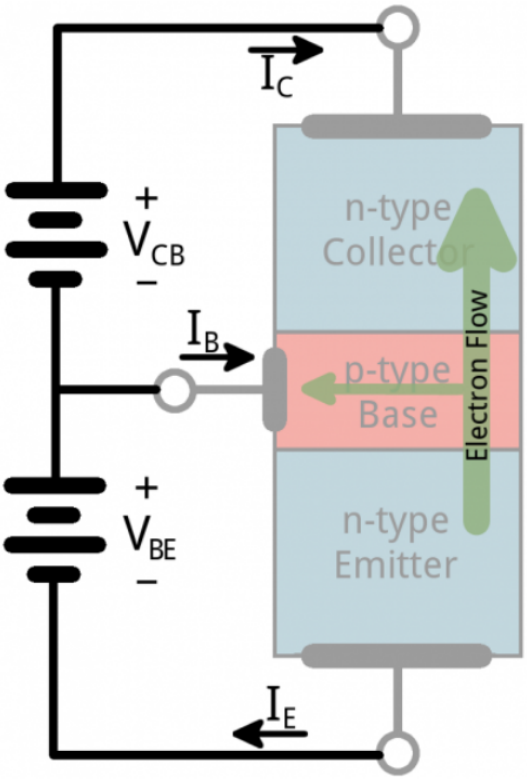

Figure 50: The schematic of a n-p-n junction transistor. Electrons cannot flow from the emitter to the collector unless a small voltage is applied to the base [121].

The phototransistor is created by starting with a highly n-doped silicon substrate. The top layer of this substrate is implanted with boron, which converts the silicon into a p-doped material after a drive-in process. After this, the top layer of the p-doped silicon is converted to an n-doped silicon again by implanting arsenic. One additional thing that is included in the design of the photoconductor is a dielectric grid that separates the p-doped layers in pixels. This separates the phototransistors such that it reduces the lateral flow of carriers. When illumination is applied to the phototransistor, the conductivity sharply increases, for it first blocks the flow in the p-doped base. The difference in conductivity between the phototransistor and the a-Si:H can be seen in figure 51. At 5 V, the phototransistor's conductivity was around 1.4 mS, while the conductivity of a-Si:H at 5 V was around 0.0028 mS.

[26] A junction is a multilayer structure.
[27] This p-n junction is also known as a diode, which we discuss again in section 5.3.1.

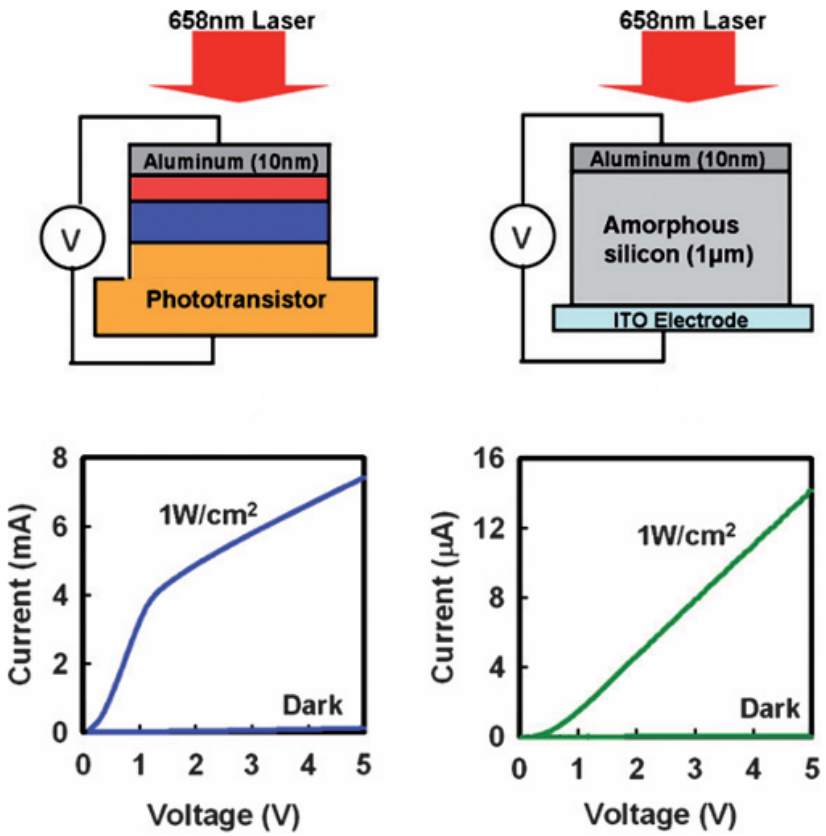

Figure 51: The difference in the current size due to an applied voltage between the phototransistor and the a-Si:H photoconductor [49].

To understand the advantage of this increased conductivity, we first need to model the system as an electric diagram modeling both the photoconductive layer and the medium using an impedance or resistance as we did similarly in section 2.3. This is shown in figure 52. The schematic shows two resistances in series coupled to an AC voltage.

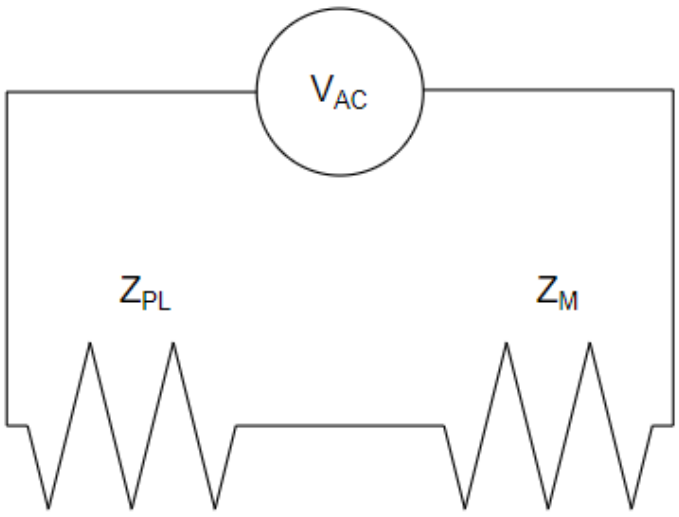

Figure 52: A basic schematic of the OET setup as an electric diagram. V_{AC} is the applied AC voltage, Z_M is the impedance of the medium and Z_{PL} is the impedance of the photoconductive layer.

Using Ohm's law, we can see that the current flow in this system is equal to

$$I = \frac{V_{AC}}{Z_{PL} + Z_M}$$

The voltage drop over both the photoconductor and the medium can be calculated using this calculated current and again using Ohm's law.

$$V_{PL} = \frac{V_{AC} Z_{PL}}{Z_{PL} + Z_M}$$
$$V_M = \frac{V_{AC} Z_M}{Z_{PL} + Z_M}$$

Using the standard equation of the electric field in a parallel plate capacitor, $E = \frac{V}{d}$ with d being the distance between the plates, we can see that the bigger the voltage is over the medium, the bigger the electric field will be in the medium as well. Therefore, when the illumination is on, we want to have an electrical field as big as possible, while we want to have an electrical field as small as possible when the light is off. Therefore, when the illumination is turned on, we want $V_M = V_{AC} - V_{PL}$ to be as big as possible. We want V_M as small as possible when the illumination is turned off.

$$\begin{aligned} V_M &= \frac{V_{AC} Z_M}{Z_{PL} + Z_M} \\ &= \frac{V_{AC}}{\frac{Z_{PL}}{Z_M} + 1} \\ \frac{Z_{PL}}{Z_M} + 1 &\gg 0 \\ Z_{PL} &\gg Z_M \end{aligned} \tag{97}$$

If we do the same when the illumination is on, we want V_M to be as close as possible to V_{AC}. In this case, we need Z_M to be much bigger than Z_{PL}. So to summarize, we want to have in general $Z_{PL,dark} > Z_M > Z_{PL,light}$ and therefore, $\sigma_{PL,dark} < \sigma_M < \sigma_{PL,light}$ where $\sigma \sim 1/Z$ is the conductivity.

When OET is needed in a setup that requires the cells to stay alive, the medium is often highly conductive. This means that the light conductivity of our photoconductor also needs to be high, which is impossible with simple a-Si:H. The introduced phototransistor can have a photoconductivity that is high enough with relatively low optical intensity. This difference is shown in figure 53 where we can see that the phototransistor is above the threshold of the cell culture medium with an optical power of 1 W/cm^2. The hydrogenated amorphous silicon layer can also top this threshold with an optical power that is strong enough. Still, this power will be so high that it will often cause undesirable effects, such as heating the medium so much that it causes damage to the cells.

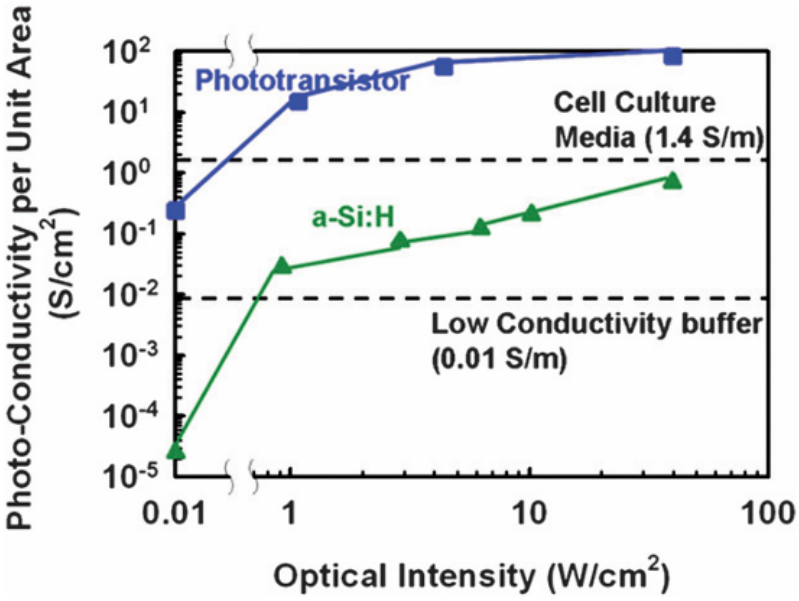

Figure 53: Photoconductivity per unit area of both the phototransistor and a-Si:H against optical intensity. The dashed lines denote the threshold for low conductive media and high conductive media, such as respectively deionized water and phosphate-buffered saline [49].

The last interesting thing in comparing the phototransistor to the standard a-Si:H is comparing the induced DEP forces. As shown in figure 54, the manipulation speed around 6 Vpp is 4 $\mu m/s$. When we take a HeLa size to have an average diameter between 20 μm and 40 μm, we can compare it to known literature using a-Si:H [122]. When comparing it to an MCF-7 cell using a 6 Vpp, 20 kHz sine wave, we find a cell speed larger than 22 $\mu m/s$ [27]. This means that, so far, we can compare these different cells, the a-Si:H chip seems to work better, although it is confined to working with dead cells. The primary added value of the phototransistor is that it opens up the possibility of working with cells that are alive.

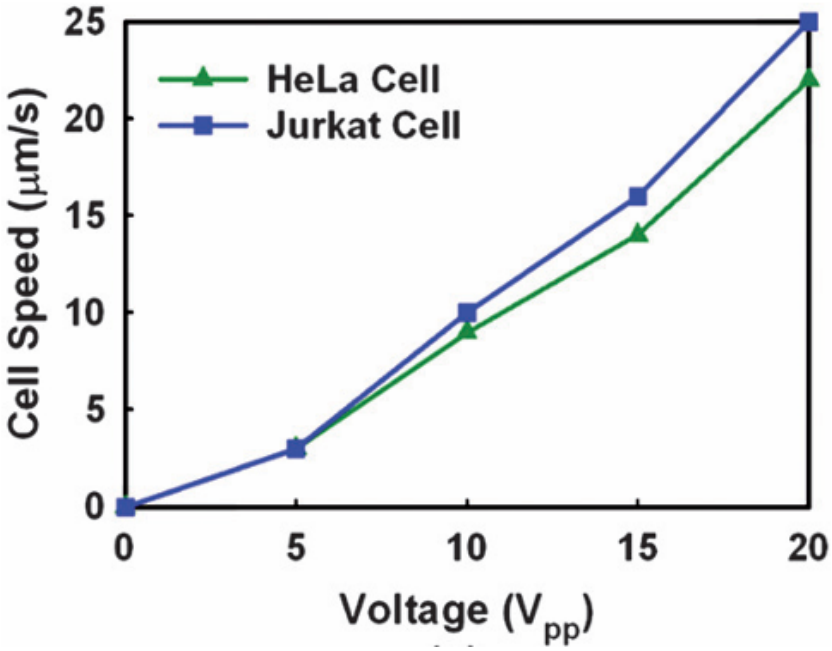

Figure 54: Manipulation speed for different applied voltages of HeLa and Jurkat cells using the phototransistor OET chip [49].

4

The dynamics of the dielectric particle

In this section, we will introduce the comprehensive dynamics of the dielectric particle. To achieve this, we must examine the various forces acting on the particle, in addition to the dielectrophoretic (DEP) force. We begin by considering the forces of gravity and buoyancy, which account for vertical displacement. We also incorporate random forces, such as those arising from Brownian motion. The drag force, which arises from the interaction between the particle's velocity and that of the surrounding medium, is explored in detail. This examination includes the necessary assumptions leading to Stokes' law, which is widely referenced in literature for quantifying the DEP force on particles. These assumptions do, however, constrain the applicability of Stokes' law, prompting a discussion on its validity in comparison to form drag. When a particle carries an electric charge, additional forces, namely electrophoresis and electrostatic forces, play a role.

Additionally, the medium itself exhibits dynamics that can affect the particle through the drag force, influenced by phenomena like electrophoresis and (electro)thermal flow. Therefore, these factors will also be addressed.

Finally, we will discuss frictional forces resulting from surface adhesion. By summing all these forces, we can derive a complete understanding of the particle's dynamics within the system, which can be expressed in state-space form, defined by the system's input and output states. Since certain forces dominate at specific states, we will explore the various force regimes present in this context.

The dynamics of the dielectic particle for "Jip en Janneke"

In an optoelectronic tweezer, a tiny particle moves around because of a special force called the dielectrophoretic force, which we learned about before. But there are other forces that also push and pull the particle. Think of it like when you drop a stone in water; it sinks more slowly than when you throw it in the air. Gravity pulls the stone down, while buoyancy and something called drag force slow it down. The faster you try to swim in water, the harder it gets to move. The same thing happens to our tiny particle as it moves around in a liquid.

There are more forces pushing and pulling on the particle. If the tiny particle has an electric charge, it can also move in the liquid due to a force called electrophoresis, which is a bit different from dielectrophoresis. When the particle is really small, it can move randomly and bumpy because it gets bumped by other tiny particles that we can't see. If the bottom of the microfluidic chip (where the particle is) is super sticky, the particle might get stuck there too.

The liquid itself can also move. If the liquid is charged, it can feel the force of electrophoresis, just like the charged particle. We can also move the liquid by making it hot. Like when you put your hand above hot food, you can feel warm air moving up. This happens with the liquid too when some parts get hot.

Finally, we can put all the different pushing and pulling forces together in a simple way using something called state space. This helps us describe how the particle moves using just a few important factors. When certain factors are strong, some forces become stronger than others.

The Jip and Janneke illustration is created by the renowned artist Fiep Westendorp.

4.1 Forces on the particle

We already discussed the most important force, the DEP force, in the optoelectronic tweezer setup in section 1. This is not the only force working on a particle in the system. To get a good understanding of the dynamics of a particle in the OET, we need to take all the present forces into account and sum them up according to Newton's second law [123]. All forces that we will consider are shown in figure 55 and depend on different variables. We will introduce and explain every force[28] so that we can understand the underlying effects, limitations, and assumptions made for this dynamical system.

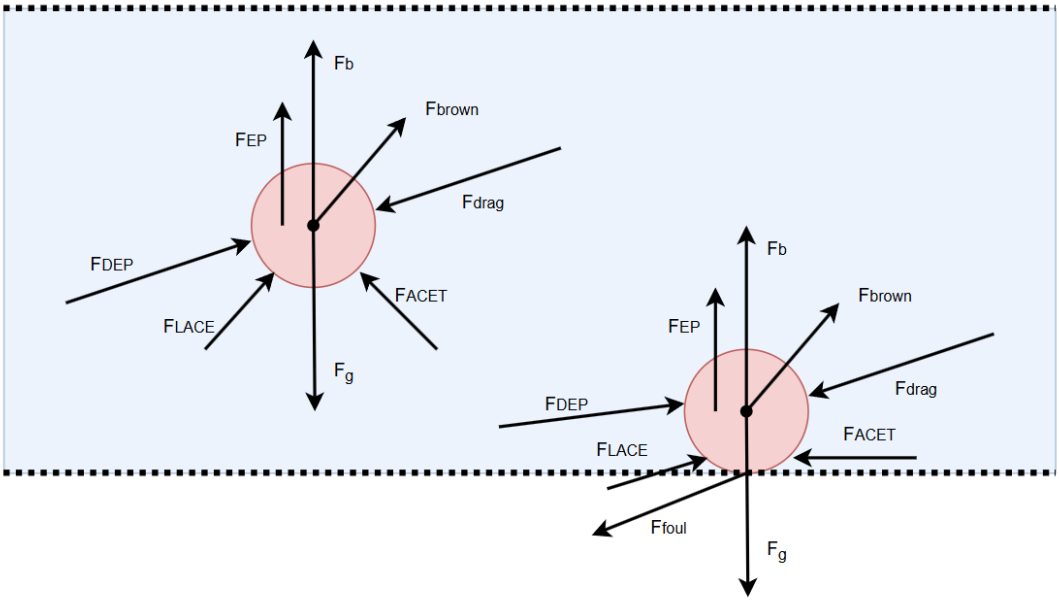

Figure 55: The OET forces that are working on a particle submerged in a medium, free to move (left) and stuck to the bottom (right).

4.1.1 Gravity

One of the most famous stories from the history of physics is how Sir Isaac Newton discovered the law of gravity when an apple fell on his head while sitting under a tree. This moment was one of the pinnacles of the theory of mechanics, although the apple never fell on his head [124]. We now know how two masses are attracted to each other due to some invisible potential. This potential has been postulated to be created due to gravitons and gravitational waves [125]. On earth, it suffices to say that the gravitational force is pointed towards the center of the earth and has a size equal to the mass of the particle times the gravity constant$g \approx 9.81 m/s^2$. We can write this mass as the density ρ_p times the volume of the particle V. The force is given in the direction $\hat{z}$ direction.

$$\mathbf{F}_g = V \rho_p g \hat{z} \tag{98}$$

4.1.2 Buoyancy

Another famous story is from Archimedes, who was asked to determine the gold volume the king's crown was made of. In the story, while Archimedes was sitting in a bath, he found out that the volume of water moved by the crown was equal to that of the crown itself. After this discovery, he went to run naked on the streets, shouting "Eureka". This was the beginning of the discovery of buoyancy [126]. Later, this principle was reformed by stating that the force pushing an object upwards when submerged equals the displaced medium's gravity force [127]. If a fully submerged particle is in a medium, the displaced water equals the particle's volume V. This helps us set up the buoyancy to be very similar to the gravity force from equation 98 by rewriting it using the density of the medium ρ_m. The force is given in direction $\hat{z}$.

$$\mathbf{F}_b = V \rho_m g \hat{z} \tag{99}$$

[28] Except for the DEP force that is already described in section 1.

4.1.3 Brownian motion

If we manipulate very small particles in the OET, the particles will have dynamics due to the collisions with the molecules in the medium. Scottish botanist Robert Brown discovered this in 1828 [128]. He observed rapid oscillatory motion, which was later redefined by French physicist Paul Langevin [129]. The theory of Langevin describes the motion of a small particle with a randomly distributed external force [130]. This random distribution creates a random walk that moves in random directions. A spherical particle's average speed is an expected value [131]. The Brownian motion can also be approached as a stochastic disturbance, where the effect becomes more significant with decreasing particle size.

$$\langle \dot{\mathbf{x}} \rangle = \sqrt{\frac{k_b T}{3\pi\eta r}} \tag{100}$$

With the Boltzmann constant k_b, the temperature T, the viscosity of the medium η, and the radius of a spherical particle r. Brownian motion also appears to create stochastic rotational movements [132]. Both these Brownian dynamics can be taken into account as a stochastic disturbance.

4.1.4 Drag force

If we want to know what the effect of a fluid on the particle is, we have to look at the Navier-Stokes equation [133]. This equation, named after Claude-Louis Navier and Sir George Gabriel Stokes, describes fluid dynamics.

$$\rho\left(\frac{\partial \mathbf{V}}{\partial t} + (\mathbf{V}\cdot\nabla)\mathbf{V}\right) = -\nabla p + \mu\nabla^2\mathbf{V} + \mathbf{F} \tag{101}$$

Where ρ is the density of the fluid, μ is the fluid's viscosity, $\mathbf{V}$ is the speed of the fluid, and p is the pressure on the fluid. This equation is complicated to solve and can sometimes be simplified into a less complex form. We can look at the Reynolds number [134] to do this.

$$Re = \frac{\rho V L}{\mu} \tag{102}$$

Where ρ is the density of the fluid, V is the speed of the fluid relative to the particle, L is the characteristic length of the particle (e.g., the diameter of a sphere), and μ is the viscosity of the fluid. We can transform equation 101 using equation 102.

$$Re\left(\frac{\partial \mathbf{V}}{\partial t} + (\mathbf{V}\cdot\nabla)\mathbf{V}\right) = VL\nabla^2\mathbf{V} - \frac{VL}{\mu}\nabla p + \frac{VL}{\mu}\mathbf{F} \tag{103}$$

Because the speed of the particle has not been measured bigger than $750 * 10^{-6}\ m/s$ with particle size smaller than $200 * 10^{-6}\ m$ for OET, the Reynolds number can be taken to be much smaller than 1 when using water with $\frac{\rho}{\mu}$ bigger than $10^{-6}\ s/m^2$. Also, we will take the external forces into account later but will take them to be 0 to derive the addition of the drag force only.

$$\begin{aligned} VL\nabla^2\mathbf{V} - \frac{VL}{\mu}\nabla p &= 0 \\ \mu\nabla^2\mathbf{V} &= \nabla p \end{aligned} \tag{104}$$

We can derive another condition from the steady-state continuity equation [135]. When we assume that the density of the fluid is constant and homogeneous, we can derive that the divergence of the fluid flow is 0.

$$\begin{aligned} \frac{d\rho}{dt} + \nabla\cdot(\rho\mathbf{V}) &= 0 \\ \nabla\cdot\mathbf{V} &= 0 \end{aligned} \tag{105}$$

The thing we want to solve is to find the force due to a moving fluid on an axisymmetric particle due to the viscous stress. This can be done by solving the surface integral of the viscous stress tensor over the surface of the particle [135].

$$\begin{aligned} \mathbf{F} &= \oiint_S \sigma \cdot d\mathbf{S} \\ \sigma &= -p\mathbb{I} + \mu(\nabla\mathbf{V} + (\nabla\mathbf{V})^\top) \end{aligned} \tag{106}$$

with pressure p and the identity matrix $\mathbb{I}$. To solve this, we need a description of the pressure and the fluid speed at the particle's surface. To do this, we can introduce two boundary conditions. At the surface, the speed of the fluid is 0. This is often denoted as the no-slip boundary condition and can be seen as the fluid sticking to the surface due to the roughness of the surface [136]. In some special cases, like porous materials, this condition does not apply. Still, because we are specifically looking for the viscous force, we can assume this condition to be true [137]. Another boundary condition is that far from the particle, the fluid is constant in the same direction. We will take the fluid moving in a positive z-direction, as shown in figure 56. We will consider cylindrical coordinates first, with ϕ rotating the axis r around the z-axis.

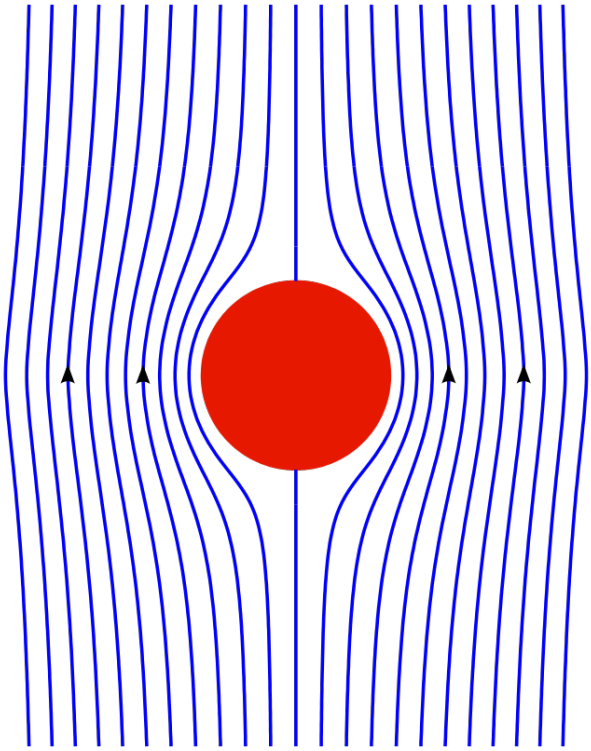

Figure 56: A schematic depiction of the stream function around an axisymmetrical particle. The direction $\hat{z}$ from equation 107 is pointing upwards [138].

In figure 56, we see that we considered a sphere for which the drag force has been well defined. In general, this should also work for every smooth axisymmetric particle. Therefore, we will write the boundary condition and the shape function to match a higher-order smooth boundary condition.

$$\begin{aligned} \mathbf{V}(\sqrt[2n]{r^{2n} + z^{2n}} \to \infty) &= V_\infty \hat{z} \\ \mathbf{V}(\sqrt[2n]{r^{2n} + z^{2n}} = R) &= 0 \end{aligned} \tag{107}$$

with n being an integer bigger than 0. The velocity of the fluid can be described by the Stokes stream function, which describes how the fluid behaves in a laminar flow around a smooth axisymmetric object [139].

$$\mathbf{V} = \frac{1}{r}\frac{\partial \Psi}{\partial r}\hat{z} - \frac{1}{r}\frac{\partial \Psi}{\partial z}\hat{r} \tag{108}$$

As can be seen, the derivative with respect to the radius must be equal to rV_∞ to validate the far-field boundary condition. We can make an Ansatz that validates both boundary conditions.

$$\begin{aligned}\Psi(r,z) &= \frac{1}{2}V_\infty r^2\left(1+\frac{AR}{\sqrt[2n]{r^{2n}+z^{2n}}}+\frac{BR^2}{(\sqrt[2n]{r^{2n}+z^{2n}})^2}+\frac{CR^3}{(\sqrt[2n]{r^{2n}+z^{2n}})^3}+\dots\right)\\ &= \frac{1}{2}V_\infty r^2\sum_{m=0,1,2,3,\dots}\frac{C_mR^m}{(\sqrt[2n]{r^{2n}+z^{2n}})^m}\end{aligned} \tag{109}$$

Filling this form of Ψ in equation 108, we can find a solution for the velocity of the fluid.

$$\begin{aligned}\mathbf{V} &= \left(V_\infty P_m-\frac{r^{2n}}{2}V_\infty Q_m\right)\hat{z}+\left(\frac{rz^{2n}}{2z}V_\infty Q_m\right)\hat{r}\\ P_m &= \sum_m C_mR^m(r^{2n}+z^{2n})^{-\frac{m}{2n}}\\ Q_m &= \sum_m mC_mR^m(r^{2n}+z^{2n})^{-1}(r^{2n}+z^{2n})^{-\frac{m}{2n}}\end{aligned} \tag{110}$$

To solve this, we need to introduce one other variable.

$$\omega = \nabla\times\mathbf{V} \tag{111}$$

ω is called the vorticity and describes how the velocity of the fluid changes in rotation around a certain point. Using the vorticity and the vector identities $\nabla^2\mathbf{x} = \nabla(\nabla\cdot\mathbf{x})-\nabla\times(\nabla\times\mathbf{x})$, and $\nabla\cdot(\nabla\times\mathbf{x})=0$, we can derive an important last condition from equation 104 to solve for $\mathbf{V}$ [140].

$$\begin{aligned}\nabla p &= \mu\nabla^2\mathbf{V}\\ &= \mu\nabla\underbrace{(\nabla\cdot\mathbf{V})}_{=0}-\underbrace{\mu\nabla\times(\nabla\times\mathbf{V})}_{=\mu\nabla\times\omega}\\ \underbrace{\nabla\times(\nabla p)}_{=0} &= -\mu\nabla\times(\nabla\times\omega)\end{aligned} \tag{112}$$

Therefore, if we solve $\nabla\times(\nabla\times(\nabla\times\mathbf{V})=0$, we can find which integers m would allow a solution of equation 112. As we can see from this triple curl of $\mathbf{V}$, this is not trivial to solve at all. The only integer of n where an easy solution is found is for $n=1$, i.e., for a sphere. For more complex shapes, it is better to find a numerical solution. We can find the integers m for a sphere to be a solution for $m=0, m=1$, and $m=3$. We can fill these in for P_m and Q_m from equation 110.

$$\begin{aligned}P_m &= C_0+C_1\frac{R}{\sqrt{r^2+z^2}}+C_3\frac{R^3}{(\sqrt{r^2+z^2})^3}\\ Q_m &= \frac{1}{r^2+z^2}\left(C_1\frac{R}{\sqrt{r^2+z^2}}+3C_3\frac{R^3}{(\sqrt{r^2+z^2})^3}\right)\end{aligned} \tag{113}$$

If we take the boundary conditions from equation 107, we can solve for the constants C_1, C_2 and C_3.

$$\begin{aligned}\mathbf{V}(\sqrt{r^2+z^2}\to\infty) &= (V_\infty C_0)\,\hat{z}+0\hat{r}\\ C_0 &= 1\\ \mathbf{V}(\sqrt{r^2+z^2}=R) &= \left(V_\infty\left[1+C_1+C_3\right]-\frac{r^2}{2}V_\infty\left[\frac{C_1}{R^2}+\frac{3C_3}{R^2}\right]\right)\hat{z}+\left(\frac{rz}{2}V_\infty\left[\frac{C_1}{R^2}+\frac{3C_3}{R^2}\right]\right)\hat{r}\\ 1+C_1+C_3 &= 0\\ C_1+3C_3 &= 0\\ C_1 &= -\frac{3}{2}\ \&\ C_3=\frac{1}{2}\end{aligned} \tag{114}$$

We now have a good idea of fluid dynamics around the sphere. To solve the surface integral, it will be easier to first change the velocity vector of the fluid to spherical coordinates. By substituting in $\sqrt{r^2+z^2}=\rho^2$, $r=\rho\sin(\theta)$, $z=\rho\cos(\theta)$, $\hat{r}=\sin(\theta)\hat{\rho}+\cos(\theta)\hat{\theta}$ and $\hat{z}=\cos(\theta)\hat{\rho}-\sin(\theta)\hat{\theta}$, we can make the equations much more compact.

$$\mathbf{V}(\rho,\theta)=V_\infty\left(1-\frac{3}{2}\frac{R}{\rho}+\frac{1}{2}\frac{R^3}{\rho^3}\right)\cos(\theta)\hat{\rho}+V_\infty\left(\frac{R^3}{4\rho^3}+\frac{3R}{4\rho}-1\right)\sin(\theta)\hat{\theta} \tag{115}$$

We can find the pressure in spherical coordinates by substituting this velocity vector in equation 104.

$$p(\rho,\theta)=-\frac{3\mu R V_\infty}{2\rho^2}\cos(\theta) \tag{116}$$

With that out the way, we only need to solve the viscous stress tensor integral from equation 106. Because the tensor consists of a part depending on the pressure and a part on the velocity, we can also write the force as a sum of those parts. We will look at the pressure part first. We will also need to derive the force in this direction because we have decided that V_∞ is in the positive z-direction. Because the sphere is axisymmetric, we can assume that this viscous force is in the same direction as V_∞.

$$\begin{aligned}
F_{z,p}&=\oiint_S \hat{z}\cdot(-p\mathbb{I})\cdot d\mathbf{S}\\
&=\int_0^{2\pi}\int_0^{\pi}-p\hat{z}\cdot\mathbb{I}\cdot\hat{\rho}R^2\sin(\theta)d\theta d\phi\\
&=\int_0^{2\pi}\int_0^{\pi}-p\begin{bmatrix}\cos(\theta) & \sin(\theta) & 0\end{bmatrix}\mathbb{I}\begin{bmatrix}1\\0\\0\end{bmatrix}R^2\sin(\theta)d\theta d\phi\\
&=2\pi\frac{3\mu R V_\infty}{2R^2}R^2\int_0^{\pi}\cos^2(\theta)\sin(\theta)d\theta\\
&=3\pi\mu R V_\infty\left[-\frac{\cos^3(\theta)}{3}\right]_{\theta=0}^{\theta=\pi}\\
&=2\pi\mu R V_\infty
\end{aligned} \tag{117}$$

We can derive the force due to the velocity of the fluid in the same manner.

$$\begin{aligned}
\hat{\rho}\cdot\left(\mu(\nabla\mathbf{V}+(\nabla\mathbf{V})^\top\right)\cdot\hat{z}&=2\frac{\partial V_\rho}{\partial\rho}\mu\cos(\theta)-\left(\frac{1}{\rho}\frac{\partial V_\rho}{\partial\theta}-\frac{V_\theta}{\rho}+\frac{\partial V_\theta}{\partial\rho}\right)\mu\sin(\theta)\\
&=V_\infty\sin^2(\theta)\frac{3}{2}\frac{R^3}{\rho^4}\mu
\end{aligned} \tag{118}$$

$$\begin{aligned}
F_{z,v}&=\int_0^{2\pi}\int_0^{\pi}\hat{\rho}\cdot\left(\mu(\nabla\mathbf{V}+(\nabla\mathbf{V})^\top\right)\cdot\hat{z}R^2\sin(\theta)d\theta d\phi\\
&=2\pi\mu\frac{3}{2}\frac{1}{R}V_\infty\int_0^{\pi}R^2\sin^3(\theta)d\theta\\
&=3\pi\mu R V_\infty\left[\frac{\cos^3(\theta)}{3}-\cos(\theta)\right]_0^{\pi}\\
&=4\pi\mu R V_\infty
\end{aligned} \tag{119}$$

Therefore, when a spherical particle moves in a fluid with a small Reynolds number, the particle feels a drag from the fluid's viscosity. If we put together the velocity and pressure components, we arrive at Stokes Law.

$$F_z=F_{z,p}+F_{z,v}=6\pi\mu R V_\infty \tag{120}$$

We have to consider that we had to make a lot of assumptions to get to this formulation of the drag force. If we would have a different shape or a fluid velocity that is too big, we would need a different model to describe the fluid force. A formula often used is called the form drag [141].

$$F = \frac{1}{2}\rho C_d A V_\infty^2 \tag{121}$$

We used A as the cross-sectional area[29] of the fluid on the particle, ρ as the density of the fluid, V_∞ is the same fluid velocity as described in Stokes law, and C_d as the drag coefficient depending on the shape of the particle and the Reynolds number of the fluid. This drag coefficient is derived from experiments and makes the force fit in the form of equation 121. As shown in figure 57, the drag coefficient is fairly constant in the range $10^3 < Re < 2 * 10^5$. At a higher Reynolds number, the drag coefficient quickly drops. This drop, called the "drag crisis", is due to the boundary layer of the fluid separating from the particle [142].

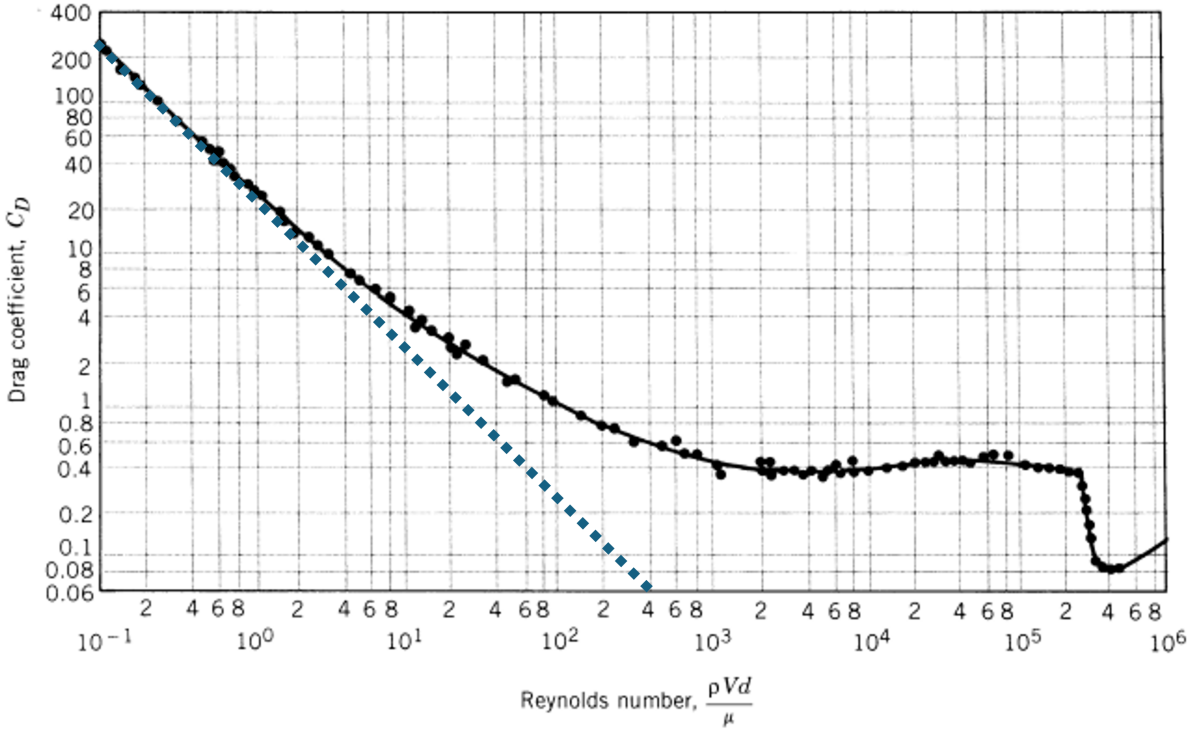

Figure 57: The drag coefficient on a spherical particle for different Reynolds numbers. At low Reynolds numbers, Stokes law is shown as a blue dashed line [142].

We can calculate the point at which Stokes's law is not a good description anymore when looking at when the drag force becomes bigger than Stokes's law. This relation is also shown in figure 57 as the blue dotted line. At low Reynolds numbers ($Re < 1$), we can see that equation 122 is satisfied. Because we will be using particles on a microscopic scale subject to tiny forces and, therefore, also very small velocities, we can conclude that Stokes's law is a valid description of the fluid force on a spherical particle.

$$\begin{aligned} F_{formdrag} &> F_{Stokeslaw} \\ \frac{1}{2}\rho C_d A V_\infty^2 &> 6\pi\mu R V_\infty \\ C_d &> \frac{24}{Re} \end{aligned} \tag{122}$$

[29] Imagine the fluid being a perfectly collimated light beam without any effects of diffraction, then the cross-sectional area would be the shadow of the particle behind the particle.

Using a similar manner as the derivation for the Stokes law, we can find the torque of a rotating spherical particle in a fluid. We can derive the velocity of the fluid with similar boundary conditions. We take the fluid velocity to be $V(\rho = R) = R\omega$ where ω is the angular velocity[30] of the sphere. At $V(R = \infty)$, we will assume zero velocity.

$$\mathbf{V}(\rho, \theta) = \omega \frac{R^4}{\rho^3} \sin(\theta)\hat{\phi} \tag{123}$$

Using equation 104, we can derive the pressure, which we can use again to calculate the force using the shear tensor from equation 106. Notice that we want to find the torque, which means that we have to take the cross product of the force on the particle with the distance to the center of rotation of the particle. The torque is assumed to be in the z-direction due to rotation in the ϕ-direction.

$$\begin{aligned} T &= \oiint_S R\hat{\rho} \times \sigma \cdot d\mathbf{S} \\ &= 8\pi\mu R^3\omega \end{aligned} \tag{124}$$

Unfortunately, the correlation between the torque on a particle in a rotating fluid is more complex than in the case of linear drag. A fluid is often described as having a linear and rotational direction. In literature, descriptions are in the same form as equation 121, but this is not a very useful assumption for non-spherical particles [143] [144].

$$T = \rho\pi R^5 C_T \omega^2 \tag{125}$$

4.1.5 Electrophoresis

In the 18th century, scientists found that the force responsible for binding atoms could be related to the charge and distance in the system. This phenomenon is called Coulomb's law, named after Charles Coulomb [145]. For two charges, this is found to be proportional to the distance between the two charges squared.

$$F_c = \frac{1}{4\pi\epsilon_0} \frac{|q_1 q_2|}{r^2} \tag{126}$$

Where ϵ_0 is the permittivity in a vacuum. q_1 and q_2 are two point charges. If they have an opposite sign, the two charges attract each other. If they have an equal sign, they repel each other. Keep in mind that this formula is only valid for point charges in a vacuum. We can write Couloms's law in terms of the electrical field $\mathbf{E}$, which is more helpful for OET cases.

$$\mathbf{F} = q\mathbf{E} \tag{127}$$

The force on a charge q has the same direction as the electrical field if the charge is positive. This Coulomb force is also known as the electrostatic force because we disregard the effects of the magnetic field. The magnetic field would have an effect when the charges move, which can be seen in equation 1. Therefore, this formula can only be used in OET for particular cases: static electrical fields and charged particles. When the particles are neutrally charged, the static electrical force is negligible.

If we would have a charged particle in a medium, the force due to the electrical field would be slightly different. A negatively charged submerged in a medium attracts positive ions from this medium, which neutralizes the total charge. This layer with positive ions around the particle is called the Stern layer, named after German scientist Otto Stern [146]. After this layer is formed, it attracts ions with different charges again and forms the diffuse layer. The outer boundary of this diffuse layer is called the slipping plane. This two-layer description of a charged particle in an ionic medium is called the electric double layer. These layers are shown in figure 58. The electrical potential decreases due to this double layer. At the slipping plane, the potential equals the ζ-potential, which depends on the Debye length [147].

[30] Notice that this angular velocity is not the same as the vorticity $\nabla \times \mathbf{V}$. In the drag of the Stokes law, we assumed that the velocity was rotational symmetric, but here, we consider a slightly different assumption.

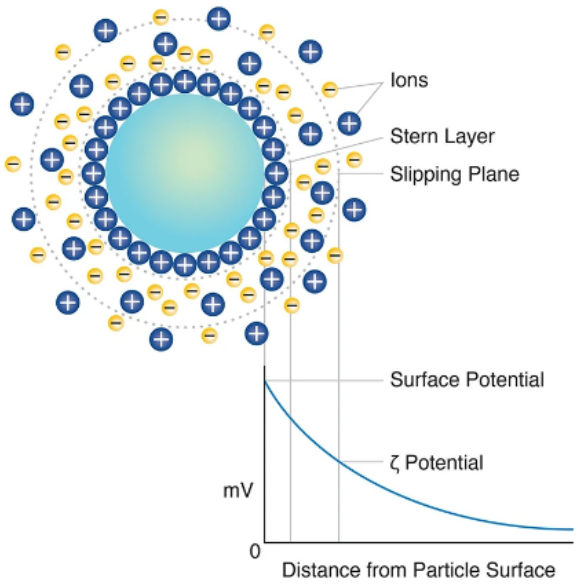

Figure 58: The electric double layer around a submerged negatively charged particle. The surface charge decreases with radial distance. At the Stern layer, the potential is the Stern potential. At the slipping plane, the potential is the ζ-potential [148].

The slip velocity due to the double layer depends on the electrophoretic mobility, which depends on the ζ-potential [149] [150].

$$\begin{aligned} \mu_e &= \frac{v}{E} \\ &= \frac{2\epsilon_r \epsilon_0}{3\mu_m} \zeta f(\kappa a) \end{aligned} \tag{128}$$

The velocity of the particle is given as v. The electrical field is given as E. ϵ_r and ϵ_0 are respectively the relative permittivity and the permittivity of vacuum. μ_m is the viscosity of the medium and ζ is the discussed potential at the slipping plane. $f(\kappa a)$ is the Henry coefficient named after William Henry, depending on the particle's radius a and the Debye length κ [151]. Marian Smoluchowski found the limit of the Henry coefficient to be $f(\kappa a) = \frac{3}{2}$ when $\kappa a \gg 1$. When the Debye length is much bigger than the particle's radius, i.e., $\kappa a \ll 1$, the limit of the Henry coefficient is $f(\kappa a) = 1$, as found by Erich Hückel [152]. Similar to the electrostatic force from Coulomb's law, we need an electrically charged particle for the electrophoretic force to play a role in the dynamics. In many cases in OET experiments, the particle is not electrically charged.

4.2 Forces on the medium

4.2.1 Light-actuated AC electroosmosis

Electrophoresis does not play a significant role in the dynamics of the particle on many occasions because the particles are neutrally charged on these occasions. We do have charge on the electrodes in the microfluidic chip. These electrodes, therefore, experience an electrophoretic force when the medium has enough ions. The charge on the electrodes creates a diffusive layer with a ζ-potential. Because the surfaces of the electrodes are flat, we can use Smoluchowksi's limit for the Henry coefficient. At the slipping plane, the ions in the medium start to move tangentially to the electrical field and toward the illuminated spot with the bigger surface potential. This means that a fluid velocity is induced within the microfluidic chip. This phenomenon is called light-actuated AC electroosmosis and is depicted in figure 59 [153].

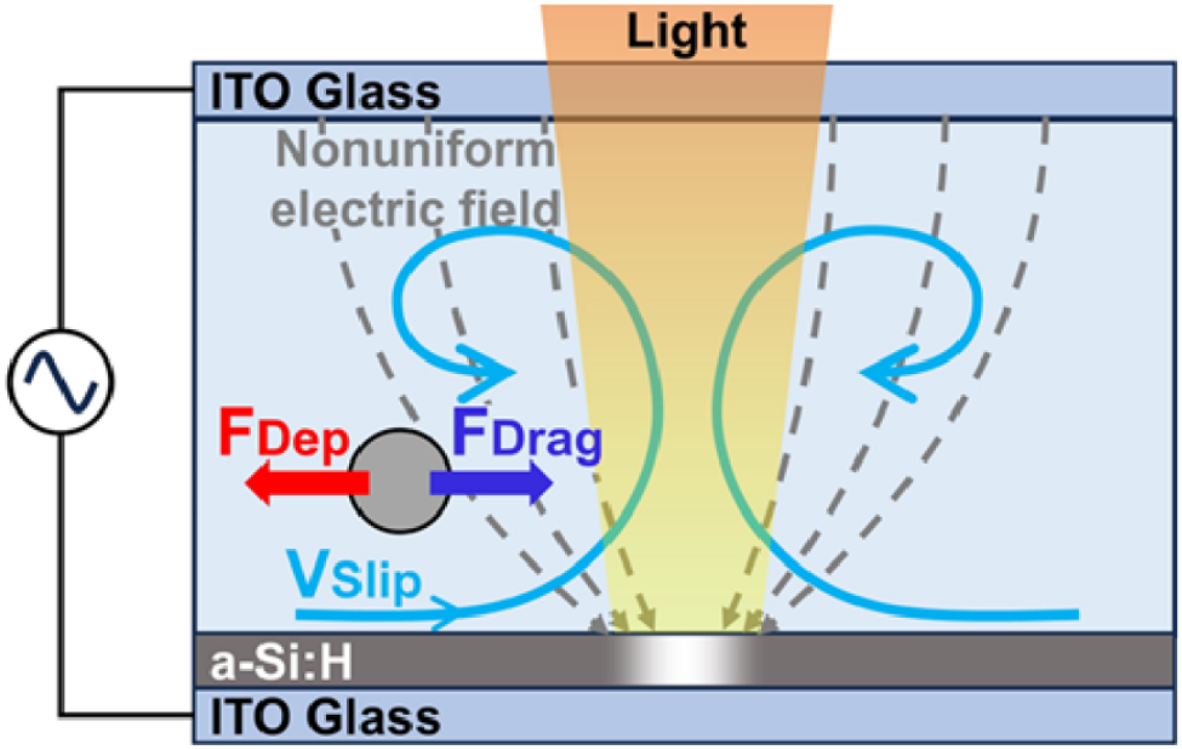

Figure 59: The fluid has a certain slip velocity due to the light-induced AC electroosmosis [153].

The slip velocity of the fluid is given by the Helmholtz-Smoluchowski equation, which is a limit of the electrophoresis formula given in equation 128.

$$V_{slip} = \frac{\epsilon_r \epsilon_0}{\mu_m} \zeta E_t \tag{129}$$

E_t is the tangential component of the electrical field concerning the photoconductive layer. If we had a dielectrophoretic force that repels a particle from the illuminated spot, we would have this force be opposed due to Stokes's law with V_{slip}. Due to this duality, a certain stable distance from the illuminated spot is created. This is shown in figure 60 where a simulation was done on a 12 μm diameter polystyrene bead in a medium with a conductivity of $5 * 10^{-5}$ S/m and a relative permittivity of 2.56 [153]. The stable distance depends on frequency due to the DEP force.

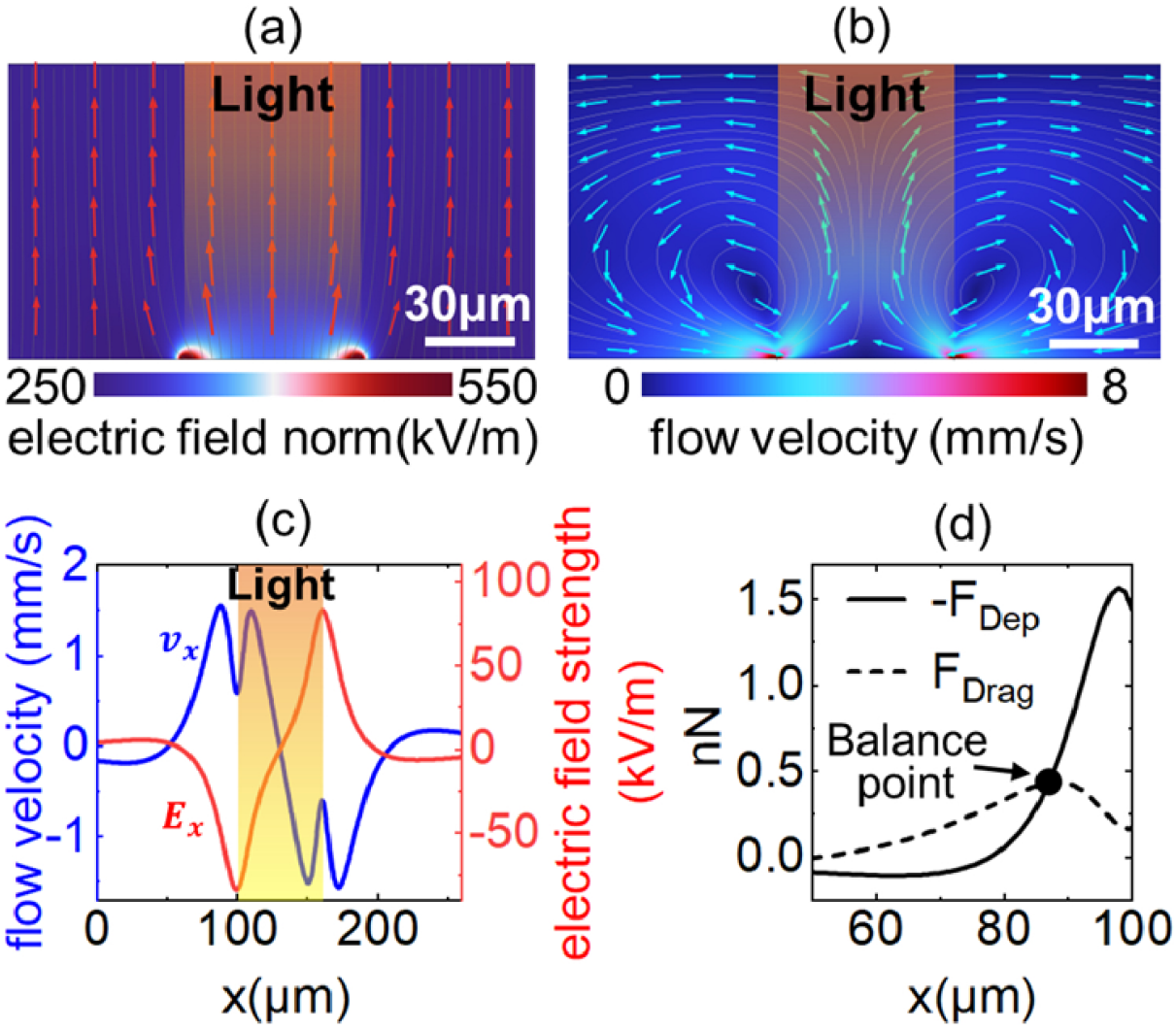

Figure 60: (a) The electrical field in an OET chip where the middle is illuminated. (b) The fluid flow in an OET chip is due to the light-induced AC electroosmosis. (c) Simulated electrical field data and fluid velocity data in the x-direction (horizontal) at 10 μm from the bottom. (d) The force due to the dielectrophoresis and Stokes law. At a certain point, there is a stable point. [153]

Suppose we want a dominant light-induced AC electroosmosis fluid force in the OET system. In that case, we need to have the frequency so that the impedance of the electric capacitor does not differ too much from the resistance of the medium. This will result in an optimal combination of the ζ-potential and the tangential electrical field [154].

$$f_{opt} = \frac{\sigma \lambda_d}{2\pi \epsilon L} \tag{130}$$

σ is the conductivity of the medium. λ_d is the thickness of the double layer. L is the height of the medium and, thus, the microfluidic chip. ϵ is the permittivity of the medium.

4.2.2 Electrothermal flow

The last electromagnetic process that we need to discuss is the induced temperature change from the electrical field. The internal energy of the fluid per unit volume can be found to be related to the temperature and the electrical field [155].

$$\rho_m c_p \left(\frac{dT}{dt} + (\mathbf{V} \cdot \nabla) T \right) = k \nabla^2 T + \sigma E^2 \tag{131}$$

The density of the medium is given as ρ_m. c_p and k are the specific heat and the thermal conductivity of the fluid. σ is the conductivity. We can rewrite this equation in steady state to the Peclet number Pe, named after Jean Claude Eugene Peclet [156].

$$\begin{aligned} \rho_m c_p (\mathbf{V} \cdot \nabla) T &= k \nabla^2 T + \sigma \langle E^2 \rangle \\ \underbrace{\frac{\rho_m c_p \mathbf{V}}{k}}_{\sim Pe} \cdot \nabla T &= \nabla^2 T + \frac{\sigma}{k} \langle E^2 \rangle \end{aligned} \tag{132}$$

When we consider the Peclet number to be very small due to the small velocity, we find Poisson's equation, which relates the Joule heating to the change in temperature.

$$k \nabla^2 T = -\sigma \langle E^2 \rangle \tag{133}$$

Due to high illuminating power, the temperature can also be increased locally. As we did by deriving the dielectrophoretic force, we want to see how this increased temperature impacts the electric force. This time, we will calculate the force on the medium fluid, which will induce an electrothermal flow. We want to find the time-average force per unit volume.

$$\mathbf{f}_{ET} = \rho_q \mathbf{E} - \frac{1}{2} \mathbf{E}^2 \nabla \epsilon + \frac{1}{2} \nabla \left(\rho_m \frac{\partial \epsilon}{\partial \rho_m} \mathbf{E}^2 \right) \tag{134}$$

ρ_q is the charge density in the volume and ϵ is the permittivity of the medium. The last term is related to the electrostriction, which creates pressure in the fluid. We will assume the medium to be incompressible and therefore ignore the last term [157]. We can relate the charge density to Gauss's law and the conservation of charge.

$$\begin{aligned} \rho_q &= \nabla \cdot (\epsilon \mathbf{E}) \\ \frac{d\rho_q}{dt} &= -\nabla \cdot (\rho_q \mathbf{V}) - \nabla \cdot (\sigma \mathbf{E}) \end{aligned} \tag{135}$$

If we assume a low Reynold's number, as we did in deriving the drag force, we can ignore the velocity term in the charge conservation. To solve this, we will use perturbation theory to expand the electrical field $\mathbf{E} = \mathbf{E}_0 + \mathbf{E}_1$, where $|\mathbf{E}_0| \gg |\mathbf{E}_1|$ [158]. We will assume that we have no free charge in the medium, and the electrical field is only due to the electrodes of the microfluidic chip. This means that $\nabla \cdot \mathbf{E}_0 = \frac{\rho_q}{\epsilon_0} = 0$ [159].

$$\begin{aligned} \rho_q &= \nabla \cdot (\epsilon(\mathbf{E}_0 + \mathbf{E}_1)) \\ &= \nabla \epsilon \cdot \underbrace{(\mathbf{E}_0 + \mathbf{E}_1)}_{\approx \mathbf{E}_0} + \epsilon(\underbrace{\nabla \cdot \mathbf{E}_0}_{=0} + \nabla \cdot \mathbf{E}_1) \\ &\approx \nabla \epsilon \cdot \mathbf{E}_0 + \epsilon(\nabla \cdot \mathbf{E}_1) \end{aligned} \tag{136}$$

We will also assume that the electrical field can be described using a complex vector amplitude times a complex exponential with angular frequency ω, i.e., $\mathbf{E}(\mathbf{r},t) = [E_{real}(\mathbf{r}) + E_{imag}(\mathbf{r})]e^{i\omega t}$. This means that the time derivative of the charge density is a product of $i\omega$ times the charge density.

$$\begin{aligned}
\frac{d\rho_q}{dt} &= \nabla \cdot (\sigma \mathbf{E}) \\
i\omega(\nabla\epsilon \cdot \mathbf{E}_0 + \epsilon(\nabla \cdot \mathbf{E}_1)) &= \nabla\sigma \cdot \underbrace{(\mathbf{E}_0 + \mathbf{E}_1)}_{\approx \mathbf{E}_0} + \sigma(\underbrace{\nabla \cdot \mathbf{E}_0}_{=0} + \nabla \cdot \mathbf{E}_1) \\
i\omega\nabla\epsilon \cdot \mathbf{E}_0 + i\omega\epsilon(\nabla \cdot \mathbf{E}_1) &= \nabla\sigma \cdot \mathbf{E}_0 + \sigma(\nabla \cdot \mathbf{E}_1) \\
(i\omega\epsilon + \sigma)\nabla \cdot \mathbf{E}_1 &= -(i\omega\nabla\epsilon + \nabla\sigma) \cdot \mathbf{E}_0 \\
\nabla \cdot \mathbf{E}_1 &= \left[\frac{-i\omega\nabla\epsilon - \nabla\sigma}{(i\omega\epsilon + \sigma)}\right] \cdot \mathbf{E}_0
\end{aligned} \tag{137}$$

We can now combine equation 136 and equation 137 to find a description of the charge density in the volume.

$$\begin{aligned}
\rho_q &= \nabla\epsilon \cdot \mathbf{E}_0 + \epsilon(\nabla \cdot \mathbf{E}_1) \\
&= \nabla\epsilon \cdot \mathbf{E}_0 - \left[\frac{i\omega\nabla\epsilon + \nabla\sigma}{(i\omega\epsilon + \sigma)}\right] \cdot \mathbf{E}_0 \\
&= \left(\frac{i\omega\epsilon\nabla\epsilon + \sigma\nabla\epsilon - i\omega\epsilon\nabla\epsilon - \epsilon\nabla\sigma}{i\omega\epsilon + \sigma}\right) \cdot \mathbf{E}_0 \\
&= \left(\frac{\sigma\nabla\epsilon - \epsilon\nabla\sigma}{i\omega\epsilon + \sigma}\right) \cdot \mathbf{E}_0
\end{aligned} \tag{138}$$

The gradient of the permittivity and the conductivity can be related to a linear change with respect to the temperature. $\nabla\epsilon = k_\epsilon\epsilon\nabla T$ and $\nabla\sigma = k_\sigma\sigma\nabla T$ where k_ϵ and k_σ are empirically found constants [160].

$$\rho_q = \left(\frac{\epsilon\sigma}{i\omega\epsilon + \sigma}\right)(k_\epsilon - k_\sigma)\nabla T \cdot \mathbf{E}_0 \tag{139}$$

We now have everything we need to compute the electrothermal force on the fluid per unit volume from equation 134. Because the electrical field is alternating, we will need to take the time-average[31] as we did for the DEP force. We will also need only to use the real part of the volume force.

$$\langle \mathbf{f}_{ET} \rangle = \frac{1}{2}\mathrm{Re}\left[\left(\left(\frac{\epsilon\sigma}{i\omega\epsilon + \sigma}\right)(k_\epsilon - k_\sigma)\nabla T \cdot \mathbf{E}\right)\mathbf{E}^*\right] - \frac{1}{4}|\mathbf{E}^2|\epsilon k_\epsilon \nabla T \tag{140}$$

Where we changed $\mathbf{E}_0(\mathbf{r})$ to $\mathbf{E}$. Because $\mathbf{E} \approx \mathbf{E}_0$, this fairly approximates the physics behind the electrothermal phenomenon. An example of the flow due to the electrothermal effects is shown in figure 61. Because this force depends on the electrical field's frequency, we can find the cross-over frequency for when the ET effect changes signs [161].

$$f_{ET,cross-over} \approx \frac{\sigma}{2\pi\epsilon}\sqrt{2\frac{|\frac{1}{\sigma}\left(\frac{\partial\sigma}{\partial T}\right)|}{|\frac{1}{\epsilon}\left(\frac{\partial\epsilon}{\partial T}\right)|}} \tag{141}$$

[31] The time-average real part of the product of two vectors is given as $\mathrm{Re}\left[\langle \mathbf{A}(\mathbf{r},t)\mathbf{B}(\mathbf{r},t)\rangle\right] = \frac{1}{2}\mathrm{Re}\left(\mathbf{A}(\mathbf{r})\mathbf{B}^*(\mathbf{r})\right)$.

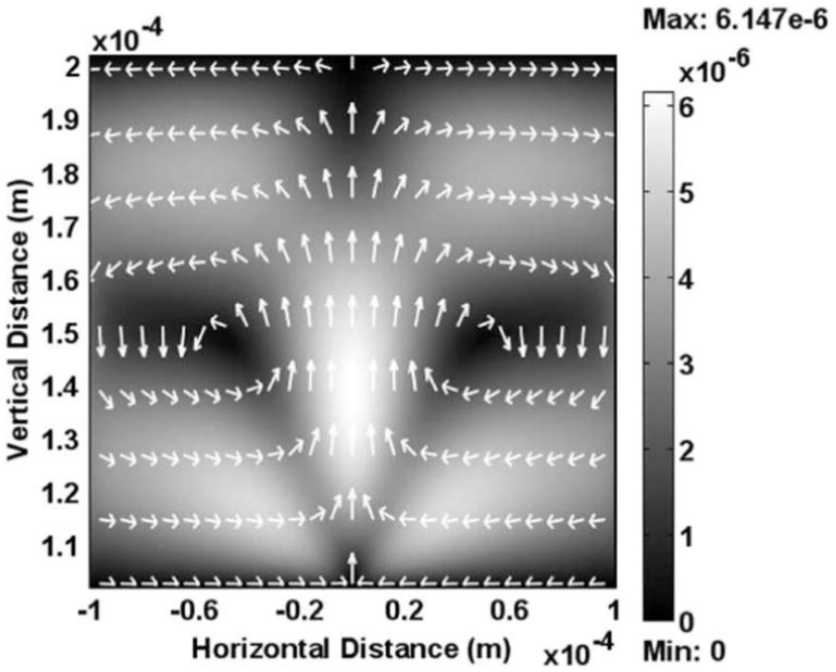

Figure 61: Simulation of flow due to electrothermal effects. This simulation is from an OET setup with a bias voltage of 20 Vpp and 100 kHz. The illumination power is 250 W/cm^2 [160].

4.2.3 Thermal flow

When heating a medium, it will start to flow naturally. The density depends on temperature and will decrease with increasing temperature in most cases. This means the buoyancy effects change locally, causing the fluid to induce natural convection. This can happen without applying an electrical field but only illuminating the surface with high enough energy [162]. This force, per unit volume, can replace the buoyancy formula from equation 99 by changing the density to the temperature-dependent temperature.

$$\mathbf{f}_{nc} = \frac{\partial \rho_m}{\partial T} \nabla T g \hat{z} \tag{142}$$

4.3 Situational forces

The last force we need to consider is the static friction force. The drag force is a friction force that works against a moving system but has no effect when the particle is stationary. Moving the particle from stationary can be challenging due to the fouling effects explained in section 3.3.1. The force due to the surface energy is given in equation 96. The force must be greater than this adhesion force to get the particle to move. This force can be modeled as a threshold, which is removed when the particle is not stuck to the surface anymore [163].

4.4 State space

If we want to create a working dynamical system of our particle in the OET chip, we need to combine all discussed dynamics. Most forces that we discussed are only valid for spherical particles in a Newtonian fluid due to all the assumptions we made. We will create the dynamical system by setting up the state space. We want to find the acceleration of the particle's center of mass $\ddot{\mathbf{x}}$. The speed of the particle's center of mass is given by $\dot{\mathbf{x}}$. The angular acceleration of the particle is given by $\ddot{\theta}$. The angular speed is given by $\dot{\theta}$. The speed of the fluid is given as $\mathbf{V}(\mathbf{x})$, i.e., the velocity of the medium at the particle's location $\mathbf{x}$. The temperature is also a state of the system and is given as $T(\mathbf{x})$.

The dynamics of the particle are given by two equations, which consist of the already discussed forces.

$$m\ddot{\mathbf{x}} = \mathbf{F}_{DEP}(\mathbf{x}, f, V, P) + \mathbf{F}_{gravity} + \mathbf{F}_{buoyancy}(\mathbf{x}, T) + \mathbf{F}_{drag}(\mathbf{V}_\infty) + \mathbf{F}_{friction}(\dot{\mathbf{x}}) \tag{143}$$

$$I\ddot{\theta} = \mathbf{T}_{DEP}(\mathbf{r}, f, V, P) + \mathbf{T}_{drag}(\omega_\infty) \tag{144}$$

The velocity and the angular velocity of the medium that induces drag are the relative speeds between the medium and the particle.

$$\mathbf{V}_\infty = \mathbf{V}_m - \dot{\mathbf{x}} - \dot{\mathbf{x}}_{Brownian}(\mathbf{x}, T) \tag{145}$$

$$\omega_\infty = \mathbf{r} \times \mathbf{V}_m - \dot{\theta} - \dot{\theta}_{Brownian}(\mathbf{x}, T) \tag{146}$$

The medium's velocity consists of some body forces, as discussed, and some additional velocities.

$$\nabla^2 \mathbf{V}_f = \frac{1}{\mu}(\mathbf{f}_{ET}(\mathbf{x}, f, V, T, P) + \mathbf{f}_{nc}(\mathbf{x}, T)) \tag{147}$$

$$\mathbf{V}_m = \mathbf{V}_f + \mathbf{V}_{EP}(\mathbf{x}, f, V, P) + \mathbf{V}_{ext} \tag{148}$$

The dynamics of the temperature depend on the electrical field and the added heat energy.

$$\nabla T = -\frac{\sigma}{k}\langle E^2 \rangle - \frac{1}{k} P_{ext} \tag{149}$$

This nonlinear set of equations describes all the states. The states are the location of the particle $\mathbf{x}$, the speed of the particle $\dot{\mathbf{x}}$, the angle of the particle around its axis of rotation θ, the angular velocity of the particle $\dot{\theta}$, the speed of the fluid $\mathbf{V}_m$, and the temperature T. The inputs are the bias voltage of the AC signal V, the frequency of the AC signal f, the optical power P (which influences the electric field gradient), the external added fluid velocity $\mathbf{V}_{ext}$ (e.g., due to a pump), and the external added heat power P_{ext} (e.g., due to illumination or heating).

One important thing to keep in mind is that some forces dominate over others for specific frequency regions. Figure 62 shows an example of this. These regimes are specific for each system but usually follow the same order.

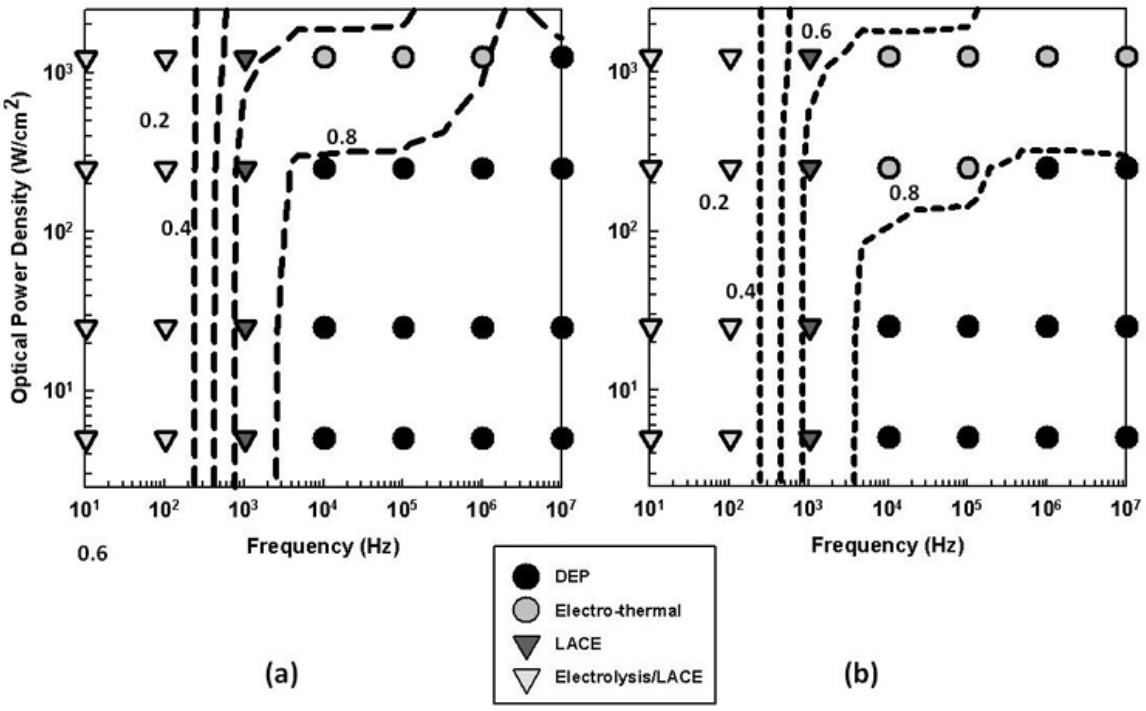

Figure 62: Regions in the frequency/optical power plot show where certain forces dominate. The particle in this system is in a liquid solution with a conductivity of 1 mS/m. The applied AC frequency is 100 kHz. In (a), the applied voltage is 20 Vpp. In (b), the applied voltage is 10 Vpp [164].

The dynamics are pretty well defined if we have a spherical particle. We already saw that we will have more complex dynamics for differently shaped particles. Therefore, to have a state space representation of a more complicated system, we need to linearize the system such that dynamics are similar but include correcting coefficients as is done similarly in the drag force formula in regions with a higher Reynolds number. This system of equations gives a good understanding of the underlying physics but include many assumptions and boundary conditions that limit the use for complex systems.

5

Optical setup

This section introduces the components of the optical setup for the optoelectronic tweezer. The optical setup essentially functions as a light microscope, enhanced with pattern illumination to generate virtual electrodes. We begin by explaining the physical principles behind light microscopy, including how light interacts with various materials. Through this explanation, we clarify the concept of focal length and identify the factors that limit image sharpness, such as aberrations. We derive the spatial resolution using Fourier optics and explore the depth of focus from a geometrical perspective. These methods highlight potential limitations of the optical system that should be considered in our setup design. We also discuss the different light sources utilized in optoelectronic tweezer setups. The role of the digital micromirror device in creating the illumination pattern for precise control is examined, focusing on optimal angling within the optical setup. To observe the images produced by the optical system, we discuss the operating principles of the necessary camera. Lastly, we present several detailed optical setups used in optoelectronic tweezers, including various optical elements commonly incorporated into these systems.

The optical setup for "Jip en Janneke"

Light always moves at the same speed depending on the material it is in. Light bends when it passes from one material to another, like from air into glass. If we shape the glass into a curve, all the bent light comes together at one point, which we call the focus point. This focus point is super important for understanding how we see things.

If we have two lenses lined up and their focus points match up, we can make images look even larger! This is how we can see things through binoculars, telescopes, and microscopes.

The optoelectronic tweezer also uses a microscope to see and manage tiny objects. However, we can't see infinitely small things because every microscope has a limit to how small it can see. In this part, we will talk about how these limits work.

The light in the microscope can come from different types of sources, like regular lamps, LED lamps, or lasers. We'll also explain something called fluorescence, which is when objects glow in the dark after being lit up for a while. This helps us take really sharp pictures of specific things in the microscope.

To control where and how we look at tiny objects, we use a special kind of technology called a digital micromirror device. It's like a tiny TV screen made of lots of little mirrors. We can move each mirror to shine light in just the right way. This lets us create images that we can then look at more closely with the microscope.

Finally, to see the things we're working with using the optoelectronic tweezer, we need a camera. The camera helps us see, but it also has its own limits because of its size and the number of pixels it has (which are tiny dots that capture the light). At the end of this section, we'll show some pictures of what the optical setup looks like when everything is put together.

The Jip and Janneke illustration is created by the renowned artist Fiep Westendorp.

5.1 The light microscope

In Middelburg in the Netherlands, around 1590, Hans and Zacharias Janssen created the first microscope based on lenses in a tube. Later, around 1740, Anthonie van Leeuwenhoek used this device to open the world too small for our naked eyes by studying biological samples [165]. It is hard today to imagine the world without microscopes, for they have become key biological, medical, and structural research devices. The optoelectronic tweezer system uses this microscope as optical setup to manipulate very small objects. To understand the physics of this optical setup, we need to start looking at the physics behind light in materials.

5.1.1 Bending of light in a material

The speed of light is constant and has a value depending on the material it travels in. Light in a vacuum travels with the speed of light that is defined as $c = (\epsilon_0\mu_0)^{-\frac{1}{2}}$ with ϵ_0 being the permittivity in a vacuum and with μ_0 being the permeability in a vacuum. When light travels through a material, it travels with the speed $v = (\epsilon\mu)^{-\frac{1}{2}}$ with again the permittivity and permeability but now in the medium. The ratio between the speed of light in a vacuum and a medium is called the refractive index [166]. This is, therefore, defined as

$$n := \frac{c}{v} = \frac{\sqrt{\epsilon\mu}}{\sqrt{\epsilon_0\mu_0}} \tag{150}$$

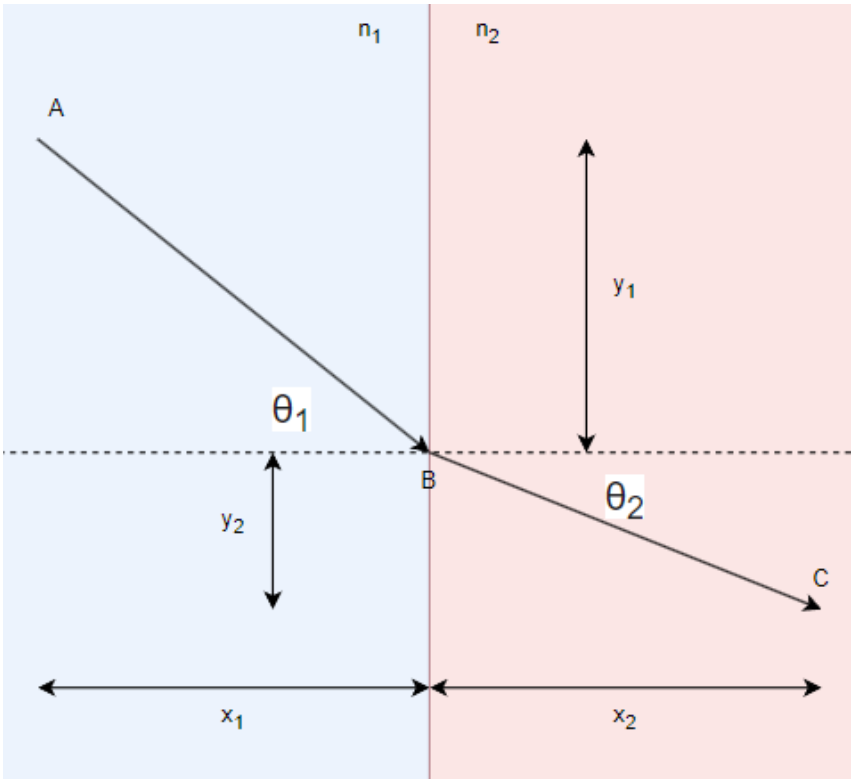

Figure 63: A schematic travel path of light from a material with refractive index n_1 to a material with refractive index n_2.

Consider a photon moving in a material with refractive index n_1 from a certain point A to a point B, which is on the interface between 2 materials. After traveling to point B, it travels to point C in a material with refractive index n_2. This traveling photon is schematically depicted in figure 63. We can calculate the length of this travel path as

$$L = \sqrt{y_1^2 + x_1^2} + \sqrt{y_2^2 + x_2^2} \tag{151}$$

We know that the speed of light in the material with refractive index n_1 is v_1. At the material with refractive index n_2, it is v_2. We can calculate the time it takes for a photon to travel from point A to point B to point C.

$$T = \frac{\sqrt{y_1^2 + x_1^2}}{v_1} + \frac{\sqrt{y_2^2 + x_2^2}}{v_2} = \frac{\sqrt{(h - y_2)^2 + x_1^2}}{v_1} + \frac{\sqrt{y_2^2 + x_2^2}}{v_2} \tag{152}$$

We wrote T as a function of y_2 using $h = y_1 + y_2$. Fermat's principle tells us that light takes the path that requires the least time compared to other possible paths [167]. In our case, this translates to T being minimal for a specific y_2. This means we can optimize T by setting the derivative to 0.

$$\begin{aligned}
\frac{\partial T}{\partial y_2} &= -2(h - y_2)\frac{1}{2v_1\sqrt{(h - y_2)^2 + x_1^2}} + 2y_2\frac{1}{2v_2\sqrt{y_2^2 + x_2^2}} \\
&= \frac{y_2}{v_2\sqrt{y_2^2 + x_2^2}} - \frac{h - y_2}{2v_1\sqrt{(h - y_2)^2 + x_1^2}} \\
&= \frac{y_2}{v_2\sqrt{y_2^2 + x_2^2}} - \frac{y_1}{v_2\sqrt{y_1^2 + x_1^2}} \\
&= \frac{\sin(\theta_2)}{v_2} - \frac{\sin(\theta_1)}{v_1}
\end{aligned} \tag{153}$$

Where we used that, in a right triangle, the opposite side dived by the hypotenuse is equal to the sine of the angle, $\sin(\theta_1) = \frac{y_1}{AB}$.

$$\begin{aligned}
\frac{\partial T}{\partial y_2} &= 0 \\
\frac{\sin(\theta_2)}{v_2} &= \frac{\sin(\theta_1)}{v_1} \\
\frac{n_2 \sin(\theta_2)}{c} &= \frac{n_1 \sin(\theta_1)}{c} \\
n_2 \sin(\theta_2) &= n_1 \sin(\theta_1)
\end{aligned} \tag{154}$$

Using Fermat's law and by implementing the definition of the refractive index, we derived Snell's law, which connects the angle of incidence θ_1, the angle of refraction θ_2 with the refractive indices of n_1 and n_2 [168].

5.1.2 Focusing light with a lens

As we saw in Snell's law, light rays bend by a defined angle in a material with a homogeneous reflective index. If we project a specific shape using illumination through a material, we would see the projection shift due to Fermat's principle, as shown in figure 64.

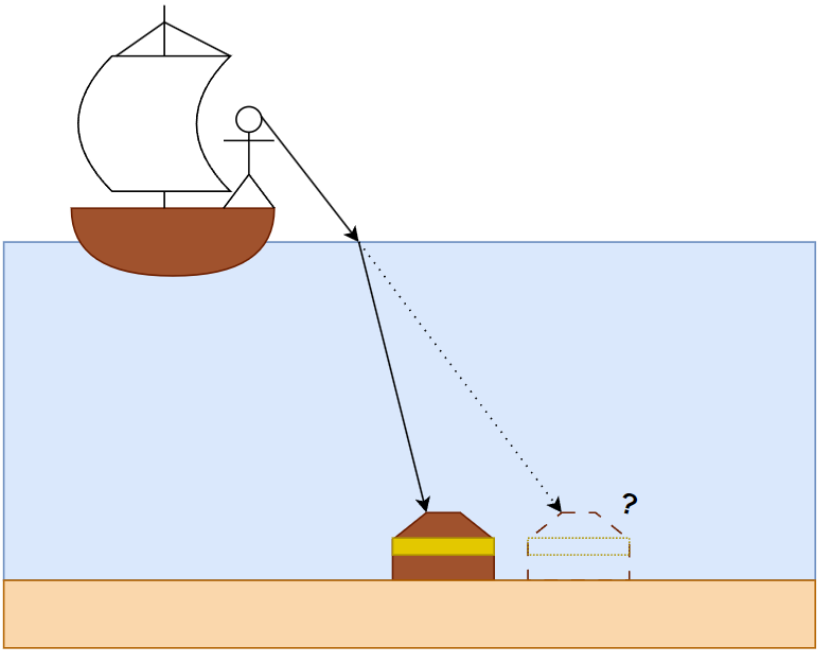

Figure 64: A schematic depiction of how an image can be shifted due to Fermat's principle. The boat's captain sees a treasure chest on the bottom of the sea and thinks he can estimate the location just by looking. He does not know that the light is shifted due to the refractive indices, making the chest appear at a different angle.

If we shape the curvature of a transmitting material, we can force the incoming angle to be an angle normal to the surface. For example, if we shape a glass with a spherical curvature, we can relate the angle of incidence with the distance from the center of the spheroid. Figure 65 shows a schematic of this shaped glass. The angle a is related to y by $\sin(a) = \frac{y}{r}$. Using this we can define angle b if we know the material's refractive index n_a and the surrounding's refractive index n_b.

$$\begin{aligned} n_a \sin(a) &= n_b \sin(b) \\ n_a \frac{y}{r} &= n_b \sin(b) \\ b &= \arcsin\left(\frac{n_a}{n_b}\frac{y}{r}\right) \end{aligned} \tag{155}$$

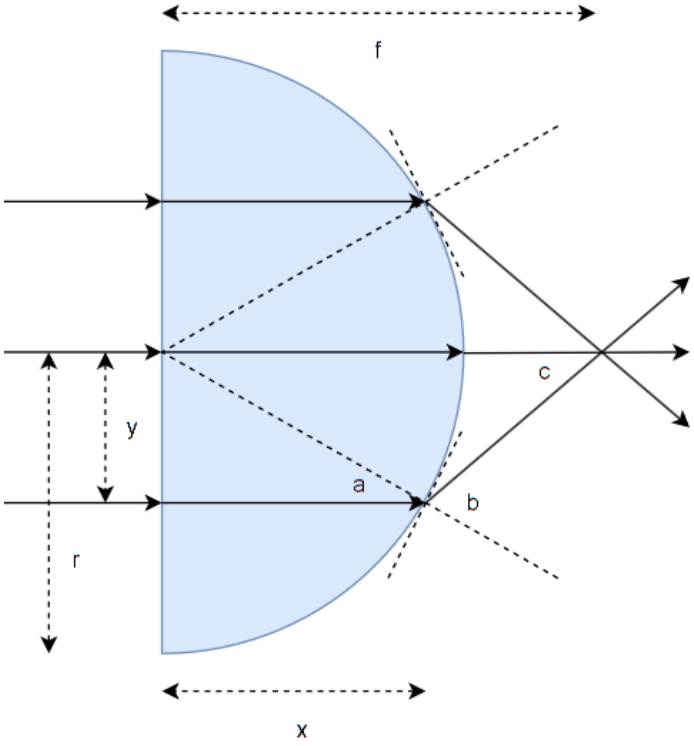

Figure 65: A schematic depiction of a spherical lens with radius r. A ray enters the lens at height y and exits the lens at width x. The angle the incoming ray makes with the normal of the curved surface on the right is called a. The angle the ray makes with the normal of the curved surface when exiting the lens is called b. The angle that the ray makes with the optical axis (y=0) is called c and is at the focal length called f.

We can see in figure 65 that the light rays cross at a certain distance. We call this distance the focal length of the lens. Every material has a certain angle at which no light is transmitted. The transmitted light would make an angle of $\pi/2$ rad (90 degrees) or more, which is impossible. This is called the critical angle and can be calculated by the refractive indices.

$$\begin{aligned} n_a \sin(a) &\leq n_b \sin(pi/2) \\ \sin(a) &\leq \frac{n_b}{n_a} \times 1 \end{aligned} \tag{156}$$

We can see that the maximum distance a light ray can be distanced from the radius in a spherical lens, like in figure 65, is defined by the critical angle as

$$y_{critical} = r \sin(a_{critical}) = r \frac{n_b}{n_a} \tag{157}$$

If we add more rays with distances ranging between 0 and $y_{critical}$, we can see the relation of the focal length depending on the distance from the center of the lens.

$$\begin{aligned} x &= r \cos(a) \\ c &= \frac{\pi}{2} + a - b \\ f &= x + y \tan(c) \\ &= r \cos\left(\arcsin\left(\frac{y}{r}\right)\right) + y \tan\left(\frac{\pi}{2} + \arcsin\left(\frac{y}{r}\right) - \arcsin\left(\frac{n_a y}{n_b r}\right)\right) \end{aligned} \tag{158}$$

This relation is shown in figure 66.

As can be seen, the bigger the distance the incoming light ray makes with the optical axis, the smaller the focal length. This change in focal lengths is also depicted in figure 67. We can see here that for a spherical lens with a refractive index of 1.5, the focal lengths differ for each incoming ray at a different height. This means that we cannot say there is only one focal length for the spherical lens.

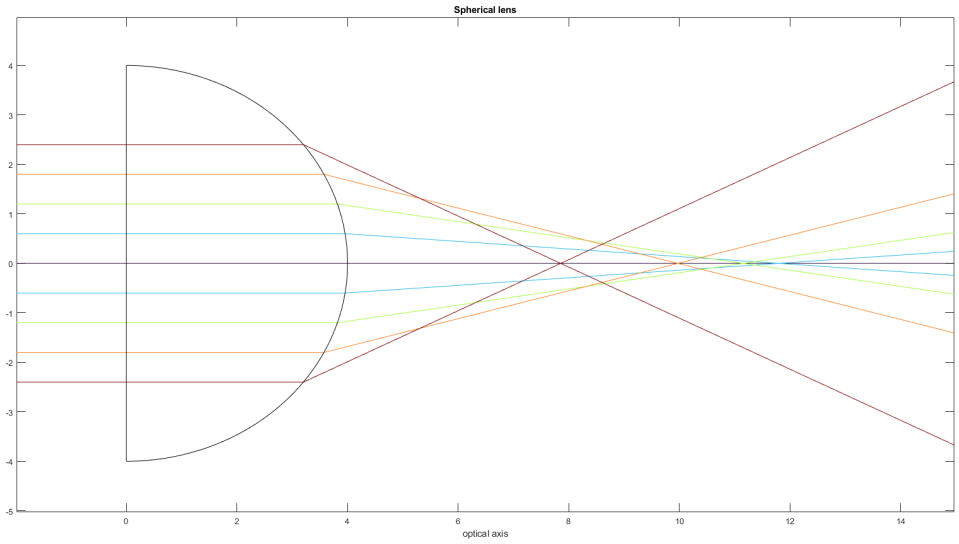

Figure 66: The ray diagram of a spherical lens with a refractive index of 1.5 and with a radius of 4 cm with incoming rays ranging between 0 cm and 2.4 cm.

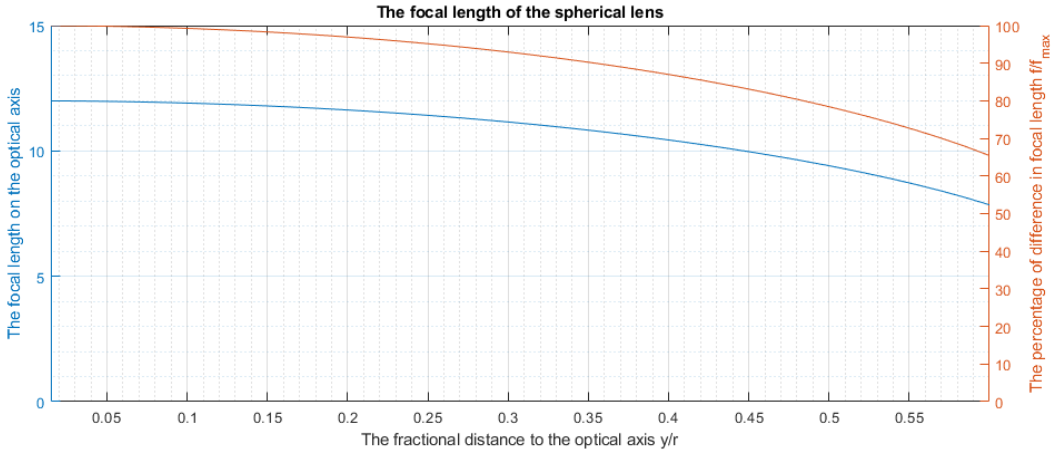

Figure 67: The relation of the focal length in a spherical lens with a refractive index of 1.5 depending on the relative distance y/r. On the right side is the percentage f/f_{max} shown to show the error in focal length scales with increasing relative distance y/r.

When imaging a pattern in the spherical lens, we can better understand the meaning of the different focal points by looking at the output pattern after all the focal points. One thing that can already be seen in figure 66 is that the projected image will be upside down after the focal points. If you follow the ray coming in most on top on the left, you will see that this same ray turns into the ray most on the bottom on the right. Another thing that happens is the image getting distorted. It spreads out more the farther the input ray is from the optical axis. This can be seen in figure 68 and figure 69. The input pattern consists of evenly spaced red and blue rings. After passing through the spherical lens, the outer rings are wider than all the inner rings. This type of deformation is called an aberration which can come in many shapes.

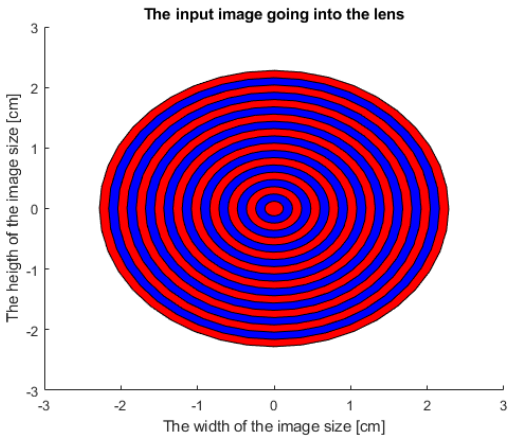

Figure 68: A pattern put through the spherical lens described in figure 66.

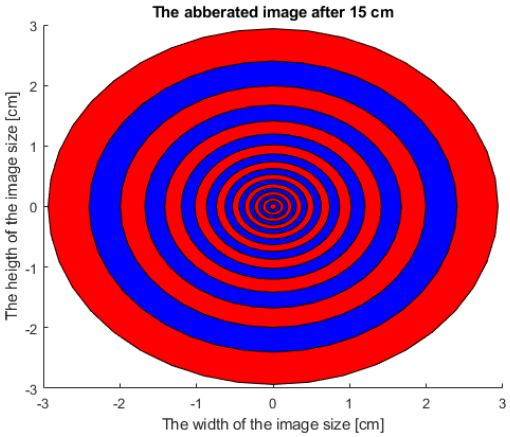

Figure 69: The pattern output at 15 cm distance from the left side of the lens, after passing all focal points.

This type of aberration is called a spherical aberration. More specifically, the shift in focal lengths is called longitudinal spherical aberration, while the shift in the pattern is called transverse spherical aberration [169]. In optics, we often want to prevent aberrations as much as possible, which can be done in multiple ways. Firstly, the lens can be shaped with an aspherical surface. A comparison between an aspherical lens and a spherical lens can be seen in figure 70. Aspherical lenses are, on the other hand, more challenging to make and will therefore also be more expensive than the simpler spherical lenses [170]. Another way to prevent the aberration is by decreasing its effect by only taking small angles and, therefore, only taking small distances from the optical axis. This is called paraxial approximation and can be done with angle $c \ll 1$ rad, with angle c as described in figure 65 [171]. As we also can see in figure 67, the focal lengths lie very closely to each other when we would only take a distance of $0.2r$ from the optical axis. Most lenses that are spherical and are in use for optics do not use half spheres as lenses but take even smaller parts of this spherical surface to remove the greater angles from the spherical surface to prevent aberrations [172].

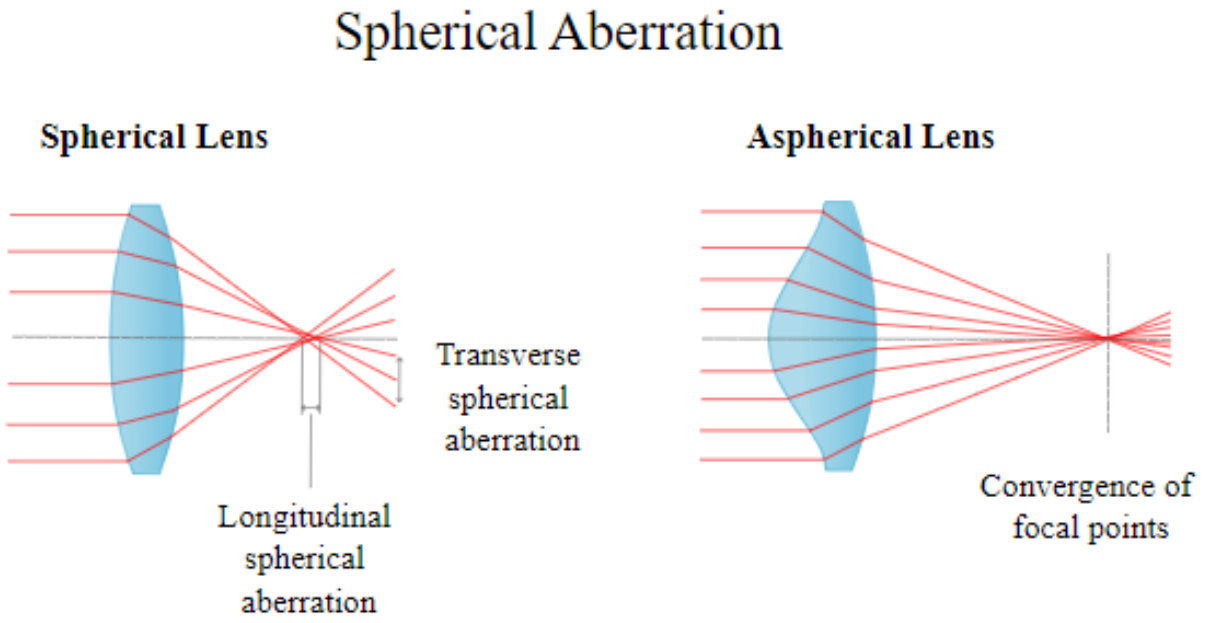

Figure 70: A comparison between a spherical lens and an aspherical lens. The aspherical lens converges the longitudinal spherical aberration [173].

5.1.3 Magnifying an image using lenses

If we had two lenses in series, we could use their focal lengths to change the size of a collimated light beam. When light rays enter a lens parallel to the optical axis, they all meet at a certain point called the focal point. When another lens is distanced from this focal point with its focal length, the rays come out of the second lens again parallel to the optical axis. The rays continue at the same angle to the optical axis after the focal point between the lenses, making the beam widths linked to each other. This phenomenon is depicted in figure 71. If we would name the distance of the blue line from the optical axis y_1, we can calculate its positions after the 2-lens system, which we will call y_2, using the ratio of the focal lengths [174].

$$\begin{aligned} \frac{y_1}{f_1} &= \tan(a) \\ \frac{y_2}{f_2} &= \tan(b) = \tan(-a) = -\tan(a) \\ \frac{y_1}{f_1} &= -\frac{y_2}{f_2} \\ \frac{y_2}{y_1} &= M = -\frac{f_2}{f_1} \end{aligned} \tag{159}$$

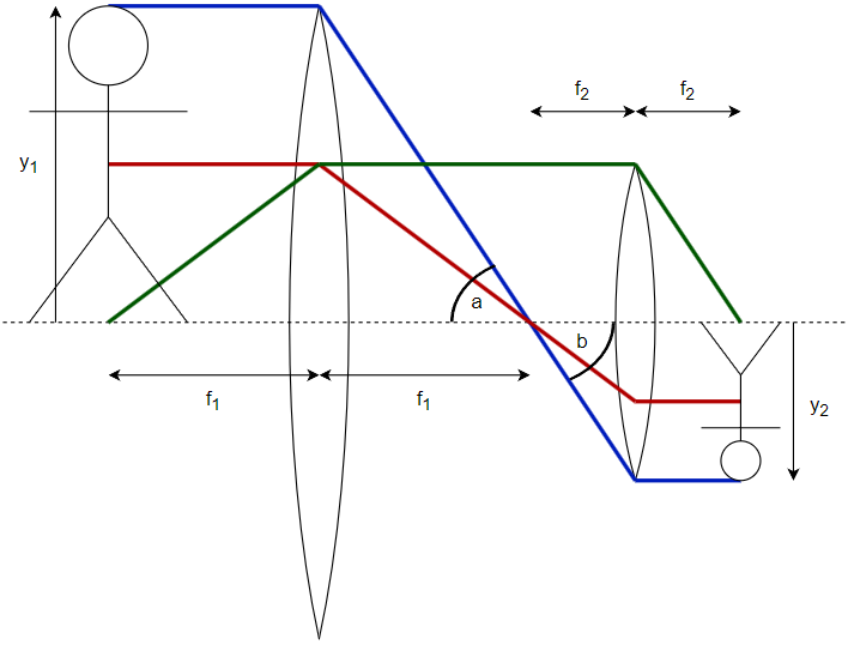

Figure 71: A schematic depiction of a telescope with two lenses. The left lens has a focal length f_1, and the second lens has a focal length f_2. On the left side, the captain from figure 64 stands at f_1 distance from the first lens. This object, the captain, is imaged, translated, and demagnified on the right side.

As we can see, the magnification is defined by the two focal lengths. The length of the full system is 4 focal lengths long. Therefore, this is also known as a 4f system. If we wanted to magnify the image back without inverting it, we could use a more complex optical system which would, for example, change the second lens into a diverging lens[32] and by moving it before the first focal length. The ray diagram of this system is shown in figure 72.

[32] A lens that converges the light is also known as a convex lens. A lens that diverges the light is also known as a concave lens.

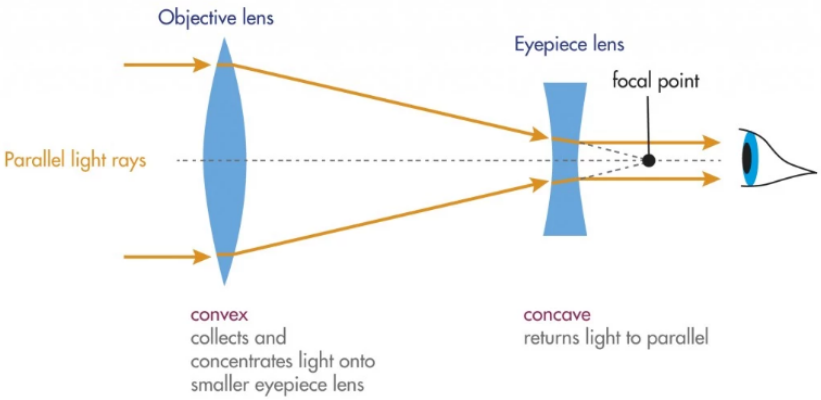

Figure 72: A schematic depiction of a binocular system where the first lens is convex and the second lens is concave. This lens system does not invert the image [175].

5.2 Resolution

One of the most important properties of our optical setup is its resolution. Optical resolution is the smallest sized feature the optical system can resolve [176]. The obvious limitations are to be caused by defective optical elements due to, e.g., dirtiness or damage. Therefore, we will assume in this section that all optical elements are working optimally and set up optimally at their proper focal lengths. The first thing that limits the optical setup is the critical angle as described in equation 157. Each optical element has its own critical angle, but the smallest critical angle in the full setup is the limiting one, as a chain is as strong as its weakest link. This critical angle is related to the numerical aperture (NA), which is defined as the smallest critical angle.

$$NA = n \sin(\theta_{critical}) \tag{160}$$

with n being the refractive index of the medium that the light transmits outside the objectives.

5.2.1 Diffraction of light

When we let light pass through an aperture, like a spherical hole, we get a phenomenon that Fransesco Maria Grimaldi first called diffraction in 1665 [177]. The interference of waves creates diffraction and can be explained by the Huygens-Fresnel principle named after Christian Huygens and Augustin-Jean Fresnel [178]. This principle tells us that every wavefront, e.g., a long ocean wave, can be seen as an infinite amount of spherical waves next to each other. Because the waves are infinitely long by a classical physics approximation, the spherical boundary effects cannot be seen, and the waves are seen as straight wavefronts. After passing an aperture, this wave cannot be approximated similarly, making the spherical end of the wavefront visible. This phenomenon is schematically shown in figure 73. This can be easily demonstrated using water as is depicted in figure 74.

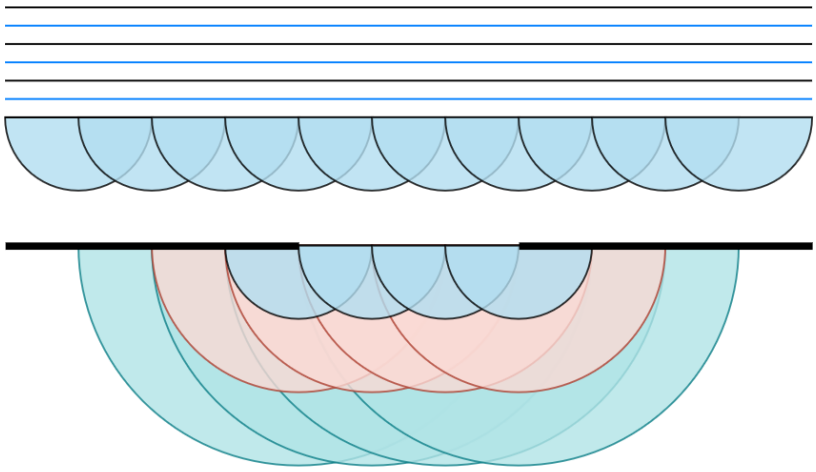

Figure 73: A schematic depiction of the Huygens-Fresnel principle, which says that a wavefront can be modeled as an infinite amount of spherical waves. In this figure, a limited number of spherical waves are shown to display the effect of this principle before and after an aperture.

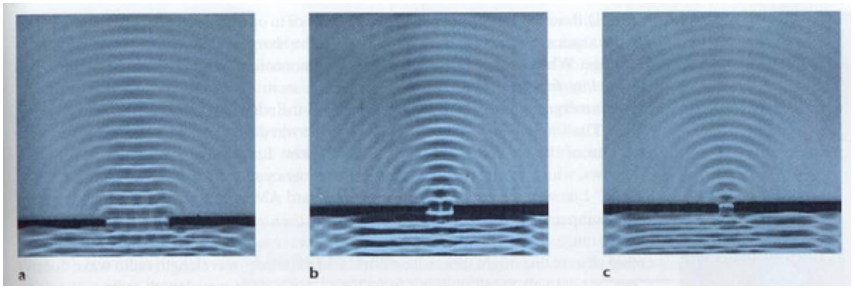

Figure 74: Diffraction seen in water waves after passing an opening in a dam [179].

Light behaves as a wave with an electric and magnetic field and can, therefore, also be diffracted. This diffraction is modeled in 3 different versions: the Kirchhoff diffraction, Fresnel diffraction, and Fraunhofer diffraction. The first is true when the waves are moved more than half of their wavelength away from the aperture. The second is true when the distance from the aperture is much bigger than the width of the aperture, and the last is true in the far field [180]. These diffraction models are shown in figure 75.

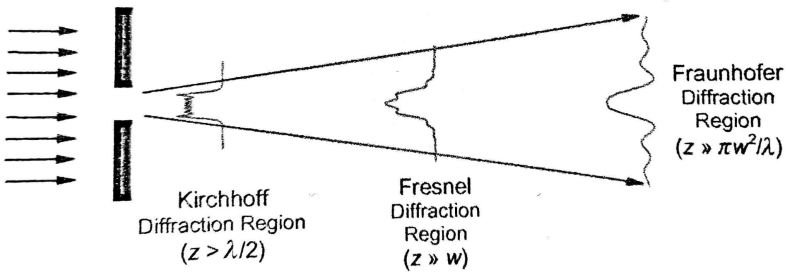

Figure 75: Comparison of the diffraction regions and the area of their accuracy. The wavelength of the light is given by λ, the width of the aperture is given by w, and the distance from the aperture is denoted by z [180].

Assuming coherent monochromatic waves, we can look at the incoming waves as all in phase and with the same wavelength. After the aperture, these waves spread out in a circular manner, making the zeros of the wave be patterned when projected again on a flat plane. This can be seen in figure 76. The light intensity is related to the squared norm of the electrical field, which means that the zeros of the waves will create dark spots in the pattern [180]. Therefore, we can see for diffraction as in figure 76 that the pattern will peak in the center due to the parallel beam but will have a dark spot at a distance x for the sloped wave.

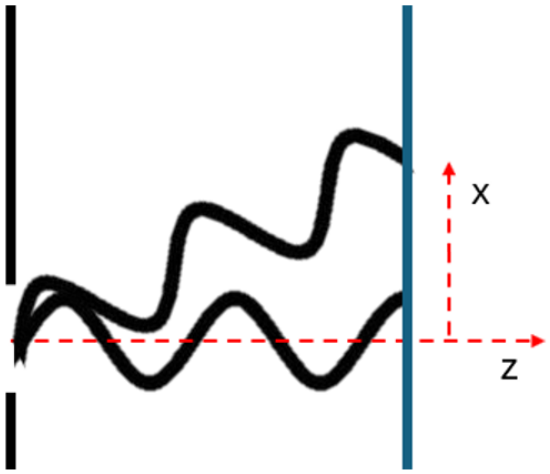

Figure 76: Spread of the sinusoidal peaks due to diffraction. The wave parallel to the z-axis peaks at the blue surface, while the sloped wave has a zero on the same parallel surface.

The image after diffraction is therefore depending on the frequency of the waves, which is defined as $f_x = \frac{nx}{\lambda z} = \frac{kx}{2\pi z}$ in the x direction[180]. This frequency relation made it possible to rewrite the diffraction pattern to a Fourier transform of the incoming wave multiplied by the aperture function. This specific Fourier transform is also known as the Fraunhofer diffraction integral.

$$\begin{aligned} E(f_x, f_y) &= C \int_{-\infty}^{\infty} \int_{-\infty}^{\infty} t_m(x_0, y_0) e^{-2\pi i (f_x x_0 + f_y y_0)} dx_0 dy_0 \\ &= C \int_{-\infty}^{\infty} \int_{-\infty}^{\infty} t_m(x_0, y_0) e^{-ki(\frac{x}{z} x_0 + \frac{y}{z} y_0)} dx_0 dy_0 \end{aligned} \tag{161}$$

with C being a constant that corrects for the electrical field amplitude. $t_m(x_0, y_0)$ is the aperture function that tells which light is transmitted in the aperture plane described by x_0 and y_0. x and y are coordinates on the imaging plane. In a general setup, the incoming monochromatic coherent light wave must go through a lens that cuts a circle out of the wavefront. This circle will be the only transmitted light. We can also see this lens as a circular aperture that transmits a part of the light. By rewriting the light waves to a Fourier form, we are working in a field called Fourier optics.

5.2.2 The Airy pattern

If we had a 4f system to image a spot such as the green line in figure 71, we could translate this ray path to Fourier optics. The system's numerical aperture limits the biggest angle that this ray can make. The aperture plane for a lens is actually buried inside the lens and has a spherical shape. This redefines our frequency to be depending on the angle of diffraction.

$$f_x = \frac{nx}{\lambda z} = k\frac{n\sin(\theta)}{2\pi n} \tag{162}$$

We already saw a maximum angle at which the lens could produce images. This limits the frequencies that can pass the aperture to be smaller to $\frac{kNA}{2\pi n}$. This information defines the Fourier transform of our circular aperture function $T_m(f_x, f_y)$.

$$T_m(f_x, f_y) = \begin{cases} 1, & \sqrt{f_x^2 + f_y^2} \leq \frac{kNA}{2\pi n} \\ 0, & \sqrt{f_x^2 + f_y^2} > \frac{kNA}{2\pi n} \end{cases} \tag{163}$$

where we redefined the circular aperture to be limited by the circle with the frequency $\frac{kNA}{2\pi n}$. We can define a point in the lens's entrance as P with coordinates f_x and f_y and a point on the imaging plane P_0 with coordinates x_0 and y_0. We can rewrite both these points to spherical coordinates.

$$\begin{aligned} x_0 &= \rho\cos(\phi) \\ y_0 &= \rho\sin(\phi) \\ \frac{x}{z} &= w\cos(\psi) = \eta \\ \frac{y}{z} &= w\sin(\psi) = \xi \end{aligned} \tag{164}$$

Using these changes in coordinates, we can also change the aperture function.

$$T_m(\eta, \xi) = \begin{cases} 1, & \sqrt{\eta^2 + \xi^2} \leq \frac{NA}{n} \\ 0, & \sqrt{\eta^2 + \xi^2} > \frac{NA}{n} \end{cases}$$

The electrical field in the image plane is given by the inverse of the Fraunhofer diffraction integral, the inverse Fourier transform. This derivation shows the same ideas as in the book of Max Born and Emil Wolf [181].

$$\begin{aligned} E(x_0, y_0) &= \mathcal{F}^{-1}[T_m(f_x, f_y)] \\ &= C\int_{-\infty}^{\infty}\int_{-\infty}^{\infty} T_m(f_x, f_y)e^{2\pi i(f_x x_0 + f_y y_0)}df_x df_y \\ &= C\int_{-\infty}^{\infty}\int_{-\infty}^{\infty} T_m(\frac{x}{z}, \frac{y}{z})e^{ki(\frac{x}{z}x_0 + \frac{y}{z}y_0)}\frac{\lambda}{n}d\left(\frac{x}{z}\right)\frac{\lambda}{n}d\left(\frac{y}{z}\right) \\ &= C_2\int_{-\infty}^{\infty}\int_{-\infty}^{\infty} T_m(\eta, \xi)e^{ki(\eta x_0 + \xi y_0)}d\eta d\xi \\ &= C_2\int_0^{\frac{NA}{n}}\int_0^{2\pi} e^{ki(w\cos(\psi)\rho\cos(\phi) + w\sin(\psi)\rho\sin(\phi))}wd\psi dw \\ &= C_2\int_0^{\frac{NA}{n}}\int_0^{2\pi} e^{kiw\rho\cos(\phi - \psi)}wd\psi dw \end{aligned} \tag{165}$$

We rewrote the constant before the integral to include the $\frac{\lambda^2}{n^2}$. We also combined the two cosines and sinuses into one cosine. Also, we changed the integral into spherical coordinates $d\eta d\xi = wd\psi dw$. A big part of this integral can be recognized as the zeroth order Bessel function [181].

$$J_n(x) = \frac{i^{-n}}{2\pi}\int_0^{2\pi} e^{ix\cos(\alpha)}e^{in\alpha}d\alpha \tag{166}$$

It is important to note that, due to the goniometric properties, a shift in α would not result in a different integral solution and would still be equal to the zeroth order Bessel function. Therefore, the $\phi - \psi$ can be taken to only depend on ψ. Another important property of this Bessel function is how each order relates to each other by a recurrence relation.

$$\begin{aligned} \frac{d}{dx}[x^{n+1}J_{n+1}(x)] &= x^{n+1}J_n(x) \\ xJ_1(x) &= \int_0^x yJ_0(y)dy \end{aligned} \tag{167}$$

Using these mathematical tricks, we can make more steps in solving equation 168.

$$\begin{aligned} E(x_0, y_0) &= C_2 \int_0^{\frac{NA}{n}} \int_0^{2\pi} e^{kiw\rho\cos(\phi-\psi)} w d\psi dw \\ &= C_2 \int_0^{\frac{NA}{n}} 2\pi J_0(kw\rho) w dw \\ &= C_2 \frac{2\pi}{k\rho} \int_0^{\frac{NA}{nk\rho}} J_0(b) b db \\ &= C_2 \frac{2\pi}{k\rho} \left(\frac{NA}{n}\right) J_1\left(k\rho\frac{NA}{n}\right) \\ &= C_3 \frac{2J_1\left(k\rho\frac{NA}{n}\right)}{k\rho\frac{NA}{n}} \end{aligned} \tag{168}$$

With $C_3 = C_2\pi\left(\frac{NA}{n}\right)^2$. Sir George Bidell Airy first derived this form and is therefore also known as the Airy disk [182]. As we already discussed, the intensity of the light depends on the squared norm of the electrical field.

$$I(x_0, y_0) = |E(x_0, y_0)|^2 = I_0 \left(\frac{2J_1\left(k\rho\frac{NA}{n}\right)}{k\rho\frac{NA}{n}}\right)^2 \tag{169}$$

This normalized function, i.e., $I(x_0, y_0)/I_0$, is also known as the point spread function (PSF) and is shown in figure 77. This is the image we will get from imaging a point through a 4f system due to diffraction. If we have two points, they will both create an Airy pattern. If we want to distinguish the points from each other, we must make sure we can distinguish both spots. This is possible when the spots are at least separated from each other with 1 radius length, as shown in figure 78. This requirement is also known as the Rayleigh criterion, named after Lord Rayleigh [183] [184].

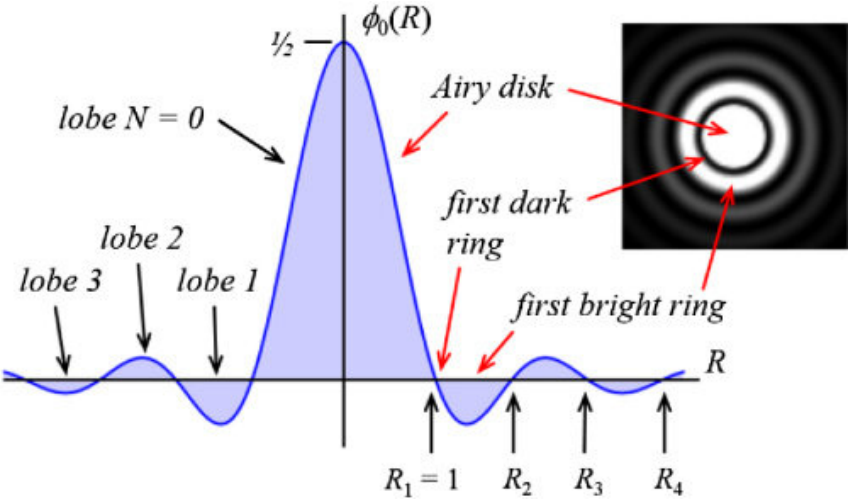

Figure 77: The intensity due to a circular aperture. This shape is called the Airy disk and consists of multiple circles. Each circle is separated due to the minima in the Airy disk function [185].

If we implement this theorem in equation 169, we can see that the disk's radius is at the first zero of the PSF. We know that this zero is located at $k\rho\frac{NA}{n} = 3.833$ [181].

$$\begin{aligned} k\rho\frac{NA}{n} &= 3.833 \\ \frac{2\pi n}{\lambda}\rho\frac{NA}{n} &= 3.833 \\ \rho &= \frac{3.833}{2\pi}\frac{\lambda}{NA} = 0.61\frac{\lambda}{NA} \end{aligned} \tag{170}$$

As equation 164 shows, ρ is the radius at the image plane where the Airy disk is projected. Also, the NA is related to the conic angle at which the light is limited. Therefore, we can say that this is the minimal spot due to a circular aperture, given the NA and the wavelength of the light. This limit is the resolution in the image plane.

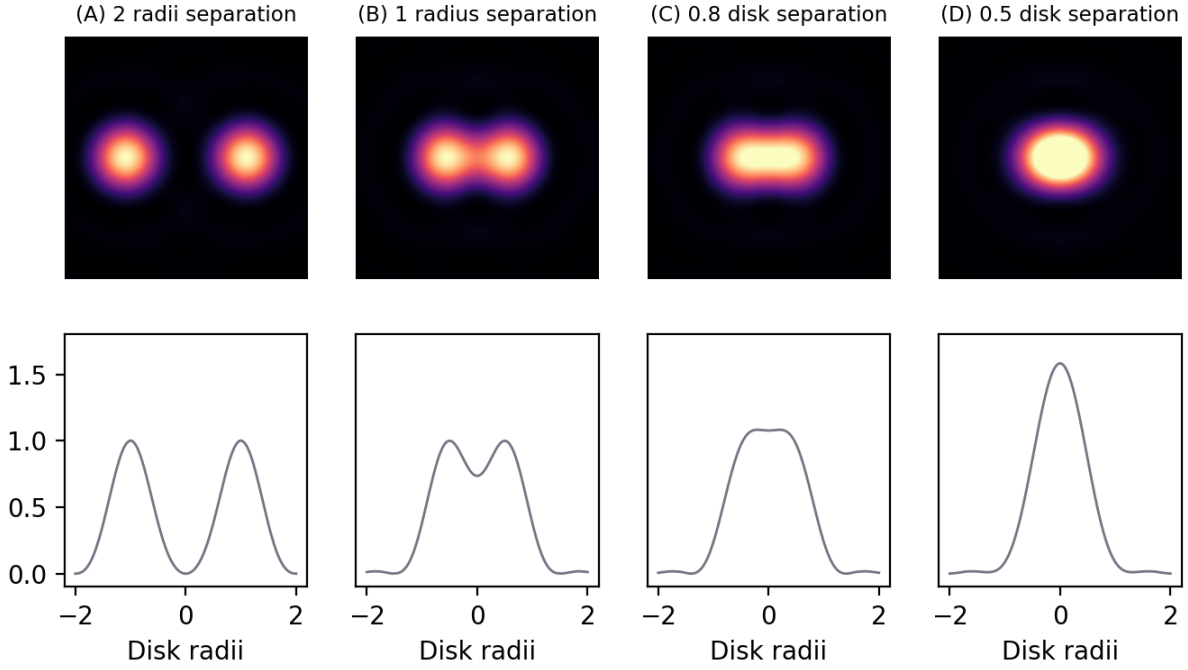

Figure 78: The effects of separation of the Airy disks are shown. If we separate the spots with a distance of at least 1 radius, the spot centers can be distinguished as two separate spots. When the separation is less than a distance of 1 radius, it is impossible to recognize individual spots anymore [186].

5.2.3 Depth of Focus

In the previous section, we described the spatial resolution using the Airy disk. We are also interested in how far a spot can be out of focus in $\hat{z}$ before it cannot be recognized anymore. As we already discussed, a light ray is a wave with peaks and zeros. The spots in the interference patterns are spaced by the zeros in the intensity. We can also look at this in the z-axis. If we take a wavefront that is in focus with focal length R and take a wavefront that is out-of-focus with focal length $R + \Delta Z$, we can derive the limit of this extra distance. This is shown in figure 79. We can limit the distance W because it cannot be more than a quarter wavelength of the incoming light rays, i.e., $W \leq \frac{\lambda}{4n}$. If we have a monochromatic wavefront with a given maximum amplitude A and shift it with a quarter wavelength, i.e., with $\sin \frac{\pi}{2}$, we would have this same wavefront with zero amplitude.

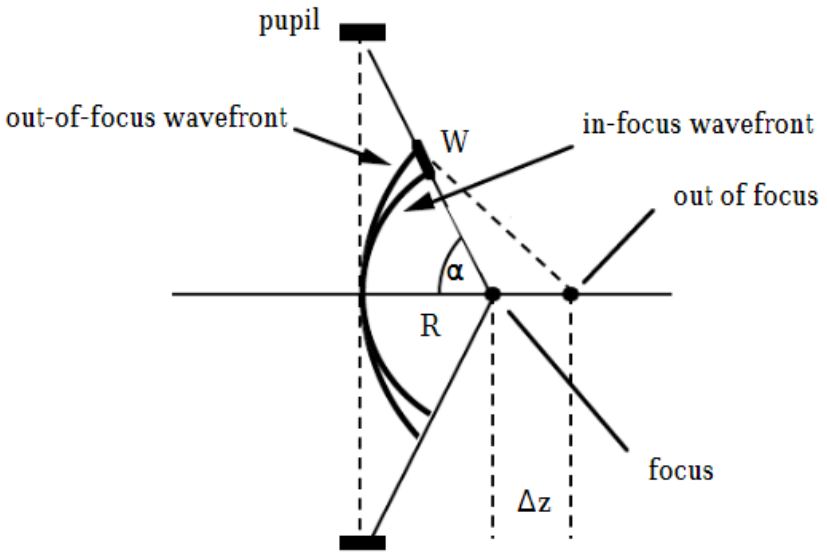

Figure 79: A schematic depiction of a wavefront compared to an out-of-focus wavefront. The wavefronts are distanced with a distance W as seen from the focal point of the focused wavefront [187].

If we assign angles and distances to the schematic of figure 79, we approach the limit of W from another perspective using the law of cosines [187].

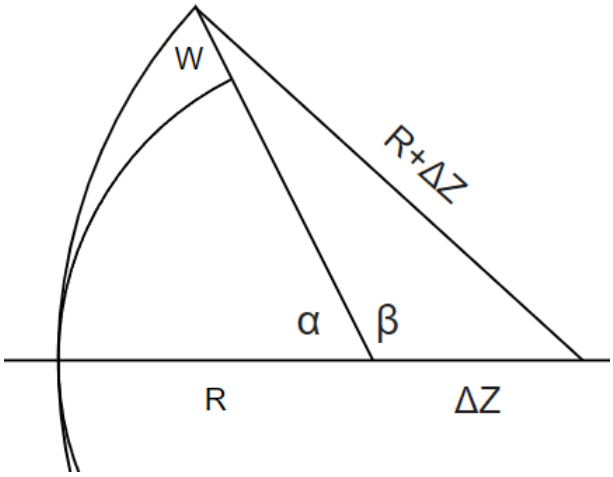

Figure 80: The same schematic figure as in figure 79 but with more assigned distances. These variables are used in equation 171.

$$
\begin{aligned}
R + \Delta Z &= \sqrt{(\Delta Z)^2 + (R+W)^2 - 2(\Delta Z)(R+W)\cos(\beta)} \\
(R + \Delta Z)^2 &= (\Delta Z)^2 + (R+W)^2 - 2(\Delta Z)(R+W)\cos(\pi - \alpha) \\
R^2 + 2\Delta Z R + (\Delta Z)^2 &= (\Delta Z)^2 + R^2 + 2RW + W^2 + 2(\Delta Z)(R+W)\cos(\alpha) \\
W^2 + 2(R + \Delta Z\cos(\alpha))W &= 2\Delta Z R(1 - \cos(\alpha)) \\
W &= -R - \Delta Z\cos(\alpha) \pm \sqrt{(R + \Delta Z\cos(\alpha))^2 + 2\Delta Z R(1-\cos(\alpha))} \\
&= -R - \Delta Z\cos(\alpha) \pm \sqrt{R^2 + (\Delta Z)^2\cos^2(\alpha) + 2\Delta Z R} \\
&= -R - \Delta Z\cos(\alpha) \pm R\sqrt{1 + \left(\frac{\Delta Z}{R}\right)^2\cos^2(\alpha) + 2\left(\frac{\Delta Z}{R}\right)} \\
&\approx -R - \Delta Z\cos(\alpha) \pm R(1 + \frac{\Delta Z}{R}) \\
&\approx \Delta Z(1 - \cos(\alpha))
\end{aligned}
\tag{171}
$$

In this derivation, we used that $R \gg \Delta Z$ such that we could use the Taylor expansion around 0 to approximate $\sqrt{1 + 2x + \cos(\alpha)x^2} \approx 1 + x$. We also used that W cannot be negative to ensure ΔZ to be only positive.

$$
\begin{aligned}
\frac{\lambda}{4n} &\geq \Delta Z(1 - \cos(\alpha)) = \Delta Z - \Delta Z\sqrt{\cos^2(\alpha)} = \Delta Z - \Delta Z\sqrt{1 - \sin^2(\alpha)} \\
&\geq \Delta Z - \Delta Z\sqrt{1 - \left(\frac{NA}{n}\right)^2} = \Delta Z\left(1 - \sqrt{1 - \left(\frac{NA}{n}\right)^2}\right) \\
\Delta Z &\leq \frac{\lambda}{4n\left(1 - \sqrt{1 - \left(\frac{NA}{n}\right)^2}\right)}
\end{aligned}
\tag{172}
$$

So here we see that we can be out of focus for a distance ΔZ to distinguish spots in a diffraction-limited optical setup. In research, an asymptotic version of this formula, with NA taken small, is often used to describe the depth of focus [181].

$$
\Delta Z = \frac{\lambda n}{2NA^2} \tag{173}
$$

When comparing these resolutions, we can find that the DOF is, on average, more forgiving. Therefore, we can conclude that, for low NA, the system is mainly limited by the spatial resolution from equation 170. At high NA, we can see that the difference between the DOF and its approximation show a difference, limited by a factor 2. The three different resolutions, the detailed DoF, the simplified DoF, and the spatial resolution, are compared and shown in figure 81 and figure 82.

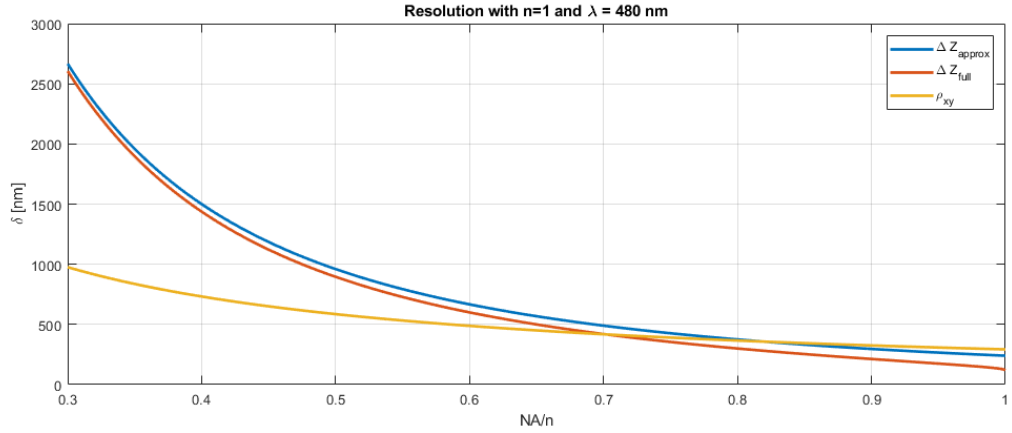

Figure 81: The resolutions from equations 170, 172, and 173 compared to each other with the same optical setup and light source.

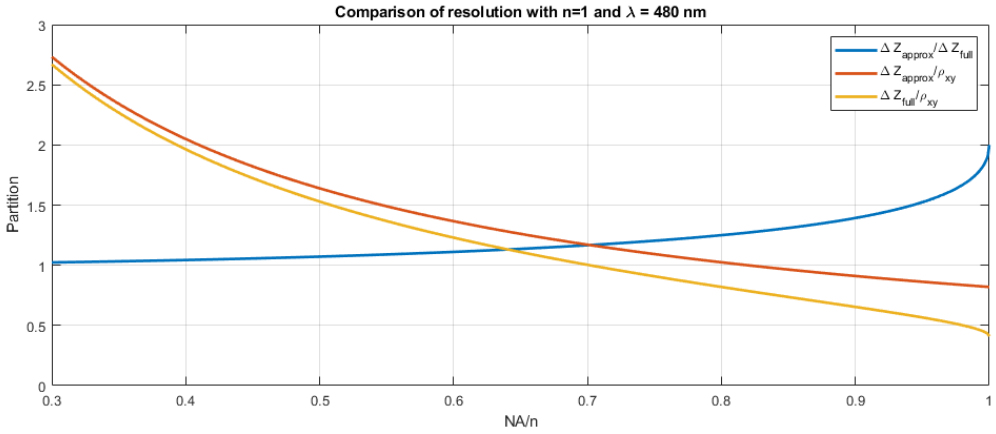

Figure 82: The scaling between the resolutions from equations 170, 172, and 173 compared to each other with the same optical setup and light source.

5.3 Light source

We already discussed how the light beams behave in the optical setup due to lenses and apertures. We have not discussed yet where those light beams originate from. In general, an optical setup for OET uses three types of light sources.

1. Light Emitting Diodes (LED)
2. Light Amplification by Stimulating Emission of Radiation (LASER)
3. Incandescent lamps

The light in the optical setup can serve multiple purposes. One needs to be used to create the pattern for the OET. Another can be used to illuminate the entire chip for imaging purposes. Another purpose we want to highlight is fluorescence imaging.

5.3.1 Different lamps

Approximately 45 years before Thomas Edison became known for inventing the light bulb, researchers in Britain demonstrated that light could be created by running an electric current through a filament, such as tungsten, which then heats it by Joule heating [188]. This radiation effect is called incandescence. In 1879, Thomas Edison added a gas-filled glass bulb to this setup to prevent the filament from burning up due to oxygen [189]. A more advanced form of this light bulb is the halogen-filled lamp. When tungsten is heated, it evaporates, burning up the filament, and, in time, stops working as a light source. Halogen gas is reactive with the tungsten vapor, re-depositing it back on the filament. This way, the filament is self-repairing, elongating the lifetime significantly [190].

Another variant of this principle is found in ultra-high-pressure lamps, often used in projectors. These lamps use a gas at high pressure instead of a filament. When a voltage is applied to this gas, it discharges and emits light. Both halogen lamps as UHP reach high temperatures (>1000 °C). Due to this heat and its thermal effects, these lights are limited to how useable they are in OET.

Since 2019, the main light source shifted from incandescent lamps to LED lights. A Light Emitting Diode (LED) has been shown to work in 1927 by Oleg Lesev [191]. An LED works similarly to a diode, the p-n junction briefly discussed in section 3.4.3. When the p-n junction is not made from the same material but from a compound, the electrons in the n-material could have a higher energy than the holes in the p-material. When the electrons and holes recombine, this extra amount of energy needs to be dissipated, which an LED does by emitting photons with energy equal to the excess energy. This phenomenon is called electroluminescence [192]. A schematic of an LED can be seen in figure 83. This structure is finite, meaning that the output light of the LED is not a point source but must be seen as an object. Due to this, it is hard to create a collimated light beam.

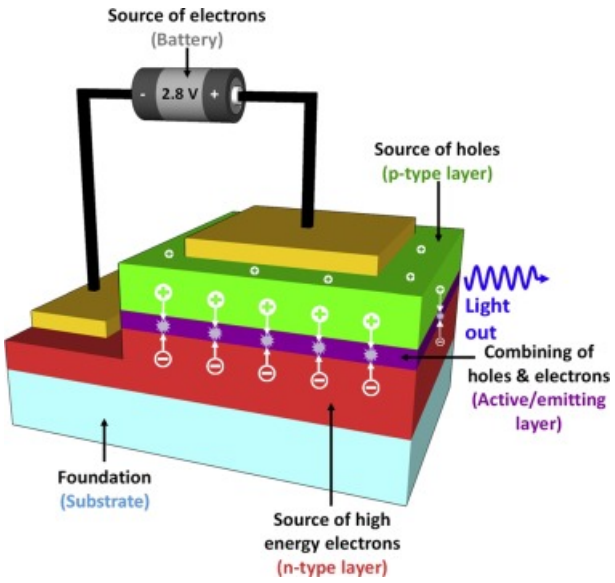

Figure 83: The schematic of an LED showing the compound layers. The battery depicts the external power that initiates the electroluminescence [193].

To collimate an LED beam as well as possible, we must look at the expected beam divergence. If we have an LED with a size d, distance from a lens with diameter D distanced at the focal length f, we can calculate the "collimated" beam width after a distance L. This expected beam divergence can be seen in figure 84. The divergence angle is related to the focal length and the size of the LED [194].

$$\frac{\Phi}{2} = \tan^{-1}\left(\frac{d}{2f}\right) \tag{174}$$

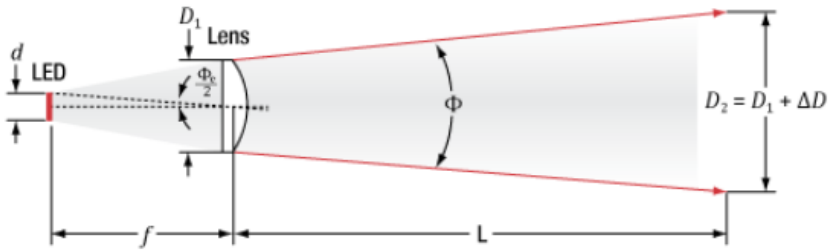

Figure 84: The expected beam divergence of an LED with size d after a distance L [194].

The last type of light source that we want to discuss is a laser. Similarly to the energy levels discrepancy in the LED creating photons with a specific energy, laser light comes from excited electrons in atoms. A typical laser setup exists of a tube with a crystal core that is encapsulated by two mirrors. Around this crystal, a tube is wired called the flash tube. This is encapsulated fully with another tube with a small aperture for the laser light to exit. This schematic is shown in figure 85.

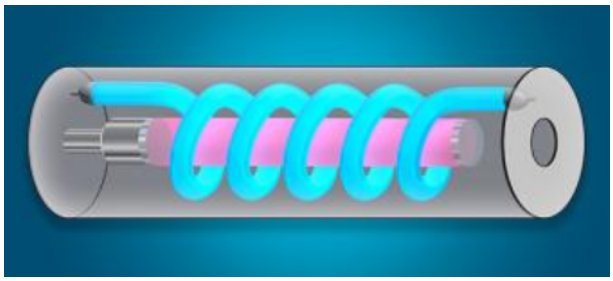

Figure 85: A schematic of a basic laser. The red tube is the crystal that emits and amplifies the photons. This crystal has a mirror on each end and is surrounded by a flash tube depicted in blue [195].

When an electric potential is applied, a light burst is emitted from the flash tube. This principle is similar to the gas-discharge lamps. When a photon from the flash tube hits an electron in the crystal, it can, if it has enough energy, move up to a higher orbital, similar to what happens in the photoconductor as discussed in section 3.2. The electron excitation can only happen when the photon's energy is higher than the gap energy between the two energy states. This is why the flash tube is also known as the laser pump; it activates the laser. An electron does not stay in this excited state forever and will relax, making it fall back into its original energy state. The extra energy this electron had is then emitted as a photon with the energy equal to the gap energy. This phenomenon is called spontaneous emission. A specific wavelength can be emitted by choosing a specific crystal. This specifically allowed amount of energy, which is why lasers are monochromatic; only photons with the same wavelength are created in the laser.

When a photon emitted from an excited electron hits the excited electron of another atom, this electron is stimulated to relax and emit a photon with the same wavelength and the same phase. This is, therefore, also known as stimulated emission. The photon inducing the stimulated emission is copied exactly, making two photons exit the atom with both the same wavelength and phase. This is why laser light is coherent,i.e., in phase. When those two photons hit another excited electron, they induce stimulated emission, creating even more identical photons. Because mirrors enclose the crystal, the photons bounce multiple times in it, multiplying itself more and more. The mirror close to the opening of the laser is slightly transmitting, making the photons exit the laser light partly at that side. This entire principle explains why lasers are called lasers. It is the abbreviation of Light Amplification by Stimulating Emission Radiation. One last important characteristic of a laser is the small divergence angle. Because the diameter D of the hole where the laser emits the light is very small, the radiation is coherent and monochromatic, and we can approximate the laser to have a divergence angle of $\theta = \lambda/D$. Due to this, laser sources can almost reach the diffraction-convergence and are a highly collimated optical source [174].

5.3.2 Fluorescence microscopy

When creating an OET, we often use the wavelengths that excite carriers the most, e.g., blue light for a-Si:H as discussed in section 3.2.2. If we only use this light for illumination, we will only be able to see the illuminated pattern and not, for example, the cells we want to image and actuate. To compensate for this, we could add a red lamp that illuminates the entire chip but does not induce such a strong photoelectric effect. This simple but effective method to see and actuate the particles also has a downside, for it induces some electroconductivity, which decreases the dielectrophoretic force. Therefore, one has to be careful to find the right trade-off.

One could also include fluorescence microscopy in the optical setup for increased imaging quality of biological cells. This could be of great added value when using the OET for, e.g. medical research. Fluorescence microscopy found its way into the world with help from Sir Frederick William Herschel, who, in 1845, found that tonic water exhibits a blue glow when illuminated with UV light [196]. The way fluorescence imaging works is very similar to the spontaneous emission in a laser. In this situation, we will look at the material we want to fluoresce as having an absorption spectrum and an emission spectrum. Figure 86 shows a typical fluorescent spectrum. When the electrons in the material's atoms are excited, they enter one of the allowed energy levels. Those levels are visualized in the Jablonski diagram, named after Aleksander Jablonski [197].

When a photon with an amount of energy that is more than the difference between the energy of the electron in the ground state and the lowest state of a higher energy level[33] is absorbed by the electron, it can cross the energy gap. The duration of this excitation is in the order of femtoseconds. When the electron relaxes, it returns to an energy state in S_0. This does not necessarily mean it goes to the ground state but can exist in a higher vibrational level in the same singlet state. The electron needs to release excess energy, which it does in the form of a photon. Due to this, how well specific photon energies are absorbed is shown in a corresponding absorption spectrum. The way photons are most likely to be emitted is shown in the emission spectrum. These spectra usually are shifted with respect to each other, called Stokes shift and is named after George Gabriel Stokes [198]. This shift makes it possible to distinguish the fluorescent light by filtering for these wavelengths before measurement [199]. When an electron is moved to a higher energy level, it is possible that the electron first crosses to a triplet state, where the total spin momentum number is 1. The energy will be lower when the electron returns to the ground singlet state, where the total spin momentum is 0. This phenomenon is called phosphorescence and has a longer relaxation time in the order of microseconds, whereas the relaxation time of fluorescence is in the order of nanoseconds. This delay in photon emission can disrupt the accuracy of imaging [200].

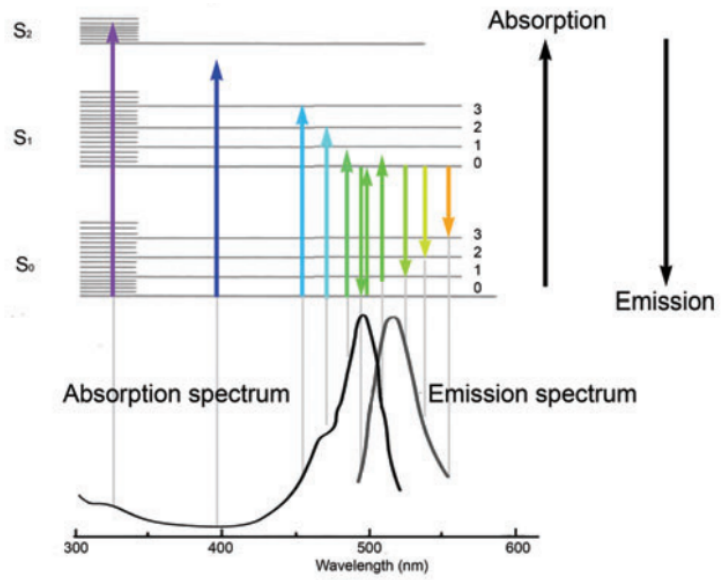

Figure 86: The absorption and emission spectrum of the fluorophore FITC shown with corresponding Jablonski diagram [201].

When a fluorophore, a particle exhibiting fluorescence, is excited too many times, the fluorescence effect will fade. This phenomenon is called bleaching and will stop the system from working properly. Often, 10000-40000 cycles are considered the limit of a good fluorophore before bleaching occurs. One should use as little intensity as is needed for imaging to counter this effect. An ideal fluorescence microscope has an objective with a high NA such that as many fluorescence photons can be captured. The light's intensity area is proportional to $(\mathrm{NA})^2$. Therefore, the amount of exciting photons is proportional to $(\mathrm{NA})^2$, as is the amount of fluorescent photons. The excited light is therefore observed to be proportional to $(\mathrm{NA})^4$ [201].

[33] For example, from the 0 line of S_0 to the 0 line S_1.

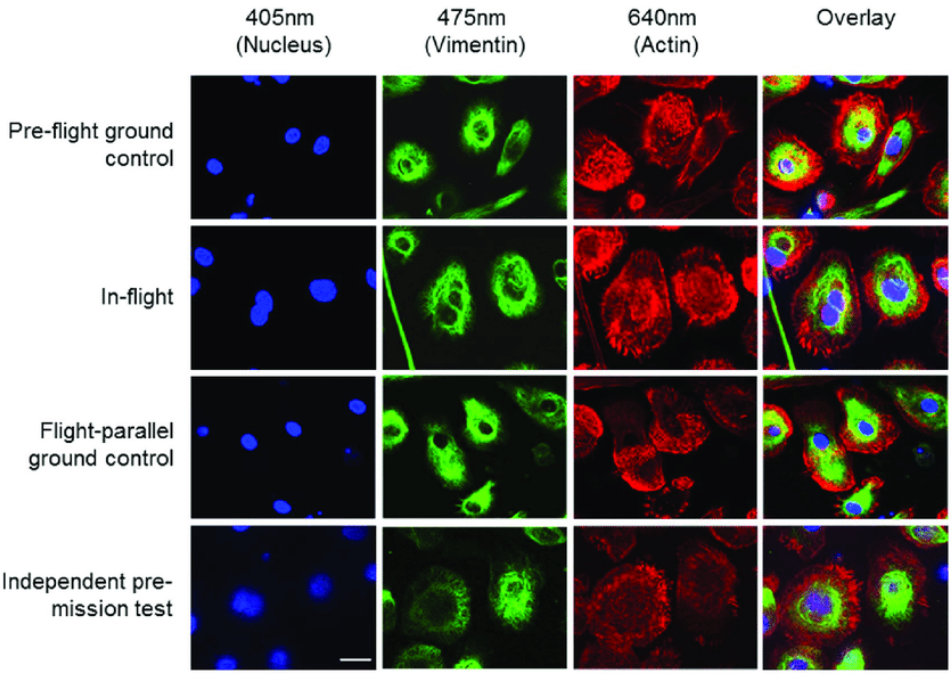

Figure 87: A human macrophage under the microscope with three different fluorescence wavelengths. Due to the different absorption- and emission spectra of the different parts in the cell, the different parts of the cell can be better recognized [202].

Figure 87 shows a good example of the useability of fluorescence microscopy. A human macrophage under a regular light microscope will look like a blob, making it hard to recognize very specific parts of the cell. Due to each part having different fluorescent characteristics, it is possible to excite the electrons in each part individually and capture the result from its fluorescence. When we have separate images of the parts as seen by a fluorescent microscope, we can combine those images to create one image with the combined information.

5.4 Digital Micromirror Device

We have discussed what kind of light sources we can use for the OET and what their pros and cons are. We did not discuss how we could get specific illumination patterns to actuate the tweezer. We do not want to use only the airy pattern as a tweezer but could need squares, rings, or more complex patterns. In literature, often consumer-grade projectors[34] or digital micromirror devices (DMD) are used. A DMD is a grid of tiny mirrors that can flip at a certain angle when powered. Light transmitted through a material will get an angle due to the refractive index as shown in equation 154. When the same material reflects light, it will not change its angle but will flip the same angle to the normal as a mirror does. Therefore, if we can control the angle of the normal of the mirror, we can control the light's direction. If we have multiple mirrors, we can decide the output direction of each light ray that enters a single mirror. Figure 88 shows a typical DMD chip. Each mirror flips a certain angle diagonally by micro torsion hinges when turned on [203]. Due to this, the full DMD needs to rotate so that the direction of the mirror flipping is in the same plane as the light path in the optical setup.

[34] Many consumer-grade projectors make use of a DMD themselves.

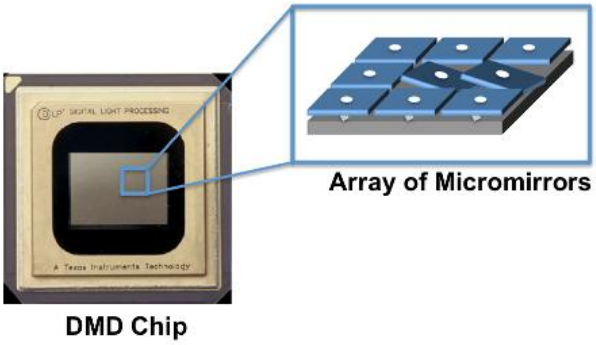

Figure 88: A digital micromirror device with a part of the array schematically shown [204].

If we take a DMD in the same configuration as in figure 89, we can see that the rays that fall on the mirrors that are switched on are reflected with $2\theta_t$ to the right relative to the incoming angle. When the mirrors are switched off, the rays are reflected $2\theta_t$ to the left. The DMD can be seen as a pixel array, which is numerically a matrix of 0 and 1 [205]. This matrix can be created, adjusted, and sent to the DMD at a certain speed using, e.g., python [206]. In general, DMD chips are around 2 cm^2 with a number of mirrors around 1 to 2 million, with a size of around 100 μm^2. The mirrors in the DMD are slightly separated from each other, which means that each mirror behaves as its own aperture. As we saw in equation 169, this limits our resolution. For square apertures, we have a more simple resolution[35] [207].

$$\sigma_{xy} = \frac{f\lambda}{d} \tag{175}$$

with σ_{xy} being spot size and, therefore, the minimal needed distance between spots. f is the focal length of the imaging lens, and d is the side length of a mirror in the DMD. Due to not all mirrors being turned on and due to the spaces between the mirrors, we have diffraction and, therefore, some loss of photons, which need to be taken into account. A DMD's efficiency is between 64-72% depending on the wavelength [208].

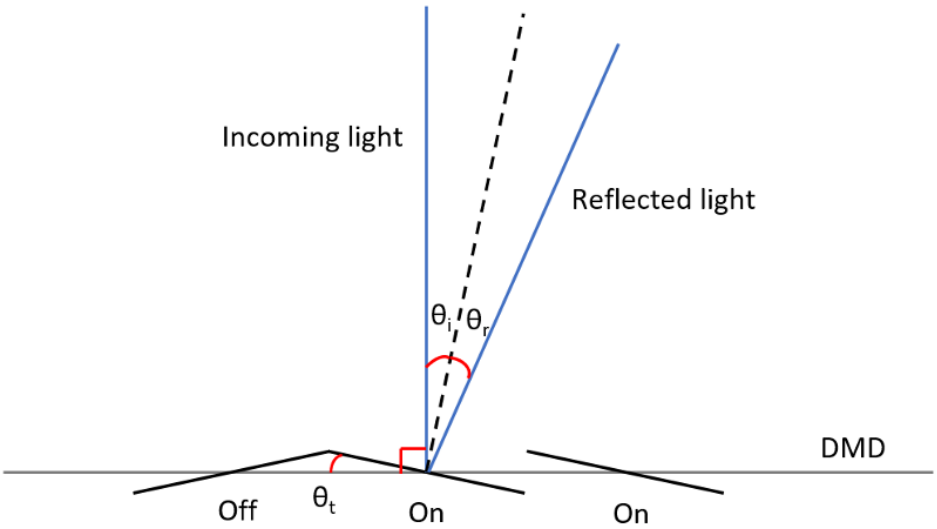

Figure 89: A schematic depiction of a DMD showing the on and off state. Light reflects on the DMD with $2\theta_t$ in the on state and with $-2\theta_t$ in the off state [209].

[35] We will not discuss the Fraunhofer integral here of the square aperture, but it follows a similar line of thought.

5.5 Camera

Only one important thing is missing if we have the full setup with lenses, DMD, and light sources. To see and analyze the results of the optical setup, we will be using a camera. Cameras have been around since 400 B.C. as camera obscuras but were first shown by Joseph Nicephore Niepce to capture images in 1826 [210]. In optical setups, digital cameras that have sensors consisting of multiple photodiodes are used. In each photodiode/pixel, the energy of photons is converged to free electrons using the photoelectric effect. The amount of charge in each pixel is then translated to the intensity of light, which can then be imaged into a computer [211]. How well a camera sensor is depends on the quantum efficiency (charge per photon), which depends on the wavelength. A very important characteristic of the camera is the number and size of the pixels. This is the grid in which we can distinguish light spots. The more pixels we have, the smaller the spots we can distinguish. The size of the sensor determines our field of view. The bigger the sensor, the larger the FoV. One last important quality of a camera is the framerate, the speed at which shots are taken. If we have, e.g., a camera framerate of 1 Hz, it captures the light once per second. If the DMD flips on and off 2 times per second, we would not see this flipping on the camera. The framerate must, therefore, be fast enough to sample everything correctly. This can be chosen to be on the Nyquist frequency, which is two times the highest frequency in the system [212]. In this example, that would mean a framerate of at least 4 Hz is needed.

5.6 Typical optical setups for optoelectronic tweezers

We have now discussed the elements needed for the optical setup for the OET. To put these elements together, we need to put them at the right focal lengths to get the images as sharp as possible. This can be adjusted and optimized by including moving stages. The lenses used must correspond to the needed magnification such that the pattern from the DMD is small enough to actuate small particles accurately. If we want to use a single objective for both projecting the DMD pattern and imaging the chip using the camera, we will need a beam splitter, which is essentially a mirror that partly transmits the light. If we want to reduce the intensity, we can use filters that transmit some wavelengths better than other frequencies. This way, we can even out the light in the camera so that it does not oversaturate from certain wavelengths. One last thing we could use if needed, is a dichroic mirror, which is a combination of a beam splitter and a filter. Some wavelengths are mostly transmitted, and some are mostly reflected. Some typical OET setups found in literature are shown in figure 90, figure 91, and figure 92.

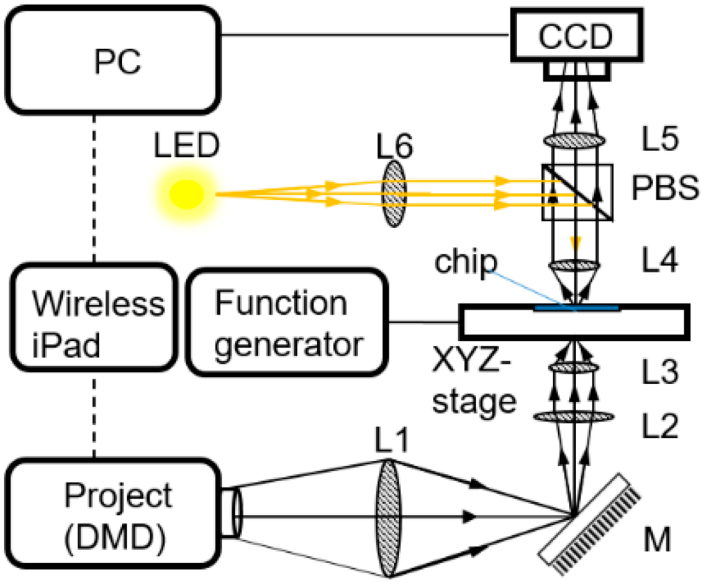

Figure 90: A typical OET setup with a consumer-grade projector focused on the OET chip on a moving stage. An LED images the full chip using a beam splitter to have a complete view [34].

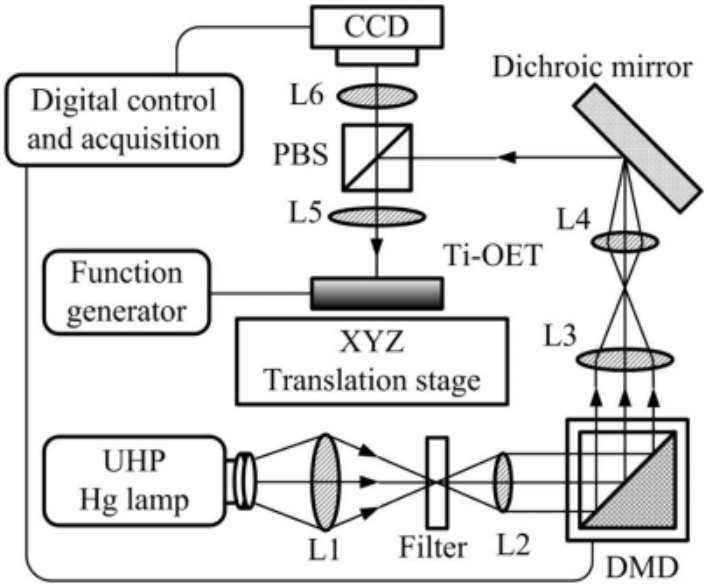

Figure 91: A typical OET setup with a DMD projector focused on the OET chip on a moving stage. The wavelength used for illumination is filtered using a dichroic mirror [119].

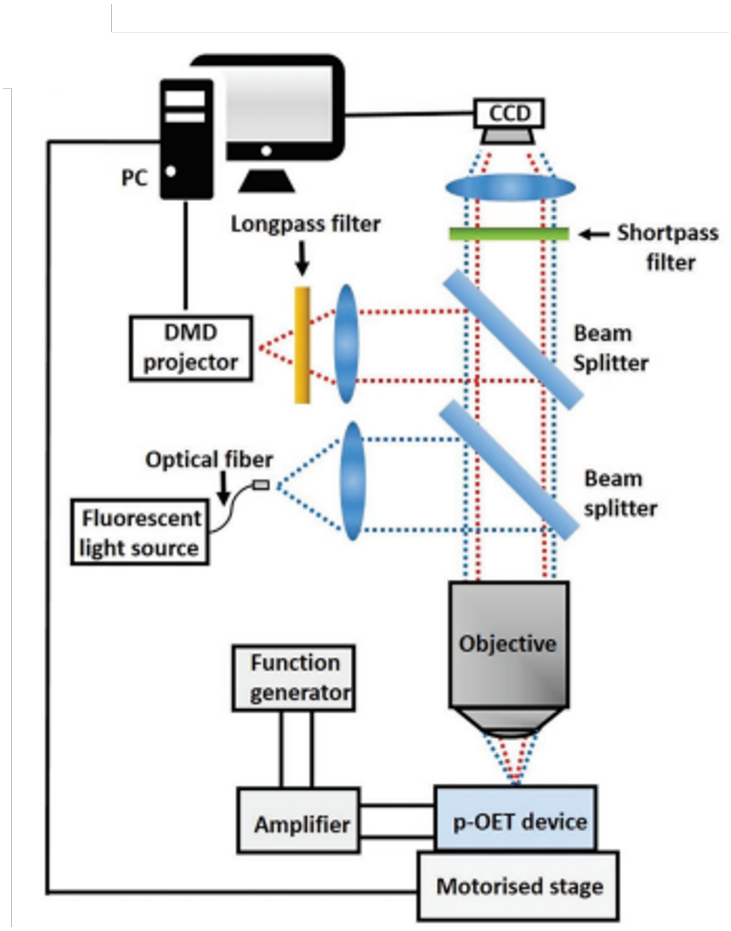

Figure 92: A typical OET setup where a DMD projector and a fluorescent light source are put in the same objective using beam splitters [28].

6

Instrumentation

In this section, we introduce the methods utilized for practically creating an optoelectronic tweezer device. We employ a Plasma Enhanced Chemical Vapor Deposition (PECVD) device to form a photoconductive layer on conductive glasses. This device applies a specific thickness of amorphous hydrogenated silicon. We explain the working principles of this device to demonstrate how it can impact the consistency of the photoconductive layer. The fabrication process for manipulating dielectric particles is also covered. To achieve particles of specific sizes and shapes, we use a Nanoscribe machine, which creates small 3D objects through photolithography. Additionally, we outline how to clean the glasses thoroughly using acetone and isopropanol. Lastly, we detail other instruments employed in the operation of optoelectronic tweezers.

Instrumentation for "Jip en Janneke"

In this section, we talk about some machines needed to create the full optoelectronic tweezer. It's not very easy to put the photoconductive layer on the glass. To do this, we use an instrument called a Plasma Enhanced Chemical Vapor Deposition machine. This machine changes gas into plasma. Plasma is a special state of matter, like solid, liquid, and gas. What makes plasma special is that it helps the tiny pieces in the gas come apart. This happens during a lightning bolt and the northern lights. The plasma from this machine is layered on the glass to make the photoconductive layer we need. With this machine, we can create a very thin layer.

The objects we want to use also need to be made. We can easily buy very small balls for the optoelectronic tweezer. If we want more complicated shapes, we need to use a Nanoscribe. This Nanoscribe uses light to carve out tiny objects from a material, kind of like ice sculpting but about 1000 times smaller.

It's very important to work with clean materials so we don't get smudges on the glass. We can clean the glasses using special chemicals. At the end of this section, we talk about other tools we need for the optoelectronic tweezers, such as a waveform generator to create the electrical signals, a computer to control everything, and a power meter to take measurements.

The Jip and Janneke illustration is created by the renowned artist Fiep Westendorp.

6.1 Fabrication of the photoconductive layer

It is impossible to easily paste a photoconductive layer with a certain height on the conductive glasses. For that, different methods of thin film deposition exist. We will focus on Plasma Enhanced Chemical Vapor Deposition (PECVD). In a vacuum chamber, two gasses are deposited, silane (SiH_4) and hydrogen (H_2) at a certain pressure. Two electrodes are positioned in this chamber, with the bottom one grounded. On this bottom electrode, a substrate is put on which the a-Si:H will be deposited. When a high enough AC voltage is applied on the top electrode, the gasses' electrons will separate from the atoms. This state of matter is called a plasma [213]. The electrons are much smaller than the ions, which makes them more mobile in the plasma. When the AC voltage on the top electrode has a positive peak, the electrons are attracted to it, and the ions are attracted to the grounded electrode, and vice versa when the AC voltage has a negative peak. Because the electrons move more quickly, an increase in the overall voltage in the plasma is created. Due to this, the ions are attracted to the substrate on the bottom electrode, creating a thin film of a-Si:H.

A typical PECVD reactor is schematically shown in figure 93. In this case, the typical frequency range of the PECVD's AC voltage is in the radio-frequency (RF) range. By heating the elements, changing the pressure or consistency of the gasses, and controlling the input voltage, the deposited sheet characteristics can be fine-tuned [214] [215]. This explanation of the PECVD is schematic and needs specific recipes for specific photoconductive layers.

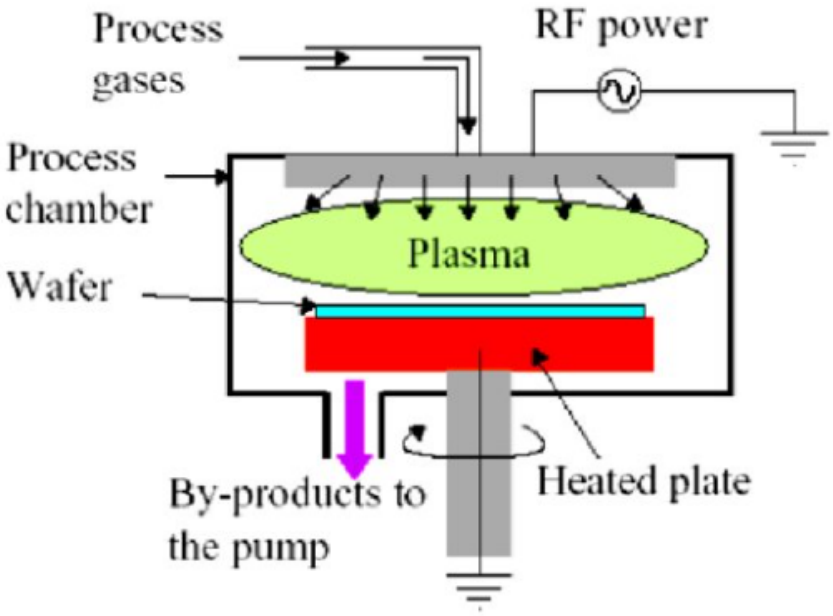

Figure 93: A schematic depiction of a typical PECVD reactor [214].

In general, the PECVD deposits a set amount of thickness per set amount of time. Different materials can be deposited on each other to make different, more complex multilayer configurations as discussed in section 3.4.3.

6.2 Fabrication of the dielectric particles

When calibrating the OET system, a polystyrene spherical bead is often taken as a dielectric particle. These beads consist of a single material with a specific diameter. These beads can be store-bought with a specific fluorescence wavelength and size [216]. If we want to use more complex particles in the OET setup, we can use a Nanoscribe to create specifically shaped microparticles. To make these microparticles, a substrate, on which the microparticles will be created, is first covered in photoresist. This photoresist is hardened at the point where the Nanoscribe laser is in focus. This way, a structure can be built from the bottom up by scanning all the parts of the photoresist that need to harden with the Nanoscribe [217]. This method can be used to create the microrobots discussed in section 1.8. An example of the possibilities of the Nanoscribe is shown in figure 94. After the print, the remaining photoresist must be removed to uncover the created structures.

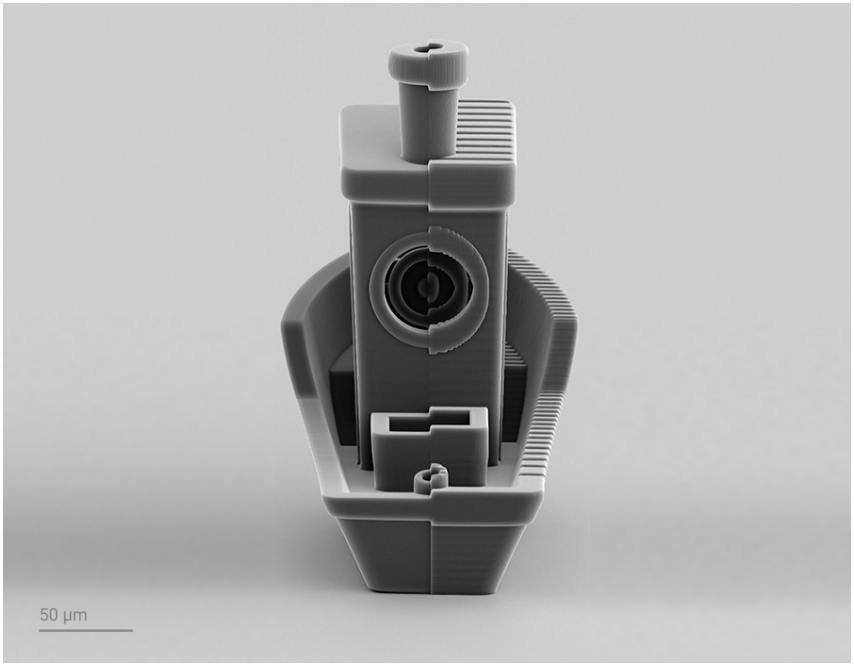

Figure 94: A Benchy, a typical calibration print used in 3D printing, to show the accuracy of a Nanoscribe [218].

Similarly, the grid from section 3.4.3 can be created by etching in the grid holes and filling them up with a conductive material. Like the PECVD, the lithography process described above is schematic, and a specific recipe must be created for particular materials.

6.3 Preparation of conductive glass

When we buy cover glasses for the microfluidic chips, we need to make sure that they are clean before putting on the ITO layer, the photoconductive layer, and before assembling the entire chip. A certain thickness of ITO on the glasses can be created by sputtering it on a clean glass with two silver contact strips [219]. The easier and more accurate solution is to buy the conductive glasses at a specialized store. When the (ITO) glasses are smudged and dirty, they can be cleaned by spraying them with acetone and isopropanol before drying them with pressurized air. This should make the glasses clean enough for each step in the fabrication process. The chemicals can impact the surface of the glass. Therefore, keeping the glasses stored clean and only touching them with gloves on is better to avoid making them dirty.

6.4 Other instrumentation

If we want to measure the DEP force on a particle, we can look at the fluid velocity at which the light pattern cannot hold the particle stationary anymore. At this point, the DEP force is overruled by the fluid force described by Stokes law as discussed in section 4.1.4. We can use a pump with enough accuracy to create a specific fluid flow. Different types of pumps that are often used in microfluidics are syringe pumps and piezoelectric pumps [220] [221].

We need to use a waveform generator to control the specific AC input voltage and frequency. The voltage amplitude can be increased by using a waveform amplifier. We can put an oscilloscope parallel to the system to monitor the exact waveform input in the chip. Figure 95 shows an example of this circuit. We can use Python or MATLAB to create a GUI to control the illumination lamp, the DMD, the waveform generator, the pump, the camera, and, if we are using electrically moving stages in the optical setup, the focus of the illumination. Using these, more sophisticated control inputs can be created to automatically control and move the particles in the OET setup [222].

We can use a spectrometer to measure the optical spectrum of the light used in the system, an optical power meter to measure the intensities at all points in the system, a multimeter or an oscilloscope to measure the electrical current and voltage in the system, and a stage micrometer to measure the resolution of the setup.

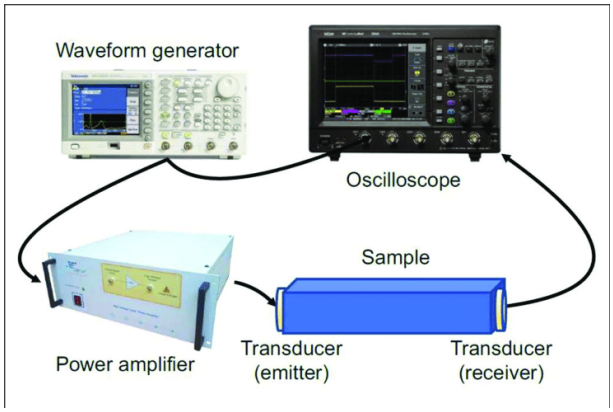

Figure 95: A typical waveform generator setup to create a specific AC voltage in a sample [223].

6

References

[1] C. Domp", ""james clerk maxwell. encyclopedia britannica."."

[2] A. Zangwill, *Modern Electrodynamics*, pp. 33–45. Cambridge University Press, 2013.

[3] Ørjan G. Martinsen and A. Heiskanen, "Chapter 3 - dielectrics," in *Bioimpedance and Bioelectricity Basics (Fourth Edition)* (Ørjan G. Martinsen and A. Heiskanen, eds.), pp. 37–73, Oxford: Academic Press, fourth edition ed., 2023.

[4] X. Wang, X.-B. Wang, and P. R. Gascoyne, "General expressions for dielectrophoretic force and electrorotational torque derived using the maxwell stress tensor method," *Journal of Electrostatics*, vol. 39, no. 4, pp. 277–295, 1997.

[5] A. Zangwill, *Modern Electrodynamics*, pp. 512–513. Cambridge University Press, 2013.

[6] E. Gregerson", ""poynting vector. encyclopedia britannica."."

[7] A. Adam", ""2023 - ap3071 advanced electrodynamics lecture 4 - electromagnetic energy. ap3071 advanced electrodynamics (2023/2024 q1)"."

[8] G. Strang and E. erman, "16.8: The divergence theorem, libretexts mathematics." Accessed: 31.05.2024.

[9] L. Bergamin, "Electromagnetic fields and boundary conditions at the interface of generalized transformation media," *Phys. Rev. A*, vol. 80, p. 063835, Dec 2009.

[10] "CUEMATH", ""maclaurin series formula"."

[11] T. Matsushita, *Dielectric Materials*, pp. 81–106. Cham: Springer International Publishing, 2021.

[12] R. F. ", ""the electric scalar potential"."

[13] l. "Ryan Melton, ""integrating even and odd functions"."

[14] W. I. o. S. "Michael Aldam, ""index gymnastics: Gauss' theorem, isotropic tensors, ns equations"."

[15] D. Chandrasekharaiah and L. Debnath, "Chapter 2 - algebra of tensors," in *Continuum Mechanics* (D. Chandrasekharaiah and L. Debnath, eds.), pp. 33–108, San Diego: Academic Press, 1994.

[16] T. E. of Encyclopaedia Britannica", ""root-mean-square voltage"."

[17] X. Wang, Y. Huang, F. Becker, and P. Gascoyne, "Unified theory of dielectrophoresis and travelling wave dielectrophoresis," *Journal of Physics D: Applied Physics*, vol. 27, p. 1571, 01 1999.

[18] T. Jones and M. Washizu, "Multipolar dielectrophoretic and electrorotation theory," *Journal of Electrostatics*, vol. 37, no. 1, pp. 121–134, 1996.

[19] K. Khoshmanesh, C. Zhang, S. Nahavandi, F. J. Tovar-Lopez, S. Baratchi, A. Mitchell, and K. Kalantar-zadeh, "Size based separation of microparticles using a dielectrophoretic activated system," *Journal of Applied Physics*, vol. 108, p. 034904, 08 2010.

[20] R. Deivasigamani, N. N. M. Maidin, M. F. M. R. Wee, M. A. Mohamed, and M. R. Buyong, "Dielectrophoresis prototypic polystyrene particle synchronization toward alive keratinocyte cells for rapid chronic wound healing," *Sensors*, vol. 21, no. 9, 2021.

[21] R. Pethig, "Review—where is dielectrophoresis (dep) going?," *Journal of The Electrochemical Society*, vol. 164, p. B3049, dec 2016.

[22] "COMSOL", ""simulate real-world designs, devices, and processes with multiphysics software from comsol."."

[23] Z. Baghdasaryan, A. Babajanyan, H. Parsamyan, B. Friedman, S. Kim, J.-H. Lee, and K. Lee, "3d visualization of microwave electric and magnetic fields by using a metasurface-based indicator," *Scientific Reports*, vol. 12, 04 2022.

[24] W. Liang, N. Liu, Z. Dong, L. Liu, J. D. Mai, G.-B. Lee, and W. J. Li, "Simultaneous separation and concentration of micro- and nano-particles by optically induced electrokinetics," *Sensors and Actuators A: Physical*, vol. 193, pp. 103–111, 2013.

[25] "MathWorks", ""math. graphics. programming."."

[26] "MathWorks", ""gradient"."

[27] S. Zhang, W. Li, M. Elsayed, P. Tian, A. W. Clark, A. R. Wheeler, and S. L. Neale, "Size-scaling effects for microparticles and cells manipulated by optoelectronic tweezers," *Opt. Lett.*, vol. 44, pp. 4171–4174, Sep 2019.

[28] S. Zhang, N. Shakiba, Y. Chen, Y. Zhang, P. Tian, J. Singh, M. Chamberlain, M. Satkauskas, A. Flood, N. Kherani, S. Yu, P. Zandstra, and A. Wheeler, "Patterned optoelectronic tweezers: A new scheme for selecting, moving, and storing dielectric particles and cells," *Small*, vol. 14, p. 1803342, 10 2018.

[29] M. C. Wu, "Optoelectronic tweezers for nanomanipulation," *2007 International Nano-Optoelectronics Workshop*, pp. 30–31, 2007.

[30] S. Zhang, J. Juvert, J. Cooper, and S. Neale, "Manipulating and assembling metallic beads with optoelectronic tweezers," *Scientific Reports*, vol. 6, p. 32840, 09 2016.

[31] D. Crecraft and S. Gergely, "2 - signals and signal processing," in *Analog Electronics* (D. Crecraft and S. Gergely, eds.), pp. 13–71, Oxford: Butterworth-Heinemann, 2002.

[32] W. Liang, S. Wang, Z. Dong, G.-B. Lee, and W. Li, "Optical spectrum and electric field waveform dependent optically-induced dielectrophoretic (odep) micro-manipulation," *Micromachines*, vol. 3, pp. 492–508, 12 2012.

[33] E. A. Kwizera, M. Sun, A. M. White, J. Li, and X. He, "Methods of generating dielectrophoretic force for microfluidic manipulation of bioparticles," *ACS Biomaterials Science & Engineering*, vol. 7, no. 6, pp. 2043–2063, 2021. PMID: 33871975.

[34] S. Zhang, E. Y. Scott, J. Singh, Y. Chen, Y. Zhang, M. Elsayed, M. D. Chamberlain, N. Shakiba, K. Adams, S. Yu, C. M. Morshead, P. W. Zandstra, and A. R. Wheeler, "The optoelectronic microrobot: A versatile toolbox for micromanipulation," *Proceedings of the National Academy of Sciences*, vol. 116, no. 30, pp. 14823–14828, 2019.

[35] C. Rosales and K. Lim, "Numerical comparison between maxwell stress method and equivalent multipole approach for calculation of the dielectrophoretic force in single-cell traps," *Electrophoresis*, vol. 26, pp. 2057–65, 06 2005.

[36] l.-h. Chau, W. Liang, F. Cheung, W. Liu, W. Li, S.-C. Chen, and G.-B. Lee, "Self-rotation of cells in an irrotational ac e-field in an opto-electrokinetics chip," *PloS one*, vol. 8, p. e51577, 01 2013.

[37] T. Jones and T. Jones, *Electromechanics of Particles*. Cambridge University Press, 1995.

[38] Y. Lin, "Numerical modeling of dielectrophoresis." Technical Report, May 2006.

[39] K. Roberta Hofman, "Which drinking water is the safest?," 2024. Accessed: 29.07.2024.

[40] Evides, "Drinkwater, wat zit erin?," 2024. Accessed: 29.07.2024.

[41] R. Jessica Clifton, "Is demineralised water the same as deionized water?," 2024. Accessed: 29.07.2024.

[42] R. F. Bader, "An introduction to the electronic structure of atoms and molecules," 1996. Geraadpleegd op 22 november 2024.

[43] C. Zhu, "Dielectric loss," 2001. Geraadpleegd op 22 november 2024.

[44] S. Mutyala, C. Fairbridge, J. J. Paré, J. M. Bélanger, S. Ng, and R. Hawkins, "Microwave applications to oil sands and petroleum: A review," *Fuel Processing Technology*, vol. 91, no. 2, pp. 127–135, 2010.

[45] M. J. da Silva, *Impedance Sensors for Fast Multiphase Flow Measurement and Imaging*. Phd dissertation, Technische Universität Dresden, Dresden, Germany, 2008. Submission: 05.05.2008, Public defense: 11.08.2008, Accessed on Nov 22, 2024.

[46] J. Voldman, "Electrical forces for microscale cell manipulation," *Annual Review of Biomedical Engineering*, vol. 8, pp. 425–454, 2006. Supported by NIH, Non-U.S. Gov't, and U.S. Gov't (Non-P.H.S.) research grants.

[47] N. Gleichmann, "Which cell culture media is right for you?," *Technology Networks*, 2024. Last updated: January 22, 2024.

[48] M. Arora, "Cell culture media: A review," *Materials and Methods*, vol. 3, p. 175, 2013. Last modified: July 8, 2023; original version: March 5, 2013.

[49] H.-y. Hsu, A. T. Ohta, P.-Y. Chiou, A. Jamshidi, S. L. Neale, and M. C. Wu, "Phototransistor-based optoelectronic tweezers for dynamic cell manipulation in cell culture media," *Lab Chip*, vol. 10, pp. 165–172, 2010.

[50] V. Miralles, A. Huerre, F. Malloggi, and M.-C. Jullien, "A review of heating and temperature control in microfluidic systems: Techniques and applications," *Diagnostics*, vol. 3, pp. 33–67, 2013. Published with the kind authorization of Marie-Caroline Jullien. Correspondence should be addressed to Marie-Caroline Jullien at marie-caroline.jullien@espci.fr; Tel.: +33-1-40-79-51-61; Fax: +33-1-40-79-51-57.

[51] T. Smolinka, "Fuels – hydrogen production — water electrolysis," in *Encyclopedia of Electrochemical Power Sources* (J. Garche, ed.), pp. 394–413, Amsterdam: Elsevier, 2009.

[52] Anon, "The gibbs free energy and cell voltage." `https://chem.libretexts.org/@go/page/41637`, 2020. Accessed November 25, 2024.

[53] M. Albornoz, M. Rivera, P. Wheeler, and R. Ramírez, "High pulsed voltage alkaline electrolysis for water splitting," *Sensors*, vol. 23, no. 8, 2023.

[54] Y.-C. Tsai, Y.-H. Hong, S.-J. Zhang, and J.-N. Kuo, "Frequency-selective electrokinetic manipulation of microparticles in gold nanofilm optically-induced dielectrophoretic device," *Microsystem Technologies*, vol. 26, no. 4, pp. 1213–1222, 2020.

[55] M. Toofan and J. Toofan, "Chapter 5 - a brief review of the cleaning process for electronic device fabrication," in *Developments in Surface Contamination and Cleaning* (R. Kohli and K. Mittal, eds.), pp. 185–212, Oxford: William Andrew Publishing, 2015.

[56] M. Ahmed, A. Bakry, E. Shaaban, and H. Dalir, "Structural, electrical, and optical properties of ito thin films and their influence on performance of cds/cdte thin-film solar cells," *Journal of Materials Science: Materials in Electronics*, vol. 32, pp. 1–12, 04 2021.

[57] E. C. Larkins and J. S. Harris, "2 - molecular beam epitaxy of high-quality gaas and algaas," in *Molecular Beam Epitaxy* (R. F. Farrow, ed.), pp. 114–274, Park Ridge, NJ: William Andrew Publishing, 1995.

[58] A. Alex-Amor, J. Moreno-Núñez, J. M. Fernández-González, P. Padilla, and J. Esteban, "Parasitics impact on the performance of rectifier circuits in sensing rf energy harvesting," *Sensors*, vol. 19, no. 22, 2019.

[59] W. H. H. Jr. and J. A. Buck, *Engineering Electromagnetics*. New York, NY: McGraw-Hill Education, 9th ed., 2019. Late Emeritus Professor Purdue University; Georgia Institute of Technology.

[60] E. B. Rosa and F. W. Grover, *Formulas and Tables for the Calculation of Mutual and Self-Inductance*. Washington, D.C.: Govt. Print. Off., 3rd ed., 1916. Issued Dec. 18, 1916.

[61] Diffen.com, "Parallel circuit vs series circuit." `https://www.diffen.com/difference/Parallel_Circuit_vs_Series_Circuit`, November 2024. Published: 2024-11-19, Accessed: 2024-11-26.

[62] J. Smith and J. Mader, "Ohm's law," 02 2015.

[63] The Editors of Encyclopaedia Britannica, "Young's modulus," *Encyclopedia Britannica*, October 26 2024.

[64] Z. Zhuang, Z. Liu, and Y. Cui, "Chapter 3 - strain gradient plasticity theory at the microscale," in *Dislocation Mechanism-Based Crystal Plasticity* (Z. Zhuang, Z. Liu, and Y. Cui, eds.), pp. 57–90, Academic Press, 2019.

[65] R. Hibbeler, *Mechanics of Materials*. Pearson, 2018.

[66] J. Ruth D, S. Zeba, V. R, R. Laishram, and G. Anand, "Design and development of robots end effector test rig," 01 2021.

[67] S. Zhang, Y. Zhai, R. Peng, M. Shayegannia, A. Flood, J. Qu, X. Liu, N. Kherani, and A. Wheeler, "Assembly of topographical micropatterns with optoelectronic tweezers," *Advanced Optical Materials*, vol. 7, p. 1900669, 08 2019.

[68] U. o. C. Michael Ashby, "About conductivity," 2007. Accessed: 28.08.2024.

[69] I. Education, "A timeline of atomic models," 2019. Accessed: 28.08.2024.

[70] L. Chemistry, "5.20: Noble gas configuration," 2022. Accessed: 28.08.2024.

[71] "Introduction to Bloch's Theorem," apr 4 2024. [Online; accessed 2024-08-30].

[72] D. J. Griffiths and D. F. Schroeter, *Introduction to quantum mechanics*. Cambridge ; New York, NY: Cambridge University Press, third edition ed., 2018.

[73] L. E. ContribMSE5317, "Density of States," sep 8 2021. [Online; accessed 2024-09-05].

[74] T. v. d. S. Anton Akhmerov, "Open solid state notes, the nearly free electron model bloch theorem," 2022. Accessed: 05.09.2024.

[75] BYJU'S, "Fermi energy," 2020. Accessed: 28.08.2024.

[76] E. E. J.M.K.C. Donev et al., "Band gap," 2024. Accessed: 28.08.2024.

[77] W. Abiola Ayodele, "N-type vs p-type: Difference between p-type and n-type semiconductors," 2024. Accessed: 28.08.2024.

[78] P. W. Anderson, "Absence of diffusion in certain random lattices," *Phys. Rev.*, vol. 109, pp. 1492–1505, Mar 1958.

[79] G. Horowitz, "Validity of the concept of band edge in organic semiconductors," *Journal of Applied Physics*, vol. 118, p. 115502, 09 2015.

[80] G. O. Inc., "An overview of the materials used for solar cells," 2018. [Online; accessed 2024-09-09].

[81] T. Belaroussi, D. Rached, W. L. Rahal, and F. Hamdache, "Sensitivity of a hit c-si solar cell to structural distortions of the hydrogenated amorphous silicon constituting the front face of the device," *Journal of Nano- and Electronic Physics*, vol. 12, p. 5023, 10 2020.

[82] H. Li and M. Matsumoto, "Optical response of hydrogenated amorphous silicon: investigation with electronic dynamics simulations," *Applied Physics A*, vol. 128, p. 924, Sep 2022.

[83] T. E. o. E. Britannica, "photoelectric effect," 2024. Accessed: 28.08.2024.

[84] C.B.Honsberg and S.G.Bowden, "photon energy," 2019. Accessed: 29.08.2024.

[85] J. P. Thomas G. Mayerhofer, Susanne Pahlow, "Understanding the limits of the bouguer-beer-lambert law," 2023. [Online; accessed 2024-09-10].

[86] Geocities, "Optical generation rate," 2009. [Online; accessed 2024-09-11].

[87] K. W. Boer and H. Pohl, *Semiconductor Physics*, ch. Photoconductivity, pp. 1182–1204. Cham: Springer, 2nd ed., 2018.

[88] Anon, "Bra-ket notation." `https://chem.libretexts.org/@go/page/1666`, 2023. [Online; accessed 2024-09-12].

[89] TU Graz, "Electrical conductivity of silicon." `https://lampz.tugraz.at/~hadley/psd/L4/conductivity.php`, 2023. Accessed: September 12, 2024.

[90] C. R. Wronski and R. E. Daniel, "Photoconductivity, trapping, and recombination in discharge-produced, hydrogenated amorphous silicon," *Phys. Rev. B*, vol. 23, pp. 794–804, Jan 1981.

[91] S. Galassini, G. Micocci, C. Pennetta, A. Rizzo, A. Tepore, and F. Zuanni, "Photoconductivity and trapping parameters in hydrogenated amorphous silicon films," *Materials Chemistry and Physics*, vol. 9, no. 1, pp. 295–300, 1983. A Special Triple Issue Containing Proceedings of the Joint Meeting of the C.N.R. Fine-Chemicals Finalized Programme and the Italian Association for Crystal Growth.

[92] W. Pickin, "The interpretation of photoconductivity measurements in hydrogenated amorphous silicon," *Solar Cells*, vol. 9, no. 1, pp. 95–111, 1983.

[93] D. E. Carlson and C. R. Wronski, "Amorphous silicon solar cell," *Applied Physics Letters*, vol. 28, pp. 671–673, 06 1976.

[94] Y. Hishikawa, N. Nakamura, S. Tsuda, S. Nakano, Y. Kishi, and Y. Kuwano, "Interference-Free Determination of the Optical Absorption Coefficient and the Optical Gap of Amorphous Silicon Thin Films," *Japanese Journal of Applied Physics*, vol. 30, p. 1008, May 1991.

[95] S. Adachi, *Optical Properties of Crystalline and Amorphous Semiconductors: Materials and Fundamental Principles*. Springer US, 1999.

[96] G. H. Döhler, "Theory of amorphous multilayer structures (superlattices)," *Journal of Non-Crystalline Solids*, vol. 77-78, pp. 1041–1050, 1985. Proceedings of the Eleventh International Conference on Amorphous and Liquid Semiconductors.

[97] M. Hundhausen and L. Ley, "Persistent photoconductivity in doping-modulated amorphous silicon superlattices," *Journal of Non-Crystalline Solids*, vol. 77-78, pp. 1051–1060, 1985. Proceedings of the Eleventh International Conference on Amorphous and Liquid Semiconductors.

[98] D. A. Smets and P. M. Zeman, "Solar energy: Photovoltaic (pv) technologies." `https://ocw.tudelft.nl/courses/solar-energy-photovoltaic-pv-technologies/`, December 2017. Last edited: 2020-03-03. Accessed: 2024-09-19.

[99] S. Choi, G. Park, C. Lee, and J. Jang, "Persistent photoconductivity in hydrogenated amorphous silicon," *Solid State Communications*, vol. 59, pp. 177–181, July 1986. Copyright: Copyright 2014 Elsevier B.V., All rights reserved.

[100] T. Singh, A. Dvivedi, S. S. Sidhu, E. S. Shlykov, K. R. Muratov, and T. R. Ablyaz, "Energy channelization analysis of rough tools developed by rm-mt-edm process during ecsm of glass substrates," *Materials*, vol. 15, no. 16, 2022.

[101] P. Tyagi, T. Goulet, C. Riso, K. Klein, and F. Garcia-Moreno, "Electropolishing of additively manufactured high carbon grade 316 stainless steel," 08 2018.

[102] M. R. Mahadeshwara, "Adhesion: Definition, theory and types." `https://www.tribonet.org/wiki/adhesion-definition-theory-and-types/`, November 21 2022. Accessed: 2024-10-12.

[103] I. Itasca Consulting Group, *Hertz Contact Model*, 2024. Accessed: 2024-10-12.

[104] I. Itasca Consulting Group, *Johnson-Kendall-Roberts (JKR) Contact Model*, 2024. Accessed: 2024-10-12.

[105] A. G. Corp., "3m adhesion basics/surface energy," 2022. Accessed: 2024-10-12.

[106] A. N. K. Lau, A. T. Ohta, H. L. Phan, H.-Y. Hsu, A. Jamshidi, P.-Y. Chiou, and M. C. Wu, "Antifouling coatings for optoelectronic tweezers," *Lab Chip*, vol. 9, pp. 2952–2957, 2009.

[107] C. J. van Oss, "Chapter six - the interfacial tension/free energy of interaction between water and two different condensed-phase entities, i, immersed in water, w," in *The Properties of Water and their Role in Colloidal and Biological Systems* (C. J. van Oss, ed.), vol. 16 of *Interface Science and Technology*, pp. 73–84, Elsevier, 2008.

[108] P. Kingshott and H. J. Griesser, "Surfaces that resist bioadhesion," *Current Opinion in Solid State and Materials Science*, vol. 4, no. 4, pp. 403–412, 1999.

[109] The Editors of Encyclopaedia Britannica, "Hela cell." `https://www.britannica.com/science/HeLa-cell`, August 2024. Accessed: 2024-09-24.

[110] J. Mizele, J. Dandurand, and J. Schott, "Determination of the surface energy of amorphous silica from solubility measurements in micropores," *Surface Science*, vol. 162, no. 1, pp. 830–837, 1985.

[111] N. Janiszewska, J. Raczkowska, A. Budkowski, K. Gajos, Y. Stetsyshyn, M. Michalik, and K. Awsiuk, "Dewetting of polymer films controlled by protein adsorption," *Langmuir : the ACS journal of surfaces and colloids*, vol. 36, 09 2020.

[112] S. Roh, E. Y. Choi, Y. S. Choi, and C. Kim, "Characterization of the surface energies of functionalized multi-walled carbon nanotubes and their interfacial adhesion energies with various polymers," *Polymer*, vol. 55, 03 2014.

[113] H. Pan, Y. Xia, M. Qin, Y. Cao, and W. Wang, "A simple procedure to improve the surface passivation for single molecule fluorescence studies," *Phys. Biol.*, vol. 12, no. 4, p. 045006, 2015. Published June 29, 2015.

[114] G. Li, V. Shrotriya, J. Huang, Y. Yao, T. Moriarty, K. Emery, and Y. Yang, "Li, g., shrotriya, v., huang, j. s., yao, y., moriarty, t., emery, k. yang, y. high-efficiency solution processable polymer photovoltaic cells by self-organization of polymer blends. nat. mater. 4, 864-868," *Nature Materials*, vol. 4, pp. 864–868, 10 2005.

[115] T. Tiedje, C. Wronski, B. Abeles, and J. Cebulka, "Electron transport in hydrogenated amorphous silicon: drift mobility and junction capacitance," *Solar Cells*, vol. 2, no. 3, pp. 301–318, 1980.

[116] W. Wang, Y.-H. Lin, R.-S. Guan, T.-C. Wen, T.-F. Guo, and G.-B. Lee, "Bulk-heterojunction polymers in optically-induced dielectrophoretic devices for the manipulation of microparticles," *Opt. Express*, vol. 17, pp. 17603–17613, Sep 2009.

[117] S. Energy, "How long do solar panels last?," 2024. Accessed: 2024-10-12.

[118] S.-J. Lin, S.-H. Hung, J.-Y. Jeng, T.-F. Guo, and G.-B. Lee, "Manipulation of micro-particles by flexible polymer-based optically-induced dielectrophoretic devices," *Opt. Express*, vol. 20, pp. 583–592, Jan 2012.

[119] S.-M. Yang, T.-M. Yu, H.-P. Huang, M.-Y. Ku, L. Hsu, and C.-H. Liu, "Dynamic manipulation and patterning of microparticles and cells by using tiopc-based optoelectronic dielectrophoresis," *Opt. Lett.*, vol. 35, pp. 1959–1961, Jun 2010.

[120] X. Li, Y. Xiao, S. Wang, and X. Li, "Ultra-photosensitive y-type titanylphthalocyanine nanocrystals: Preparation and photoelectric properties," *Dyes and Pigments*, vol. 125, pp. 44–53, 2016.

[121] S. Electronics, "Transistors - symbols, pins, and construction," 2024. Accessed: 2024-10-12.

[122] A. Bioquest, "What is the size range of mammalian cells?," 2024. Accessed: 2024-10-12.

[123] N. G. R. Center, "Newton's laws of motion," 2024. Accessed: November 4, 2024.

[124] A. Gefter, "Newton's apple: The real story," *New Scientist*, January 2010. Accessed: November 4, 2024.

[125] Encyclopaedia Britannica, T. Editors, "Graviton," July 2024. Accessed: November 4, 2024.

[126] A. Mahmood, "About eureka!," November 2024. Accessed: November 4, 2024.

[127] "Archimedes' Principle and Buoyancy," sep 13 2022. [Online; accessed 2024-11-04].

[128] Encyclopaedia Britannica, The Editors, "Robert brown," June 2024. Accessed: November 4, 2024.

[129] J. Bok and C. Kounelis, "From montmartre to the panthéon: The paris journey of an exceptional physicist," *Europhysics News*, vol. 38, no. 1, pp. 9–13, 2007. About Paul Langevin (1872-1946).

[130] J. Thijssen, *Lecture Notes Statistical Physics, Summer 2022 Course AP3021.* TU Delft, 2022. Course material for AP3021, TU Delft.

[131] J. Valley, A. Jamshidi, A. Ohta, H.-Y. Hsu, and M. Wu, "Operational regimes and physics present in optoelectronic tweezers," *Microelectromechanical Systems, Journal of*, vol. 17, pp. 342 – 350, 05 2008.

[132] S. Bandopadhyay, D. Chaudhuri, and A. M. Jayannavar, "Rotational brownian motion: Trajectory, reversibility and stochastic entropy," *Journal of Statistical Physics*, vol. 168, pp. 549–560, August 2017.

[133] K. Van Canneyt and P. Verdonck, "10.02 - mechanics of biofluids in living body," in *Comprehensive Biomedical Physics* (A. Brahme, ed.), pp. 39–53, Oxford: Elsevier, 2014.

[134] P. J. LaNasa and E. L. Upp, "2 - basic flow measurement laws," in *Fluid Flow Measurement (Third Edition)* (P. J. LaNasa and E. L. Upp, eds.), pp. 19–29, Oxford: Butterworth-Heinemann, third edition ed., 2014.

[135] P. dr. ir. C. R. Kleijn and D. ing. S. Kenjeres, "Continuum physics," 2024. Course Code: AP3032.

[136] M. Ghassemi, M. Kamvar, and R. Steinberger-Wilckens, "Chapter 6 - fundamentals of fluid flow," in *Fundamentals of Heat and Fluid Flow in High Temperature Fuel Cells* (M. Ghassemi, M. Kamvar, and R. Steinberger-Wilckens, eds.), pp. 125–140, Academic Press, 2020.

[137] S. Berg, A. Cense, J. Hofman, and R. Smits, "Two-phase flow in porous media with slip boundary condition," *Transport Porous Media*, vol. 74, pp. 275–292, 09 2008.

[138] Kraaiennest, "Potential flow around a circular cylinder. the cylinder is placed in an incompressible and otherwise uniform flow.." Own work, created with MATLAB., 2008. See: G.K. Batchelor (1967) "An introduction to fluid dynamics", Cambridge Univ. Press, page 424.

[139] G. K. Batchelor, *An Introduction to Fluid Dynamics.* Cambridge: Cambridge University Press, 1967. Fellow of the Royal Society, Professor of Applied Mathematics, University of Cambridge.

[140] F. E. Harris, "Chapter 7 - vector analysis," in *Mathematics for Physical Science and Engineering* (F. E. Harris, ed.), pp. 229–292, Boston: Academic Press, 2014.

[141] R. W. Hanks, "Fluid dynamics (chemical engineering)," in *Encyclopedia of Physical Science and Technology (Third Edition)* (R. A. Meyers, ed.), pp. 45–70, New York: Academic Press, third edition ed., 2003.

[142] J. M. Cimbala, "Drag on spheres," January 2012. Latest revision: 11 January 2012.

[143] M. Zastawny, G. Mallouppas, F. Zhao, and B. van Wachem, "Derivation of drag and lift force and torque coefficients for non-spherical particles in flows," *International Journal of Multiphase Flow*, vol. 39, pp. 227–239, 2012.

[144] A. Pantokratoras, "Lift, drag and torque on a rotating sphere in a stream of non-newtonian power-law fluid," *Rheologica Acta*, vol. 60, pp. 175–186, April 2021.

[145] Anon, "Coulomb's law," 2022. Available at: `https://phys.libretexts.org/@go/page/2537` [Accessed November 18, 2024].

[146] O. Stern, "On the theory of the electrolytic double layer," *Zeitschrift für Elektrochemie*, vol. 30, pp. 508–516, 1924. Published November 19, 1924.

[147] T. Ekinci, "Wallis - zeta potential analyzer: Laser doppler electrophoresis (lde) principle for zeta potential measurements." Available online, 04 2014. Published by Temel Ekinci.

[148] W. Technology, "Zeta potential." Wyatt's line of multi-angle static light scattering products couple to size exclusion chromatography (SEC-MALS), field-flow fractionation (FFF-MALS) and stop-flow composition-gradient systems (CG-MALS)., 2024. Accessed: 2024-11-19.

[149] A. L. Polaczyk, J. E. Amburgey, A. Alansari, J. C. Poler, M. Propato, and V. R. Hill, "Calculation and uncertainty of zeta potentials of microorganisms in a 1:1 electrolyte with a conductivity similar to surface water," *Colloids and Surfaces A: Physicochemical and Engineering Aspects*, vol. 586, p. 124097, 2020.

[150] D. Hanaor, M. Michelazzi, P. Veronesi, C. Leonelli, M. Romagnoli, and C. Sorrell, "Anodic aqueous electrophoretic deposition of titanium dioxide using carboxylic acids as dispersing agents," *Journal of the European Ceramic Society*, vol. 31, no. 6, pp. 1041–1047, 2011.

[151] R. Sander, "Compilation of henry's law constants (version 4.0) for water as solvent," *Atmospheric Chemistry and Physics*, vol. 15, pp. 4399–4981, April 2015. CC Attribution 3.0 License.

[152] M. I. Ltd, "What is the henry equation?." Available online, 2024. Accessed: 2024-11-19.

[153] J. Zhao, B. Chen, C. Gan, S. Huang, H. Xiong, J. Ye, P. Zhang, and L. Feng, "Study of particle equilibrium based on the combination of light-actuated ac electroosmosis and light-actuated dielectrophoresis," *Opt. Express*, vol. 32, pp. 24563–24572, Jul 2024.

[154] P.-Y. Chiou, A. Ohta, A. Jamshidi, H. Y. Hsu, and M. C. Wu, "Light-actuated ac electroosmosis for nanoparticle manipulation," *Journal of Microelectromechanical Systems*, vol. 17, pp. 525–531, 2008.

[155] A. Castellanos, A. Ramos, A. González, N. Green, and H. Morgan, "Electrohydrodynamics and dielectrophoresis in microsystems: Scaling laws," *Journal of Physics D: Applied Physics*, vol. 36, 10 2003.

[156] R. Shah and A. London, "Chapter iii - dimensionless groups and generalized solutions," in *Laminar Flow Forced Convection in Ducts* (R. Shah and A. London, eds.), pp. 37–60, Academic Press, 1978.

[157] N. G. Green, A. Ramos, A. González, A. Castellanos, and H. Morgan, "Electrothermally induced fluid flow on microelectrodes," *Journal of Electrostatics*, vol. 53, no. 2, pp. 71–87, 2001. Selected Papers of the International Workshop on Electrical Condu ction, Convection and Breakdown in Fluids.

[158] Anon, "Perturbation theory expresses the solutions in terms of solved problems." `https://chem.libretexts.org/@go/page/210835`, 2023. Accessed November 20, 2024.

[159] A. Ramos, H. Morgan, N. Green, and A. Castellanos, "Ac electrokinetics: A review of forces in microelectrode structures," *Journal of Physics D-applied Physics - J PHYS-D-APPL PHYS*, vol. 31, pp. 2338–2353, 09 1998.

[160] J. K. Valley, A. Jamshidi, A. T. Ohta, H. Y. Hsu, and M. C. Wu, "Operational regimes and physics present in optoelectronic tweezers," *Journal of Microelectromechanical Systems: A Joint IEEE and ASME Publication on Microstructures, Microactuators, Microsensors, and Microsystems*, vol. 17, no. 2, pp. 342–350, 2008.

[161] A. Salari, M. Navi, T. Lijnse, and C. Dalton, "Ac electrothermal effect in microfluidics: A review," *Micromachines*, vol. 10, no. 11, 2019.

[162] C. Balaji, B. Srinivasan, and S. Gedupudi, "Chapter 6 - natural convection," in *Heat Transfer Engineering* (C. Balaji, B. Srinivasan, and S. Gedupudi, eds.), pp. 173–198, Academic Press, 2021.

[163] R. Nave, "Static friction." `http://hyperphysics.phy-astr.gsu.edu/hbase/frict2.html`, n.d. Accessed: November 20, 2024.

[164] A. Ohta, P.-Y. Chiou, A. Jamshidi, H.-Y. Hsu, J. Valley, S. Neale, and M. Wu, *Optoelectronic Tweezers for the Manipulation of Cells, Microparticles, and Nanoparticles*. 01 2010.

[165] A. J. M. Wollman, R. Nudd, E. G. Hedlund, and M. C. Leake, "From animaculum to single molecules: 300 years of the light microscope," *Open Biology*, vol. 5, no. 4, p. 150019, 2015.

[166] The Editors of Encyclopaedia Britannica, "Refractive index." https://www.britannica.com/science/refractive-index, 2024. Accessed: 20 October 2024.

[167] H. E. Haber, "Fermat's principle and the laws of reflection and refraction." https://scipp.ucsc.edu/~haber/ph5B/fermat09.pdf, 2009. Accessed: 20 October 2024.

[168] The Editors of Encyclopaedia Britannica, "Snell's law." https://www.britannica.com/science/Snells-law, 2024. Accessed: 20 October 2024.

[169] MEETOPTICS, "Optical aberrations: Understanding astigmatism and other aberrations," 2024. Accessed: 20 October 2024.

[170] O. Glasses, "Spherical vs aspherical lenses: What's the difference?," 2024. Accessed: 20 October 2024.

[171] R. Photonics, "Paraxial approximation," 2024. Accessed: 23 October 2024.

[172] I. Thorlabs, "Optics guide," 2024. Accessed: 23 October 2024.

[173] MEETOPTICS, "Aspheric lenses: Understanding their benefits and applications," 2024. Accessed: 20 October 2024.

[174] S. Konijnenberg, A. Adam, and H. Urbach, *Bsc Optics*. 03 2024.

[175] O. G. Lab, "Binocular buying advice," 2024. Accessed: 2024-10-23.

[176] Scientific Imaging International, "Optical resolution of a camera and lens system." Accessed: 2024-10-26.

[177] Vatican Observatory, "Religious scientists: Fr. francesco grimaldi, s.j. (1618-1663), optics of diffraction," 2024. Accessed: 2024-10-26.

[178] LibreTexts Physics, "The huygens principle," 2024. Accessed: 2024-10-26.

[179] H. Lee, "Lecture notes on wave optics: Part ii," Accessed: 2024-10-26. Department of Physics, Duke University.

[180] C. Mack, "Fundamental principles of optical lithography: The science of microfabrication," *Fundamental Principles of Optical Lithography: The Science of Microfabrication*, pp. 1–515, 11 2007.

[181] M. Born and E. Wolf, *Principles of Optics: Electromagnetic Theory of Propagation, Interference and Diffraction of Light*. Cambridge, UK: Cambridge University Press, 7th expanded edition ed., 2002.

[182] The Editors of Encyclopaedia Britannica, "Airy disk," 2024. Accessed: 2024-10-26.

[183] The Editors of Encyclopaedia Britannica, "John william strutt, 3rd baron rayleigh," 2024. Accessed: 2024-10-26.

[184] R. Nave, "Rayleigh criterion," n.d. Accessed: 2024-10-26.

[185] I. Gris Sánchez, D. Ras, and T. Birks, "The airy fiber: an optical fiber that guides light diffracted by a circular aperture," *Optica*, vol. 3, 03 2016.

[186] P. Bankhead, "Spatial formation in fluorescence imaging," 2022–2024. Accessed: 2024-10-26.

[187] I. Young, R. Zagers, L. Van Vliet, J. Mullikin, F. Boddeke, and H. Netten, "Depth-of-focus in microscopy," *8th Scandinavian Conference on Image Analysis, Tromso, Norway*, 01 1993.

[188] A. Anvari, A. Azimi Yancheshme, K. M. Kekre, and A. Ronen, "State-of-the-art methods for overcoming temperature polarization in membrane distillation process: A review," *Journal of Membrane Science*, vol. 616, p. 118413, 2020.

[189] U.S. Department of Energy, "History of the light bulb," 2013. Accessed: 2024-10-23.

[190] HowStuffWorks.com, "How does a halogen light bulb work?," April 1 2000. Accessed: 30 October 2024.

[191] Energy Saving Lighting, "The history of led lighting." https://www.energysavinglighting.org/the-history-of-led-lighting/, 2024. Accessed: 30 October 2024.

[192] The Editors of Encyclopaedia Britannica, "LED." https://www.britannica.com/technology/LED, 2024. Encyclopedia Britannica, 25 Oct. 2024. Accessed 30 October 2024.

[193] D. Feezell and S. Nakamura, "Invention, development, and status of the blue light-emitting diode, the enabler of solid-state lighting," *Comptes Rendus Physique*, vol. 19, no. 3, pp. 113–133, 2018. LEDs: The new revolution in lighting / Les LED : la nouvelle révolution de l'éclairage.

[194] Thorlabs, "Two collimation methods for leds," 2024. Accessed 30 October 2024.

[195] Lawrence Livermore National Laboratory, "How lasers work," n.d. Accessed: 31 October 2024.

[196] M. Renz, "Fluorescence microscopy—a historical and technical perspective," *Cytometry Part A*, vol. 83, no. 9, pp. 767–779, 2013.

[197] LibreTexts, "Jablonski diagram," 2023. Accessed: 31 October 2024.

[198] Edinburgh Instruments, "What is the stokes shift?," 2024. Accessed: 31 October 2024.

[199] D. Kromm, *Pushing Light-Sheet Microscopy to Greater Depths*. PhD thesis, Ruperto Carola University Heidelberg, Heidelberg, Germany, Dec. 2021. Dissertation submitted to the Combined Faculty of Natural Sciences and Mathematics of the Ruperto Carola University Heidelberg, for the degree of Doctor of Natural Sciences. Oral examination: 17 December 2021.

[200] Ocean Optics Web Book, "Theory of Fluorescence and Phosphorescence," 2024. Accessed: 31 October 2024.

[201] J. Lichtman and J. Conchello, "Fluorescence microscopy," *Nature methods*, vol. 2, pp. 910–9, 01 2006.

[202] C. Thiel, S. Tauber, C. Seebacher, M. Schropp, R. Uhl, B. Lauber, J. Polzer, S. Neelam, Y. Zhang, and O. Ullrich, "Real-time 3d high-resolution microscopy of human cells on the international space station," *International Journal of Molecular Sciences*, vol. 20, p. 2033, 04 2019.

[203] Z. Wang, W. Yang, Y. Qin, W. Liang, H. Yu, and L. Liu, "Digital micro-mirror device -based light curing technology and its biological applications," *Optics Laser Technology*, vol. 143, p. 107344, 2021.

[204] "How does a dlp projector work?," 2024. ProjectorScreen.com.

[205] Texas Instruments, *DLP® Display Technology: Introduction to Digital Micromirror Device (DMD) Technology*, 2024. Application Report, Document Number: DLPA008B.

[206] S. Popoff, "How to optimize fluorescence imaging with wavefront shaping," 2016. Created by Sébastien Popoff on 17 October 2016. Accessed: 31 October 2024.

[207] S. Love and D. Graff, "Full-frame programmable spectral filters based on micromirror arrays," *Journal of Micro/ Nanolithography, MEMS, and MOEMS*, vol. 13, p. 011108, 01 2014.

[208] Texas Instruments, "DLP® Display System Optical Engine Reference Design," Tech. Rep. DLPA083B, Texas Instruments, 2017. Accessed: 31 October 2024.

[209] R. van Elk, "Designing a microscope for an optoelectronic tweezer to trap polystyrene beads," July 2024. Project Supervisor: C.S. Smith, Project Report, Student ID: 5617103.

[210] Capture Team, "The timeline of evolution of the camera from the 1600s to 21st century," May 2023. Accessed: 31 October 2024.

[211] J. Meyer and A. Summersby, "Image sensors explained," 2024. Accessed: 2024-10-31.

[212] H. Austerlitz, "Chapter 4 - analog/digital conversions," in *Data Acquisition Techniques Using PCs (Second Edition)* (H. Austerlitz, ed.), pp. 51–77, San Diego: Academic Press, second edition ed., 2003.

[213] Princeton Plasma Physics Laboratory, "About plasmas and fusion." https://www.pppl.gov/about/about-plasmas-and-fusion. Accessed: 2024-12-23.

[214] B. Chen, F. Tay, and C. Iliescu, "Development of thick film pecvd amorphous silicon with low stress for mems applications," *Proceedings of SPIE - The International Society for Optical Engineering*, vol. 7269, 12 2008.

[215] D. A. Smets and P. M. Zeman, "Solar energy: Photovoltaic (pv) technologies, pecvd." https://ocw.tudelft.nl/courses/solar-energy-photovoltaic-pv-technologies/, December 2017. Course info: Study load 121 hrs, Bachelor program, Licensed under a Creative Commons Attribution-NonCommercial-ShareAlike 4.0 International License. Last edited: 2020-03-03.

[216] Thermo Fisher Scientific, "Microspheres." https://www.thermofisher.com/search/browse/category/us/en/90220126, December 2024. Accessed: 2024-12-23.

[217] J. R. Stair, "Introduction to the nanoscribe." https://dozuki.umd.edu/Guide/Introduction+to+the+Nanoscribe/385#:~:text=The%20Nanoscribe%20uses%20a%20form,used%20to%20precisely%20deliver%20photons., November 2020. Accessed: 2024-12-23.

[218] Nanoscribe GmbH, "3d printing by 2gl®: Two-photon grayscale lithography now in 3d." https://www.nanoscribe.com/en/microfabrication-technologies/3d-printing-by-2gl/, n.d. Accessed: 2024-12-23.

[219] P. Lippens and U. Muehlfeld, *Indium Tin Oxide (ITO): Sputter Deposition Processes*, pp. 779–794. Berlin, Heidelberg: Springer Berlin Heidelberg, 2012.

[220] F. Scientific, "Syringe pumps." https://www.fishersci.nl/nl/en/browse/90123018/syringe-pumps, 2024. Accessed: 2024-12-23.

[221] P. Inc., "Piezoelectric pump." https://www.piezodata.com/piezoelectric-pump-3/, 2018. Accessed: 2024-12-23.

[222] C. Bendkowski, L. Mennillo, T. Xu, M. Elsayed, F. Stojic, H. Edwards, S. Zhang, C. Morshead, V. Pawar, A. R. Wheeler, D. Stoyanov, and M. Shaw, "Autonomous object harvesting using synchronized optoelectronic microrobots," 2021.

[223] M. Bentahar, A. Di Bella, C. Mechri, S. Montrésor, M. Scalerandi, and X. Yu, "Exploiting slow dynamics effects for damage detection in concrete," *Frontiers in Built Environment*, vol. 6, 06 2020.

A

Upper ITO Glass overhang simulation results

A.1 COMSOL plots

A.1.1 Electric field in OET illuminated state

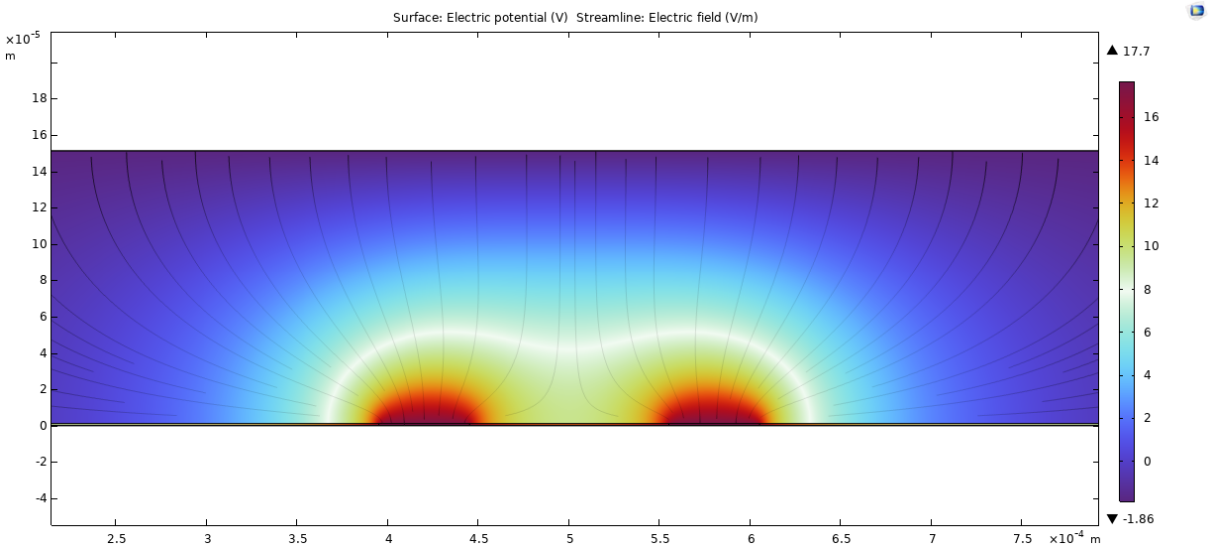

Figure 96: A COMSOL simulation of the electrical field in the OET chip due to two illuminated spots with $\frac{d_{max}}{330}$ overhang in the top ITO glass.

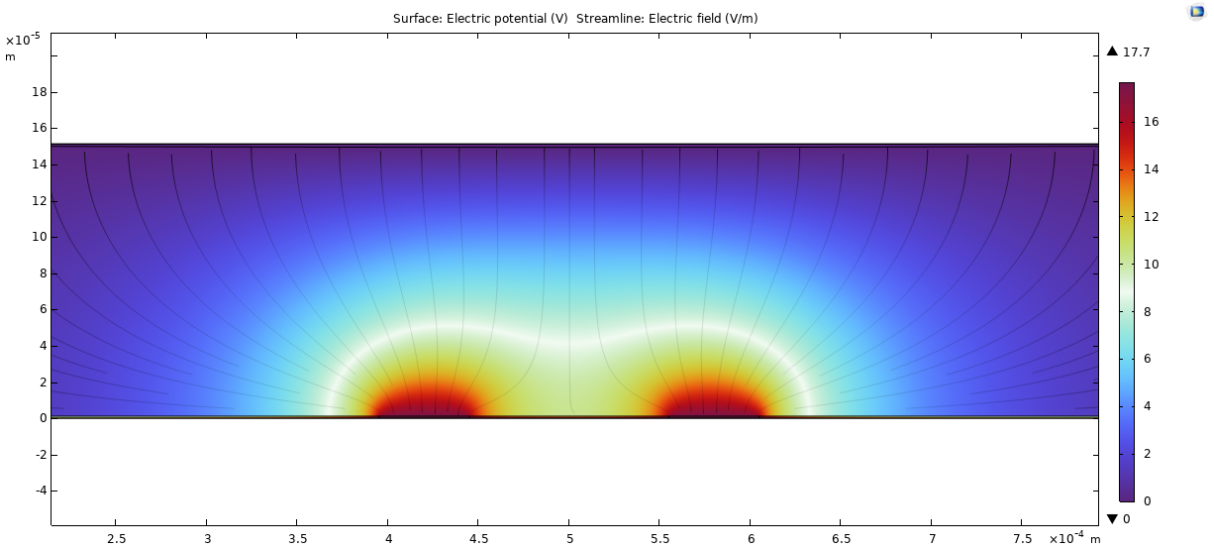

Figure 97: A COMSOL simulation of the electrical field in the OET chip due to two illuminated spots with $\frac{d_{max}}{4}$ overhang in the top ITO glass.

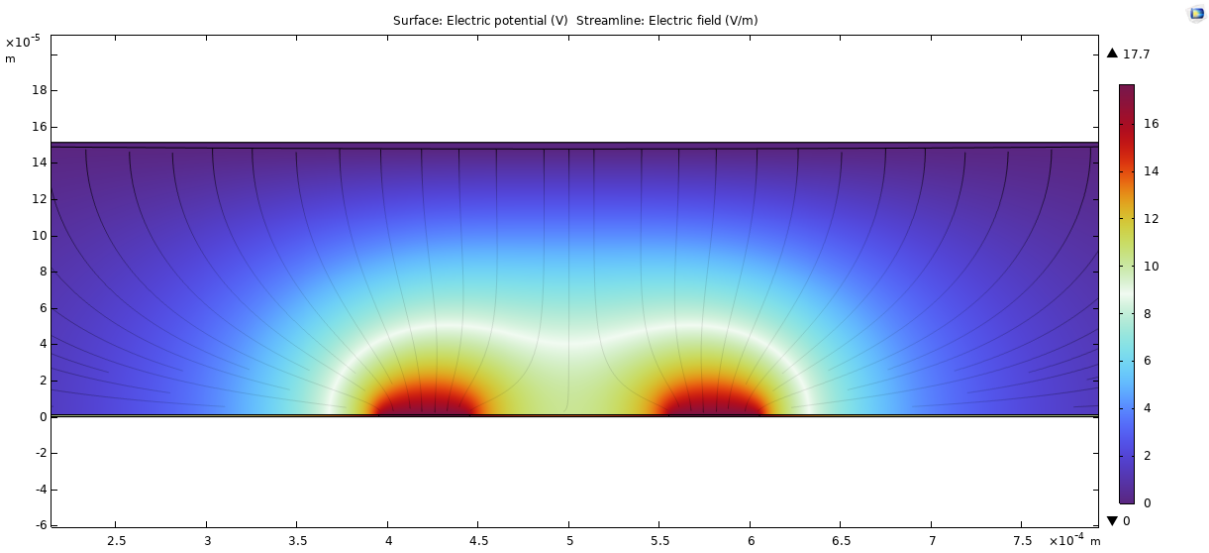

Figure 98: A COMSOL simulation of the electrical field in the OET chip due to two illuminated spots with $\frac{d_{max}}{2}$ overhang in the top ITO glass.

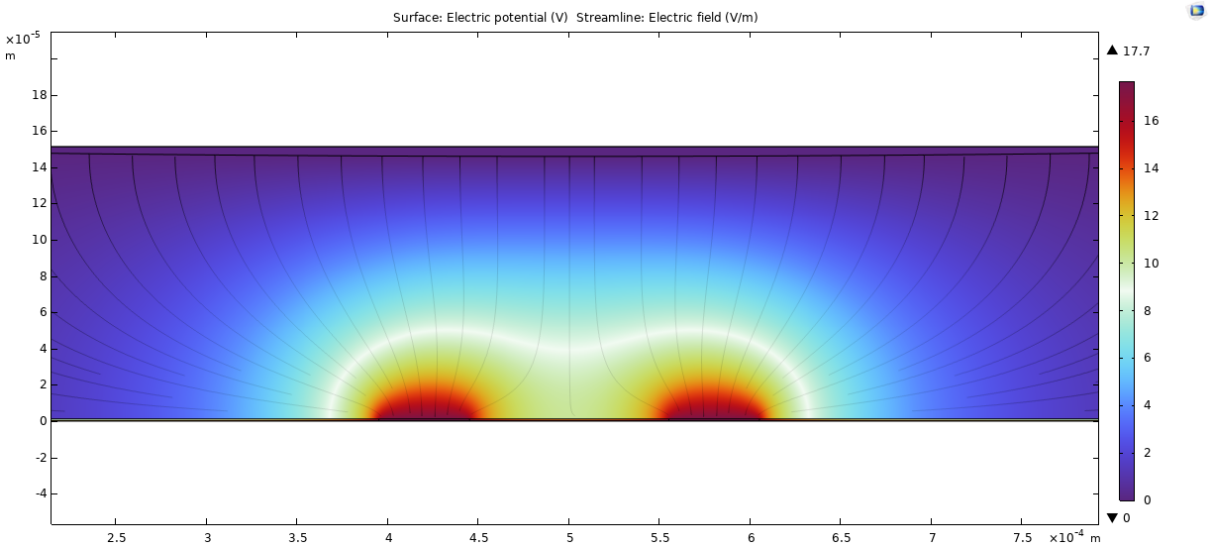

Figure 99: A COMSOL simulation of the electrical field in the OET chip due to two illuminated spots with $\frac{3d_{max}}{4}$ overhang in the top ITO glass.

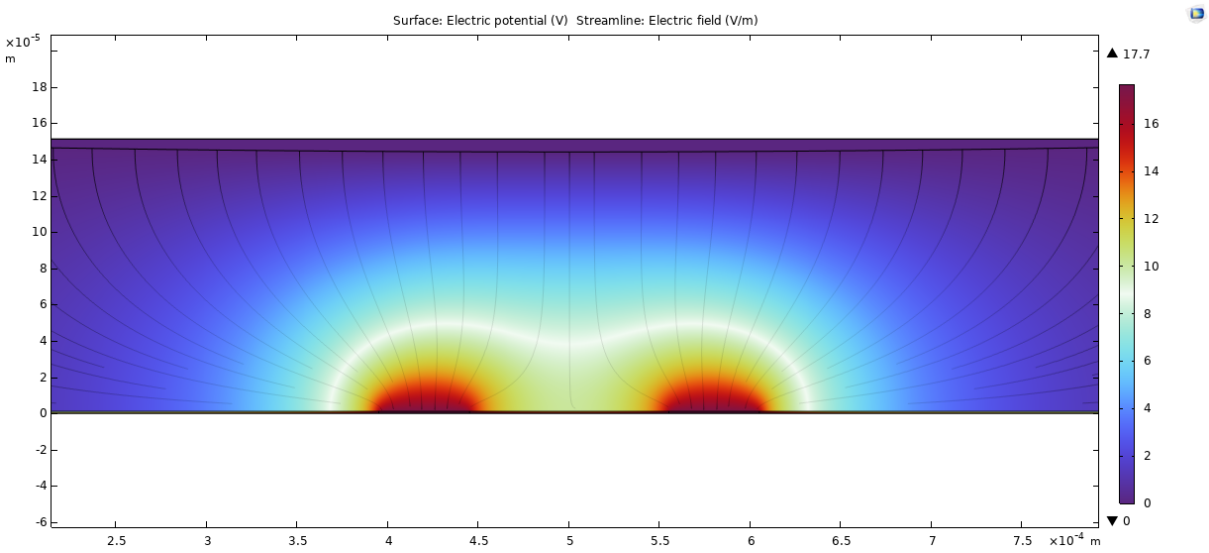

Figure 100: A COMSOL simulation of the electrical field in the OET chip due to two illuminated spots with d_{max} overhang in the top ITO glass.

A.1.2 The gradient of the square of the norm of the electric field in OET illuminated state

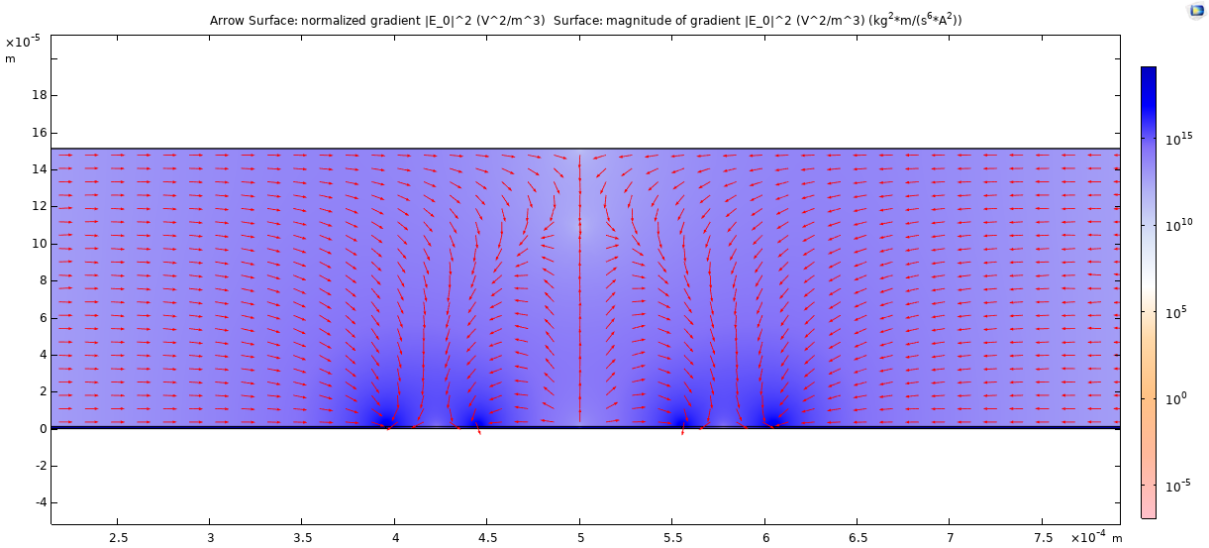

Figure 101: A COMSOL simulation of $\nabla|\mathbf{E}|^2$ in the OET chip due to two illuminated spots with $\frac{d_{max}}{330}$ overhang in the top ITO glass.

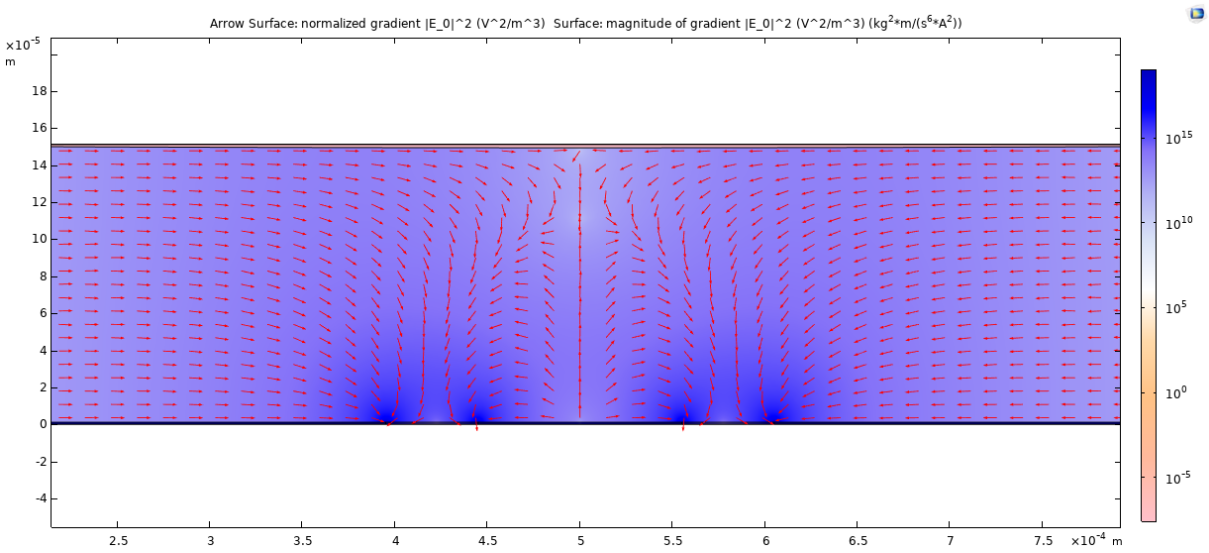

Figure 102: A COMSOL simulation of $\nabla|\mathbf{E}|^2$ in the OET chip due to two illuminated spots with $\frac{d_{max}}{4}$ overhang in the top ITO glass.

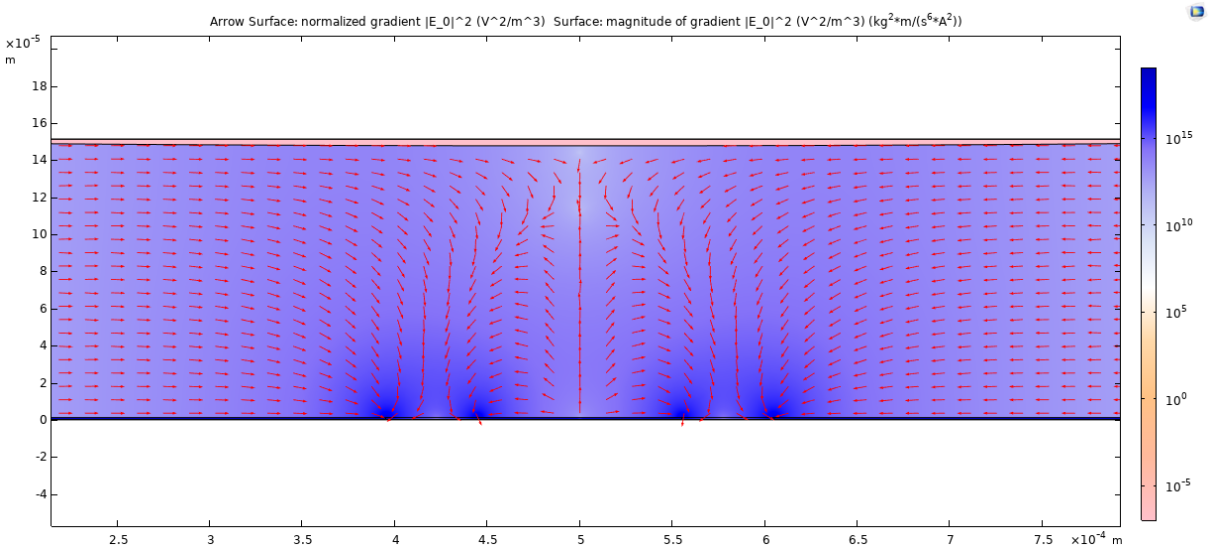

Figure 103: A COMSOL simulation of $\nabla|\mathbf{E}|^2$ in the OET chip due to two illuminated spots with $\frac{d_{max}}{2}$ overhang in the top ITO glass.

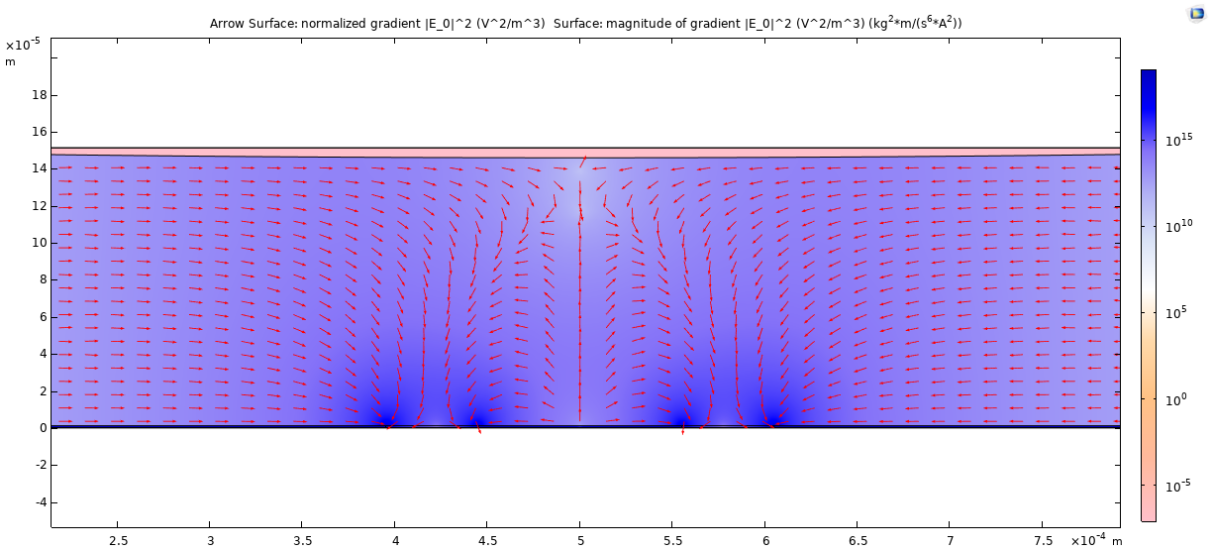

Figure 104: A COMSOL simulation of $\nabla|\mathbf{E}|^2$ in the OET chip due to two illuminated spots with $\frac{3d_{max}}{4}$ overhang in the top ITO glass.

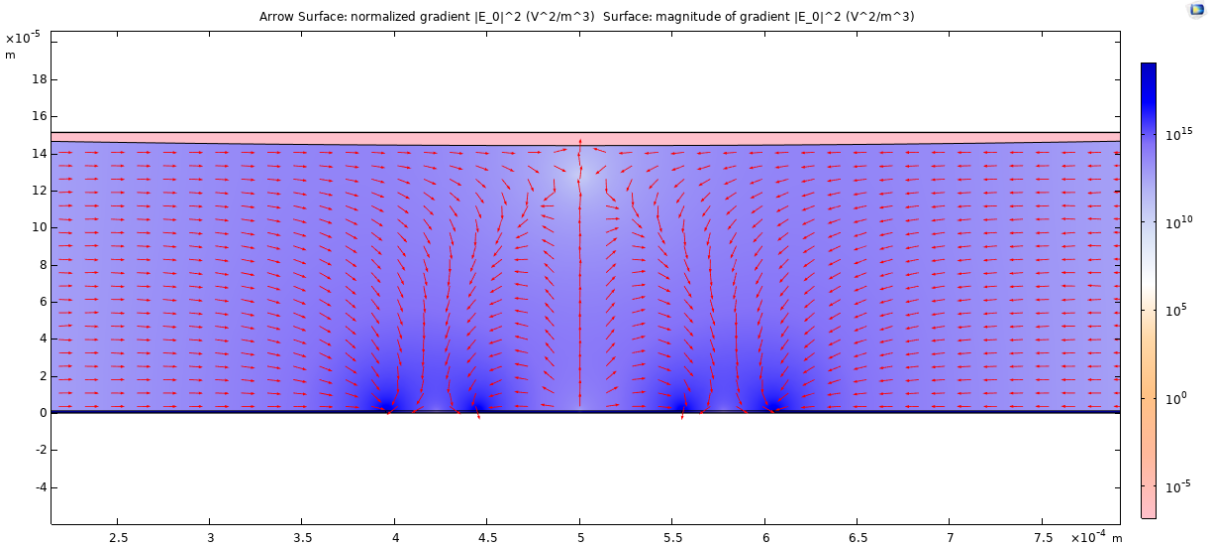

Figure 105: A COMSOL simulation of $\nabla|\mathbf{E}|^2$ in the OET chip due to two illuminated spots with d_{max} overhang in the top ITO glass.

A.1.3 Electric field in OET off state

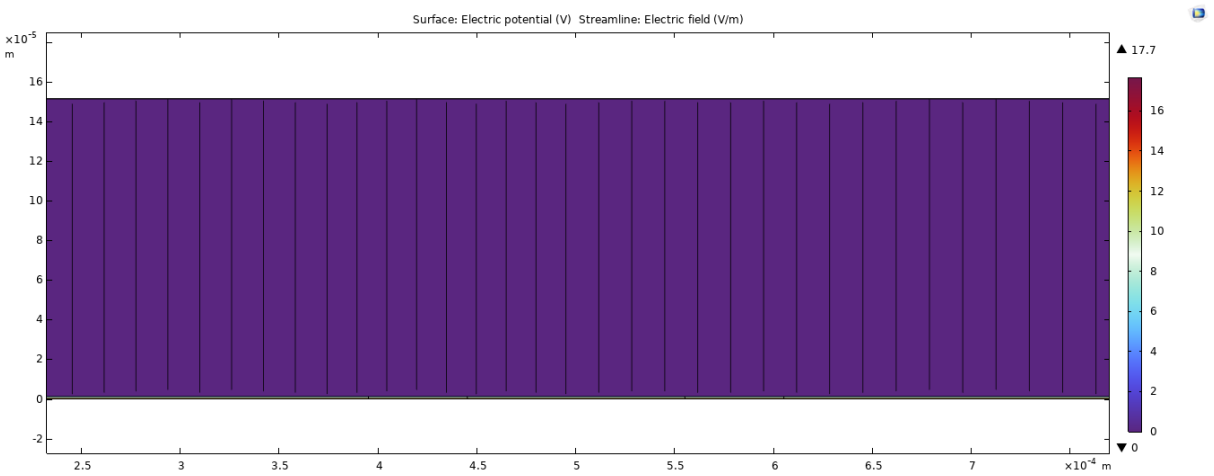

Figure 106: A COMSOL simulation of the electrical field in the OET chip without illumination with $\frac{d_{max}}{330}$ overhang in the top ITO glass.

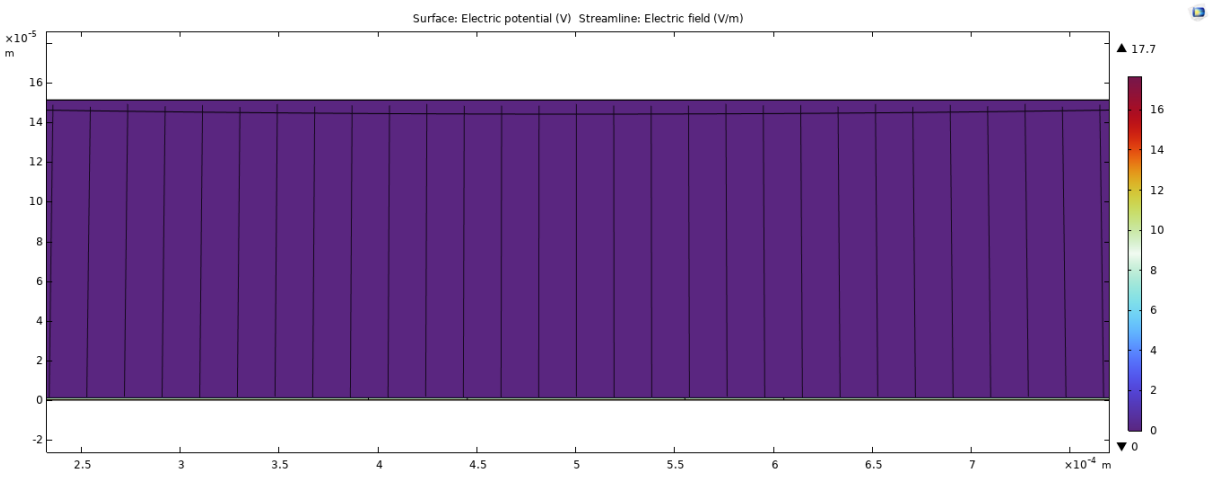

Figure 107: A COMSOL simulation of the electrical field in the OET chip without illumination with d_{max} overhang in the top ITO glass.

A.1.4 The gradient of the square of the norm of the electric field in OET off state

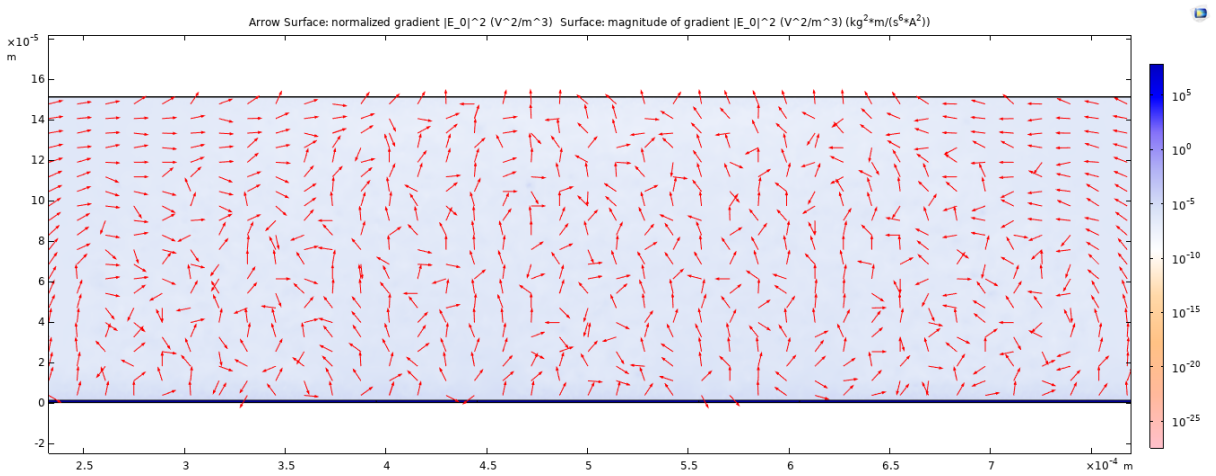

Figure 108: A COMSOL simulation of $\nabla|\mathbf{E}|^2$ in the OET chip without illumination with $\frac{d_{max}}{330}$ overhang in the top ITO glass.

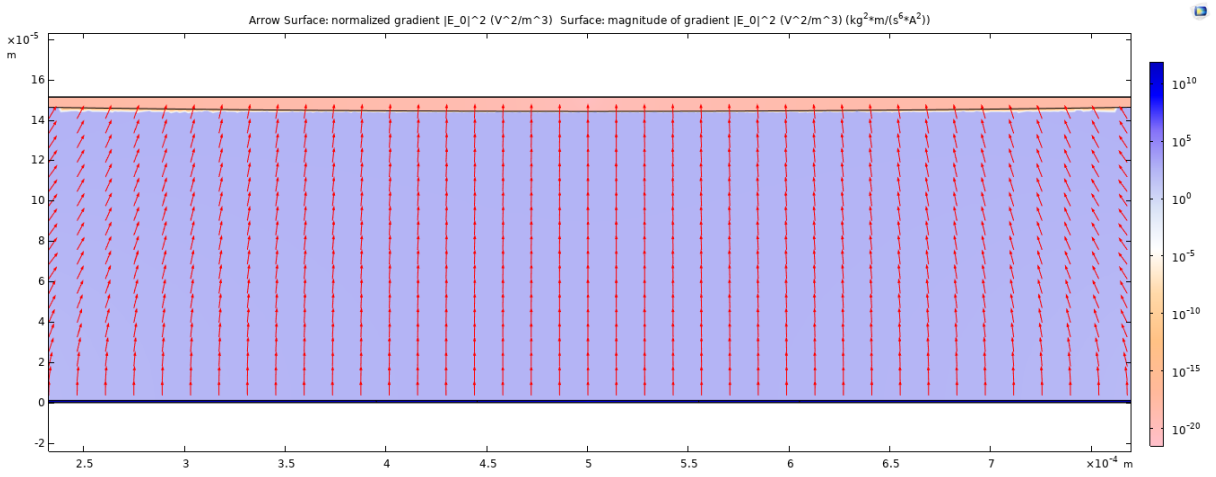

Figure 109: A COMSOL simulation of $\nabla|\mathbf{E}|^2$ in the OET chip without illumination with d_{max} overhang in the top ITO glass.

A.2 MATLAB plots

A.2.1 Electric field in OET illuminated state

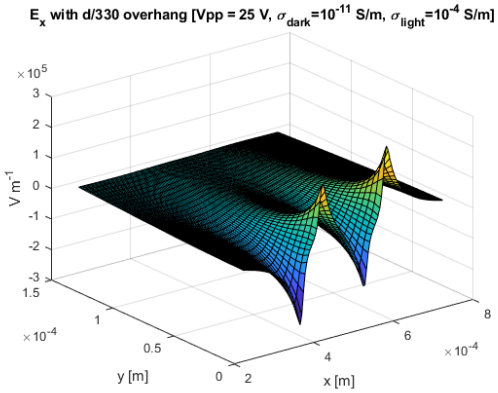

The electrical field strength in x direction

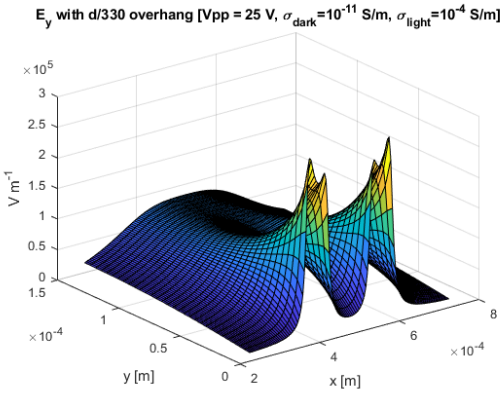

The electrical field strength in y direction

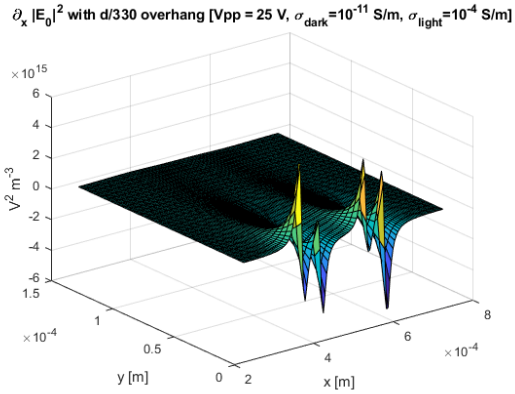

The partial derivative of $|\mathbf{E}|^2$ in x direction

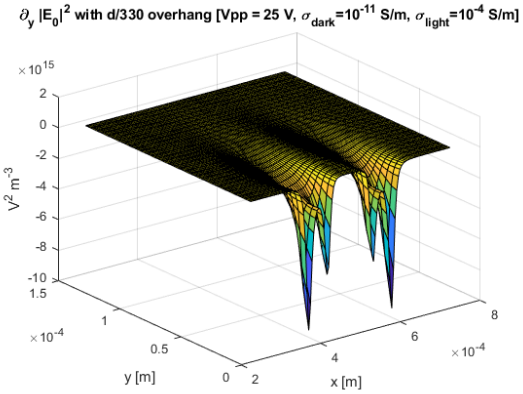

The partial derivative of $|\mathbf{E}|^2$ in y direction

Figure 110: The MATLAB plots of the electrical field using simulated data from COMSOL with $\frac{d_{max}}{330}$ overhang in the top ITO glass.

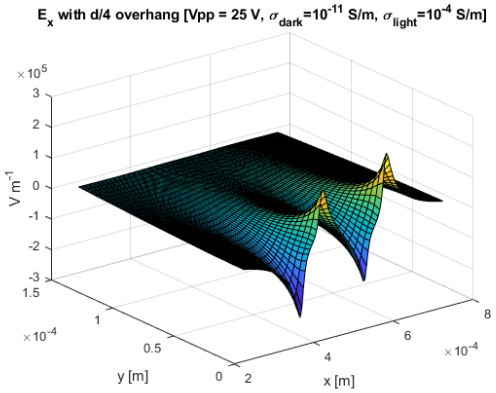

The electrical field strength in x direction

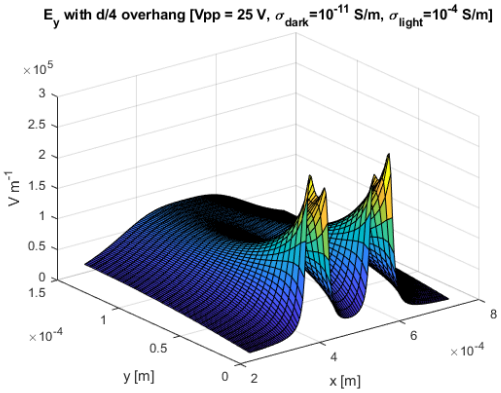

The electrical field strength in y direction

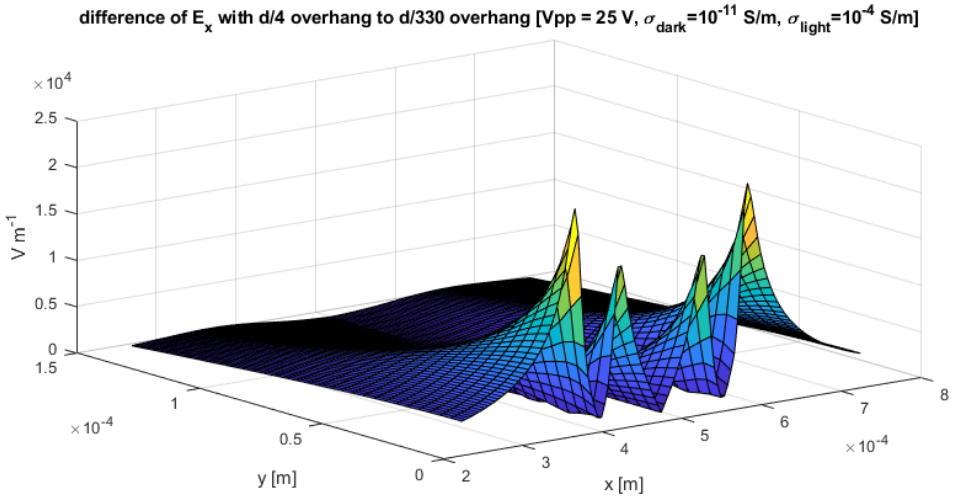

The difference in electrical field strength in x direction between the simulation with $\frac{d_{max}}{4}$ overhang and with $\frac{d_{max}}{330}$ overhang.

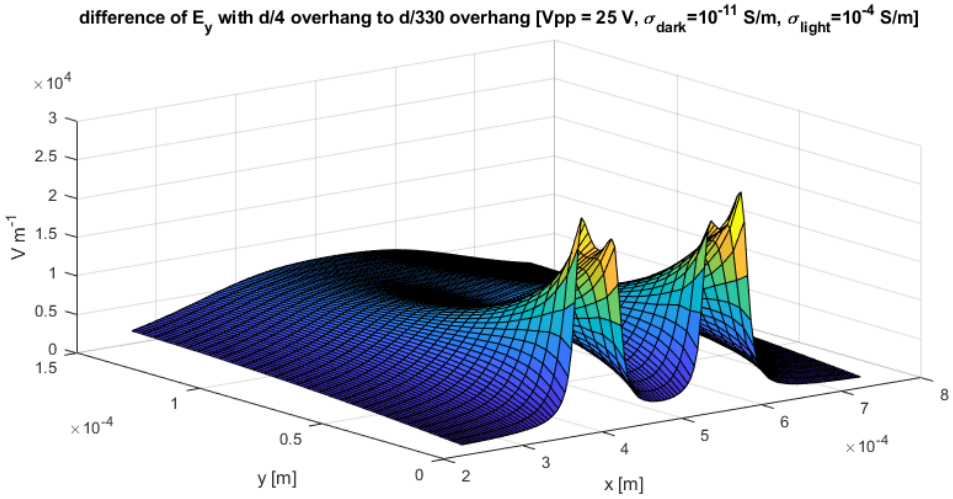

The difference in electrical field strength in y direction between the simulation with $\frac{d_{max}}{4}$ overhang and with $\frac{d_{max}}{330}$ overhang.

Figure 111: The MATLAB plots of the electrical field using simulated data from COMSOL with $\frac{d_{max}}{4}$ overhang in the top ITO glass.

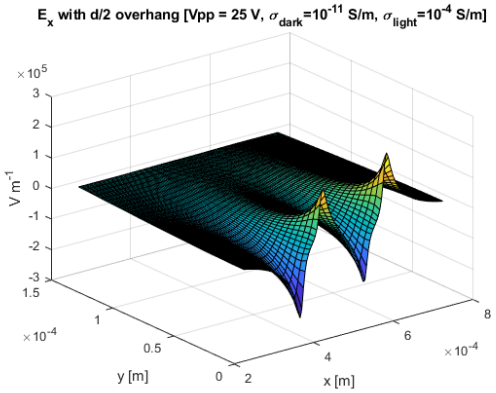

The electrical field strength in x direction

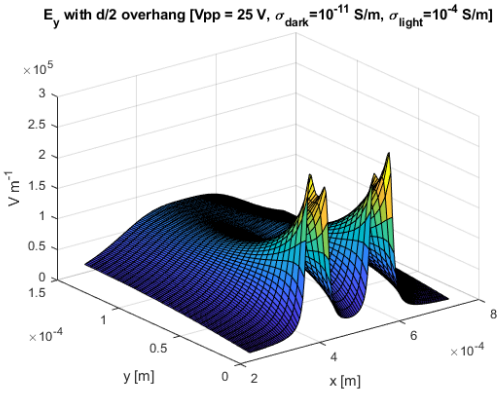

The electrical field strength in y direction

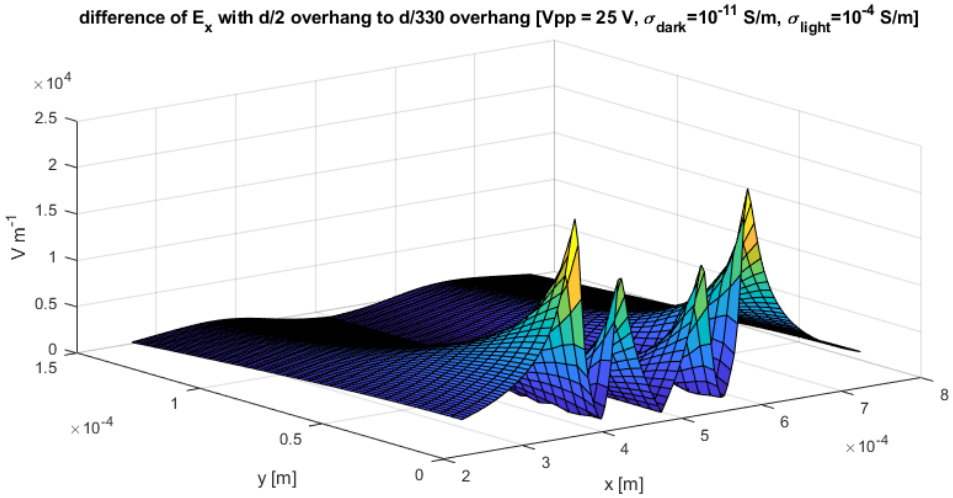

The difference in electrical field strength in x direction between the simulation with $\frac{d_{max}}{2}$ overhang and with $\frac{d_{max}}{330}$ overhang.

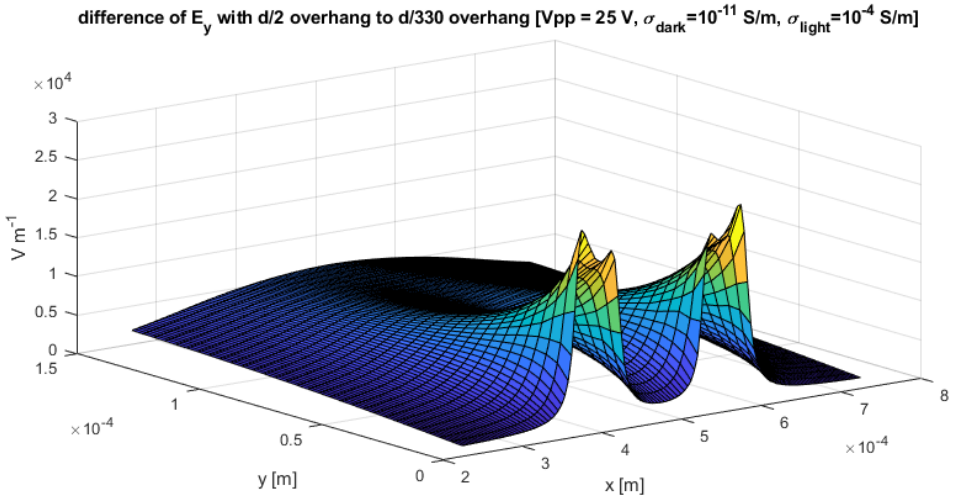

The difference in electrical field strength in y direction between the simulation with $\frac{d_{max}}{2}$ overhang and with $\frac{d_{max}}{330}$ overhang.

Figure 112: The MATLAB plots of the electrical field using simulated data from COMSOL with $\frac{d_{max}}{2}$ overhang in the top ITO glass.

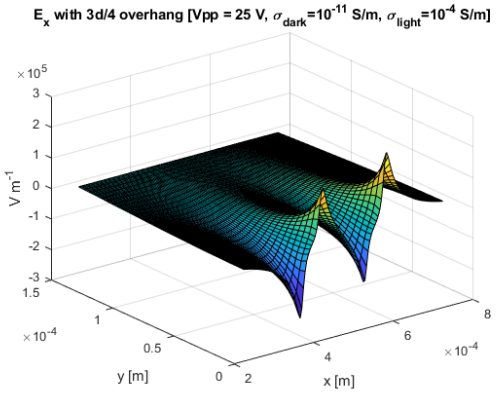

The electrical field strength in x direction

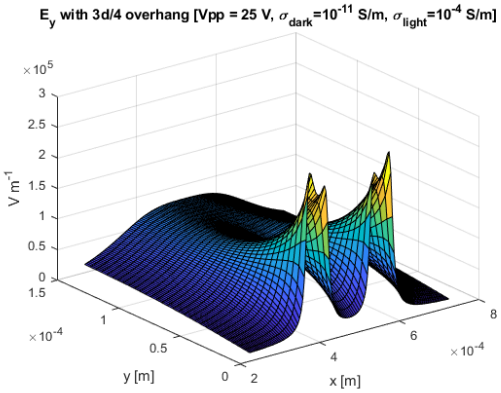

The electrical field strength in y direction

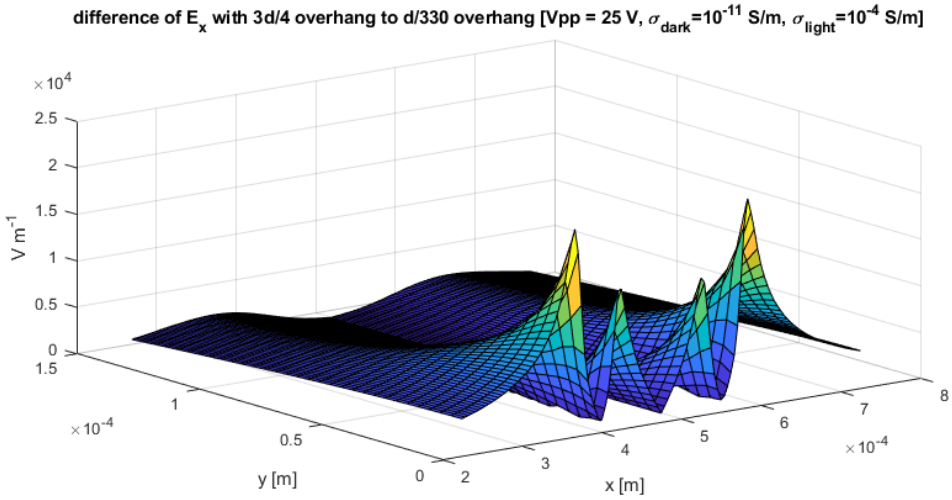

The difference in electrical field strength in x direction between the simulation with $\frac{3d_{max}}{4}$ overhang and with $\frac{d_{max}}{330}$ overhang.

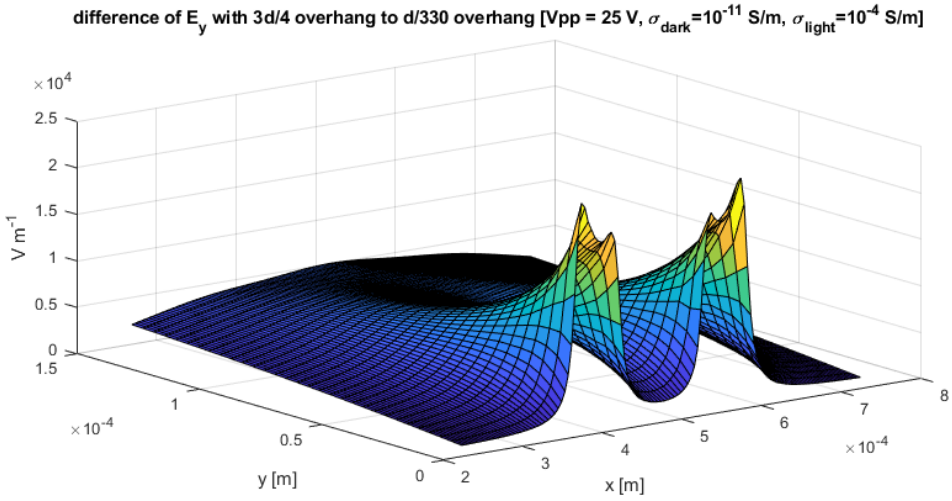

The difference in electrical field strength in y direction between the simulation with $\frac{3d_{max}}{4}$ overhang and with $\frac{d_{max}}{330}$ overhang.

Figure 113: The MATLAB plots of the electrical field using simulated data from COMSOL with $\frac{3d_{max}}{4}$ overhang in the top ITO glass.

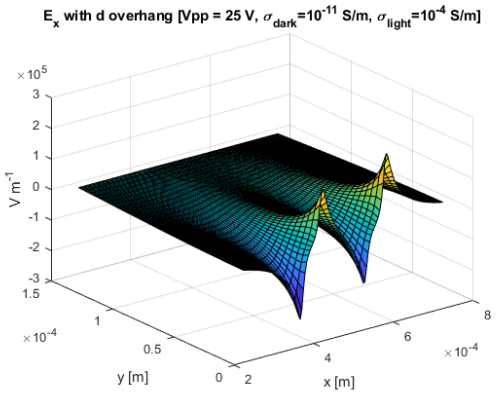

The electrical field strength in x direction

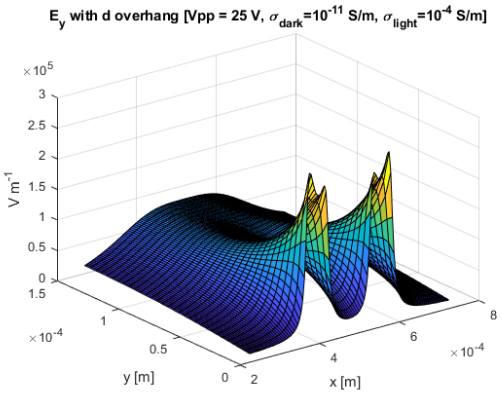

The electrical field strength in y direction

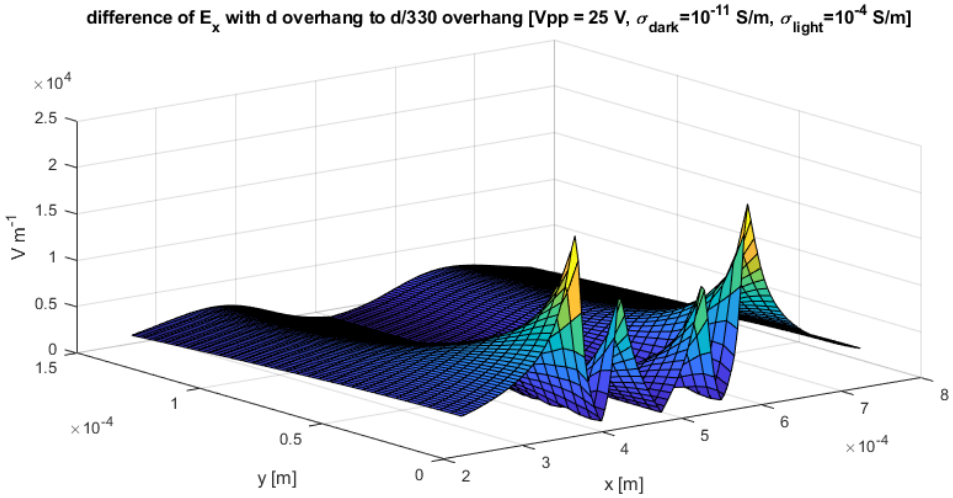

The difference in electrical field strength in x direction between the simulation with d_{max} overhang and with $\frac{d_{max}}{330}$ overhang.

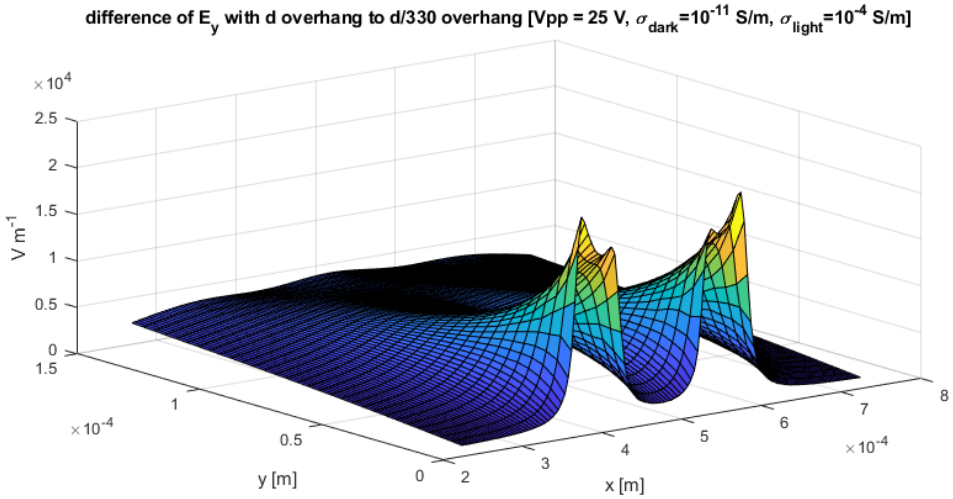

The difference in electrical field strength in y direction between the simulation with d_{max} overhang and with $\frac{d_{max}}{330}$ overhang.

Figure 114: The MATLAB plots of the electrical field using simulated data from COMSOL with d_{max} overhang in the top ITO glass.

A.2.2 The gradient of the square of the norm of the electric field in OET illuminated state

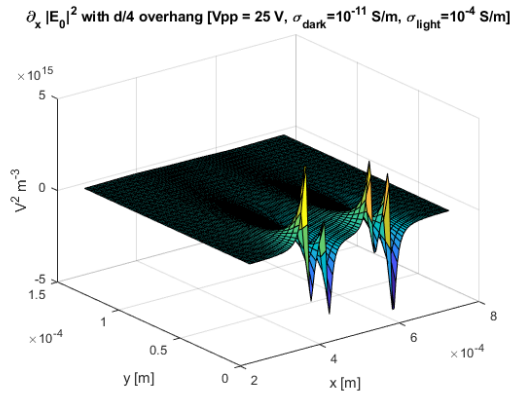

The partial derivative in x direction of $|\mathbf{E}|^2$

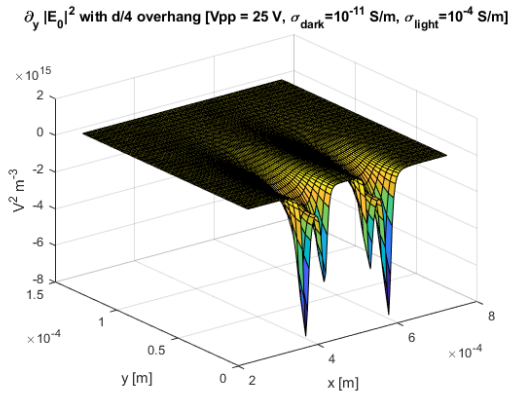

The partial derivative in y direction of $|\mathbf{E}|^2$

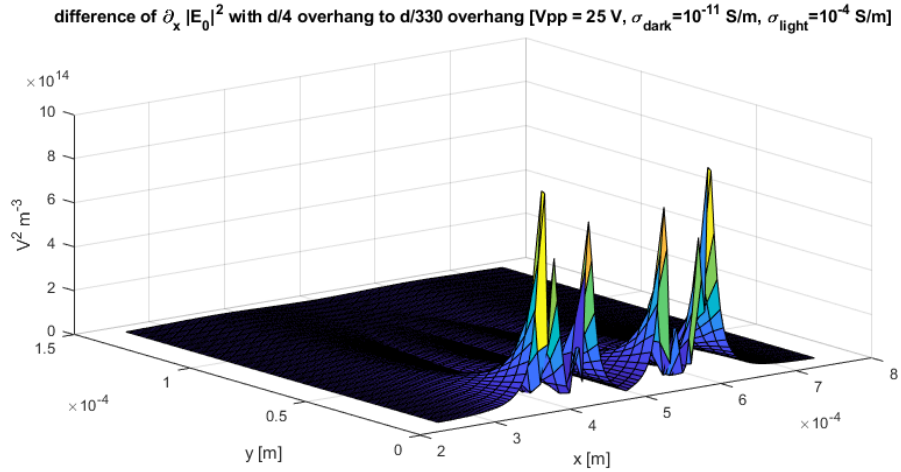

The difference in the partial derivative in x direction of $|\mathbf{E}|^2$ between the simulation with $\frac{d_{max}}{4}$ overhang and with $\frac{d_{max}}{330}$ overhang.

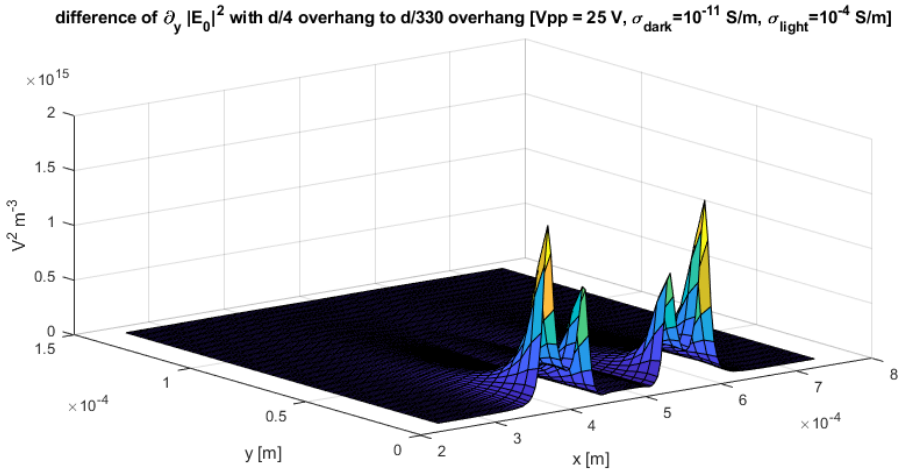

The difference in the partial derivative in y direction of $|\mathbf{E}|^2$ between the simulation with $\frac{d_{max}}{4}$ overhang and with $\frac{d_{max}}{330}$ overhang.

Figure 115: The MATLAB plots of $\nabla|\mathbf{E}|^2$ with illumination and with $\frac{d_{max}}{4}$ overhang in the top ITO glass.

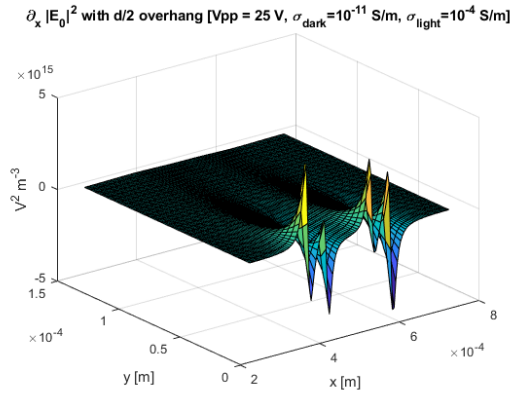

The partial derivative in x direction of $|\mathbf{E}|^2$

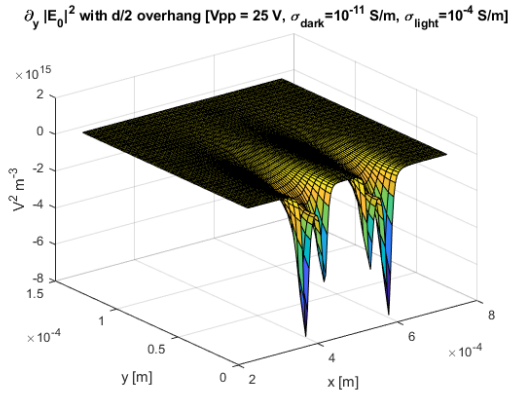

The partial derivative in y direction of $|\mathbf{E}|^2$

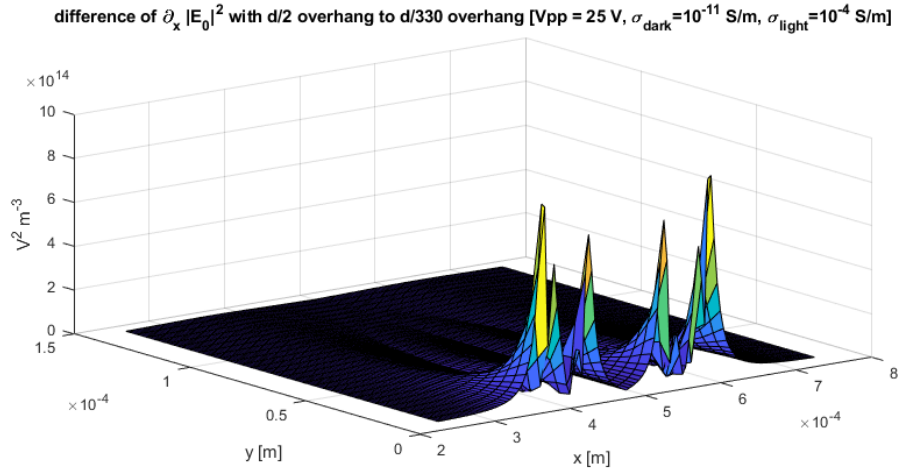

The difference in the partial derivative in x direction of $|\mathbf{E}|^2$ between the simulation with $\frac{d_{max}}{2}$ overhang and with $\frac{d_{max}}{330}$ overhang.

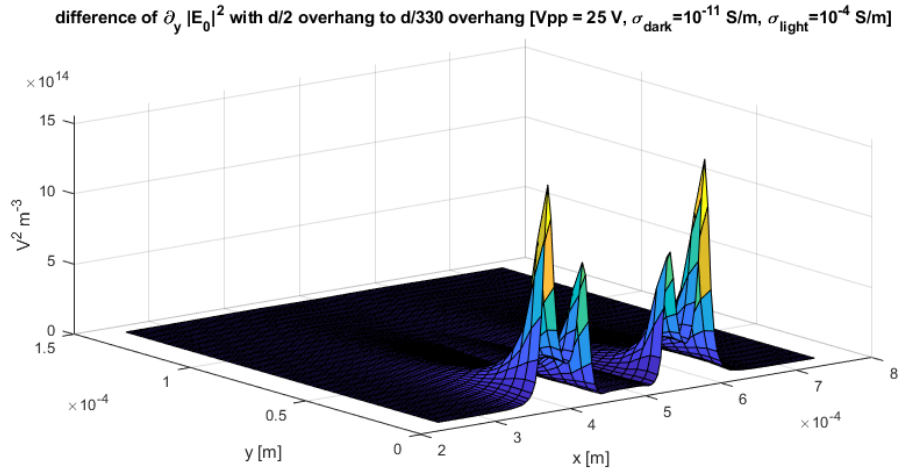

The difference in the partial derivative in y direction of $|\mathbf{E}|^2$ between the simulation with $\frac{d_{max}}{2}$ overhang and with $\frac{d_{max}}{330}$ overhang.

Figure 116: The MATLAB plots of $\nabla|\mathbf{E}|^2$ with illumination and with $\frac{d_{max}}{2}$ overhang in the top ITO glass.

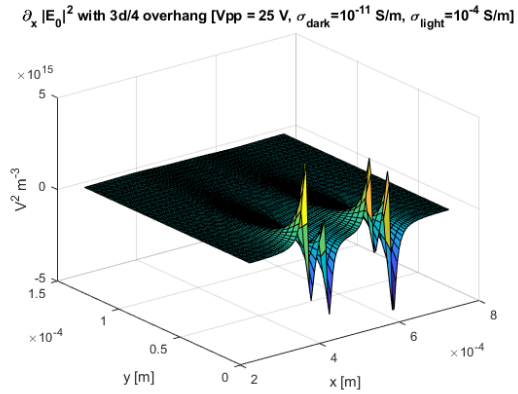

The partial derivative in x direction of $|\mathbf{E}|^2$

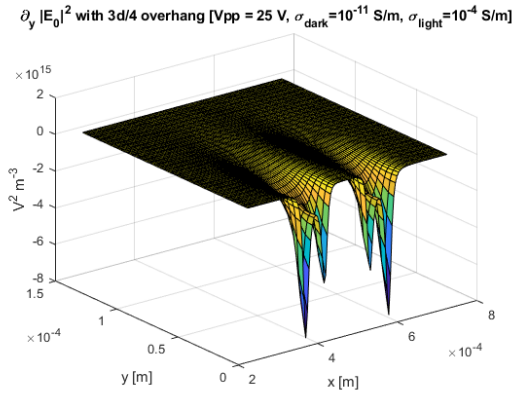

The partial derivative in y direction of $|\mathbf{E}|^2$

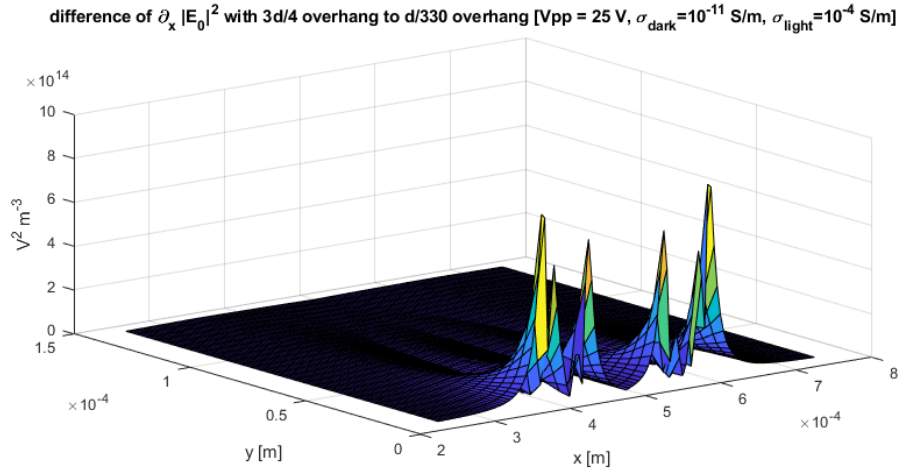

The difference in the partial derivative in x direction of $|\mathbf{E}|^2$ between the simulation with $\frac{3d_{max}}{4}$ overhang and with $\frac{d_{max}}{330}$ overhang.

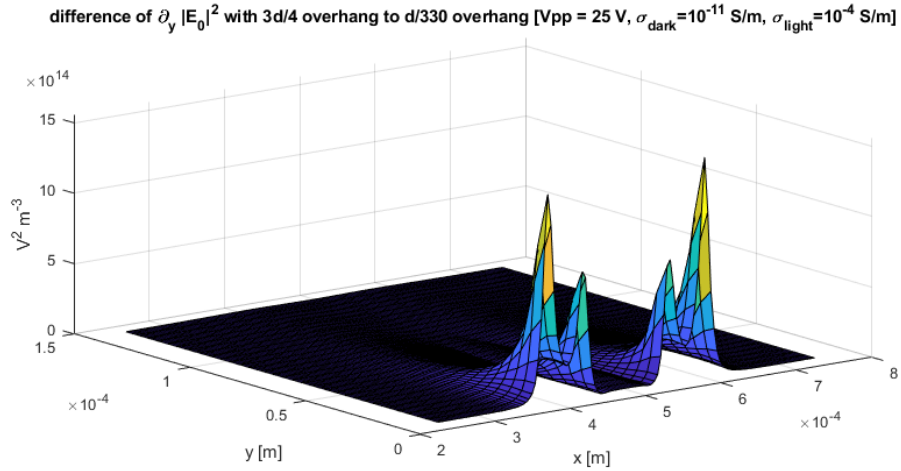

The difference in the partial derivative in y direction of $|\mathbf{E}|^2$ between the simulation with $\frac{3d_{max}}{4}$ overhang and with $\frac{d_{max}}{330}$ overhang.

Figure 117: The MATLAB plots of $\nabla|\mathbf{E}|^2$ with illumination and with $\frac{3d_{max}}{4}$ overhang in the top ITO glass.

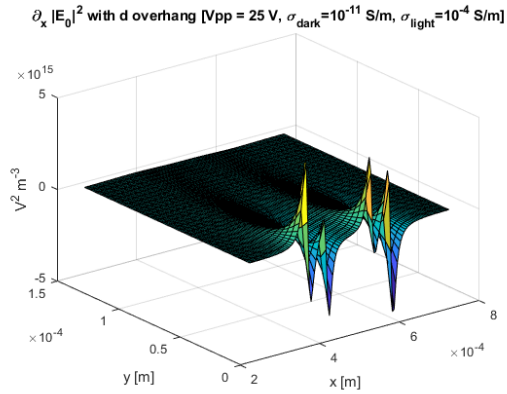

The partial derivative in x direction of $|\mathbf{E}|^2$

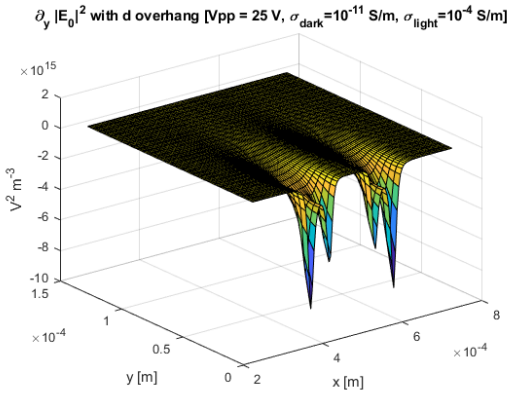

The partial derivative in y direction of $|\mathbf{E}|^2$

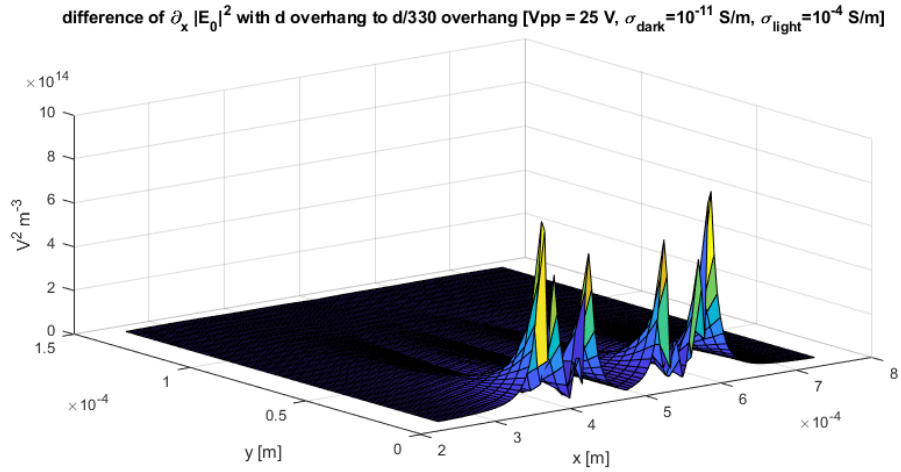

The difference in the partial derivative in x direction of $|\mathbf{E}|^2$ between the simulation with d_{max} overhang and with $\frac{d_{max}}{330}$ overhang.

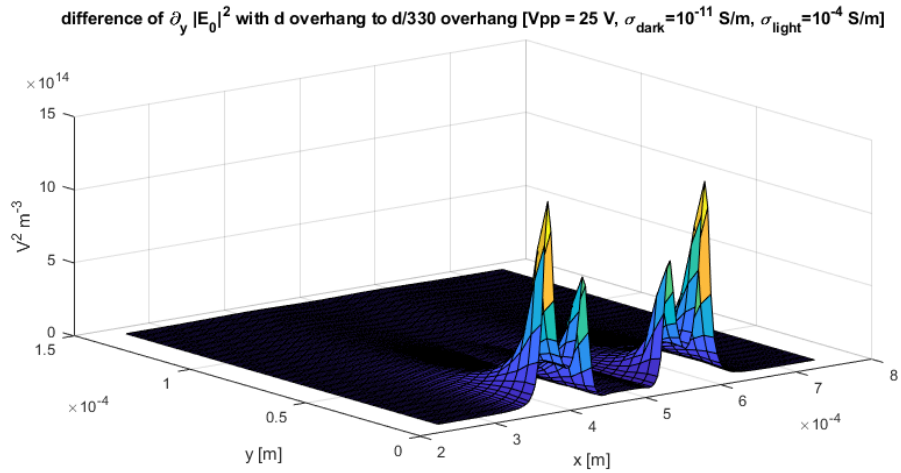

The difference in the partial derivative in y direction of $|\mathbf{E}|^2$ between the simulation with d_{max} overhang and with $\frac{d_{max}}{330}$ overhang.

Figure 118: The MATLAB plots of $\nabla|\mathbf{E}|^2$ with illumination and with d_{max} overhang in the top ITO glass.

A.2.3 Electric field in OET off state

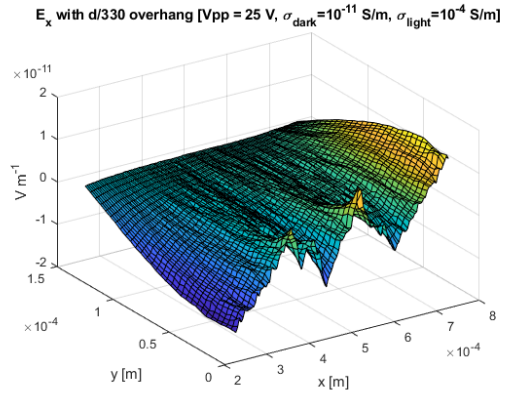

The electrical field strength in x direction

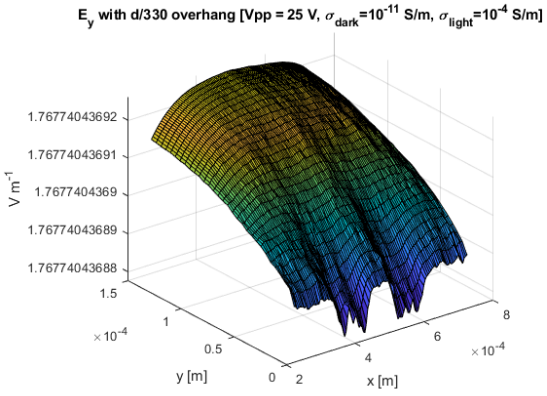

The electrical field strength in y direction

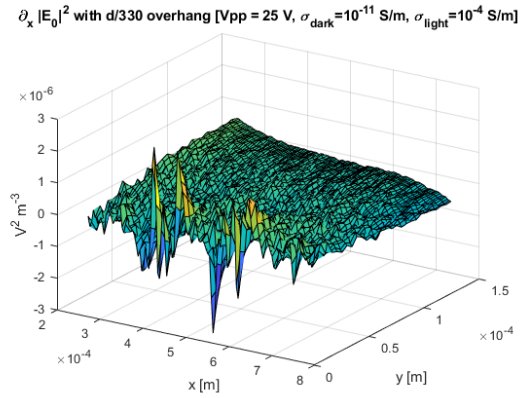

The partial derivative of $|\mathbf{E}|^2$ in x direction

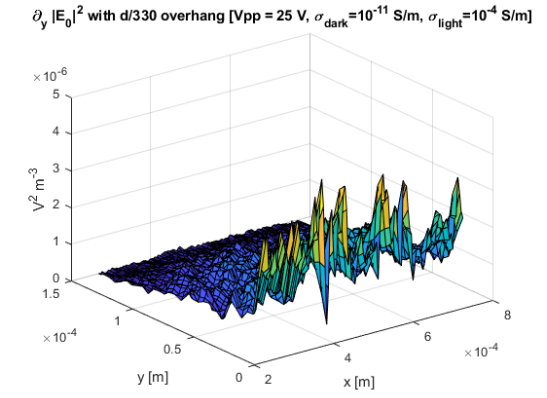

The partial derivative of $|\mathbf{E}|^2$ in y direction

Figure 119: The MATLAB plots of the electrical field without simulation using simulated data from COMSOL with $\frac{d_{max}}{330}$ overhang in the top ITO glass.

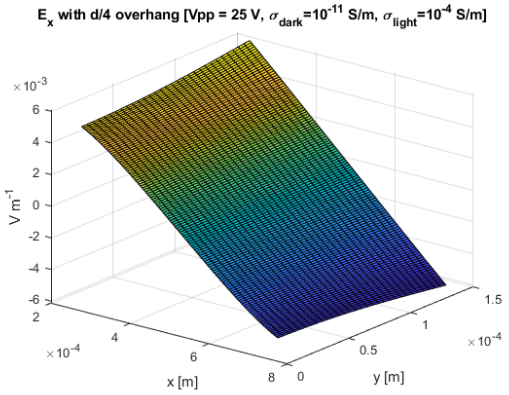

The electrical field strength in x direction

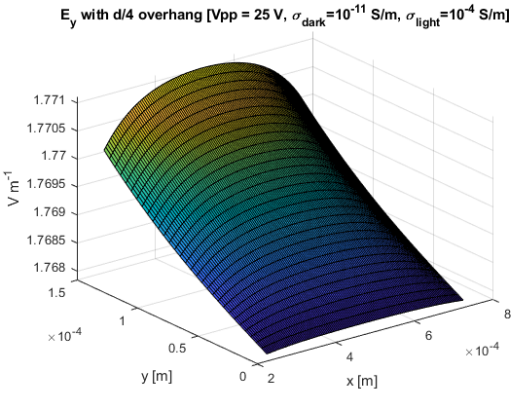

The electrical field strength in y direction

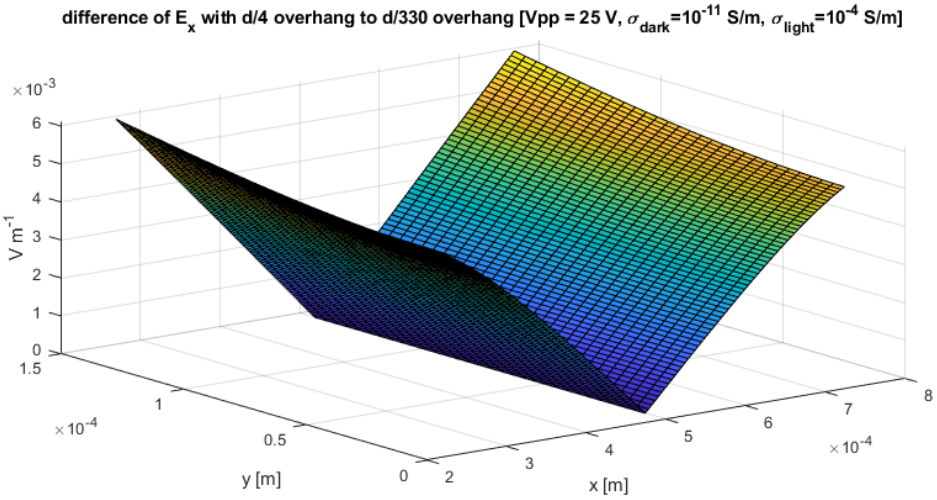

The difference in electrical field strength in x direction between the simulation with $\frac{d_{max}}{4}$ overhang and with $\frac{d_{max}}{330}$ overhang.

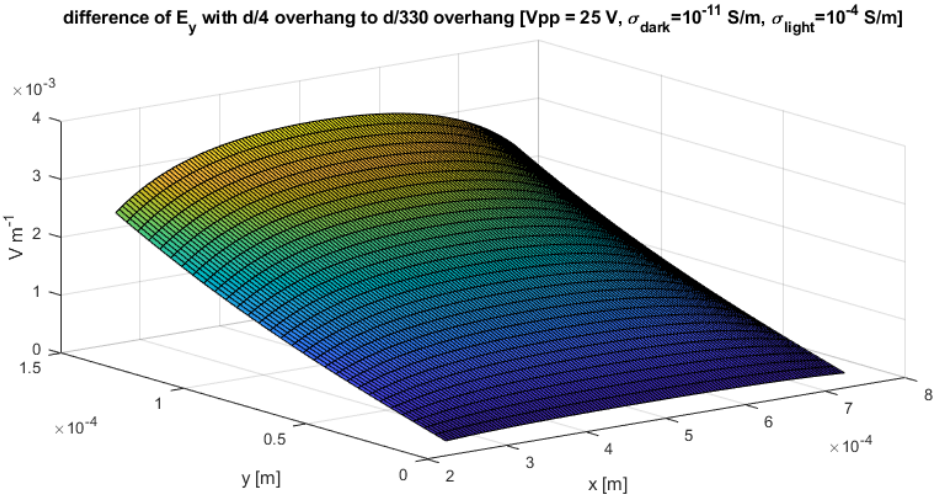

The difference in electrical field strength in y direction between the simulation with $\frac{d_{max}}{4}$ overhang and with $\frac{d_{max}}{330}$ overhang.

Figure 120: The MATLAB plots of the electrical field without illumination using simulated data from COMSOL with $\frac{d_{max}}{4}$ overhang in the top ITO glass.

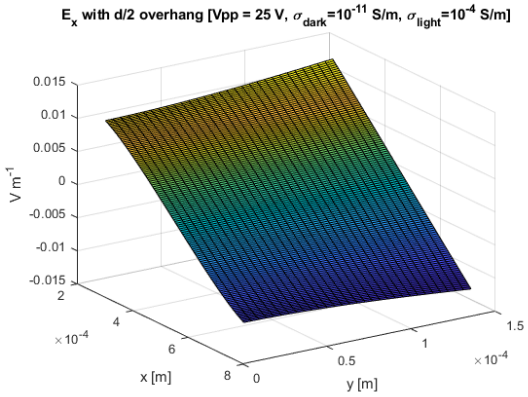

The electrical field strength in x direction

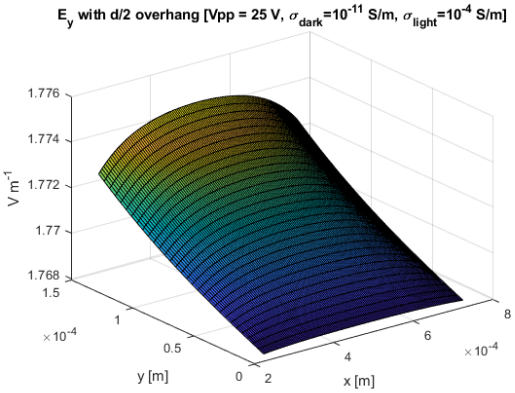

The electrical field strength in y direction

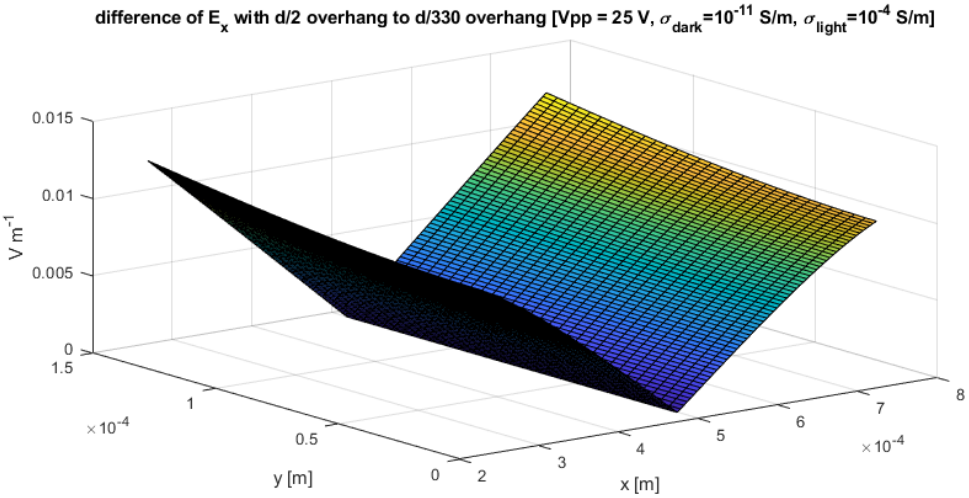

The difference in electrical field strength in x direction between the simulation with $\frac{d_{max}}{2}$ overhang and with $\frac{d_{max}}{330}$ overhang.

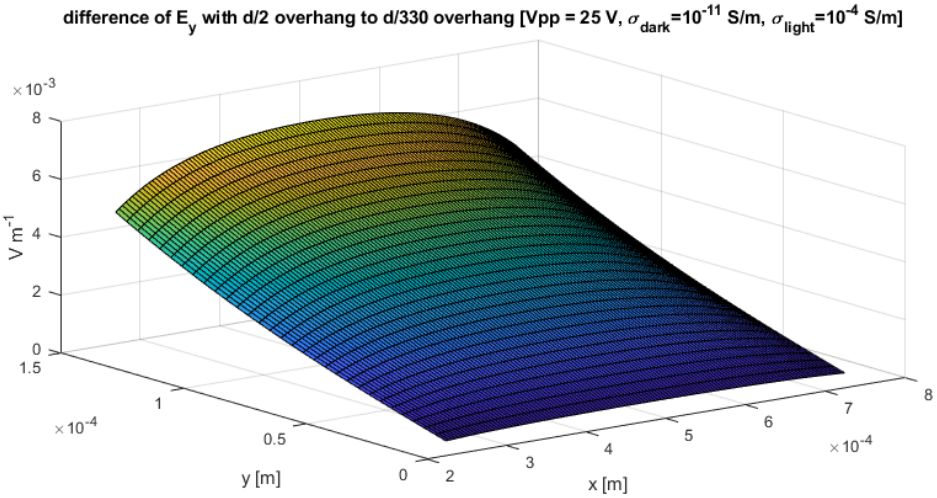

The difference in electrical field strength in y direction between the simulation with $\frac{d_{max}}{2}$ overhang and with $\frac{d_{max}}{330}$ overhang.

Figure 121: The MATLAB plots of the electrical field without illumination using simulated data from COMSOL with $\frac{d_{max}}{2}$ overhang in the top ITO glass.

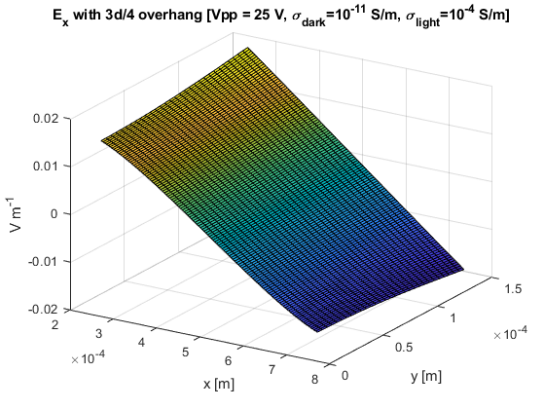

The electrical field strength in x direction

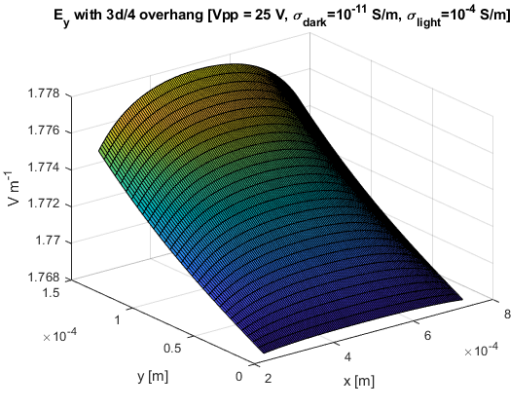

The electrical field strength in y direction

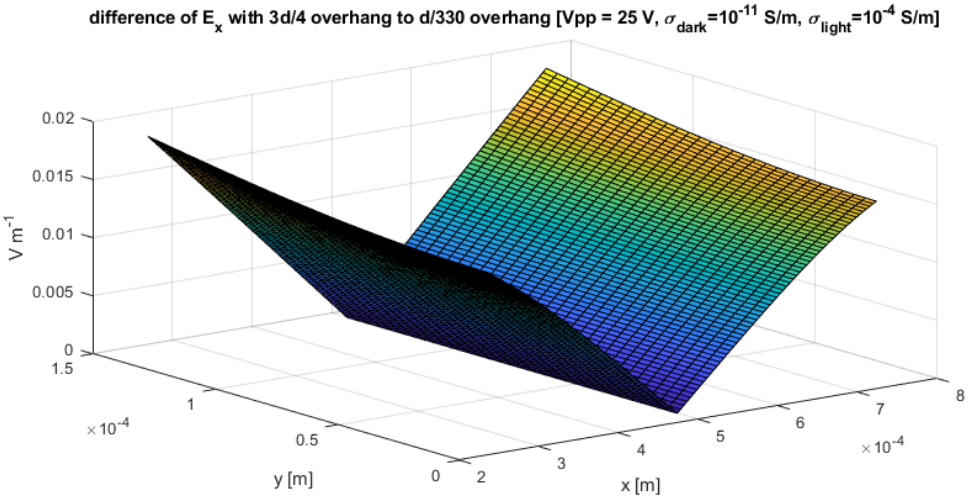

The difference in electrical field strength in x direction between the simulation with $\frac{3d_{max}}{4}$ overhang and with $\frac{d_{max}}{330}$ overhang.

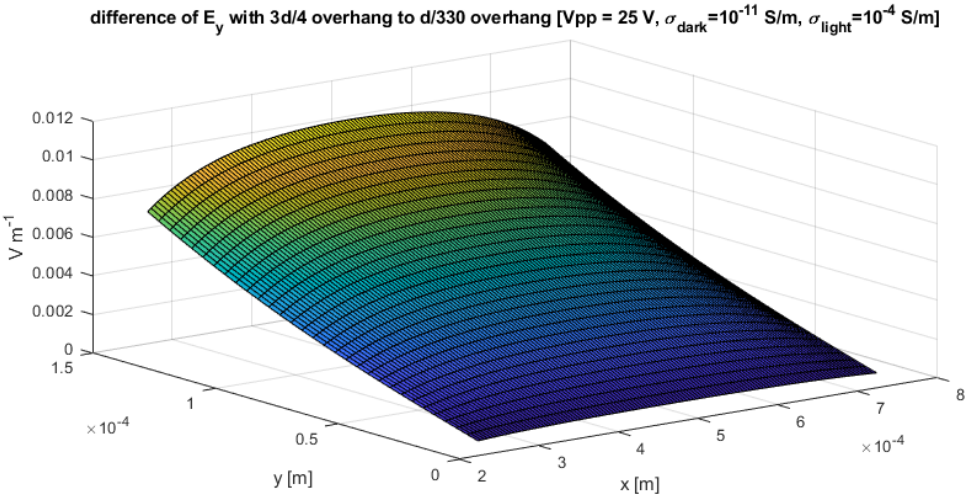

The difference in electrical field strength in y direction between the simulation with $\frac{3d_{max}}{4}$ overhang and with $\frac{d_{max}}{330}$ overhang.

Figure 122: The MATLAB plots of the electrical field without illumination using simulated data from COMSOL with $\frac{3d_{max}}{4}$ overhang in the top ITO glass.

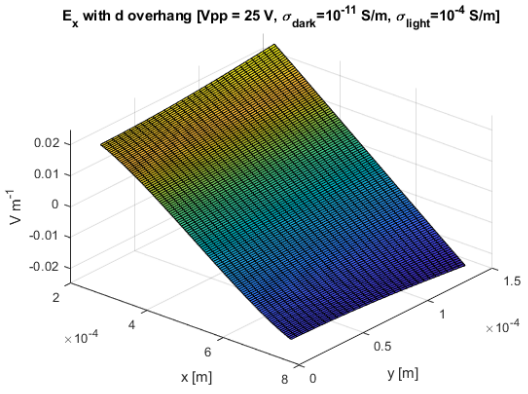

The electrical field strength in x direction

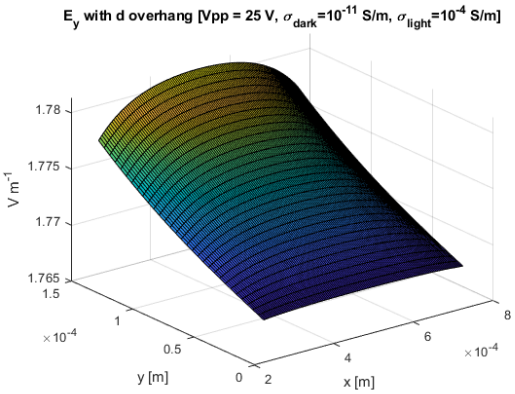

The electrical field strength in y direction

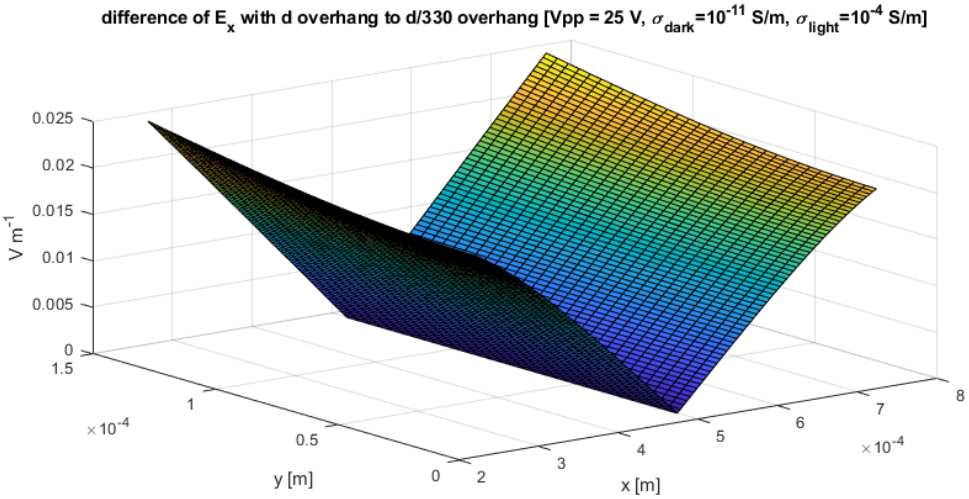

The difference in electrical field strength in x direction between the simulation with d_{max} overhang and with $\frac{d_{max}}{330}$ overhang.

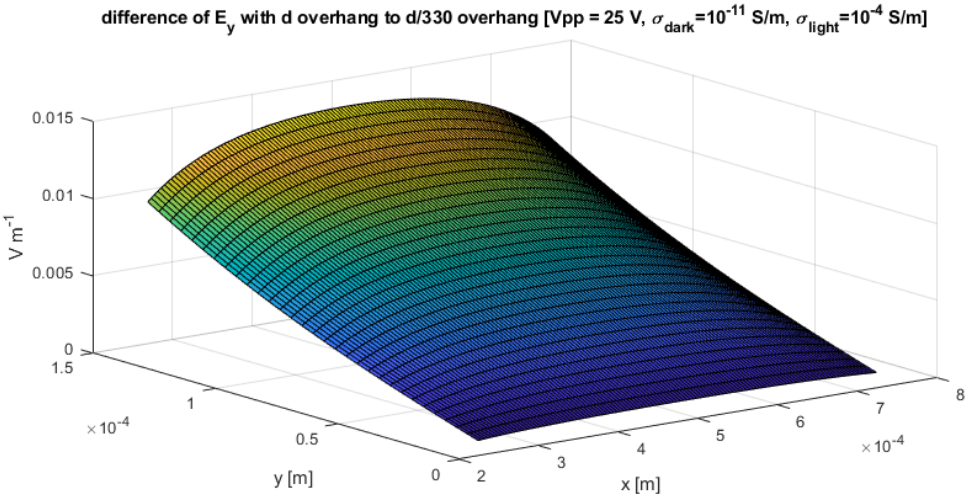

The difference in electrical field strength in y direction between the simulation with d_{max} overhang and with $\frac{d_{max}}{330}$ overhang.

Figure 123: The MATLAB plots of the electrical field without illumination using simulated data from COMSOL with d_{max} overhang in the top ITO glass.

A.2.4 The gradient of the square of the norm of the electric field in OET off state

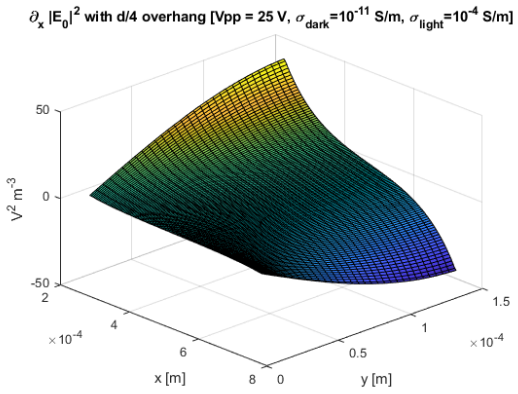

The partial derivative in x direction of $|\mathbf{E}|^2$

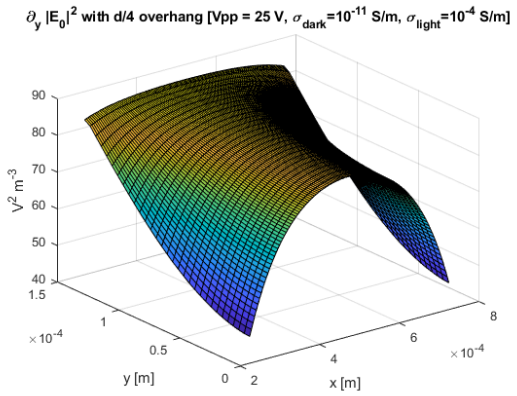

The partial derivative in y direction of $|\mathbf{E}|^2$

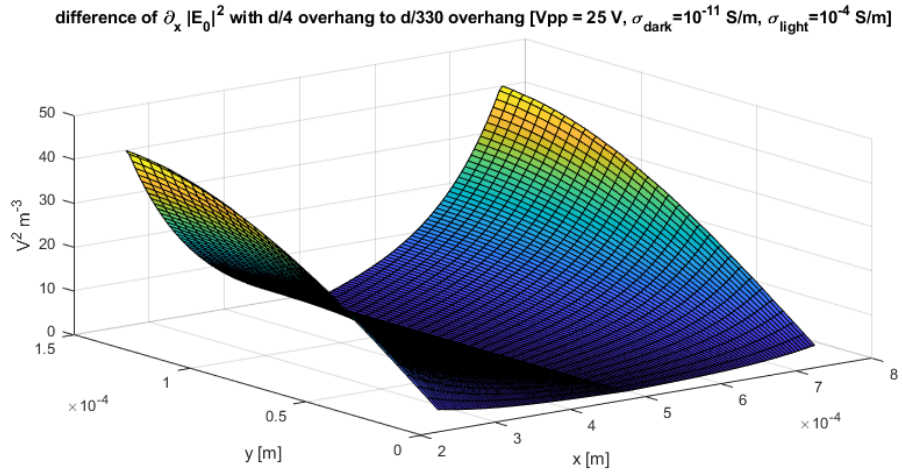

The difference in the partial derivative in x direction of $|\mathbf{E}|^2$ between the simulation with $\frac{d_{max}}{4}$ overhang and with $\frac{d_{max}}{330}$ overhang.

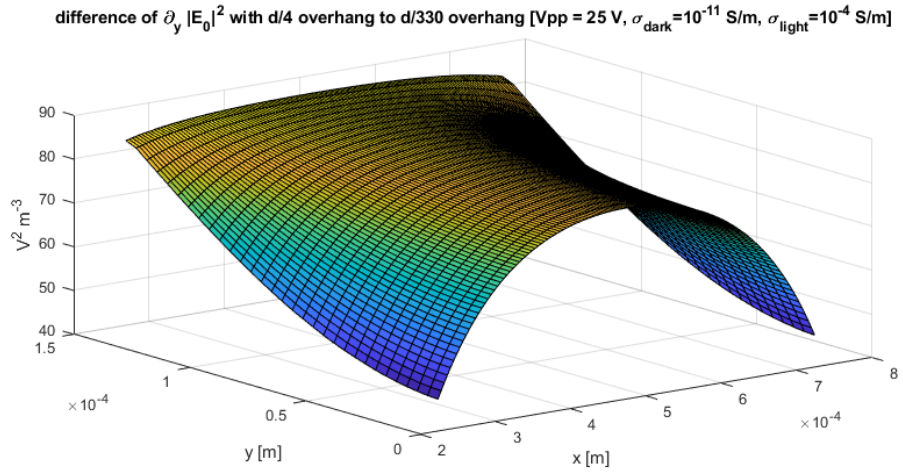

The difference in the partial derivative in y direction of $|\mathbf{E}|^2$ between the simulation with $\frac{d_{max}}{4}$ overhang and with $\frac{d_{max}}{330}$ overhang.

Figure 124: The MATLAB plots of $\nabla|\mathbf{E}|^2$ without illumination and with $\frac{d_{max}}{4}$ overhang in the top ITO glass.

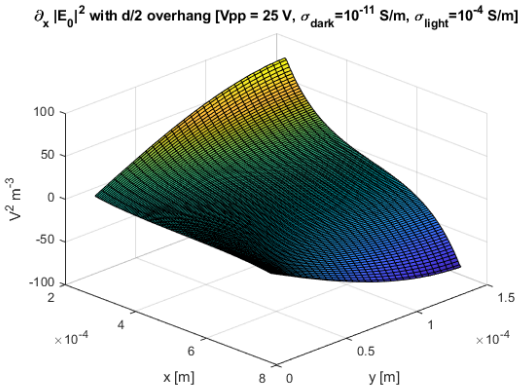

The partial derivative in x direction of $|\mathbf{E}|^2$

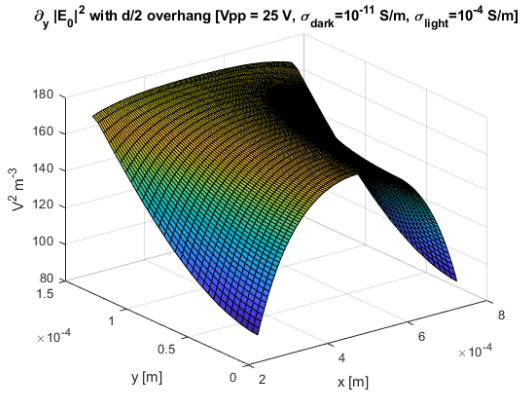

The partial derivative in y direction of $|\mathbf{E}|^2$

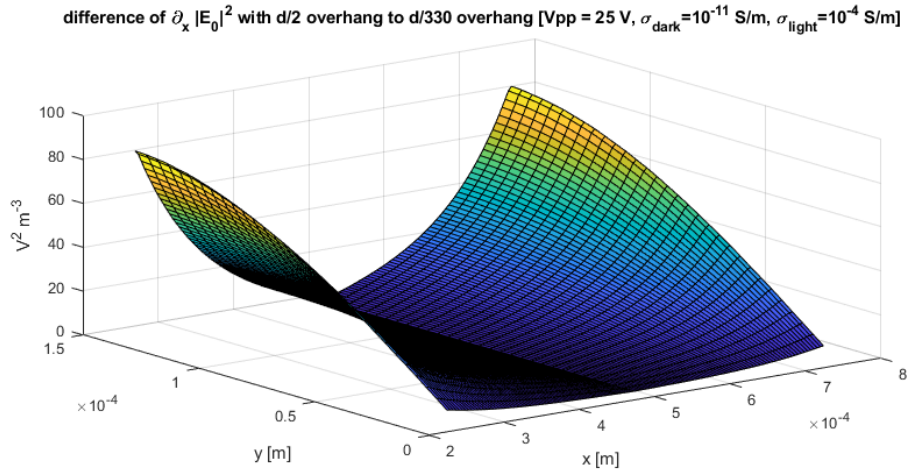

The difference in the partial derivative in x direction of $|\mathbf{E}|^2$ between the simulation with $\frac{d_{max}}{2}$ overhang and with $\frac{d_{max}}{330}$ overhang.

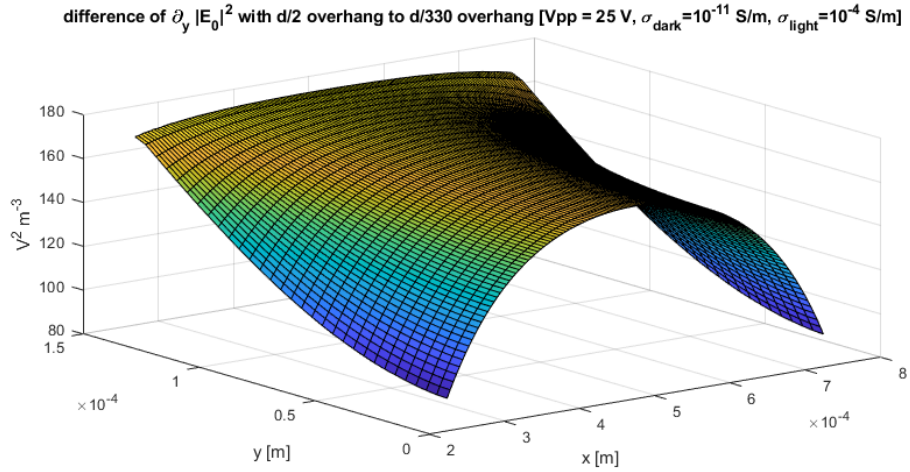

The difference in the partial derivative in y direction of $|\mathbf{E}|^2$ between the simulation with $\frac{d_{max}}{2}$ overhang and with $\frac{d_{max}}{330}$ overhang.

Figure 125: The MATLAB plots of $\nabla|\mathbf{E}|^2$ without illumination and with $\frac{d_{max}}{2}$ overhang in the top ITO glass.

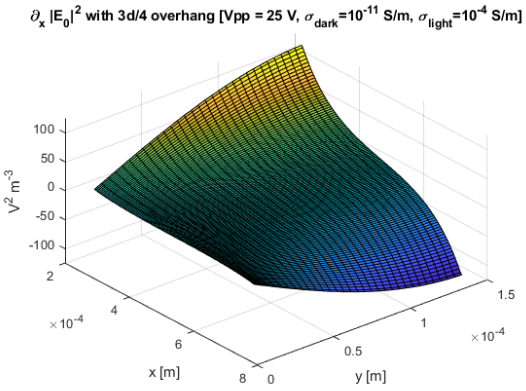

The partial derivative in x direction of $|\mathbf{E}|^2$

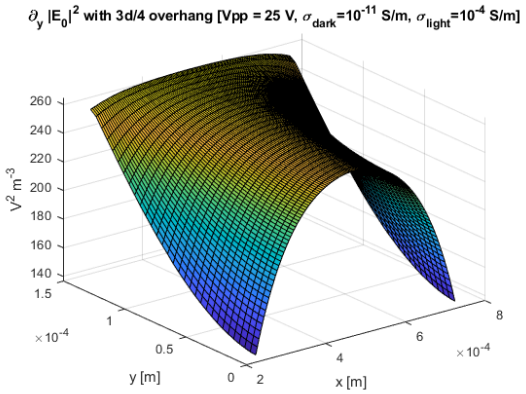

The partial derivative in y direction of $|\mathbf{E}|^2$

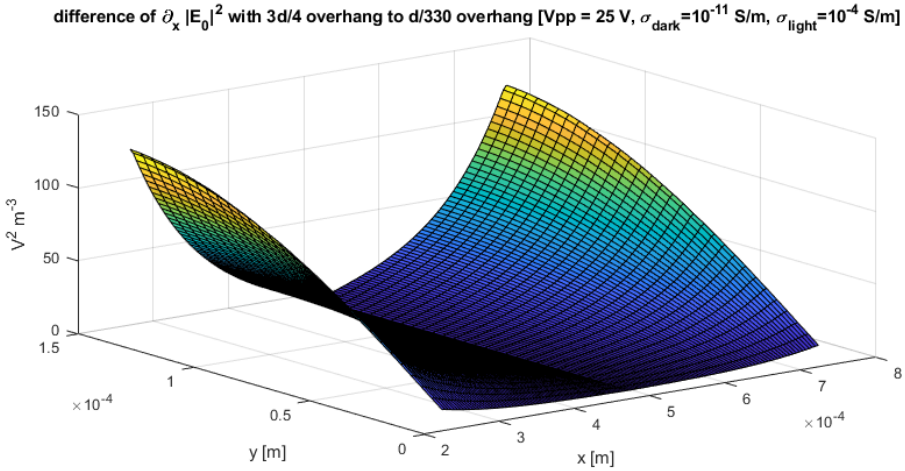

The difference in the partial derivative in x direction of $|\mathbf{E}|^2$ between the simulation with $\frac{3d_{max}}{4}$ overhang and with $\frac{d_{max}}{330}$ overhang.

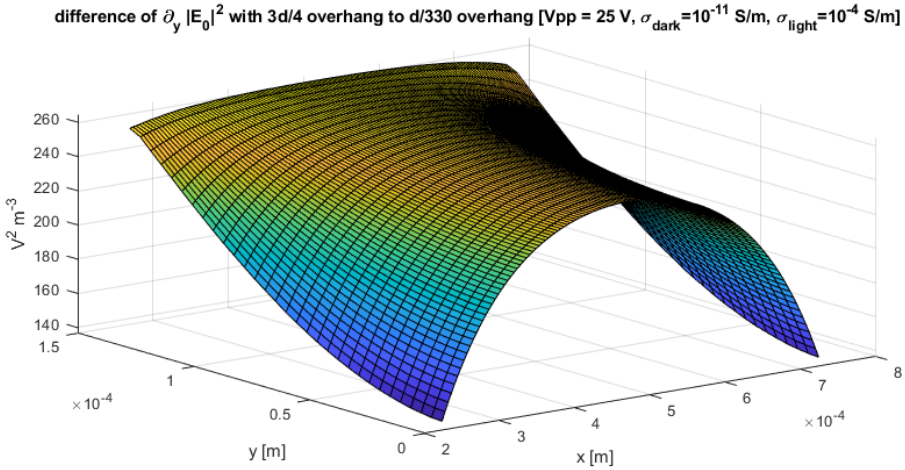

The difference in the partial derivative in y direction of $|\mathbf{E}|^2$ between the simulation with $\frac{3d_{max}}{4}$ overhang and with $\frac{d_{max}}{330}$ overhang.

Figure 126: The MATLAB plots of $\nabla|\mathbf{E}|^2$ without illumination and with $\frac{3d_{max}}{4}$ overhang in the top ITO glass.

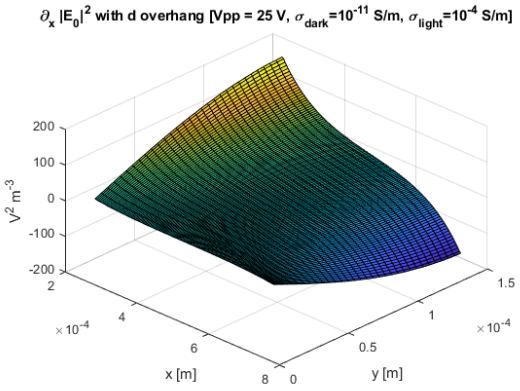

The partial derivative in x direction of $|\mathbf{E}|^2$

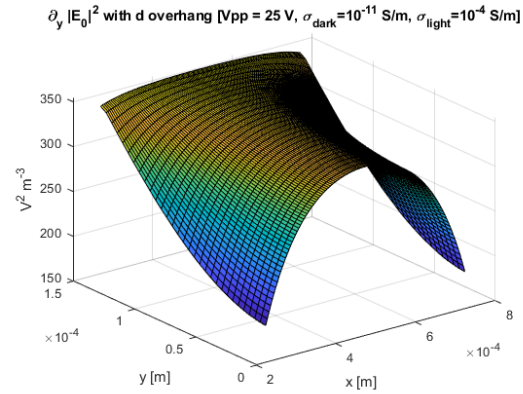

The partial derivative in y direction of $|\mathbf{E}|^2$

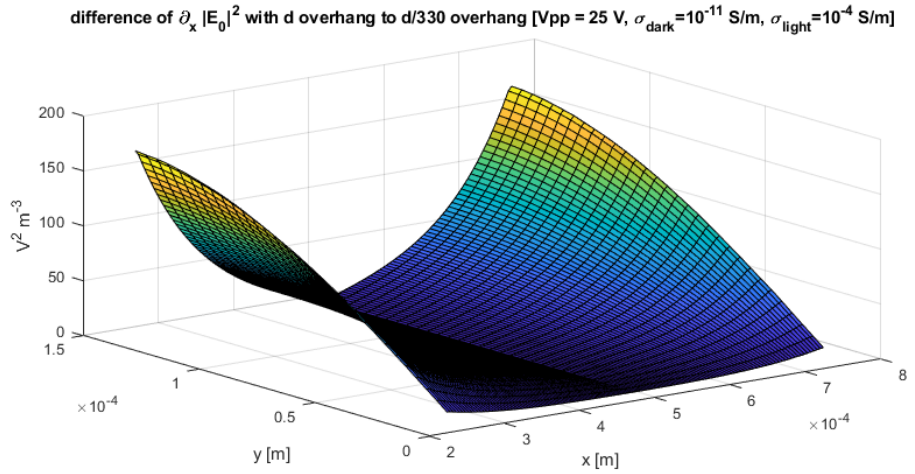

The difference in the partial derivative in x direction of $|\mathbf{E}|^2$ between the simulation with d_{max} overhang and with $\frac{d_{max}}{330}$ overhang.

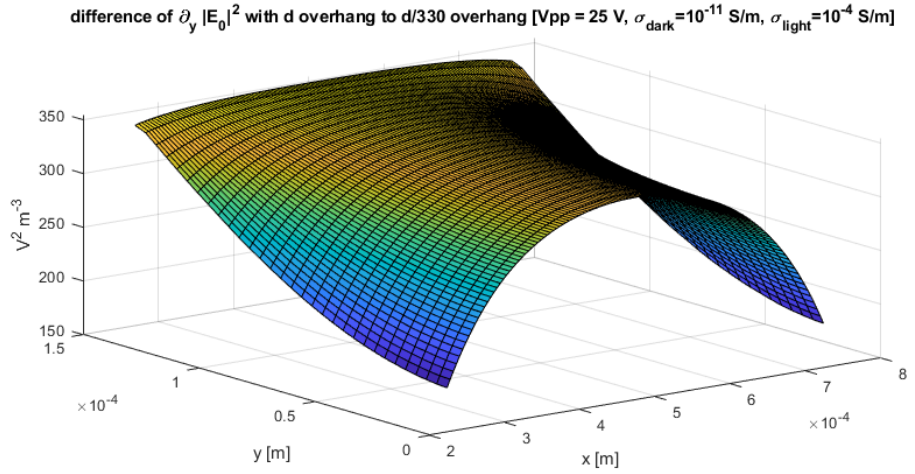

The difference in the partial derivative in y direction of $|\mathbf{E}|^2$ between the simulation with d_{max} overhang and with $\frac{d_{max}}{330}$ overhang.

Figure 127: The MATLAB plots of $\nabla|\mathbf{E}|^2$ without illumination and with d_{max} overhang in the top ITO glass.

B

Surface roughness simulation results

B.1 COMSOL plots

B.1.1 Electric field in OET illuminated state

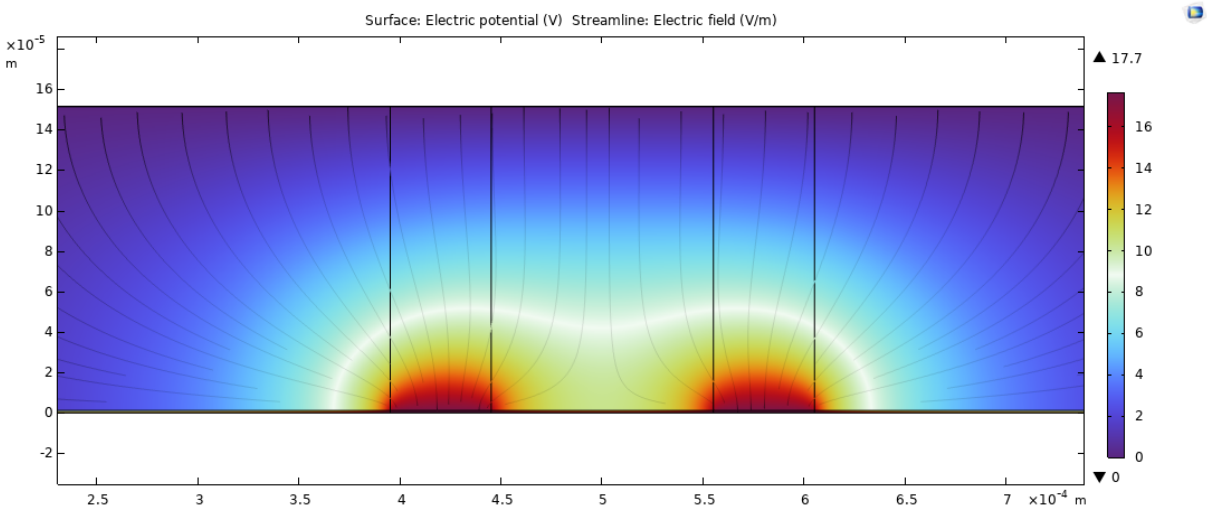

Figure 128: A COMSOL simulation of the electrical field in the OET chip due to two illuminated spots with 0 randomness on the surface

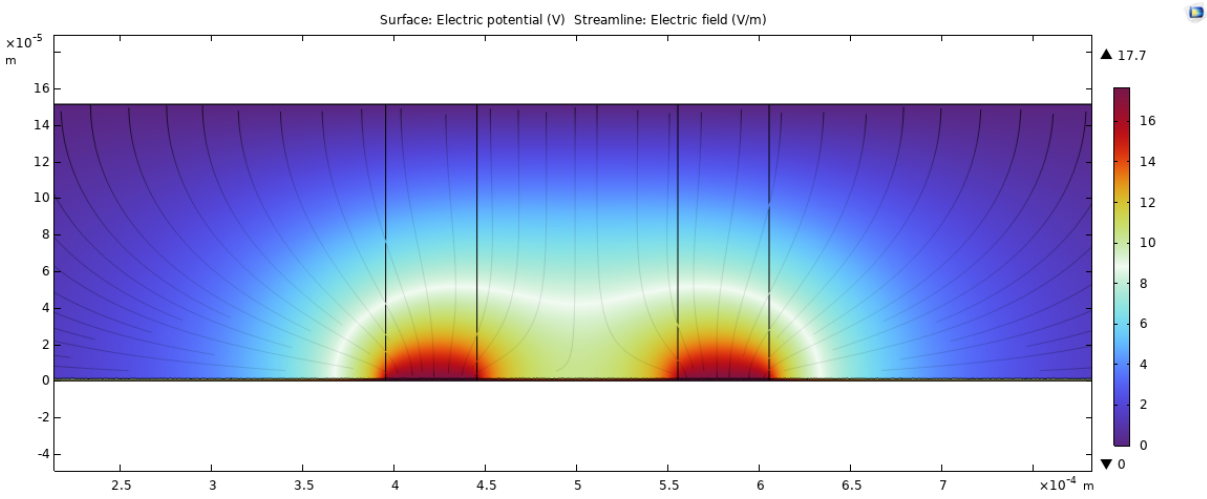

Figure 129: A COMSOL simulation of the electrical field in the OET chip due to two illuminated spots with 0.5 randomness on the surface

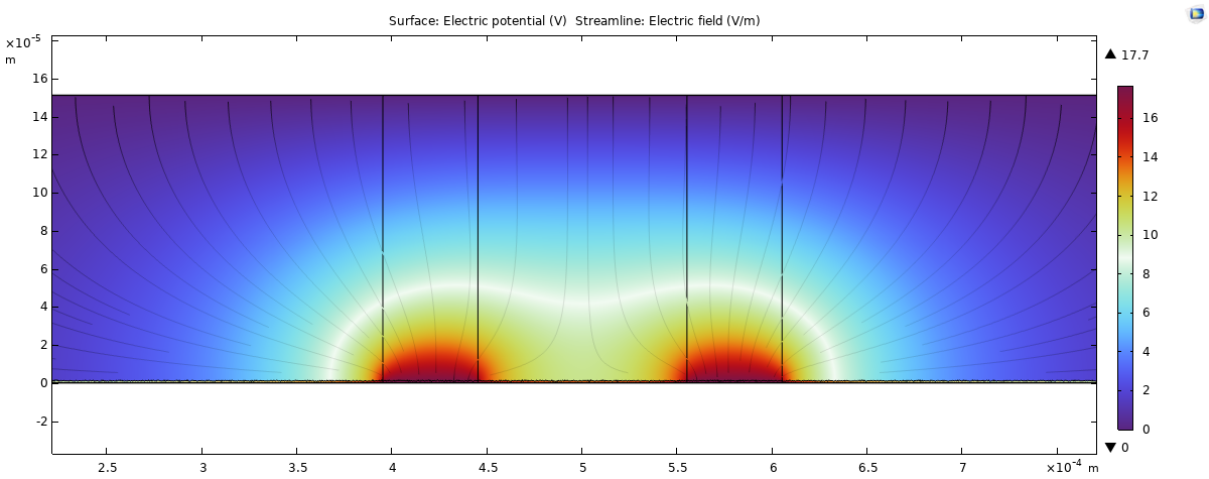

Figure 130: A COMSOL simulation of the electrical field in the OET chip due to two illuminated spots with 1 randomness on the surface

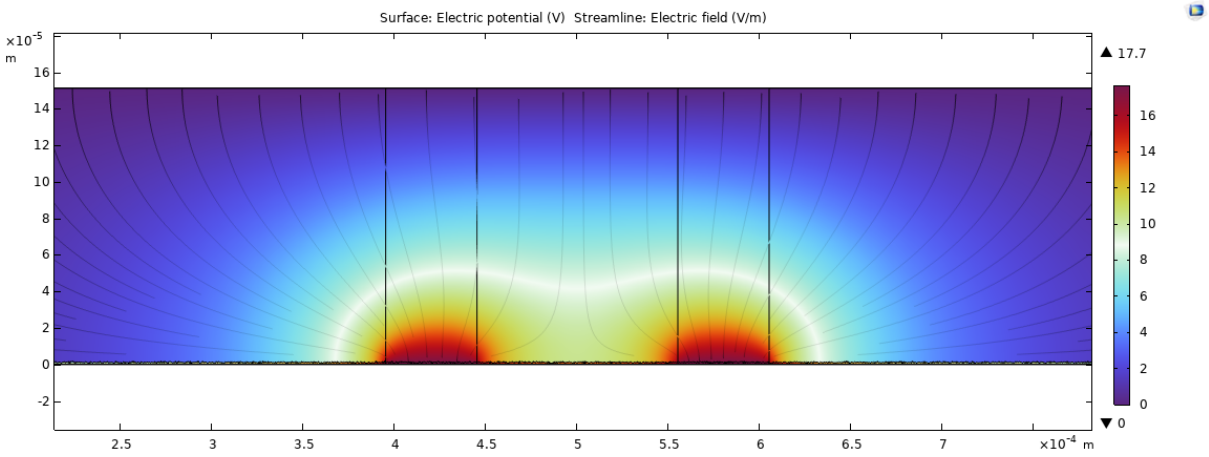

Figure 131: A COMSOL simulation of the electrical field in the OET chip due to two illuminated spots with 1.5 randomness on the surface

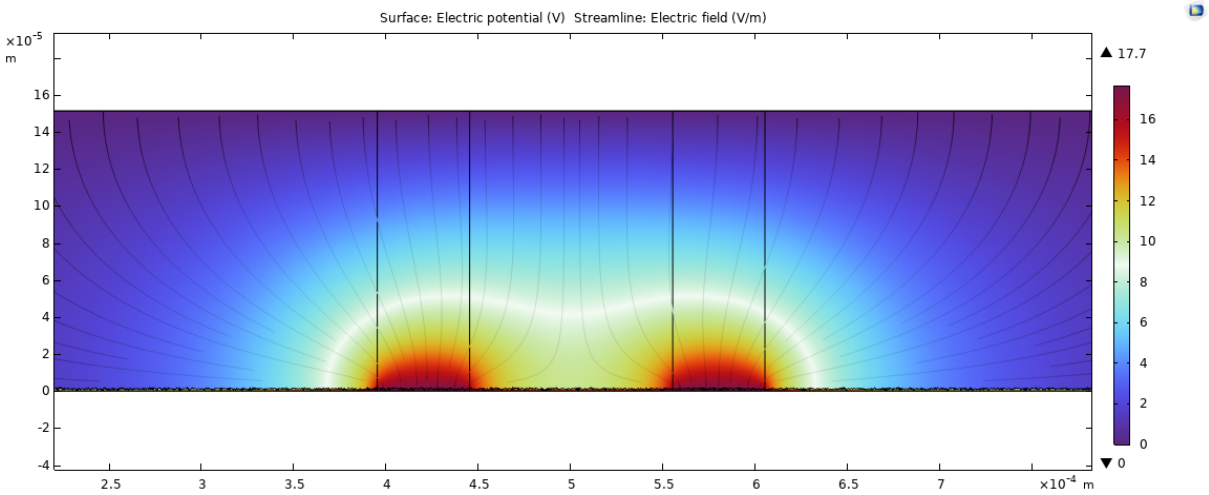

Figure 132: A COMSOL simulation of the electrical field in the OET chip due to two illuminated spots with 2 randomness on the surface

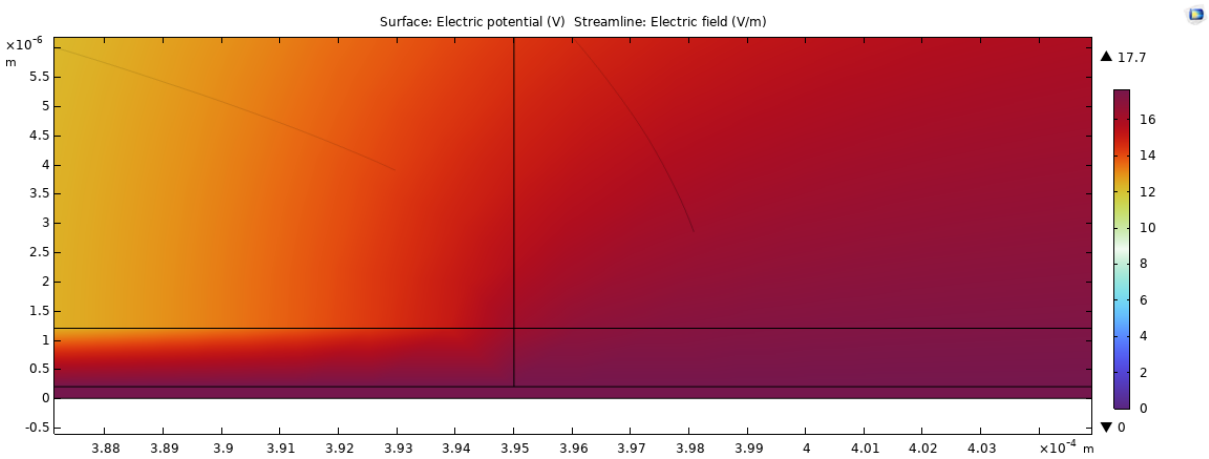

Figure 133: A zoomed-in view of the COMSOL simulation of the electrical field in the OET chip due to two illuminated spots with 0 randomness on the surface

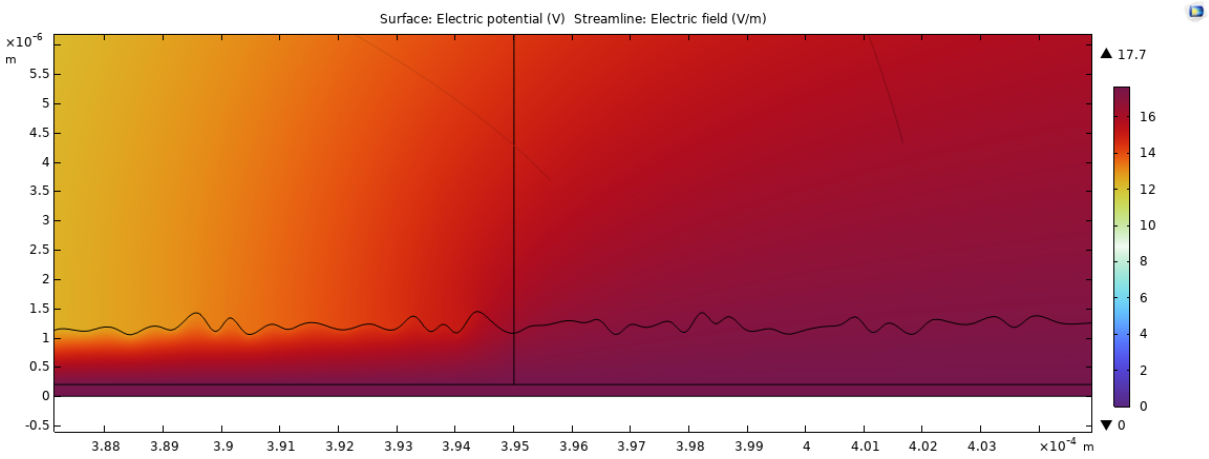

Figure 134: A zoomed-in view of the COMSOL simulation of the electrical field in the OET chip due to two illuminated spots with 0.5 randomness on the surface

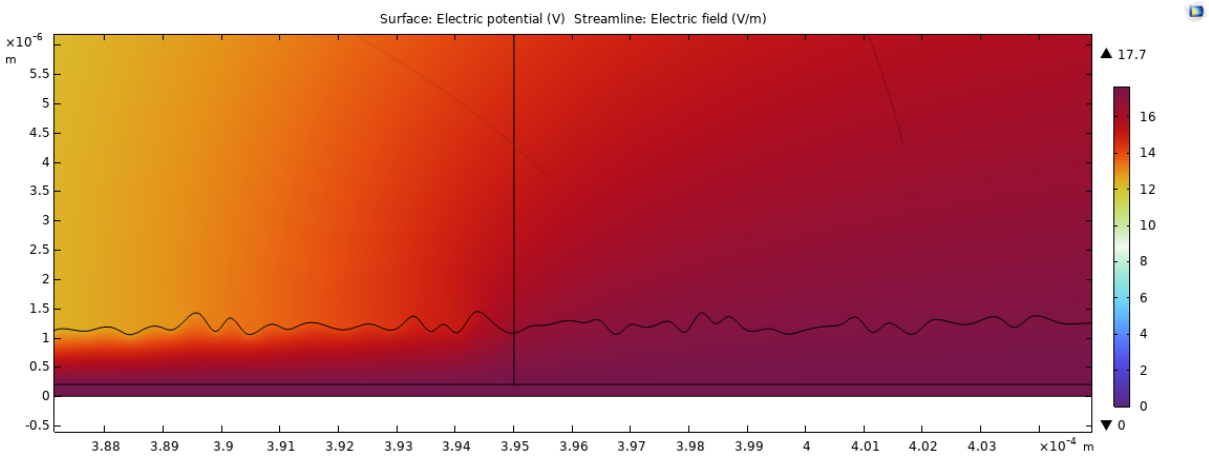

Figure 135: A zoomed-in view of the COMSOL simulation of the electrical field in the OET chip due to two illuminated spots with 1 randomness on the surface

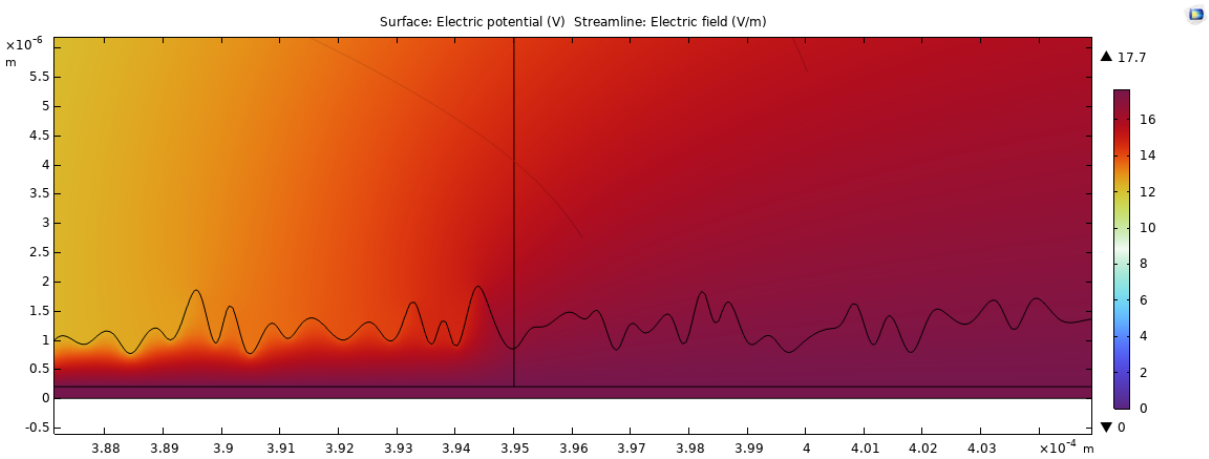

Figure 136: A zoomed-in view of the COMSOL simulation of the electrical field in the OET chip due to two illuminated spots with 1.5 randomness on the surface

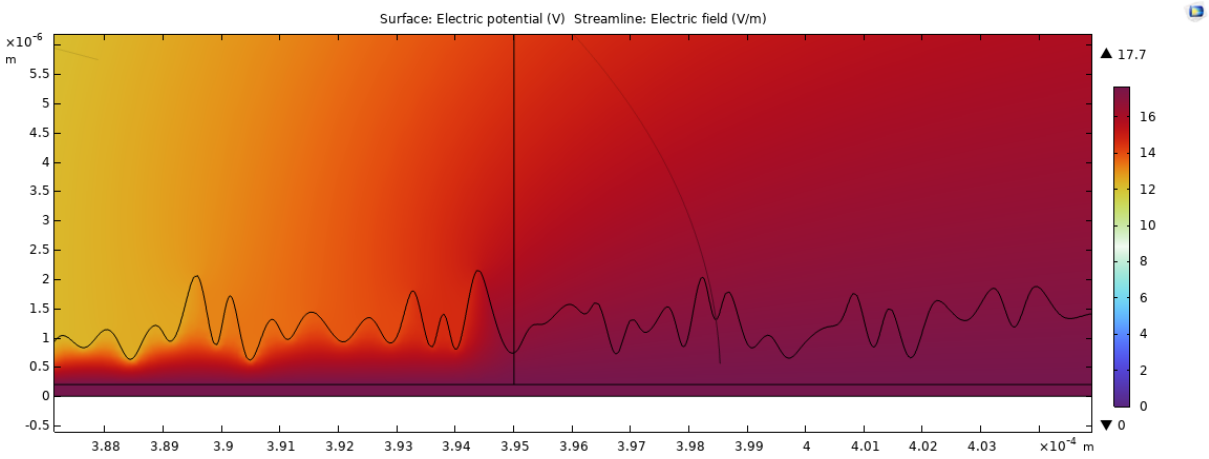

Figure 137: A zoomed-in view of the COMSOL simulation of the electrical field in the OET chip due to two illuminated spots with 2 randomness on the surface

B.1.2 The gradient of the square of the norm of the electric field in OET illuminated state

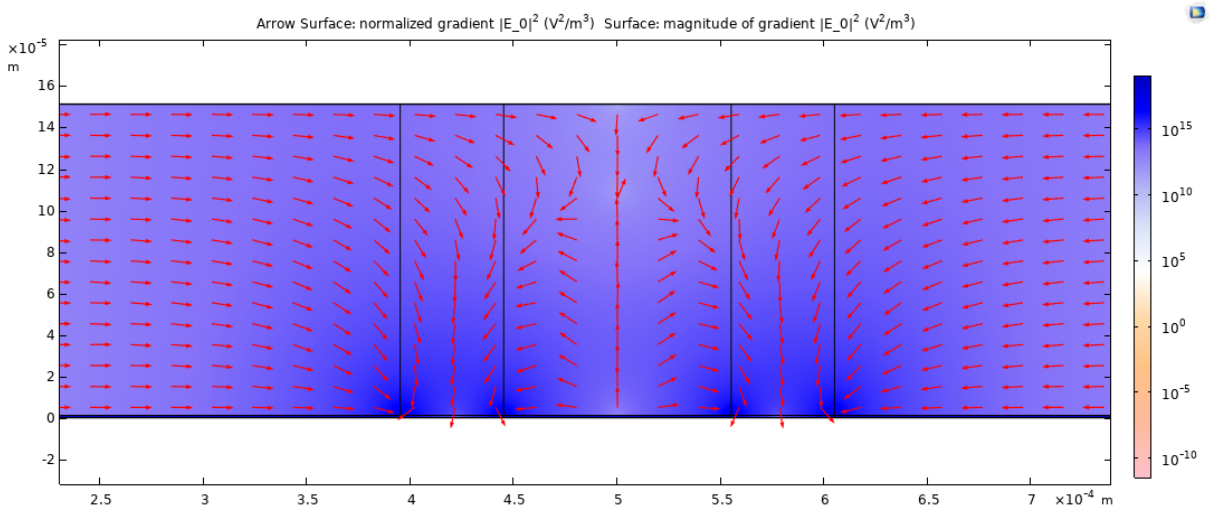

Figure 138: A COMSOL simulation of $\nabla|\mathbf{E}|^2$ in the OET chip due to two illuminated spots with 0 randomness on the surface

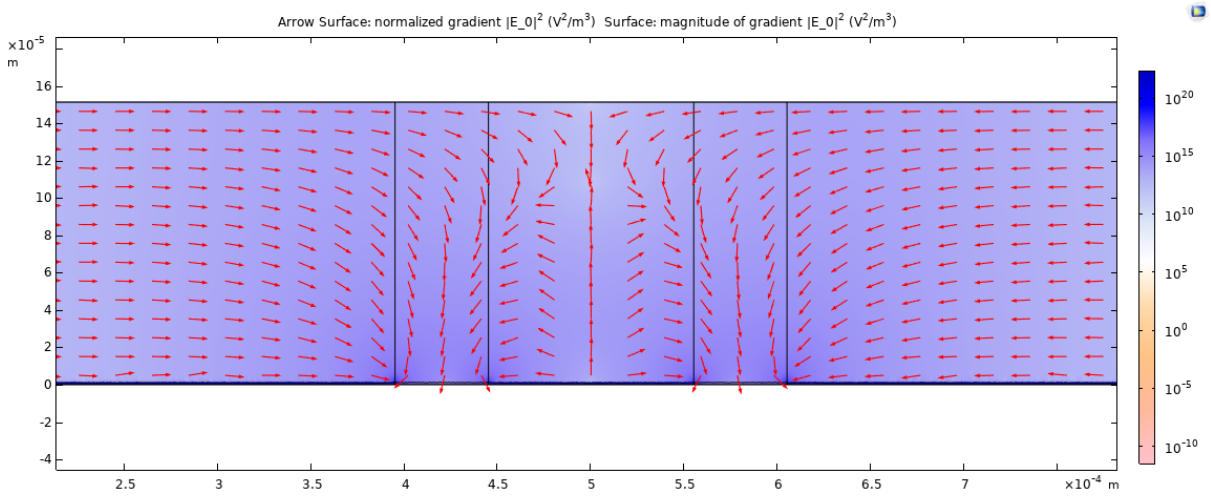

Figure 139: A COMSOL simulation of $\nabla|\mathbf{E}|^2$ in the OET chip due to two illuminated spots with 0.5 randomness on the surface

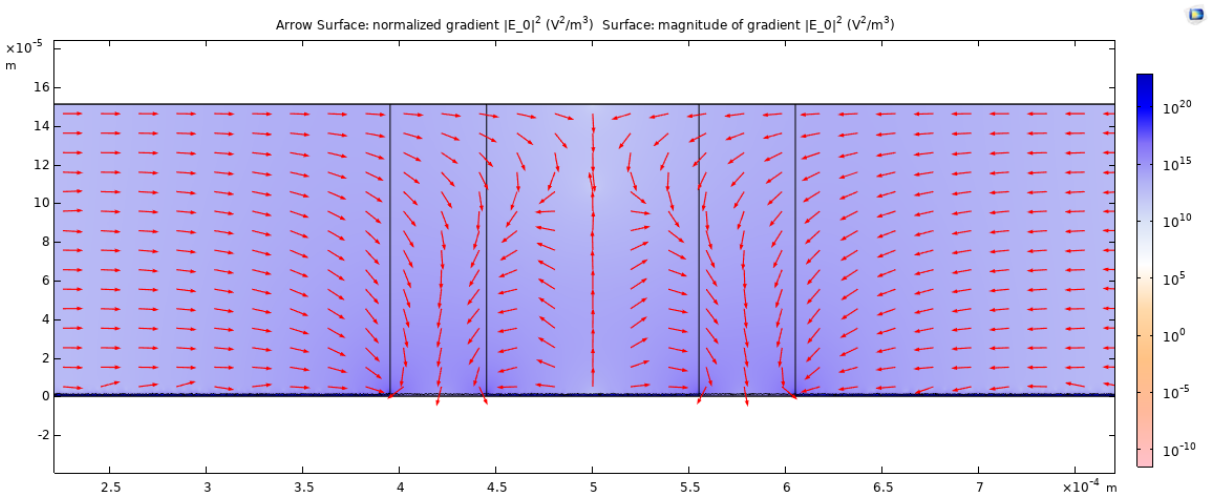

Figure 140: A COMSOL simulation of$\nabla|\mathbf{E}|^2$ in the OET chip due to two illuminated spots with 1 randomness on the surface

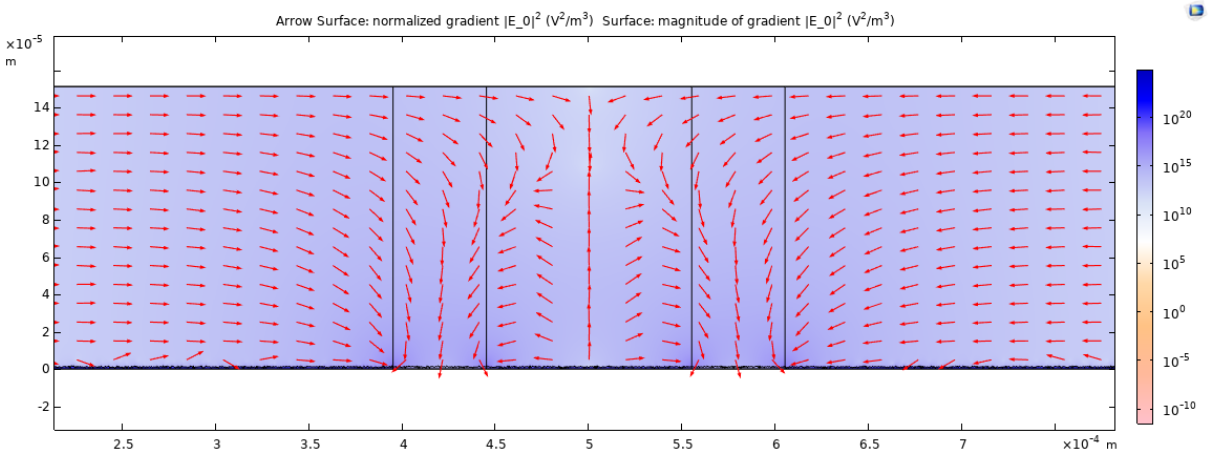

Figure 141: A COMSOL simulation of $\nabla|\mathbf{E}|^2$ in the OET chip due to two illuminated spots with 1.5 randomness on the surface

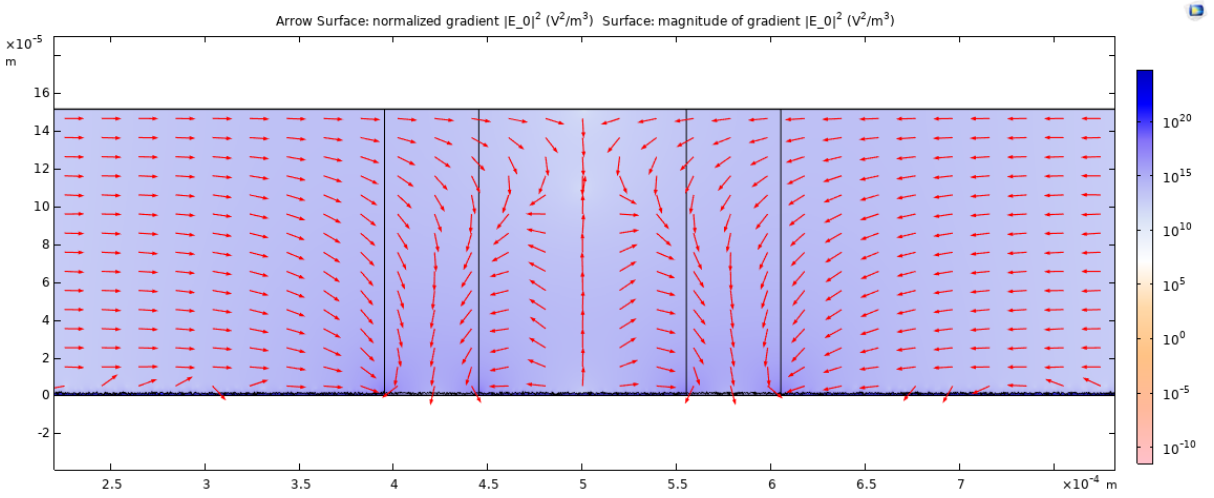

Figure 142: A COMSOL simulation of $\nabla|\mathbf{E}|^2$ in the OET chip due to two illuminated spots with 2 randomness on the surface

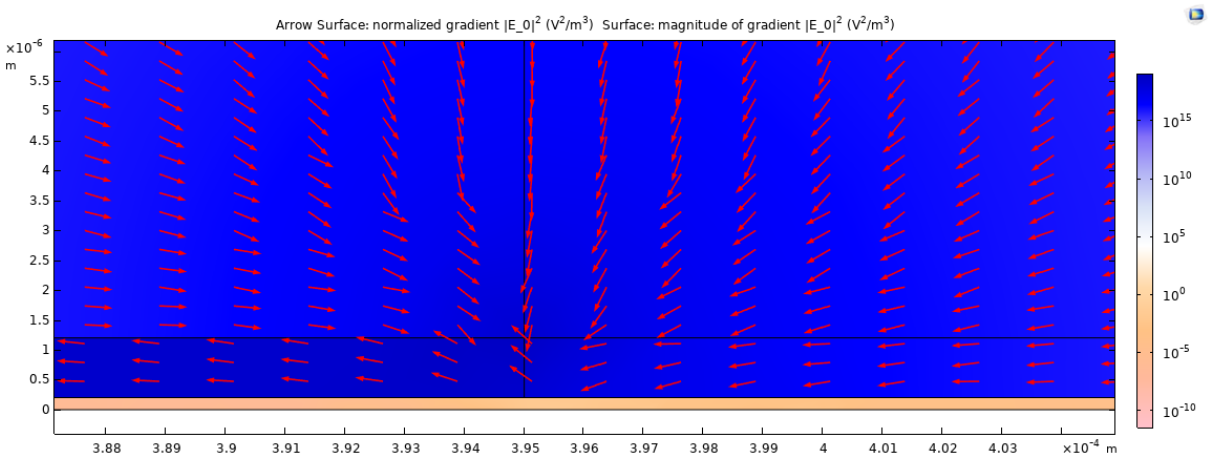

Figure 143: A zoomed-in view of the COMSOL simulation of $\nabla|\mathbf{E}|^2$ in the OET chip due to two illuminated spots with 0 randomness on the surface

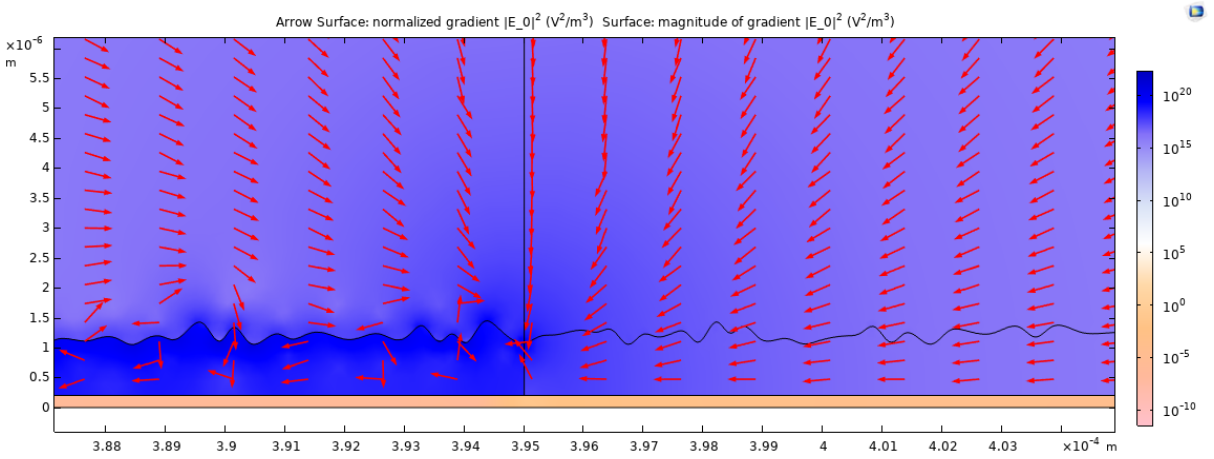

Figure 144: A zoomed-in view of the COMSOL simulation of $\nabla|\mathbf{E}|^2$ in the OET chip due to two illuminated spots with 0.5 randomness on the surface

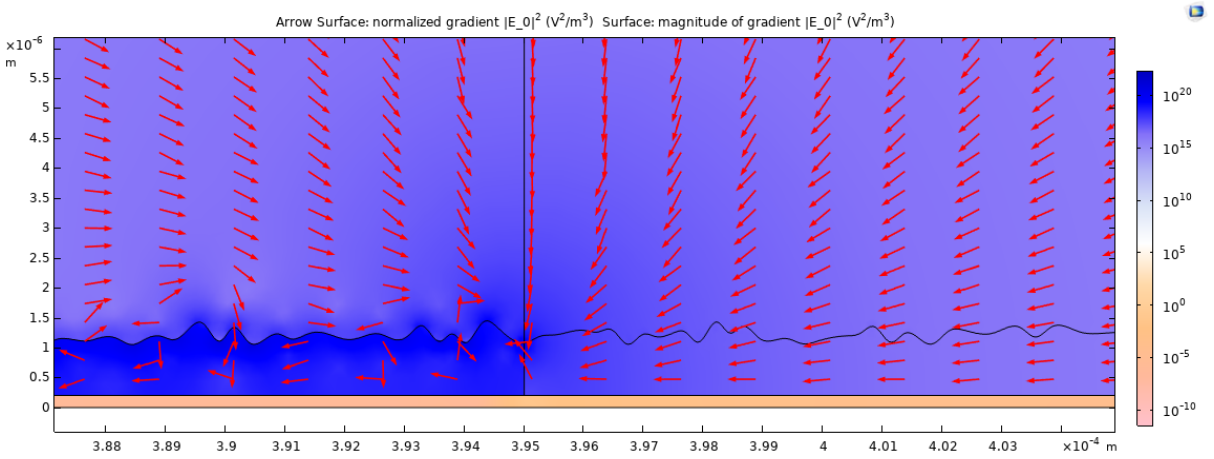

Figure 145: A zoomed-in view of the COMSOL simulation of $\nabla|\mathbf{E}|^2$ in the OET chip due to two illuminated spots with 1 randomness on the surface

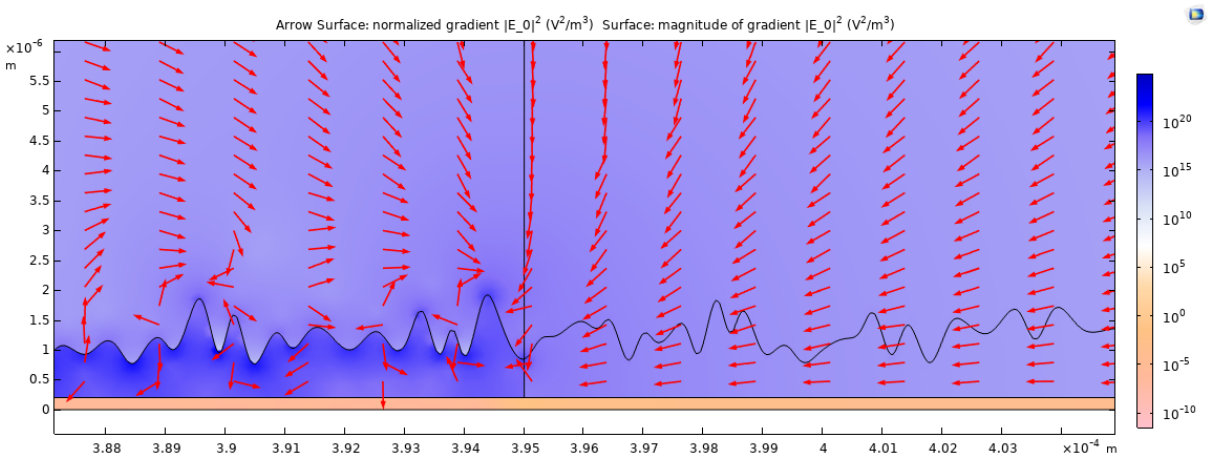

Figure 146: A zoomed-in view of the COMSOL simulation of $\nabla|\mathbf{E}|^2$ in the OET chip due to two illuminated spots with 1.5 randomness on the surface

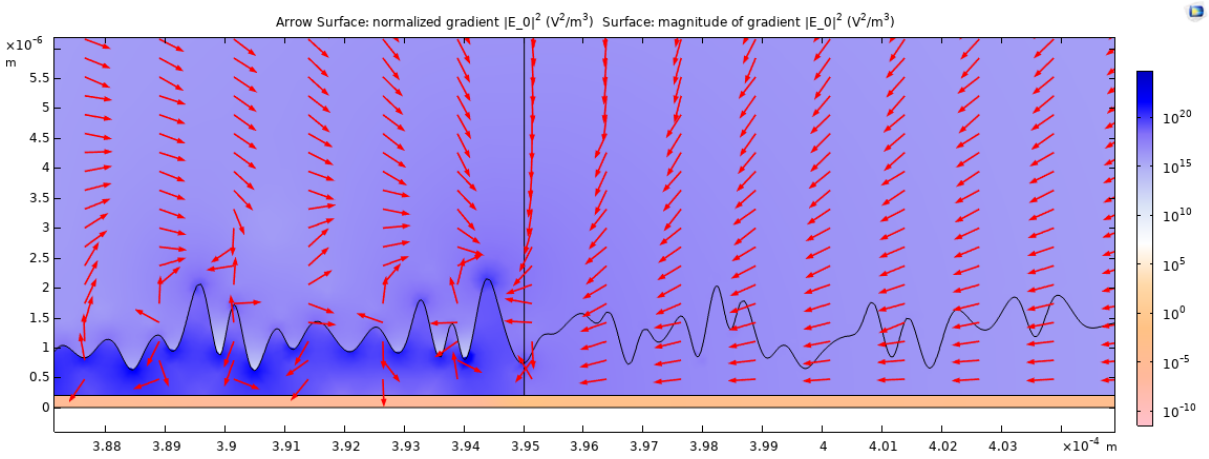

Figure 147: A zoomed-in view of the COMSOL simulation of $\nabla|\mathbf{E}|^2$ in the OET chip due to two illuminated spots with 2 randomness on the surface

B.1.3 The gradient of the square of the norm of the electric field in OET off state

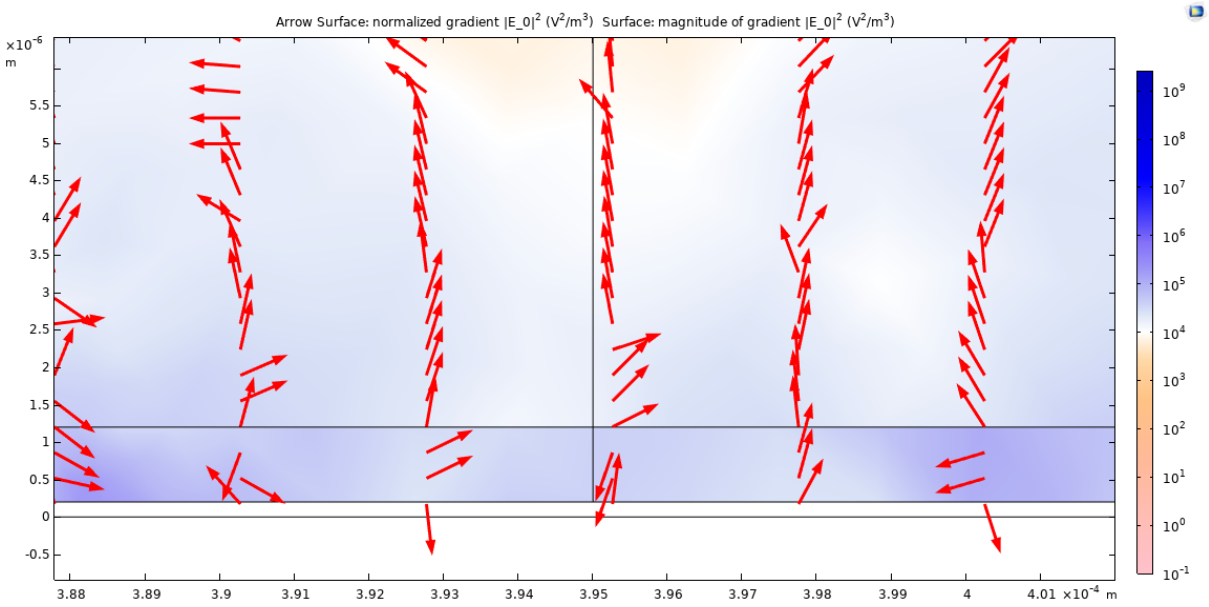

Figure 148: A zoomed-in view of the COMSOL simulation of $\nabla|\mathbf{E}|^2$ in the OET chip without illumination with 0 randomness on the surface

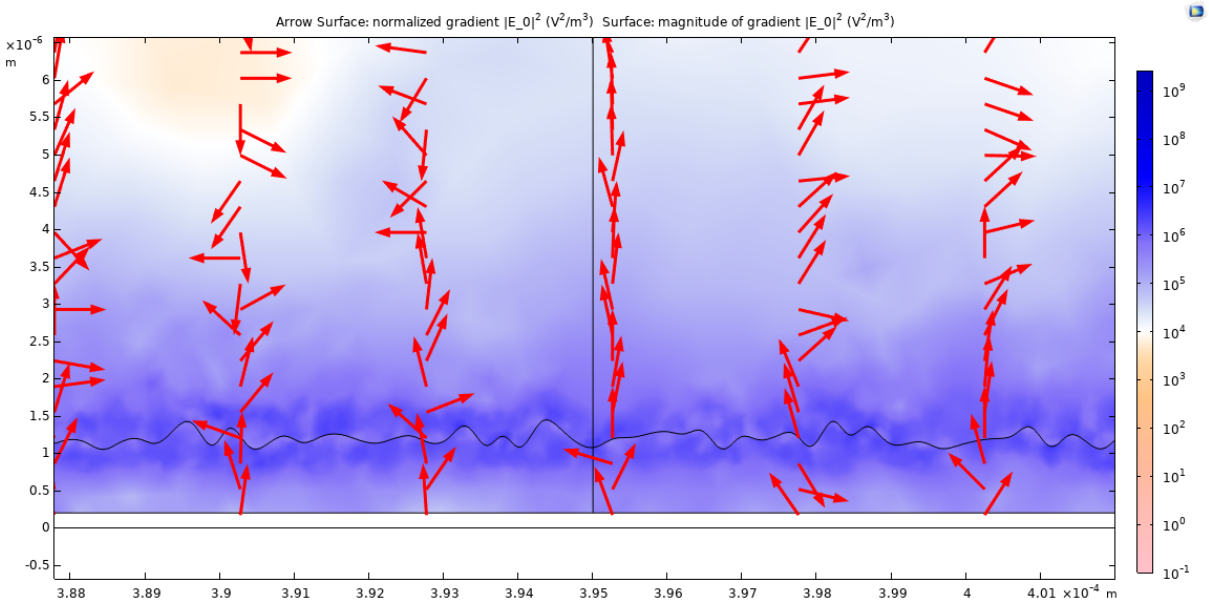

Figure 149: A zoomed-in view of the COMSOL simulation of $\nabla|\mathbf{E}|^2$ in the OET chip without illumination with 0.5 randomness on the surface

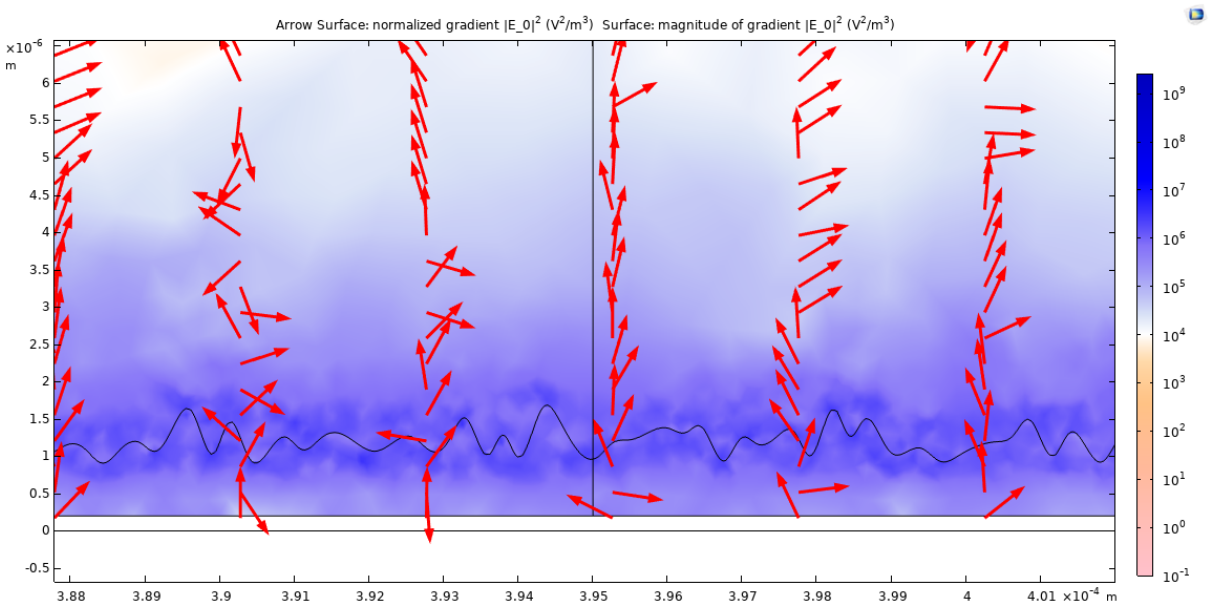

Figure 150: A zoomed-in view of the COMSOL simulation of $\nabla|\mathbf{E}|^2$ in the OET chip without illumination with 1 randomness on the surface

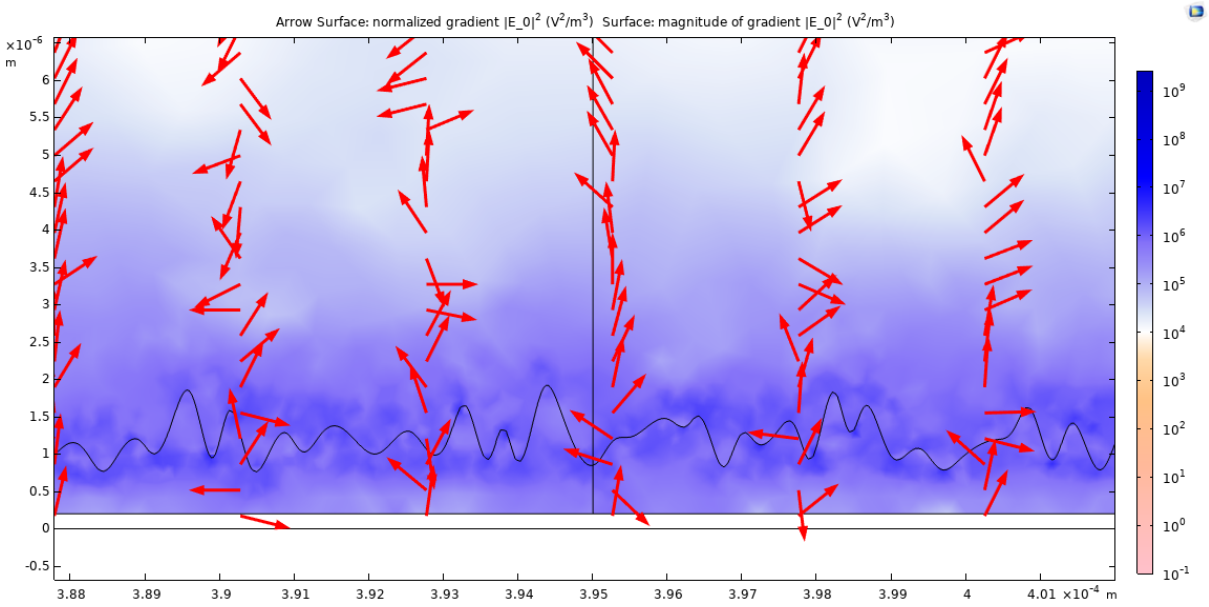

Figure 151: A zoomed-in view of the COMSOL simulation of $\nabla|\mathbf{E}|^2$ in the OET chip without illumination with 1.5 randomness on the surface

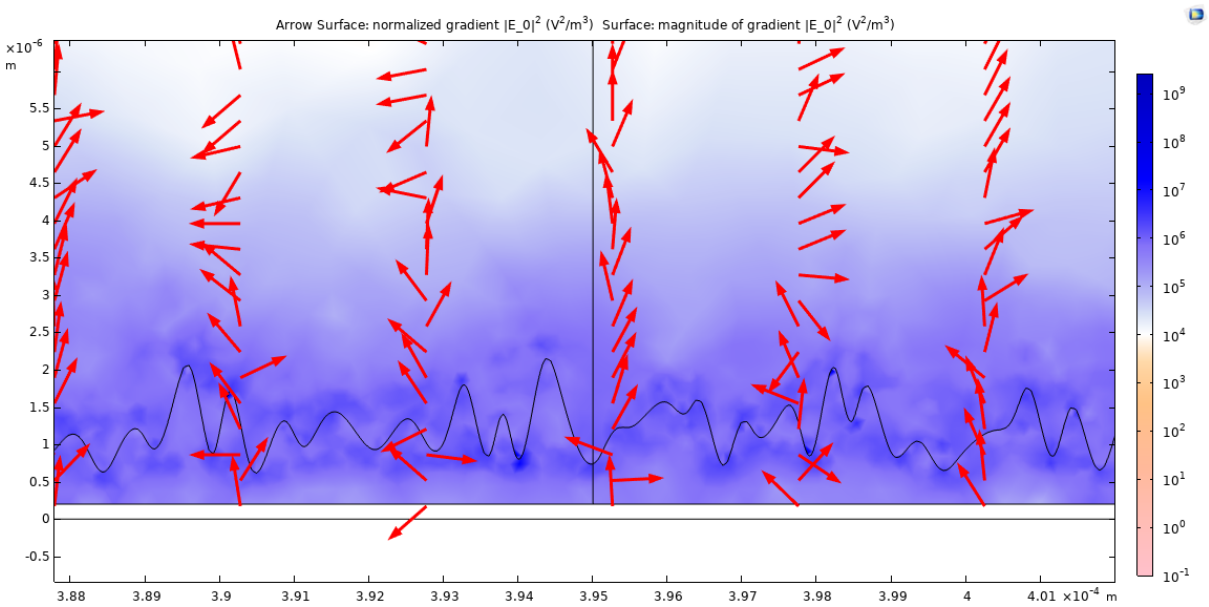

Figure 152: A zoomed-in view of the COMSOL simulation of $\nabla|\mathbf{E}|^2$ in the OET chip without illumination with 2 randomness on the surface

B.2 MATLAB plots

B.2.1 Electric field in OET illuminated state

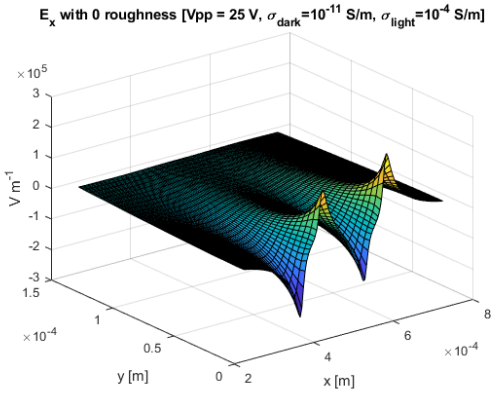

The electrical field strength in x direction

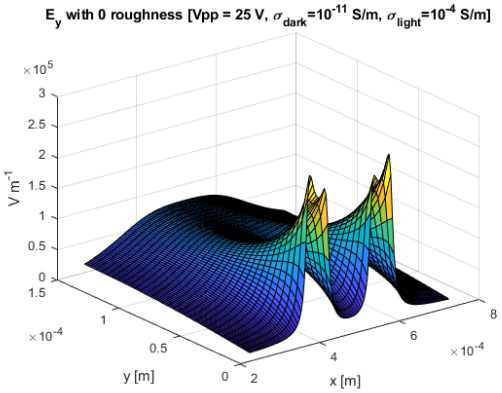

The electrical field strength in y direction

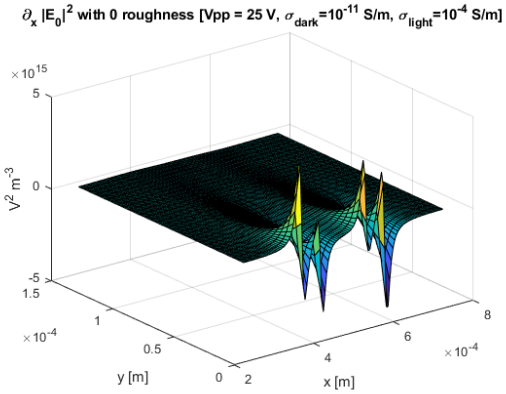

The partial derivative of $|\mathbf{E}|^2$ in x direction

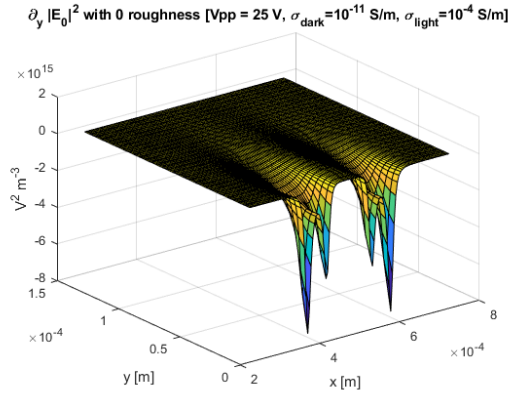

The partial derivative of $|\mathbf{E}|^2$ in y direction

Figure 153: The MATLAB plots of the electrical field using simulated data from COMSOL using a surface randomness of 0

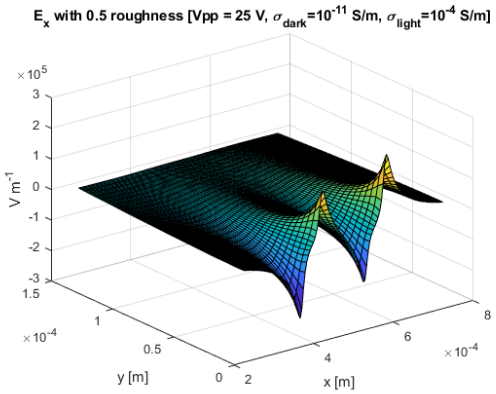

The electrical field strength in x direction

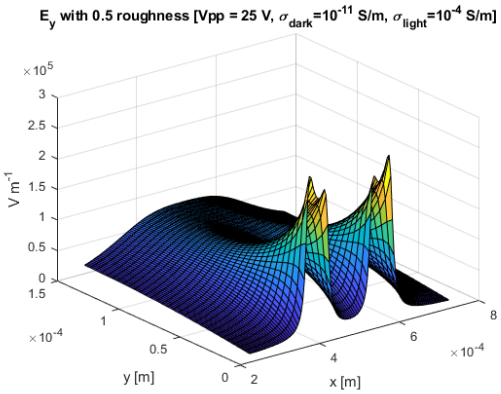

The electrical field strength in y direction

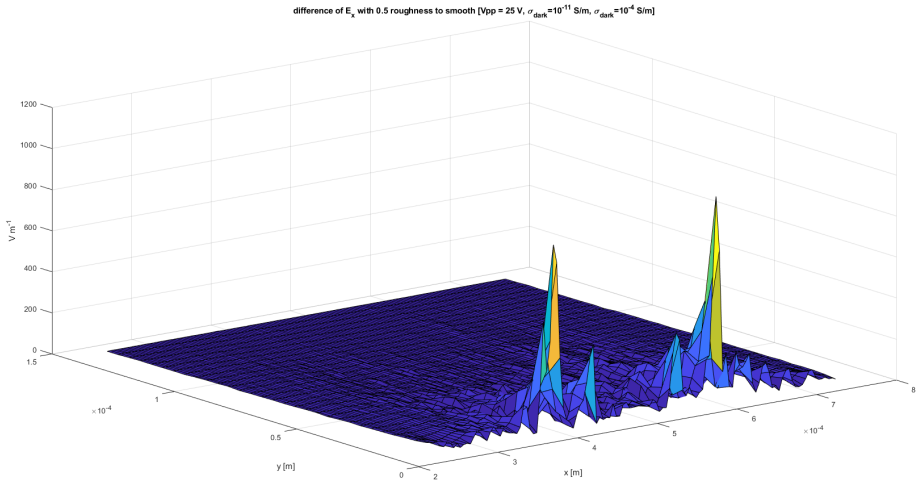

The difference in electrical field strength in x direction between the rough surface simulation and the smooth surface simulation

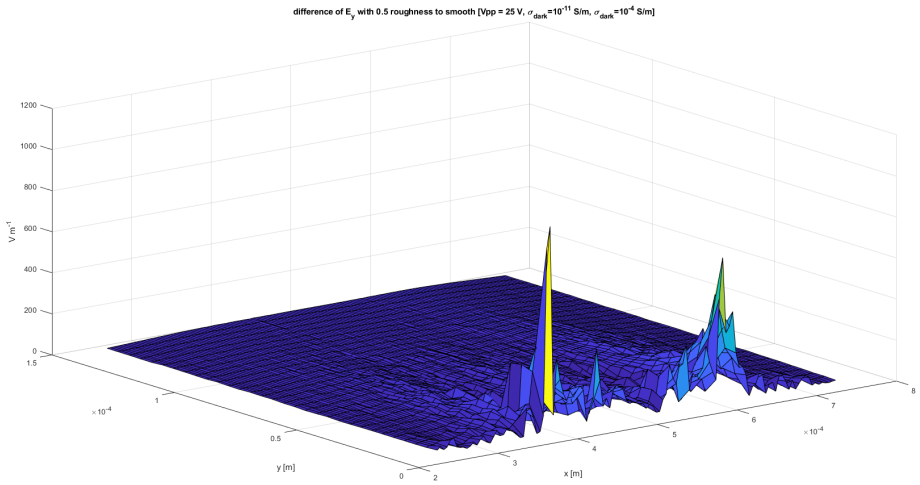

The difference in electrical field strength in y direction between the rough surface simulation and the smooth surface simulation

Figure 154: The MATLAB plots of the electrical field using simulated data from COMSOL using a surface randomness of 0.5

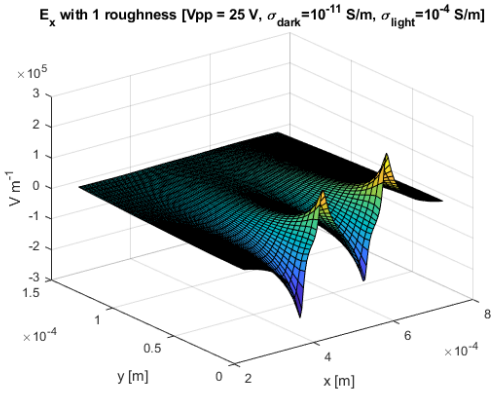

The electrical field strength in x direction

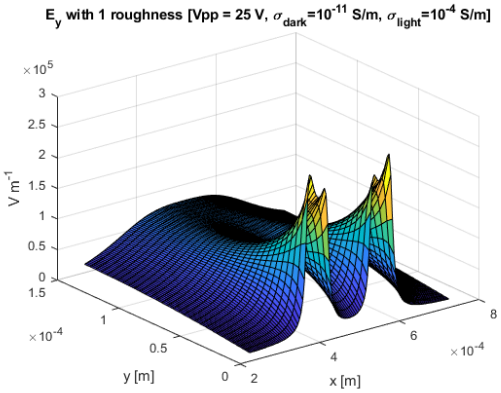

The electrical field strength in y direction

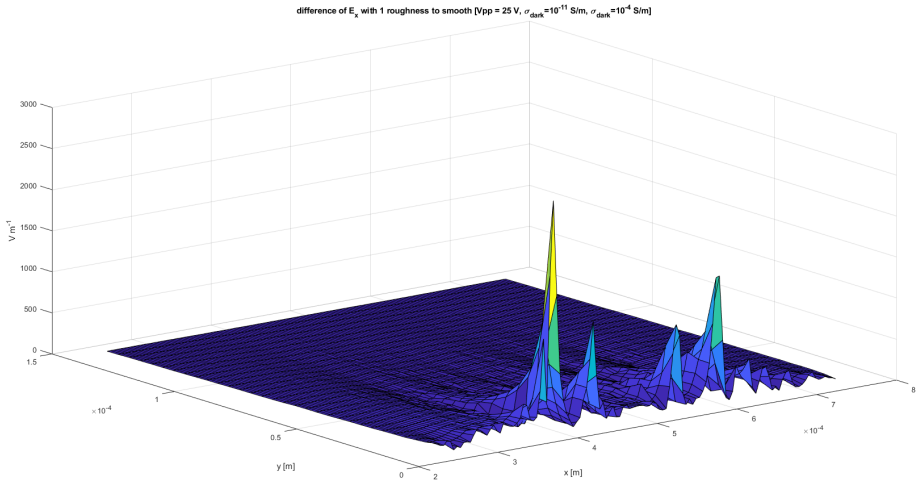

The difference in electrical field strength in x direction between the rough surface simulation and the smooth surface simulation

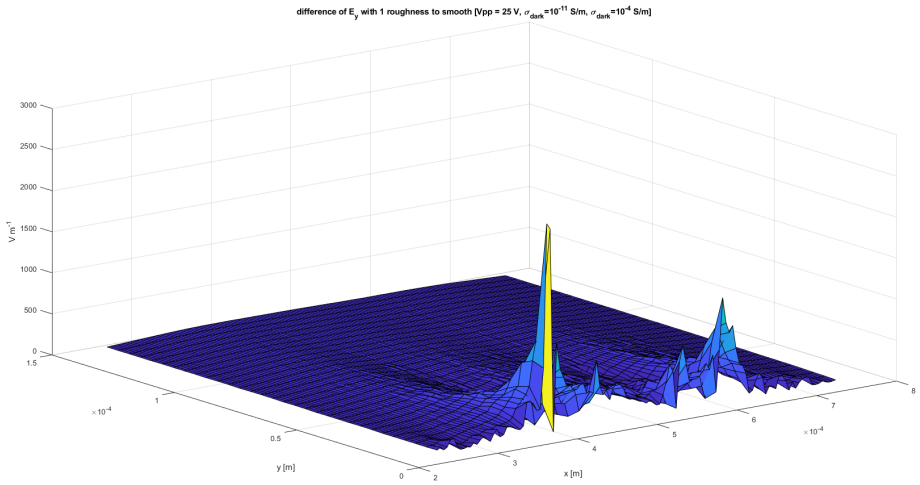

The difference in electrical field strength in y direction between the rough surface simulation and the smooth surface simulation

Figure 155: The MATLAB plots of the electrical field using simulated data from COMSOL using a surface randomness of 1

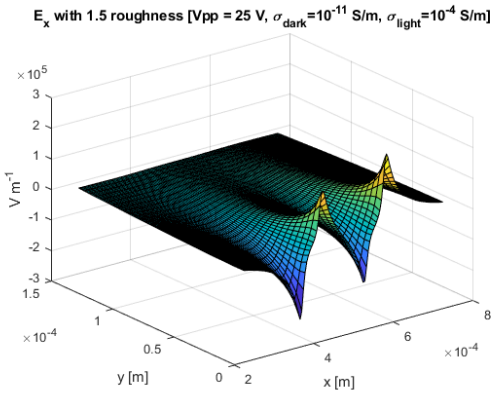

The electrical field strength in x direction

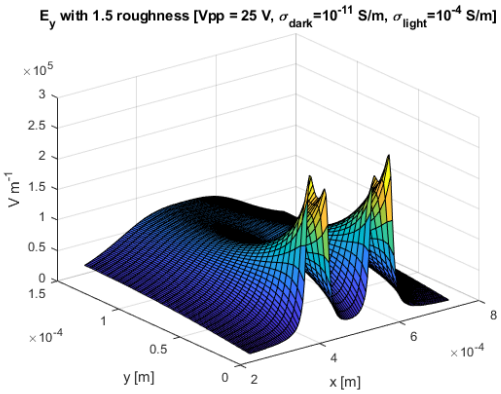

The electrical field strength in y direction

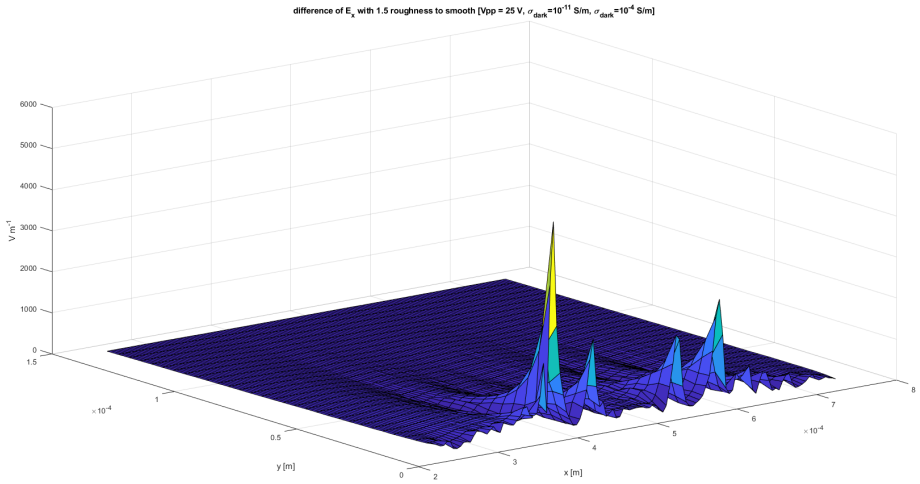

The difference in electrical field strength in x direction between the rough surface simulation and the smooth surface simulation

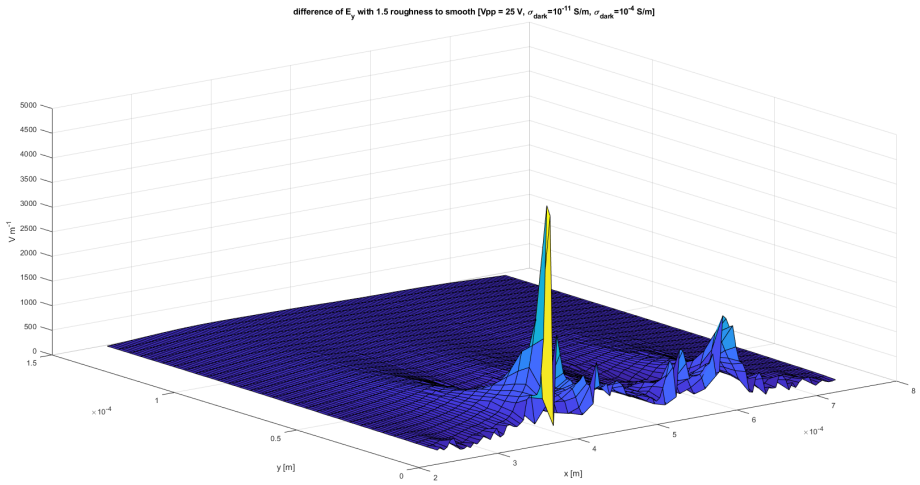

The difference in electrical field strength in y direction between the rough surface simulation and the smooth surface simulation

Figure 156: The MATLAB plots of the electrical field using simulated data from COMSOL using a surface randomness of 1.5

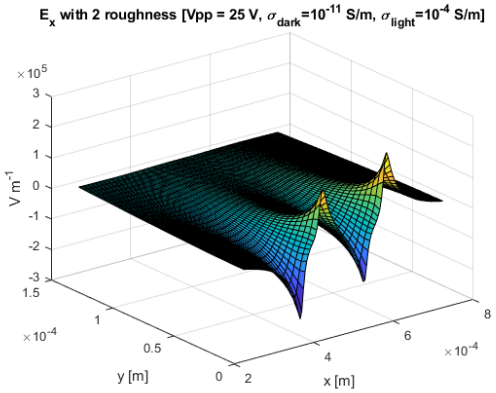

The electrical field strength in x direction

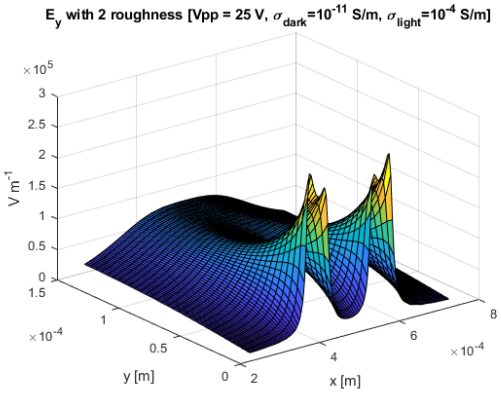

The electrical field strength in y direction

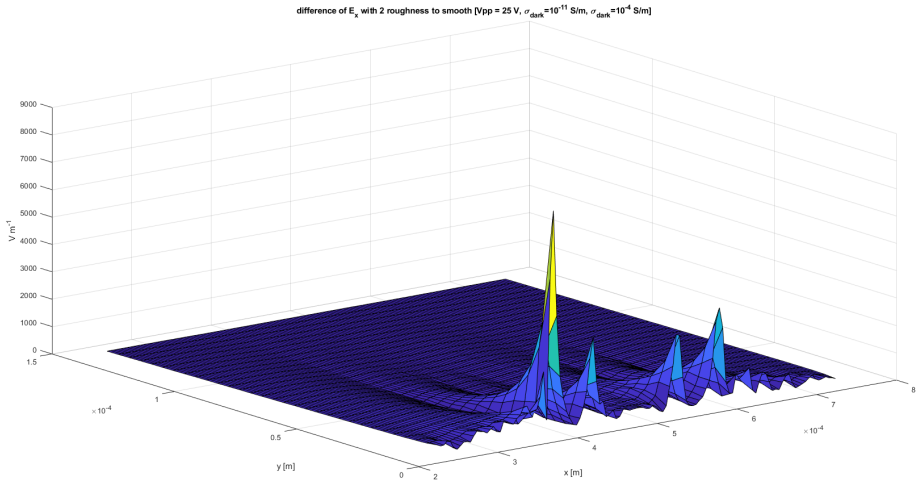

The difference in electrical field strength in x direction between the rough surface simulation and the smooth surface simulation

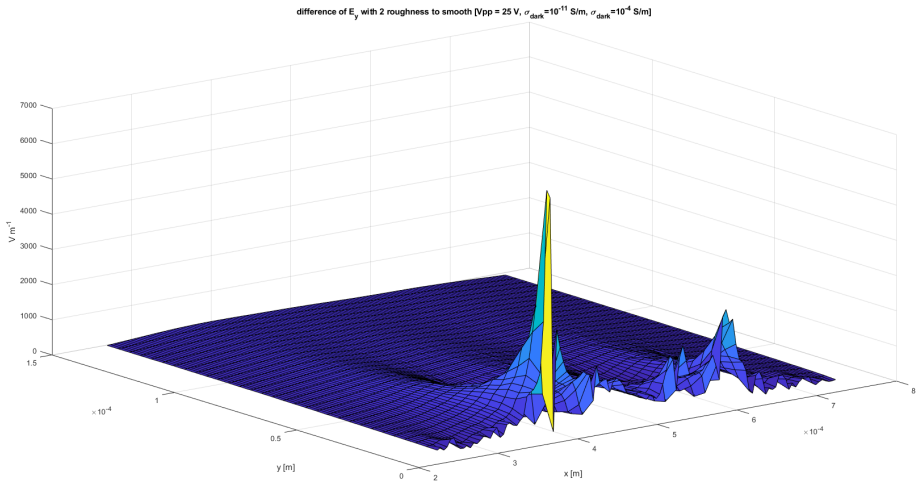

The difference in electrical field strength in y direction between the rough surface simulation and the smooth surface simulation

Figure 157: The MATLAB plots of the electrical field using simulated data from COMSOL using a surface randomness of 2

B.2.2 The gradient of the square of the norm of the electric field in OET illuminated state

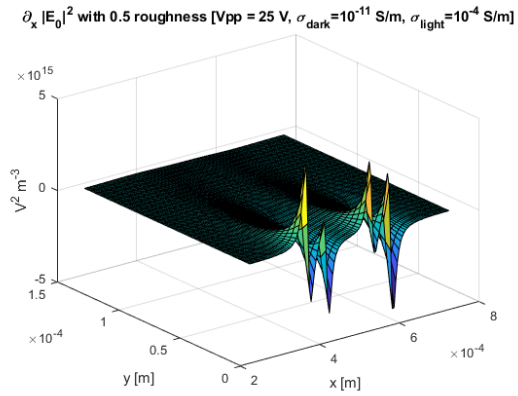

The partial derivative in x direction of $|\mathbf{E}|^2$

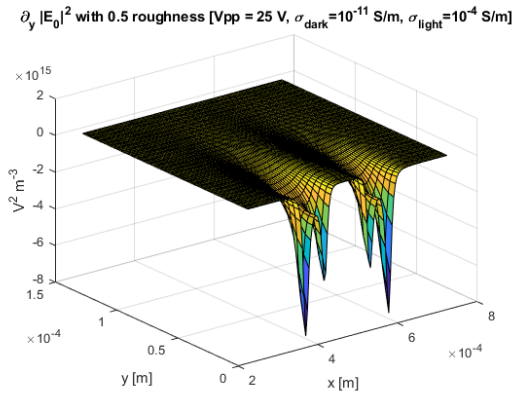

The partial derivative in y direction of $|\mathbf{E}|^2$

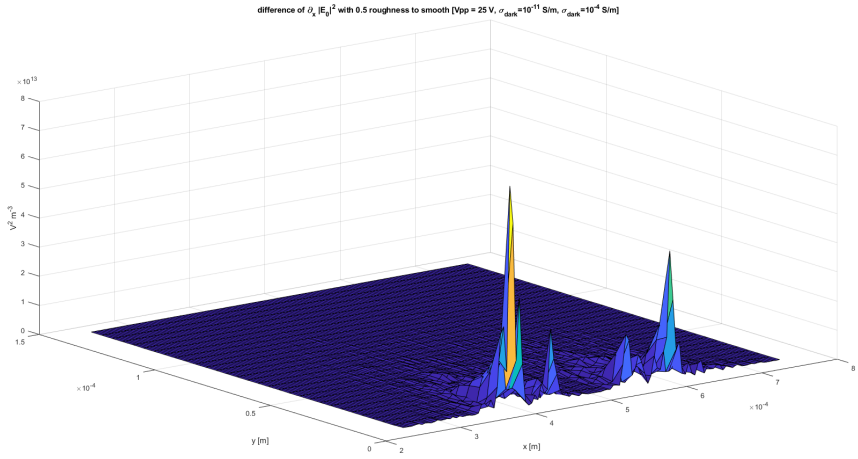

The difference in the partial derivative in x direction of $|\mathbf{E}|^2$ between the rough surface simulation and the smooth surface simulation

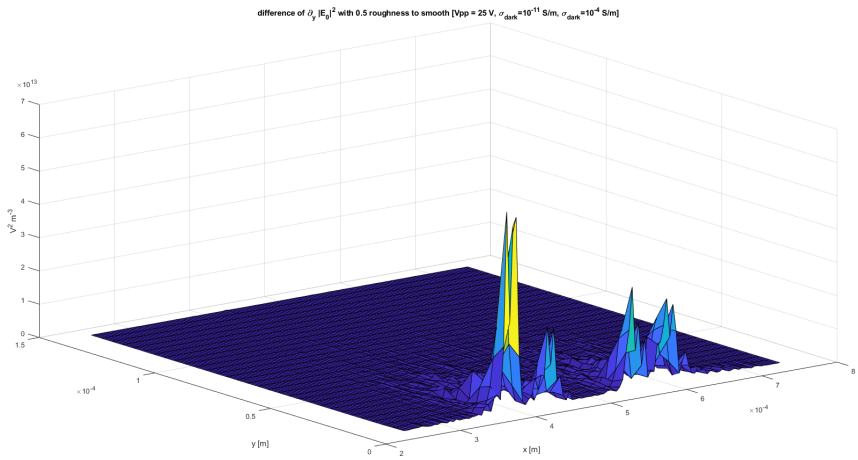

The difference in the partial derivative in y direction of $|\mathbf{E}|^2$ between the rough surface simulation and the smooth surface simulation

Figure 158: The MATLAB plots of $\nabla|\mathbf{E}|^2$ using simulated data from COMSOL using a surface randomness of 0.5

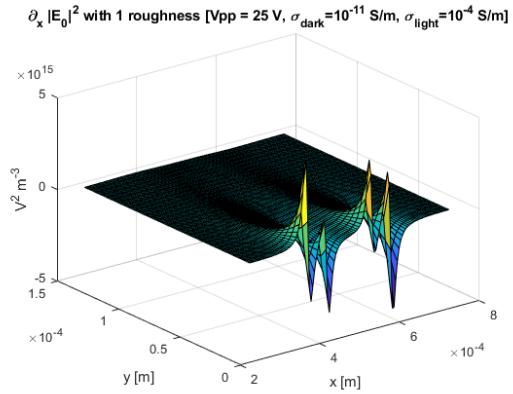

The partial derivative in x direction of $|\mathbf{E}|^2$

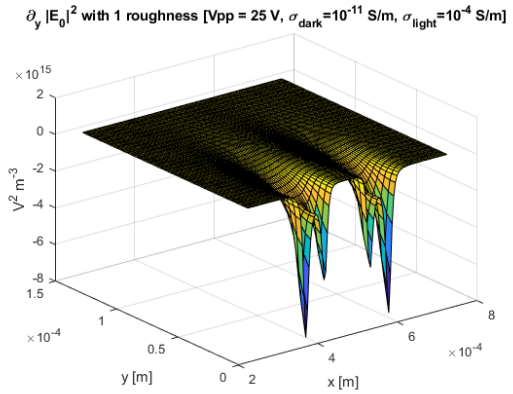

The partial derivative in y direction of $|\mathbf{E}|^2$

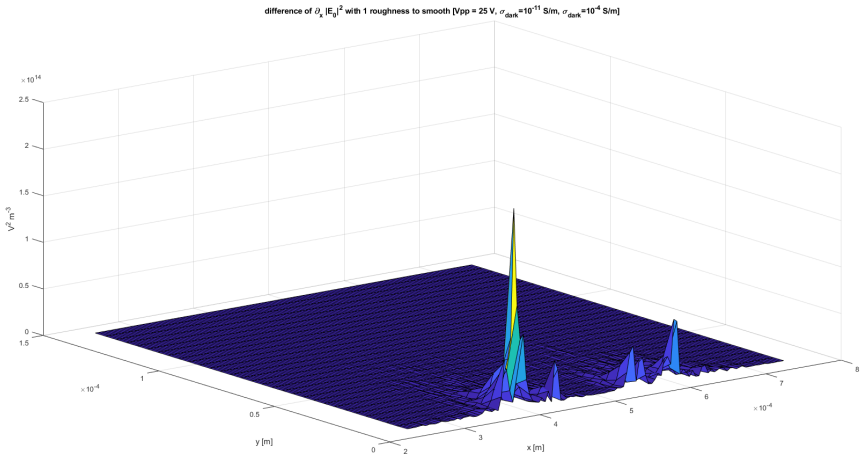

The difference in the partial derivative in x direction of $|\mathbf{E}|^2$ between the rough surface simulation and the smooth surface simulation

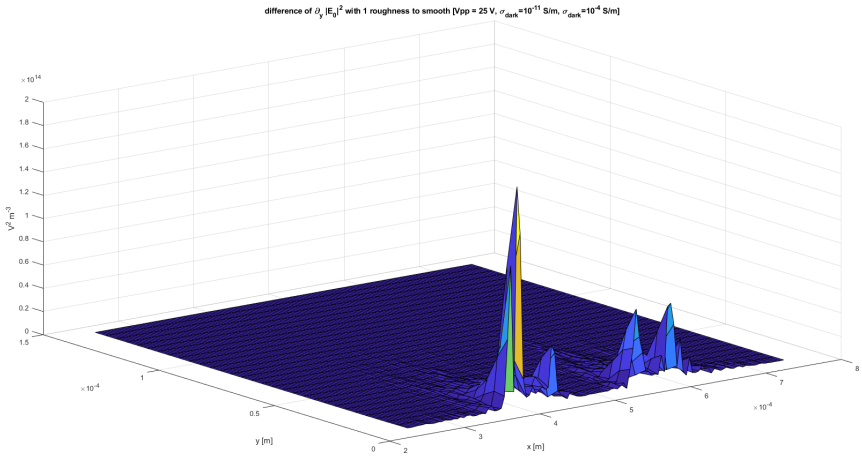

The difference in the partial derivative in y direction of $|\mathbf{E}|^2$ between the rough surface simulation and the smooth surface simulation

Figure 159: The MATLAB plots of $\nabla|\mathbf{E}|^2$ using simulated data from COMSOL using a surface randomness of 1

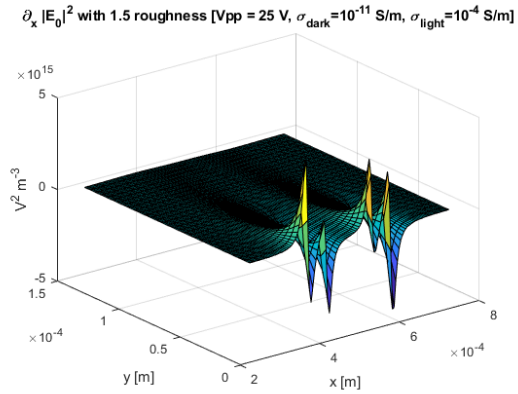

The partial derivative in x direction of $|\mathbf{E}|^2$

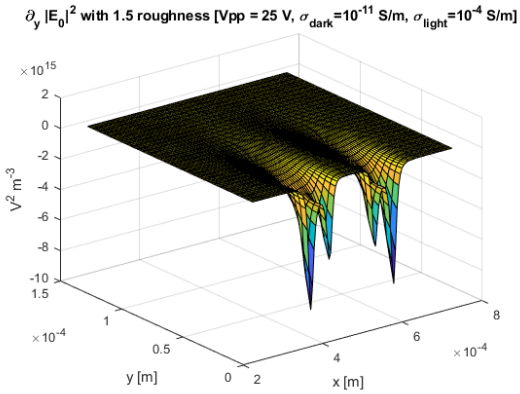

The partial derivative in y direction of $|\mathbf{E}|^2$

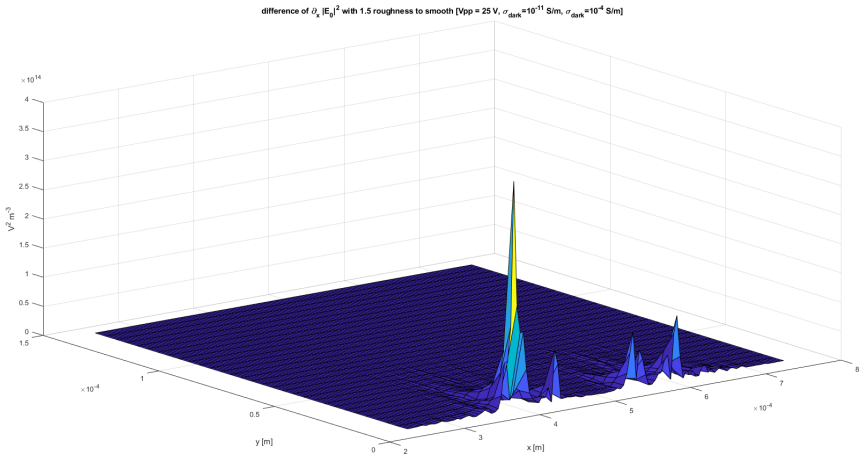

The difference in the partial derivative in x direction of $|\mathbf{E}|^2$ between the rough surface simulation and the smooth surface simulation

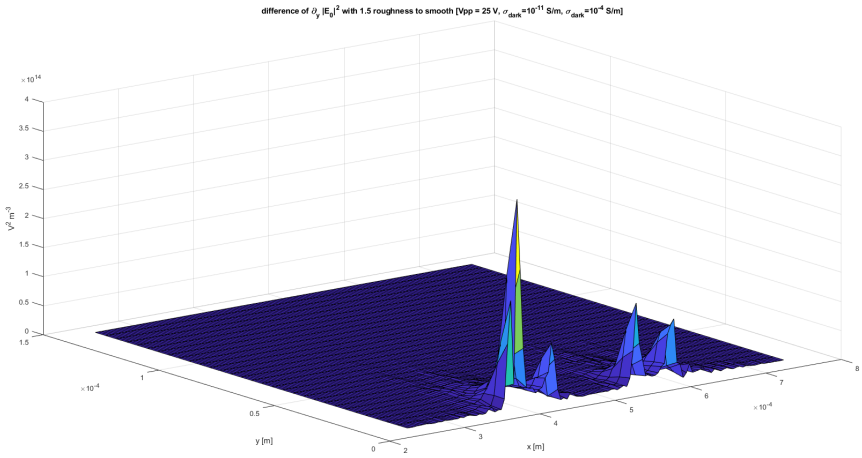

The difference in the partial derivative in y direction of $|\mathbf{E}|^2$ between the rough surface simulation and the smooth surface simulation

Figure 160: The MATLAB plots of $\nabla|\mathbf{E}|^2$ using simulated data from COMSOL using a surface randomness of 1.5

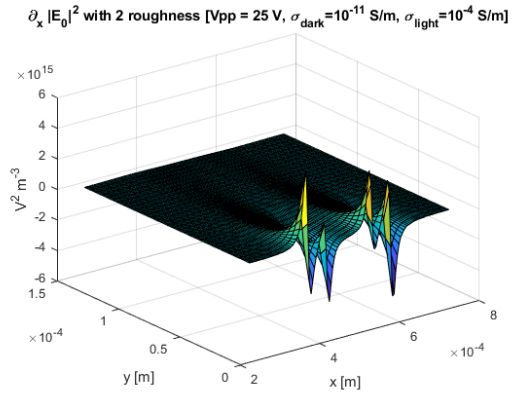

The partial derivative in x direction of $|\mathbf{E}|^2$

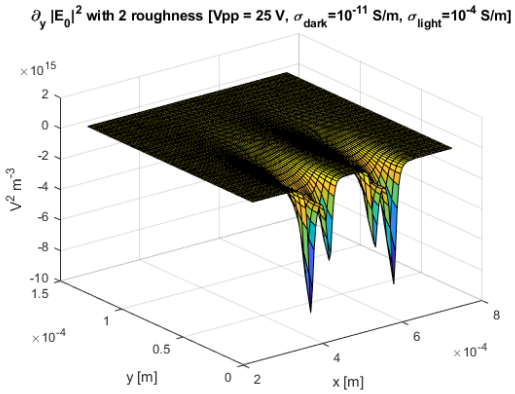

The partial derivative in y direction of $|\mathbf{E}|^2$

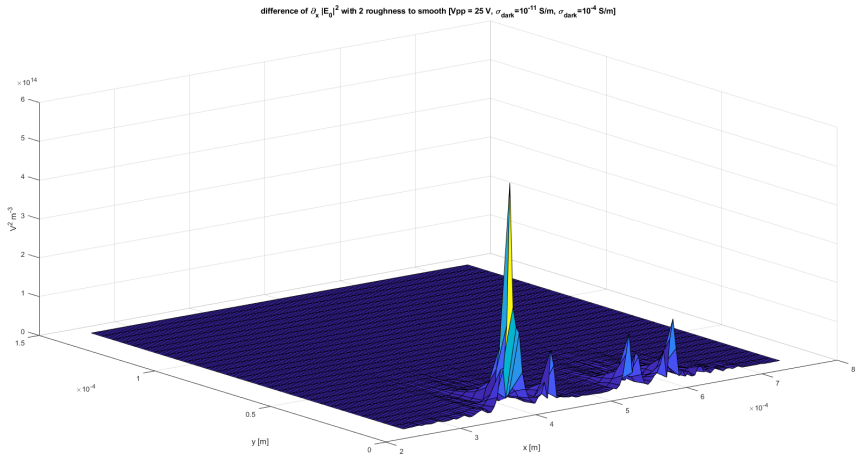

The difference in the partial derivative in x direction of $|\mathbf{E}|^2$ between the rough surface simulation and the smooth surface simulation

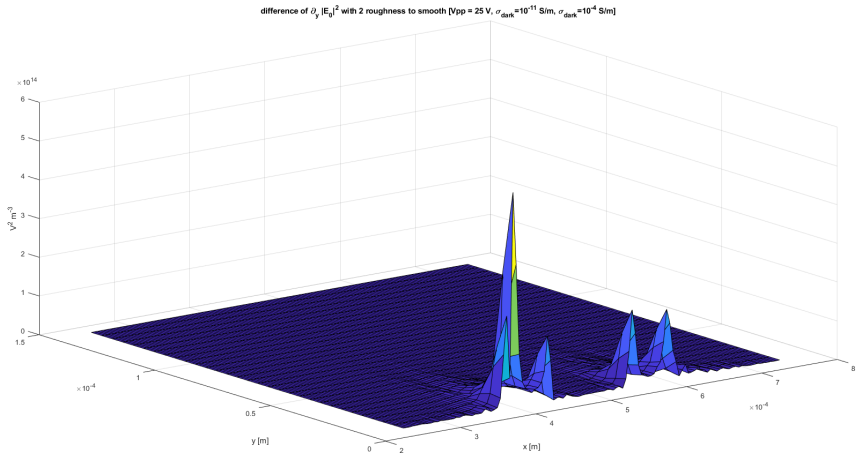

The difference in the partial derivative in y direction of $|\mathbf{E}|^2$ between the rough surface simulation and the smooth surface simulation

Figure 161: The MATLAB plots of $\nabla|\mathbf{E}|^2$ using simulated data from COMSOL using a surface randomness of 2

B.2.3 Electric field in OET off state

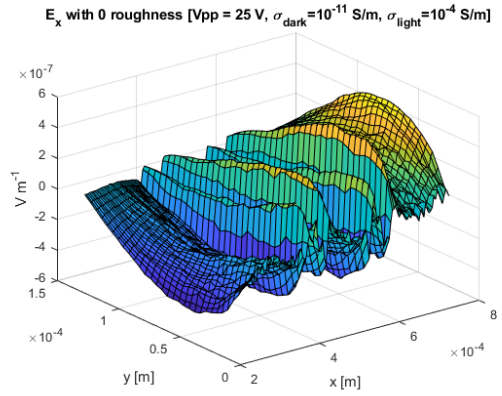

The electrical field strength in x direction

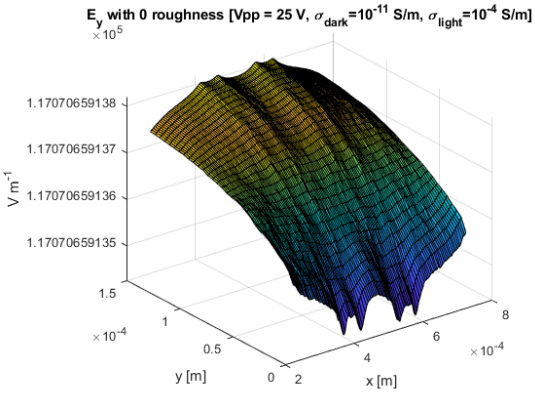

The electrical field strength in y direction

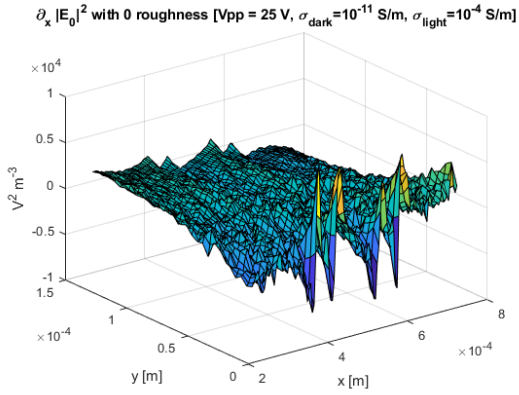

The partial derivative of $|\mathbf{E}|^2$ in x direction

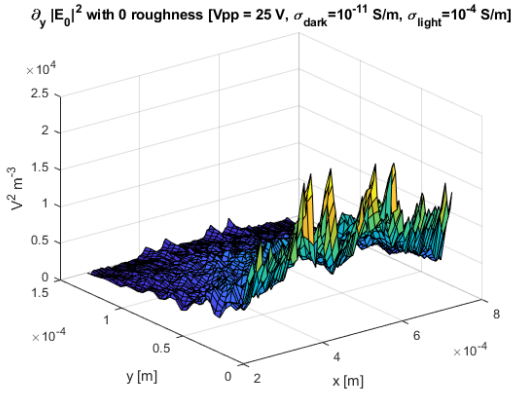

The partial derivative of $|\mathbf{E}|^2$ in y direction

Figure 162: The MATLAB plots of the electrical field without illumination using simulated data from COMSOL using a surface randomness of 0

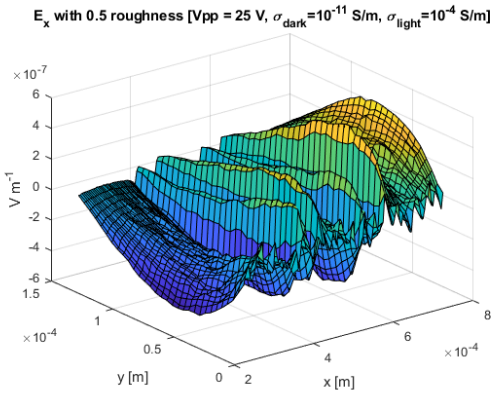

The electrical field strength in x direction

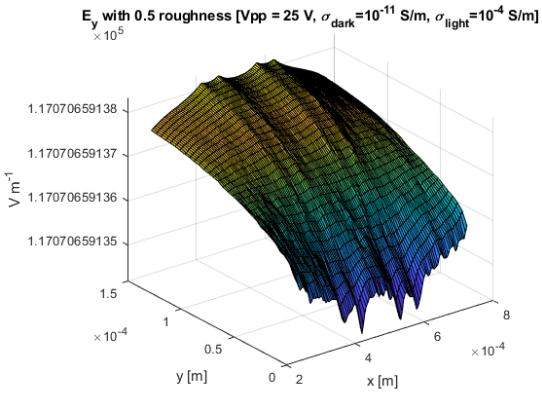

The electrical field strength in y direction

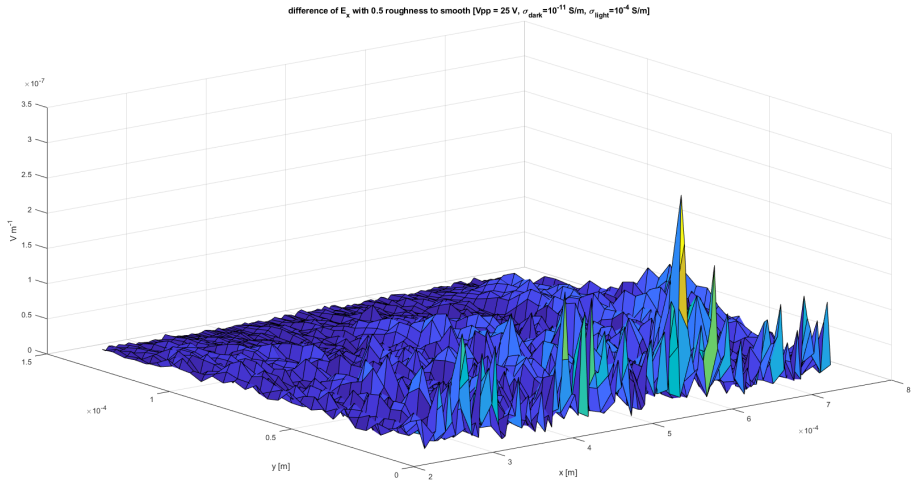

The difference in electrical field strength in x direction between the rough surface simulation and the smooth surface simulation

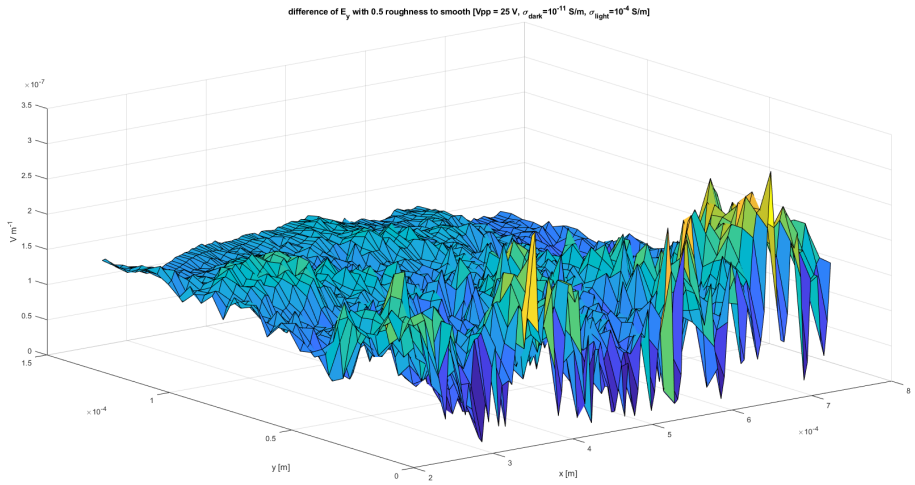

The difference in electrical field strength in y direction between the rough surface simulation and the smooth surface simulation

Figure 163: The MATLAB plots of the electrical field without illumination using simulated data from COMSOL using a surface randomness of 0.5

B.2.4 The gradient of the square of the norm of the electric field in OET off state

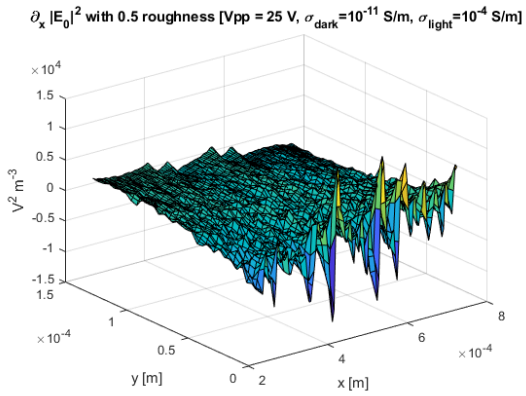

The partial derivative in x direction of $|\mathbf{E}|^2$

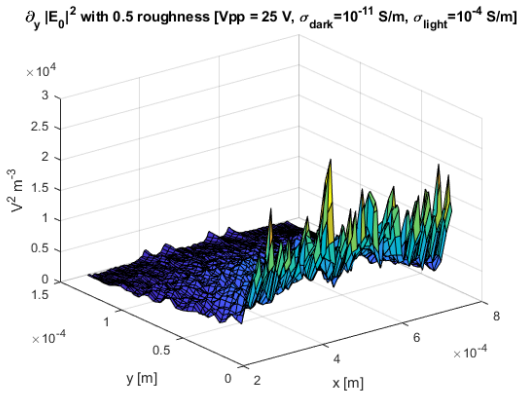

The partial derivative in y direction of $|\mathbf{E}|^2$

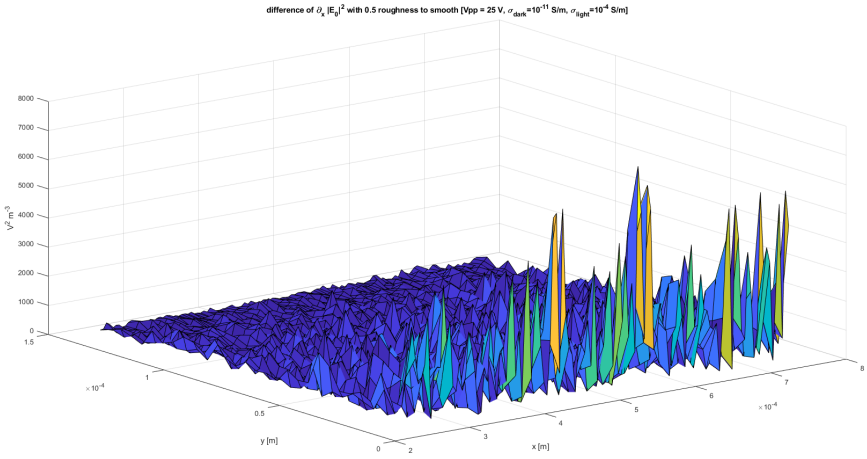

The difference in the partial derivative in x direction of $|\mathbf{E}|^2$ between the rough surface simulation and the smooth surface simulation

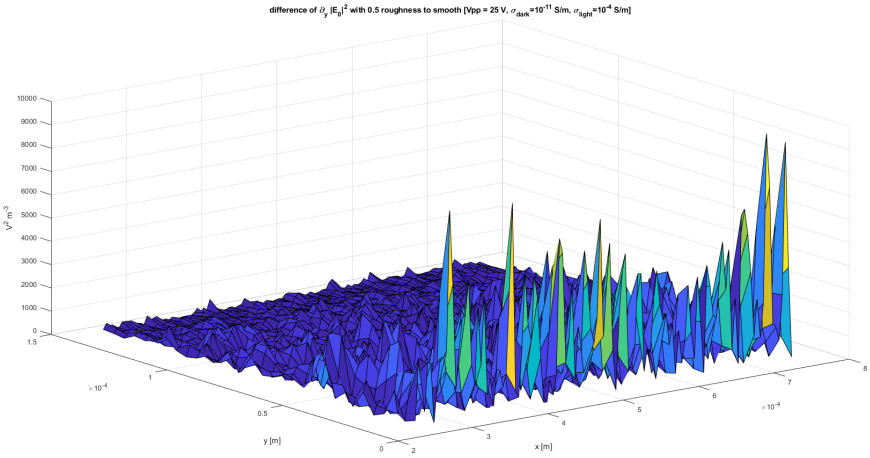

The difference in the partial derivative in y direction of $|\mathbf{E}|^2$ between the rough surface simulation and the smooth surface simulation

Figure 167: The MATLAB plots of $\nabla|\mathbf{E}|^2$ without illumination using simulated data from COMSOL using a surface randomness of 0.5

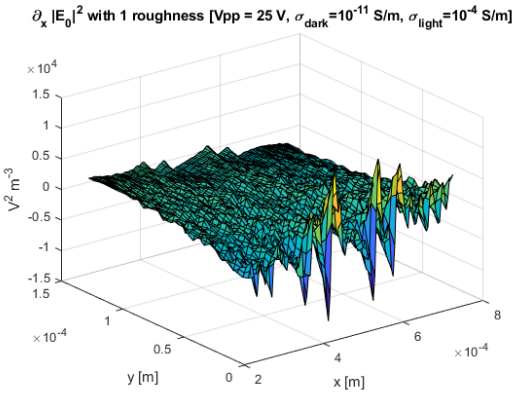

The partial derivative in x direction of $|\mathbf{E}|^2$

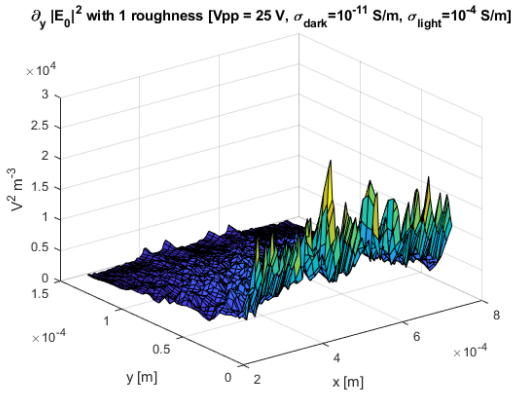

The partial derivative in y direction of $|\mathbf{E}|^2$

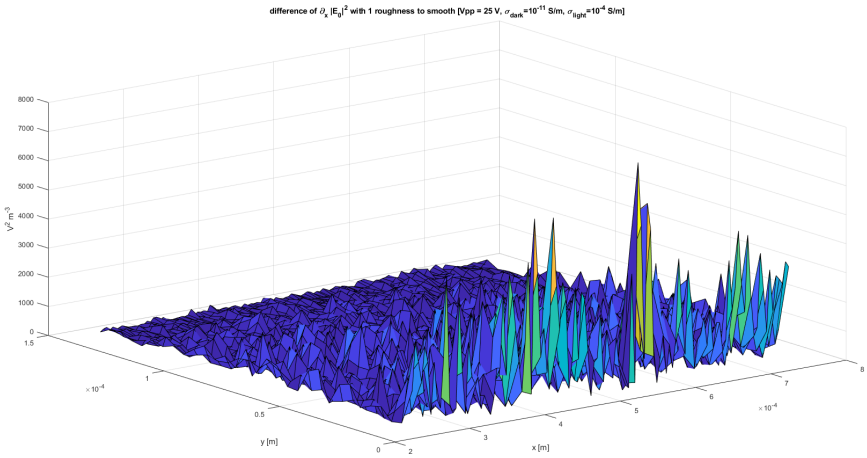

The difference in the partial derivative in x direction of $|\mathbf{E}|^2$ between the rough surface simulation and the smooth surface simulation

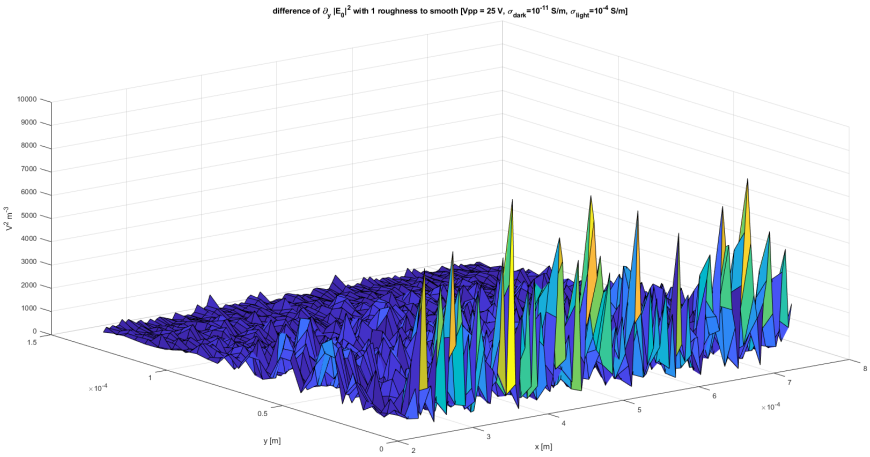

The difference in the partial derivative in y direction of $|\mathbf{E}|^2$ between the rough surface simulation and the smooth surface simulation

Figure 168: The MATLAB plots of $\nabla|\mathbf{E}|^2$ without illumination using simulated data from COMSOL using a surface randomness of 1

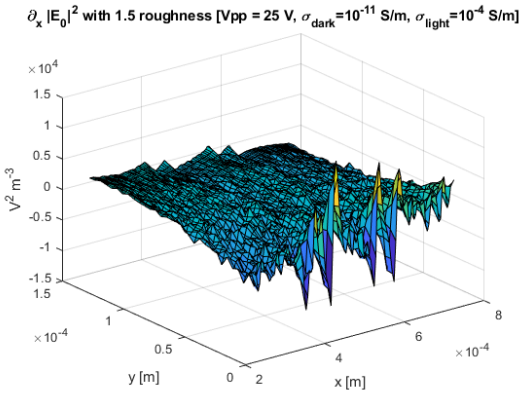

The partial derivative in x direction of $|\mathbf{E}|^2$

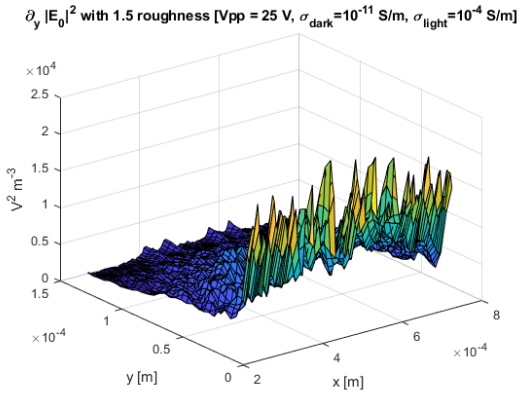

The partial derivative in y direction of $|\mathbf{E}|^2$

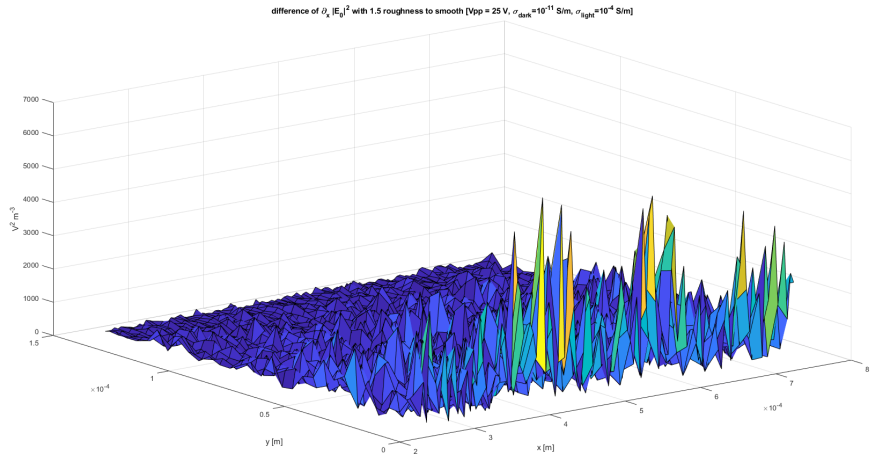

The difference in the partial derivative in x direction of $|\mathbf{E}|^2$ between the rough surface simulation and the smooth surface simulation

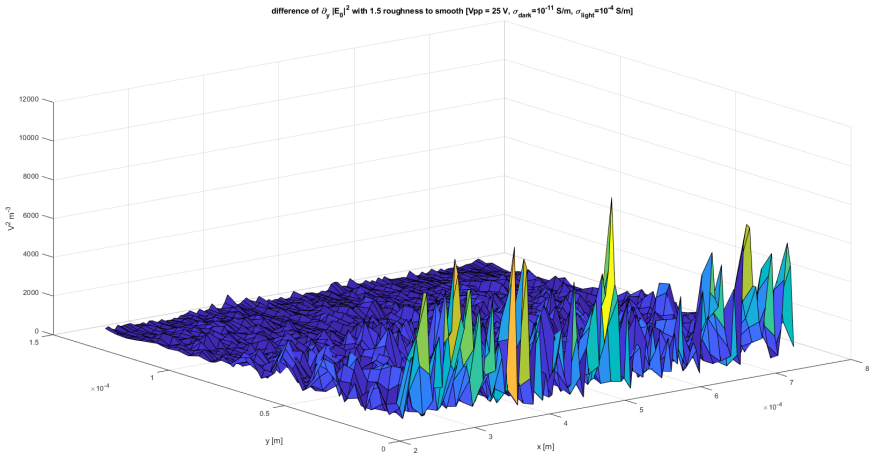

The difference in the partial derivative in y direction of $|\mathbf{E}|^2$ between the rough surface simulation and the smooth surface simulation

Figure 169: The MATLAB plots of $\nabla|\mathbf{E}|^2$ without illumination using simulated data from COMSOL using a surface randomness of 1.5

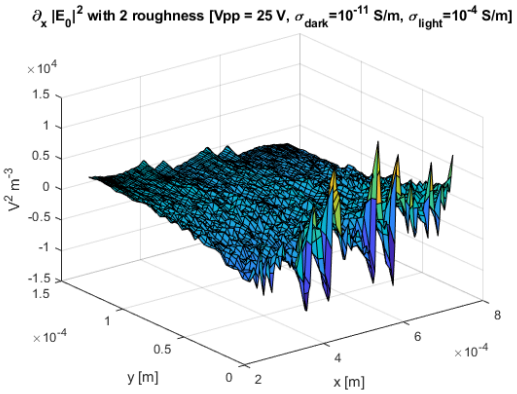

The partial derivative in x direction of $|\mathbf{E}|^2$

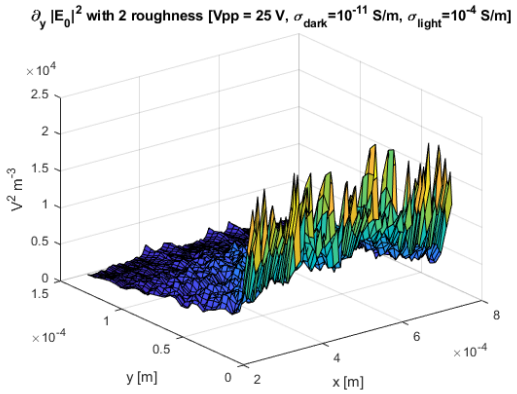

The partial derivative in y direction of $|\mathbf{E}|^2$

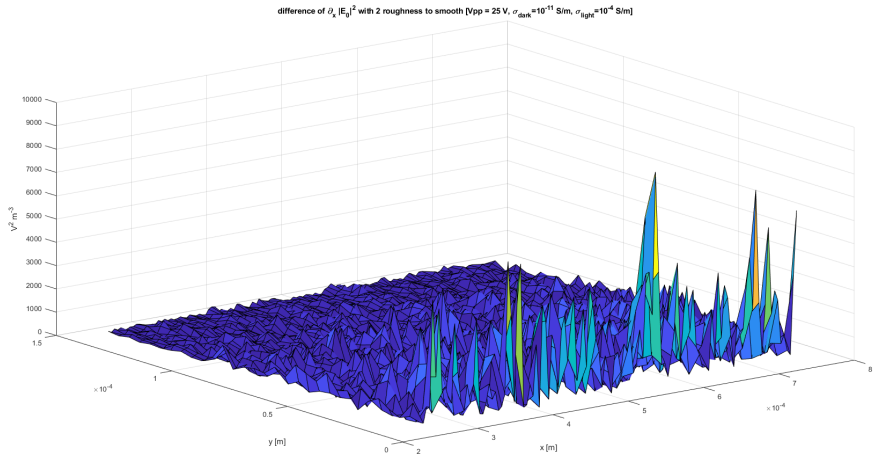

The difference in the partial derivative in x direction of $|\mathbf{E}|^2$ between the rough surface simulation and the smooth surface simulation

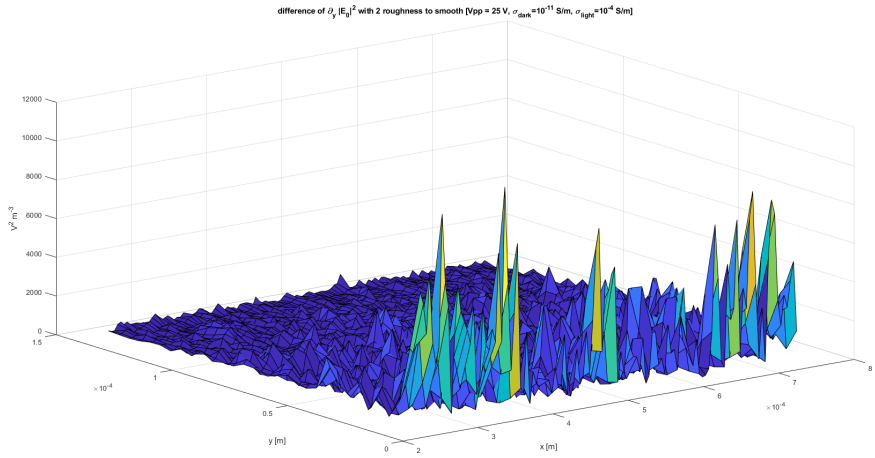

The difference in the partial derivative in y direction of $|\mathbf{E}|^2$ between the rough surface simulation and the smooth surface simulation

Figure 170: The MATLAB plots of $\nabla|\mathbf{E}|^2$ without illumination using simulated data from COMSOL using a surface randomness of 2

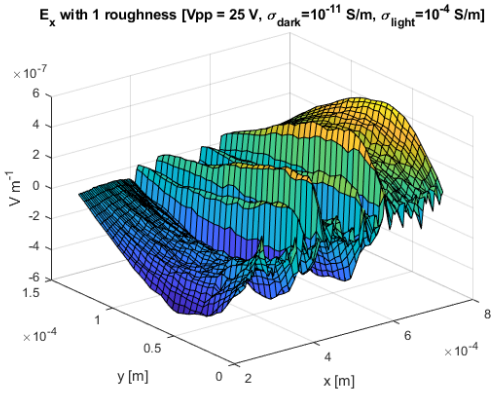

The electrical field strength in x direction

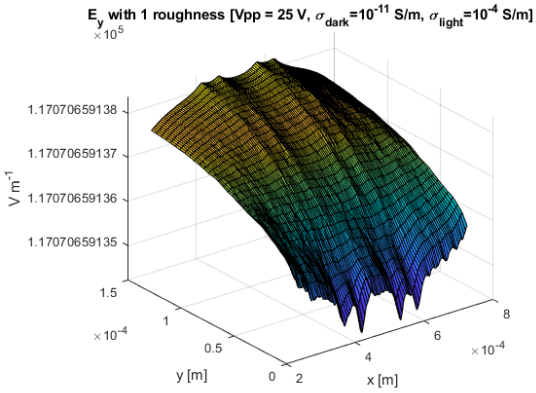

The electrical field strength in y direction

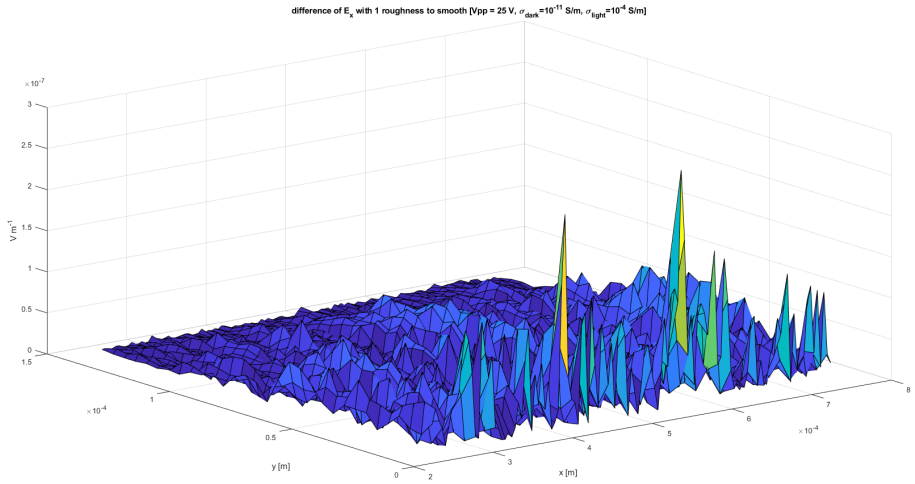

The difference in electrical field strength in x direction between the rough surface simulation and the smooth surface simulation

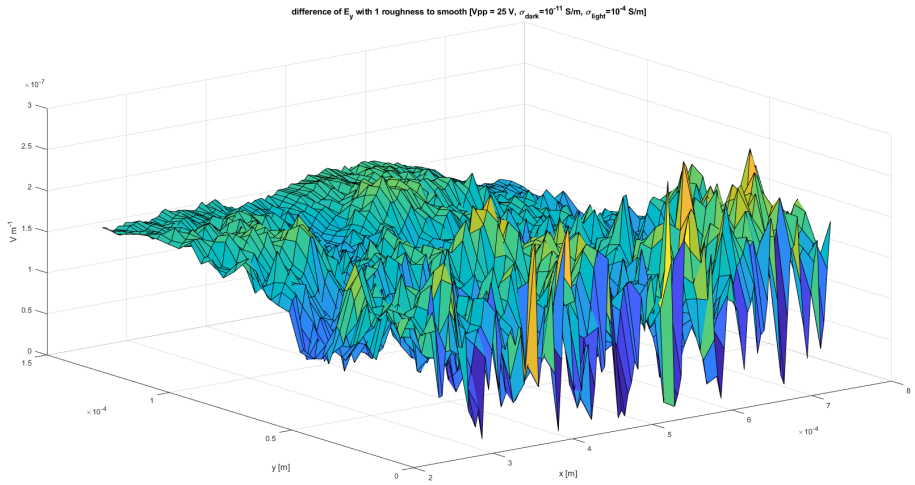

The difference in electrical field strength in y direction between the rough surface simulation and the smooth surface simulation

Figure 164: The MATLAB plots of the electrical field without illumination using simulated data from COMSOL using a surface randomness of 1

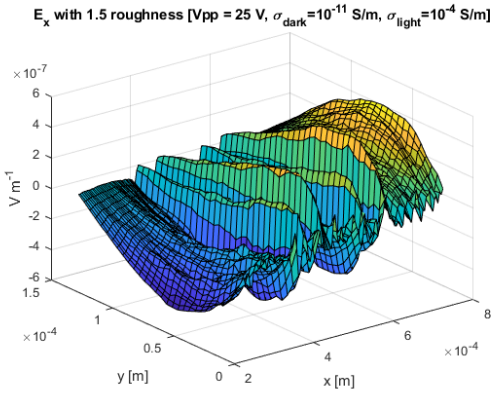

The electrical field strength in x direction

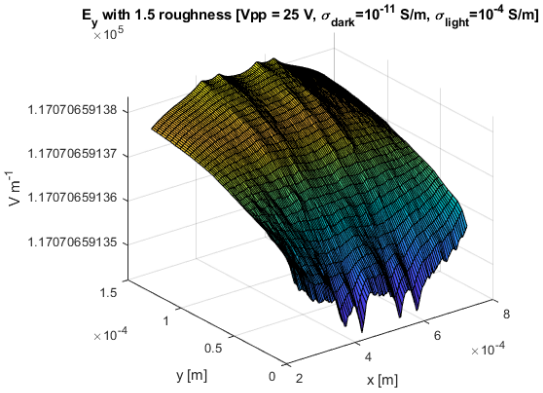

The electrical field strength in y direction

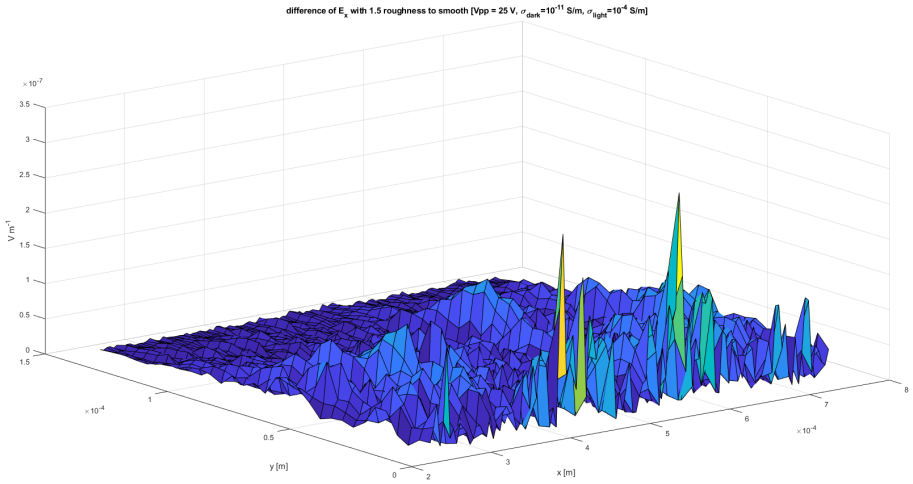

The difference in electrical field strength in x direction between the rough surface simulation and the smooth surface simulation

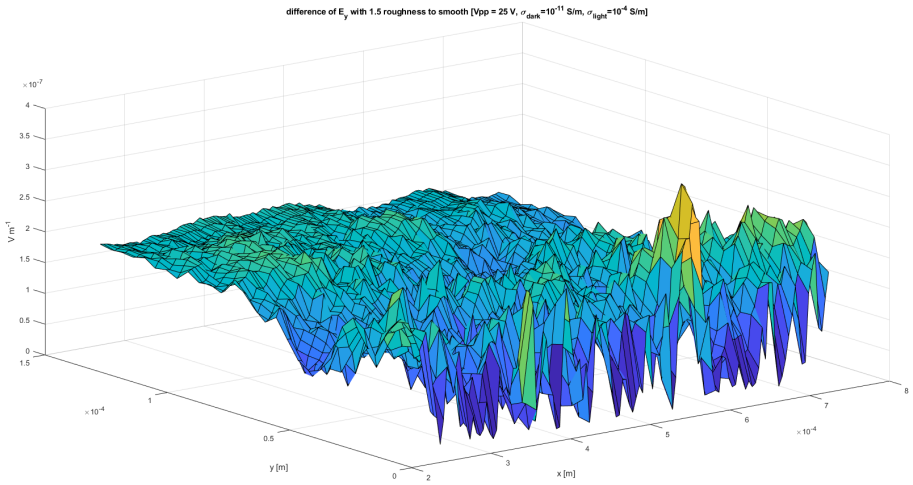

The difference in electrical field strength in y direction between the rough surface simulation and the smooth surface simulation

Figure 165: The MATLAB plots of the electrical field without illumination using simulated data from COMSOL using a surface randomness of 1.5

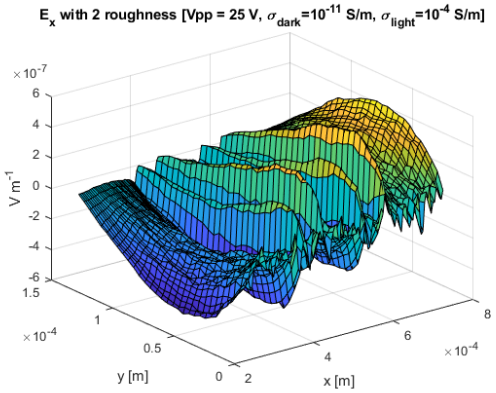

The electrical field strength in x direction

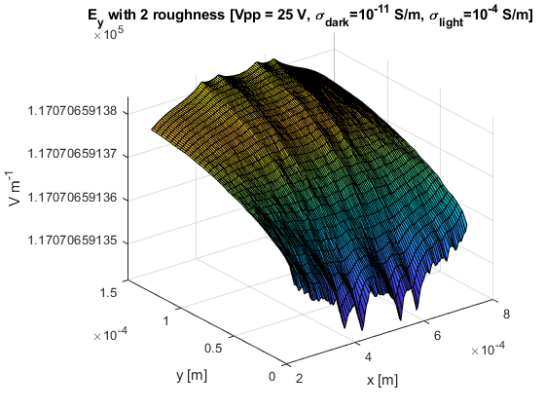

The electrical field strength in y direction

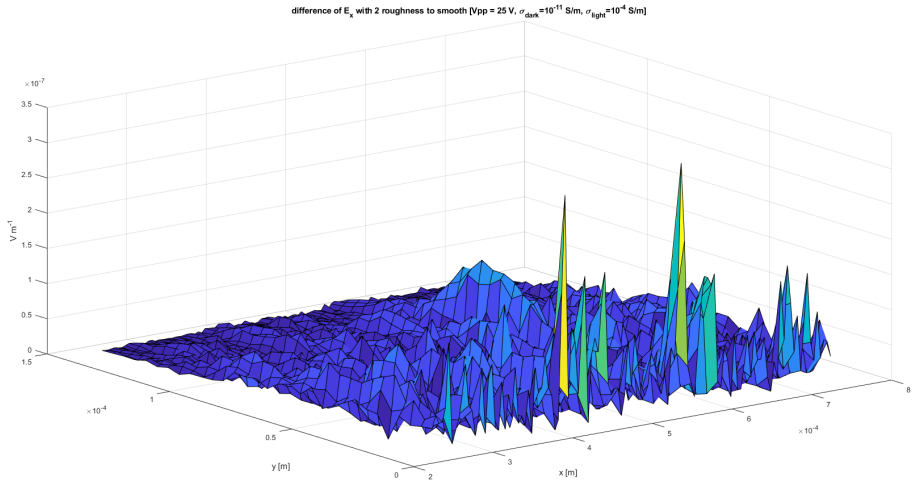

The difference in electrical field strength in x direction between the rough surface simulation and the smooth surface simulation

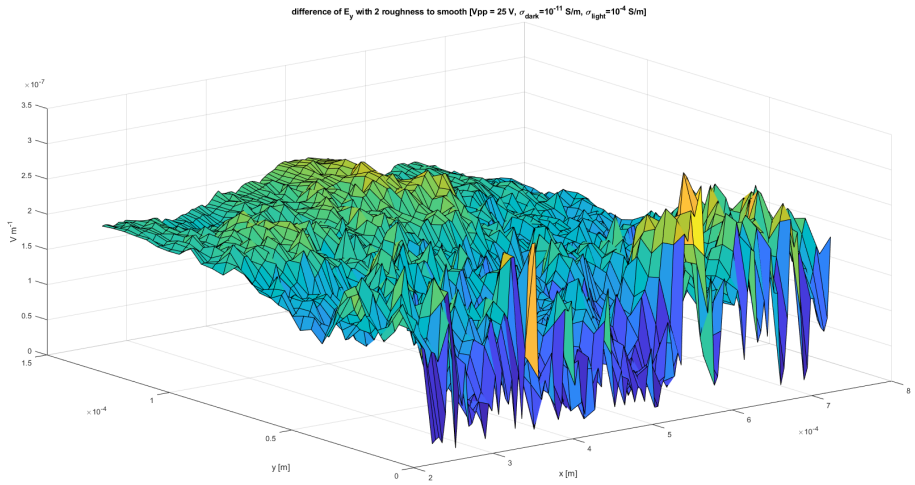

The difference in electrical field strength in y direction between the rough surface simulation and the smooth surface simulation

Figure 166: The MATLAB plots of the electrical field without illumination using simulated data from COMSOL using a surface randomness of 2